# A STUDY OF THE NEAR WAKE OF A MODEL WIND TURBINE USING PARTICLE IMAGE VELOCIMETRY

by

Jonathan Whale

Doctor of Philosophy

The University of Edinburgh

1996

## Abstract

Whole-field velocity and vorticity measurements have been obtained in the near wake of a model wind turbine using the technique of Particle Image Velocimetry (PIV). The experiments were conducted in a water channel with the turbine operating over a range of tip speed ratios, $\lambda = 1.6 - 8$. These are tip speed ratios pertinent to full-scale turbine operation which assured that the ratio of velocities at a full-scale machine were reproduced at the model. The corresponding range of Reynolds numbers, based on blade chord, was $2,600 - 16,000$. Results have been presented for both a 2-blade flat-plate rotor and a 3-blade model replica of a full-scale wind turbine.

An analysis of the velocity structure of the wakes produced mean and turbulent velocity profiles and made comparisons with results from both full-scale measurements and wind tunnel tests. Scale effect was isolated as a limiting factor in extrapolating velocity deficits from the PIV results to full-scale. An analysis of the vorticity structure identified behaviour in the wake which influenced the geometry and stability of the vortex system. The PIV images confirmed that the simple models currently being used by the wind turbine industry for design purposes are fundamentally flawed. Comparisons were made with simulations from a sophisticated vortex wake code being developed at the University of Stuttgart. Significant discrepancies were identified in wake development.

The study is viewed as a first step in determining the detailed physical processes governing wind turbine wake behaviour in order that advanced rotor performance methods may be developed.

## Acknowledgements

I am indebted to my supervisor, Colin Anderson, for providing inspiration and motivation throughout this work. His enthusiasm and dedication to the project were greatly appreciated. I am also grateful to David Skyner for his encouragement and advice and to Francis Barnes and Clive Greated for their guidance.

I would like to thank various members of the Fluid Dynamics Unit for their assistance with the experiments, particularly Tom Bruce, for teaching me the art of PIV, Jean Baptiste Richon, for helping me with the image-shifting system and Michael Linde Jakobsen, for aiding with laser beam alignment.

Thanks are also due to the technical staff of the Department of Physics, especially to Andrew Downie, for constructing the model rig, Derek Low, for building the turbulence manipulators and Frank Morris, for general assistance in the laboratory. I would also like to acknowledge Peter Tuffy for some superb photographs.

In the collaborative projects, I am indebted to Rainer Bareiß of the University of Stuttgart, for the numerical simulations of the PIV experiments, and for his enthusiastic ideas and discussion concerning wake vorticity. I am also very grateful to Prof. C.G. Helmis and Kostas Papadopoulos of the University of Athens for providing data from a full-scale wind turbine with which to compare my results, and for their support of the work at Edinburgh.

I would like to thank the following committees, institutions and companies for their financial support of my work:

The University of Western Australia; The Committee of Vice-Chancellors and Principals of the Universities of the U.K. (CVCP); The Science and Engineering Research Council (SERC); The British Council in Athens; Aerpac U.K.

Finally, I would like to thank my family and my friends for providing moral support during this project, especially to my office-mate, Michael, for pretending to recognise my Simpsons impressions.

## Declaration

This thesis has been composed by myself and, except where stated, the work contained is my own. The material of this thesis has not been submitted in any previous application for a degree.

'..Etch out a future of our own design
Well-tailored to our needs
Then fan the flames and keep the dream alive
Of a continent...

There is no enemy!
Switch off the mind and let the heart decide
We're a continent..'

**Windpower**
Thomas Dolby, 1981.

# Contents

# List of Figures

# List of Tables

# Nomenclature

## Fluid Notation

| | |
|---|---|
| $\rho$ | Density |
| $\nu$ | Kinematic viscosity |
| $V$ | A general velocity in the flow |
| $c_f$ | Speed of sound |
| $p_{vp}$ | Vapour pressure of water |
| $Re$ | Reynolds number |
| $M$ | Mach number |

## Wind Turbine Notation

| | |
|---|---|
| $R$ | Radius of the rotor blade |
| $c$ | Blade chord |
| $\Omega$ | Rotational speed of the rotor |
| $W$ | Relative velocity at the blade |
| $\lambda$ | Tip speed ratio |
| $C_Q$ | Coefficient of torque on the rotor |

## PIV Notation

| | |
|---|---|
| $L$ | Distance from the camera to the laser sheet |
| $m$ | Image/object magnification |
| $T$ | Illumination interval of the scanning laser beam |
| $\delta$ | Particle image displacement on film |
| $\Delta t du/dx$ | Displacement gradients in the flow |
| $\delta u_p$ | Perceived axial velocity due to parallax error |
| $\varepsilon$ | Absolute error in velocity measurement |
| $u_s$ | Slip velocity of seeding particle |

**Wake Notation**

| | |
|---|---|
| $x$ | Downstream distance (measured from the hub of the model rotor) |
| $y$ | Cross-wake distance (measured from the hub of the model rotor) |
| $h$ | Depth below water surface |
| $b$ | Width of the wake |
| $U_0$ | Freestream velocity |
| $u$ | Component of velocity in downstream direction |
| $v$ | Component of velocity in cross-wake direction |
| $u'$ | Axial velocity ratio |
| $U_c$ | Velocity on wake centreline |
| $V_s$ | Swirl velocity in the wake |
| $\sigma_0$ | Mean velocity fluctuations in the freestream |
| $\sigma_u$ | Longitudinal velocity fluctuations in the wake |
| $\sigma_u'$ | Turbulent velocity ratio |
| $\Delta\sigma_u'$ | Added turbulence in the wake |
| $\zeta$ | Vorticity |
| $\zeta'$ | Normalised vorticity |
| $\zeta_c$ | Vorticity translated from offset plane onto wake centreline |
| $\Gamma$ | Vortex strength |
| $a$ | Vortex radius |
| $\Phi$ | Flux of vorticity across downstream station in the wake |
| $\Phi'$ | Normalised vorticity flux |
| $p_0$ | Pressure at a point far upstream |
| $p$ | Pressure at a point in the wake |
| $p_{hs}$ | Hydrostatic pressure in the wake |
| $\epsilon_{sb}$ | Solid blockage factor in the water channel |
| $\epsilon_{wb}$ | Wake blockage factor in the water channel |

S.I. units used throughout

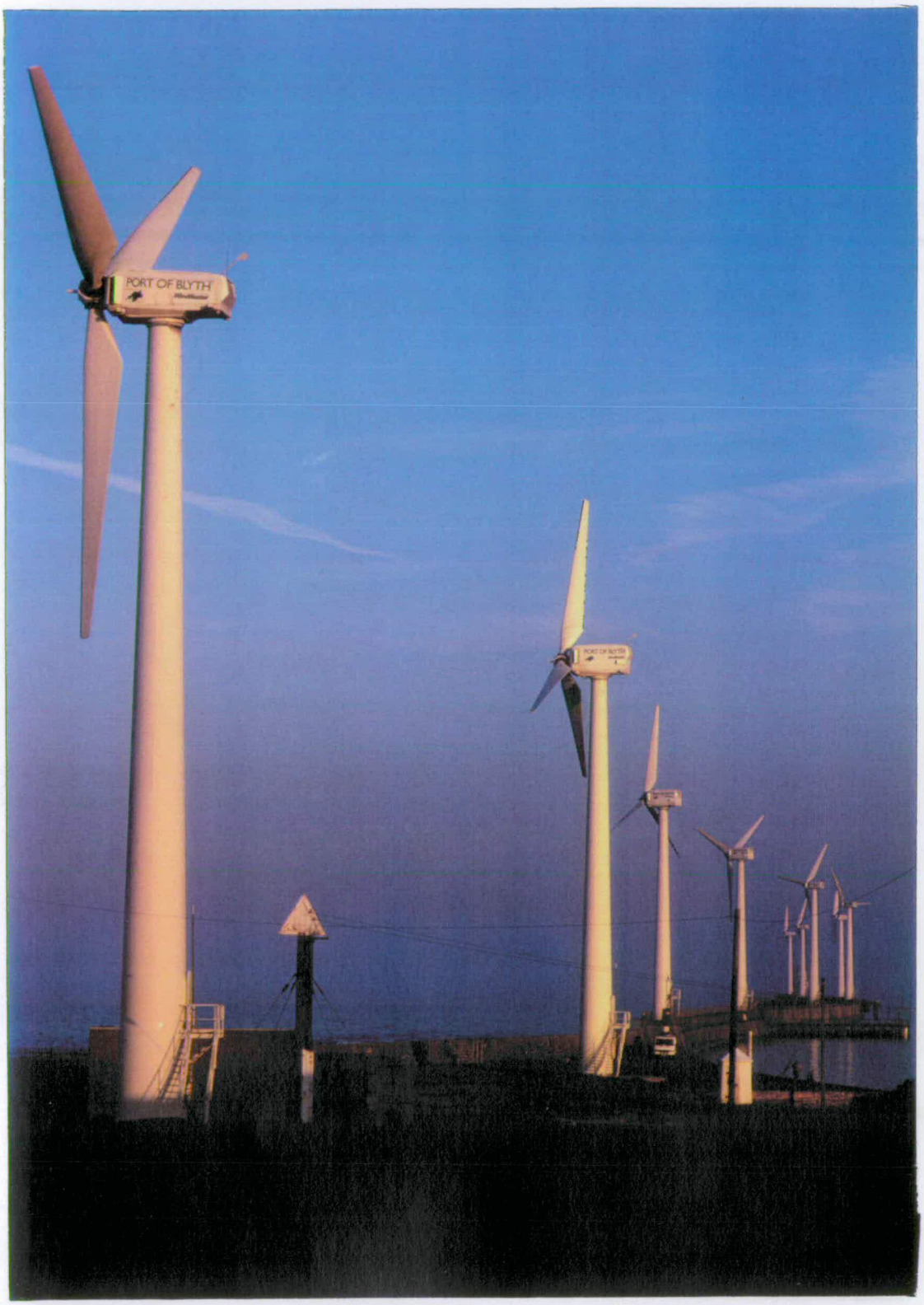


Growth of wind energy in the U.K. – turbines at Blyth Harbour.

# Chapter 1

## INTRODUCTION

### Overview

This thesis concerns an experimental study of the flow past a model wind turbine in a water channel using the technique of Particle Image Velocimetry (PIV). The motivation for the PIV experiments is examined in this chapter. Some background material in the study of wind turbine wakes is presented with reference to full-scale measurements, wind tunnel tests and numerical prediction codes. Studies examining the wake vortex structure and studies relevant to the mean and turbulence characteristics in the wake are reviewed separately. The objectives of the PIV experiments are listed.

## 1.1 Motivation for the Study

The growth of wind energy in recent years has been dramatic to say the least. In July 1995, it was estimated that the installed wind turbine capacity worldwide was 4000 MW[75]. The rate of growth is also impressive. In the European Union, 471 MW were installed in 1994 compared with 370 MW the previous year. According to the EWEA[1], 10% of the European Union's electricity could realistically be generated by wind power by the year 2030[91]. To meet this demand would require

[1]European Wind Energy Association

the installation of about 200,000 500kW turbines. As these expectations become more attainable, the technical challenges that face the wind energy industry have become more urgent.

Windfarm planning and design has become a growing concern, and incorporates a desire for reliability and efficiency of wind turbines. Numerical models are used by workers in the wind turbine industry to assess the aerodynamic performance of a wind turbine. This involves predicting the thrust on the blades, the torque on the rotor and the power output of the machine. However, despite the advanced commercial development of wind turbines, some of the most fundamental assumptions of current rotor aerodynamic prediction codes appear to be in error[74]. It is widely acknowledged that present prediction codes rely heavily on empirical methods, which leads to uncertainty in the design of full-scale machines. With wind turbines of rotor diameter 45m now entering serial production, the margin for error in design becomes less and the need for accurate aerodynamic loading and performance prediction becomes paramount.

The numerical models remain inaccurate, as many of the features of the wake of a wind turbine are not fully understood or simply remain unknown. Wind turbine performance is critically dependent on the vortex structure of the rotor wake[5]. There is an interdependence between the vorticity in the wake of a turbine and the rotor inflow conditions (and hence the forces on the blades). A detailed knowledge of the vortex wake structure of a wind turbine is therefore a prerequisite for accurate modelling.

In addition, a detailed knowledge of wind turbine wake characteristics is urgently needed for the design of windfarms. It is not only the mean flow characteristics but also the turbulence structure of the wake which is of interest. In arrays of turbines, turbulence causes high fatigue rates on machines with subsequent energy production losses. Wind farm models are used by researchers in the wind energy industry to predict mean flow properties and turbulence characteristics both in arrays and within individual wind turbine wakes. More detail on the turbulence levels involved in the wake of a turbine could lead to greater insight

into the additional loads and higher rates of fatigue damage that a wind turbine experiences in a wind farm by operating in wake flow. This may indicate an optimum layout for wind turbine arrays.

The motivation for this study is the need for detailed experimental measurements to gain an understanding of the physical processes involved in the flow behind a wind turbine so that current numerical models for prediction of aerodynamic performance may be improved. Additionally, obtaining detailed experimental data can lead to the development and validation of wind farm models used in calculations of wind farm wake interaction and power output.

## 1.2 Background to the Study

Though investigations of wind turbine wakes are comparatively recent, a considerable number of reports on wind turbine wake flow have been produced in several countries [81, 72]. This thesis is solely concerned with those studies relating to horizontal-axis wind turbines (HAWTs).

### 1.2.1 Wind Turbine Wakes

The operating condition of a wind turbine is dictated by the tip speed ratio, $\lambda$. This is the ratio of the tangential speed of the blade tips to the undisturbed wind speed, $U_0$. Thus,

$$\lambda = \frac{\Omega R}{U_0} \tag{1.1}$$

where $\Omega$ is the rotational speed and $R$ is the blade radius of the machine. The wind turbine extracts kinetic energy from the approaching air flow and converts some of it to useful work by placing a torque on the rotor shaft. The air flow downwind of the rotor suffers a loss in momentum resulting in a region of reduced mean velocity known as the wake.

The wake of a wind turbine can be divided into near, intermediate and far wake regions. The extent of each region is dependent on the processes that govern the wake during the different stages of its development. The earliest theoretical models of the wind turbine wake are attributed to Lissaman[67], who used equations describing turbulent jet flow (see Section 1.2.3). The model was refined by Vermeulen[100], and later by Ainslie[8], and a general description of the development of a wind turbine wake, based on their models, is presented here.

The flow in the near wake is dictated by the extraction of pressure energy, in a step-like manner, from the mean flow at the rotor disk. The width of the wake increases and the centreline velocity drops as the air moves downstream of the rotor plane. The extent of the near wake region is typically of the order of 2 to 4 rotor diameters (D) downstream. The minimum centreline velocity is reached between 1D and 2D downstream and beyond this, fluid mixing dominates the pressure gradient effects allowing the velocity to recover. As the flow proceeds downstream, turbulence generated by the wind turbine blades gradually decays until only ambient and shear-generated turbulence remain. This signals the onset of the intermediate wake region where mean wind speed and turbulence profiles are smoother, but continue to change.

The intermediate wake region is characterised by large scale turbulence, generated in the annular shear layer of the wake, spreading into the core of the wake and reaching the centreline at around 3D–5D downstream. The wake structure evolves as the wake turbulence seeks equilibrium with the turbulence produced by the local velocity gradients in the free stream flow.

The far wake region exists beyond approximately 5 diameters downstream. The flow is characterised by a state of self-similarity. The shape of the mean velocity profiles and turbulence profiles remain unchanged with increasing downstream distance as the ambient turbulence governs the decay of the magnitude of the wake disturbances.

Turbulence in the wake and in the freestream plays an important role in the devel-

opment of a wind turbine wake. The speed and extent to which the perturbed flow recovers to free stream conditions is largely determined by the level of turbulence. There are a number of possible sources of turbulence in the wake. These include the boundary layers that form on the rotor blades, the flow separating from the nacelle and tower, the mean velocity gradient of the wake itself and the natural atmospheric turbulence in the free stream. Vortices shed by the blades could also be included as a source of turbulence, however, in keeping with the theme of this thesis, studies examining the blade tip vortex structure and studies relevant to the turbulence characteristics in the wake are reviewed separately.

### 1.2.2 Vortex Structure in the Wake

Wind turbine performance is critically dependent on the vortex structure of the rotor wake. The wake geometry determines the rotor inflow conditions and hence the forces on the blades. For design purposes it is essential to predict the blade loads accurately, to estimate rotor power output and structural stress. Thus, an accurate prediction of the underlying coherent structure in the wake is a dominant factor for reliable wind turbine aerodynamic prediction codes. An excellent summary of HAWT aerodynamics and its relation to rotor design has been provided by Hansen and Butterfield[53]. To date, a number of investigations of wake vortex structure have been attempted. The most important of these are now described.

#### (a) Full-scale visualisation

Full-scale studies aiming to capture the general flow field in the wake and around the rotor are not common. They are difficult to perform and it is hard to achieve detailed measurements of the coherent structure in the wake. They are also limited by the problems of expense and non-repeatable conditions. Flow visualisation, using tufts and high-speed flash photography has enabled flow effects on the blades of a full-scale turbine to be investigated[11]. Adopting the methods used in helicopter rotor studies[30, 65], visualisation using smoke grenades has been

undertaken by some researchers[77, 85] to gain at least a qualitative description of the flow field. Attaching the smoke grenades to either upstream masts at hub-height or the trailing edge of blades, the flow patterns were recorded on CCD video and photographic film. These indicated that the the coherent structure in the wake of a wind turbine consisted of a helical vortex system. The system comprised a weak diffused vortex-sheet core region which was shed from the trailing edge of the blades and assumed the form of a screw surface due to the rotation of the blades. In the near-wake region, this was dominated by an intense helical tip vortex system.

Savino and Nyland[85] undertook a NASA-sponsored flow visualisation study on a 100kW Mod-0 turbine. At high tip speed ratios, the air flowed around the rotor as if it were a solid disk, forming a mass of stagnant air immediately downstream of the rotor. As the wind speed increased, an expanding inboard wake was observed although this was less prominent at higher wind speeds. This is important, as stream expansion was neglected by many of the vortex wake aerodynamic models at that time. Finally, the blade tip vortex was claimed to persist not more than 2D downstream.

While the experiment served in revealing many general wake properties, it lacked detail concerning the formation and dissipation of the tip and hub vortices. Flow visualisation studies at the Test Station for Windmills, Risø[77] were more comprehensive, focusing on the formation and downstream progression of the tip vortices. The tip vortices behaved as if independent, quickly becoming out of step with the wake. This pointed towards the presence of a strong shear layer between the outer wake and the retarded wake core. The size of the tip vortices increased with windspeed and downstream distance. As they advanced downstream, they became unstable and irregular in shape. The presence of root vortices were also noted though they quickly dissipated within one blade revolution. This discovery questioned the assumption used in some vortex wake models that the tip and root vortex are of equal but opposite strength. The tip vortices are seen to persist longer at moderate wind conditions ($\lambda = 6-8$) and travel a distance of 2D−3D downstream before dispersion. The researchers made the observation that energy

was preserved within the tip vortex when there was a high difference between the freestream flow outboard of the tip vortex system and the retarded windspeed inside the system. Another reason for breakdown of the tip vortex system is due to the interference of the tip vortices. From visualisations using smoke grenades on two different blade tips, a preceeding vortex was seen to roll up over its neighbour. This 'pairing process' has also been reported by Langrebe[64] in helicopter studies.

### (b) Wind tunnel tests

The mixing and spreading of smoke has caused problems at full scale. For greater detail of the vortex structure, the techniques of hot-wire or laser doppler anemometry (LDA) are preferred. The use of these techniques at full-scale has not been justified in terms of results versus expense and researchers have thus opted for wind-tunnel testing. Experiments in this controlled environment reduce flow complexity and time consumption and allow for the repeatability of experiments.

Some preliminary flow visualisation studies in a wind tunnel were undertaken by Alfredsson[10] who looked at the vortex structure shed by the blade tip subject to various ambient turbulence levels. The tip vortex was seen to dissipate earlier in the presence of higher turbulence. This observation, along with the 'pairing' behaviour of mutually interacting vortices were later confirmed at full-scale at Risø.

A more comprehensive study of tip vortices and vortex sheets was performed by Green[52] using LDA on a modified aircraft propeller of 150mm diameter. Traverses of the wake with the LDA equipment highlighted the initial development of the wake and results were displayed in the form of velocity deficit profiles and turbulence intensity profiles. The experiments revealed that measurements along the axis did not adequately represent the state of the whole flow. Instead, the velocity deficit was predominantly contained in an annulus remote from the centreline. Flow visualisation was used to reveal an intense tip vortex structure. Smoke was

injected into the wind tunnel and a camera used to take pictures of stroboscopically illuminated flow. Green also witnessed the 'pairing process' reported by Alfredsson and questioned whether it was a natural consequence of vortex sheet roll-up. The strength and persistence of tip vortices was consistent with the Risø findings although Green viewed the tip vortices as a 'roller-bearing mechanism' between the retarded wake and the faster external stream. He proposed this roller-bearing action delays the entrainment and mixing with the outer flow that occurs in less structured wakes.

Wind tunnel investigations of the near wake include Vermeer and van Bussel[98] who performed axial and radial traverses with a cross-wire probe on a 1.2 metre, two-bladed rotor. Measurements of the instantaneous velocity in the near wake were separated into effects due to blade passage (a fast but consistent fluctuation) and effects due to the trailing vortex sheets (a region with more stochastic character). A similar study was conducted on a 1.0 metre, two-bladed model using a laser doppler facility[22]. The LDV data produced cyclic time histories with the downstream passage of the wake sheet identified as a concentration of turbulence after the passing of the blade. This effect was seen most clearly at high $\lambda$ as a smaller proportion of the blade is experiencing stall and thus the near wake is less turbulent.

### (c) Prediction codes

A basic requirement for estimating turbine performance is a realistic definition of the field of flow. By incorporating an accurate representation of the geometry of the rotor wake, numerical models can be developed to predict aerodynamic loading and performance. Many of the methods concerned with prediction of HAWT performance are based on conventional helicopter and propeller theories[63, 43]. A review of these methods is given by DeVries[35].

The accuracy of performance estimates depend on the validity of the assumptions used in the models. Even assuming ideal flow (inviscid and incompressible),

the resulting integral equations contain nonlinearities and singularities. Despite advances in computational power, computer codes employing inviscid flow theory remain, in general, complex and computationally intensive. Combined blade-element/momentum (BEM) theories[37] are of a more simplified theoretical nature and form the most common basis for HAWT performance prediction codes. BEM theories, such as that incorporated in the PROP code of Wilson and Walker[106], are easy to use and require little computing time. However, as indicated in Section 1.1, there are problems with the theory. In high winds, where the rotor is partially or wholly stalled, the method often underpredicts rotor power. The discrepancy has been the subject of experimental and theoretical examination for some time. Viterna[101] developed an empirical correction for stalled flow which remains a widely used stall performance model, even though it has little foundation in the basic physical mechanisms of stall. The theory is also deficient at very low windspeeds, where high blockage exists. Predicted values of thrust fail to agree with measured results and empirical methods are usually employed in this region.

Vortex wake models attempt a more realistic representation of the wake, consistent with Glauert's[43] notion of helical vortex filaments shed from the trailing edge of the blade and convected downstream at the wake velocity. These trailing vortex filaments undergo self-induced distortions as well as being influenced by other filaments. The wake deforms into a vortex system comprising an intense tip-vortex outer region and a weak diffused vortex sheet inner region. The vortex system in the wake induces velocities at the rotor plane which affect the flow around the blade.

Classification of the various theories are based on the method in which the induced velocity is calculated at a blade section. BEM theory replaces the rotor with an actuator disk having an infinite number of blades. The method assumes the blades can be analysed as a number of blade elements (strips), which operate independently of each other. The induced velocity at a blade element is evaluated by performing a momentum balance on an annular streamtube containing the blade element. The flow is assumed to be planar or without swirl. The effect of

the induced velocity on the geometric angle of attack of the blade element, with respect to the local flow velocity, is determined. Finally, the aerodynamic forces on the element are calculated using two-dimensional lift and drag coefficients for the new angle of attack. Vortex theories are more involved and the induced velocity is determined from an analysis of the flow field created by the vortex system in the wake. Vortex methods can account for a finite number of blades as well as finite blade span and finite blade chord.

The first vortex wake models were rigid wake models. In these, the rotor wake is composed of a number of discrete helical vortex filaments of constant pitch and diameter. The velocities induced by this system of trailing filaments at each blade segment are found by integration of the Biot-Savart law[12]. Because of the assumption of constant diameter, rigid wake models are restricted to relatively low values of $\lambda$ where wake deformation effects are negligible. At these low tip speed ratios, the modelling of stalled flow poses further problems. Kocurek[62] emphasizes the importance of a stall model and states that blade stall is responsible for major uncertainty in any performance or loads analysis.

Free wake methods (FWM), however, do not require the trailing vortices to lie within circular cylinders of fixed radii. They model the self-induced wake distortions, allowing the geometry of the wake to develop under the mutual influence of the wake elements[44]. A closed solution cannot be obtained directly due to the unknown shape of the wake and its influence on the vortex distribution at the blades. An iterative process is employed in which blade vorticity and wake shape are alternatively solved until a converged solution is reached. This interdependence of the rotor and wake flows, combined with the problems of non-linearities in the flow field calculations, results in high computational costs for free wake analyses.

A third type of vortex wake model is a prescribed wake model which accounts for wake expansion or contraction through prescribed geometry functions[46, 4]. With the wake geometry defined, a prescribed wake analysis can be undertaken to predict performance. The position of the vortices and wake shape are specified

*a priori* and the Biot-Savart law applied. However, the results are sensitive to the assumed geometry and vorticity distribution.

A full vortex wake analysis is rarely used for performance prediction work, its computational expense outweighing the improvement in results. To date, HAWT designers have not found a vortex wake code that is preferred to BEM techniques. No programs are currently available that can calculate the details of an unsteady, three-dimensional free wake in a reasonable time. A balance is required between model simplification and computation time.

A variety of techniques have been employed in order to formulate a less computationally intensive free wake method[5, 6]. These are largely based on the fast free wake method (FFWM) modified from helicopter studies by Miller[73]. Attention is paid to separate sections of the wake to produce a more flexible and efficient method for each. Most promising are the vortex lattice methods[87, 82] which discretise the rotor blade and vortex sheet by a large number of surface elements (panels) with a singularity distribution on the surface or inside the blade volume. Panel methods have lead to some results which are comparable with experimental values. In the free wake code ROVLM, Bareiss[19] extends the vortex lattice method to simulate the effects of vortex shedding and roll-up in the wake.

After twenty years of research the theory for wind turbine wakes remains incomplete. The main reason is that programs are based on potential flow theory and neglect the important influence of viscous effects. In addition, the models do not take into account the concentration of the trailing vorticity, leading to inaccuracies in modelling the induced velocities at the tips of the blades. Finally, the rotor state referred to as the 'turbulent wake state'[38] can still not be accurately predicted.

### 1.2.3 Mean and Turbulence properties of the Wake

An accurate knowledge of the mean flow and turbulent structure in the wake of a wind turbine is important for two reasons. Firstly, to further the development of numerical models in predicting mean wind velocity distributions in a wind turbine wake for application to wind farms. This information will assist the planning of wind farm layout by providing reliable estimates of energy production losses due to machine interactions. Secondly, to gain insight into the additional loads and higher rates of fatigue damage that a wind turbine experiences in a wind farm by operating in wake flow. Since the late 1970s, much work has been carried out in making measurements and developing numerical methods, to predict flow properties and turbulence characteristics, both in arrays and within individual wind turbine wakes. Various references have been collected in a literature data base by Luken[69]. A review is presented here.

#### (a) Full-scale measurements

Full-scale experiments have the advantage that measurements are made at the correct scale. Difficulties arise, however, in interpretation of the data because external conditions cannot be controlled and are not always adequately known. The problems associated with full-scale measurements have often limited surveys to the near wake. Specifically, wake decay measurements are not common due to either complicated terrain or the high costs of tall meteorological masts. In addition, only a small number of campaigns have included measurements of turbulence.

A number of reports in the literature concern a similar type of study: comparing results from wake measurements from two different wind turbines on the same site. Scott[86] conducted an experimental campaign on the WEG MS-1 and Howden 300 machines on Burgar Hill, Orkney. Taylor[94] made measurements on the twin 40m diameter Nibe wind turbines in Denmark. Meteorological masts were used to record velocity deficits and turbulence contour plots in the wake of the machines. Although accurate, measurement with mast-mounted anemometers can lack flex-

ibility due to the need for one particular wind direction. This had led to various alternatives being employed including TALA[2] kites, tethered balloon soundings and acoustic sounding (sodar) techniques. Tala kites were used by Baker *et al.*[16], in investigating the wake of the 91m diameter MOD-2 turbines at Goodnoe Hills. The most comprehensive investigation using a number of these techniques was that of Högström[57] at the Näsudden site in Sweden. Measurements were taken in the wake of the 2MW, 75m diameter machine. The sodar turbulence profiles show turbulence maxima at a distance away from the centre line which is roughly equal to the rotor radius up to x $\approx$ 2D and then decreases to zero at about 4D. This is consistent with tip vortex degeneration and shear generation at the edges of the wake; the major sources of turbulence in the near wake region. Comparison with computer codes found that calculation on the Näsudden turbine generally tended to overestimate the velocity deficit although current models can now provide reasonable estimates of wake decay rates. Together with measurements from the Tændpibe wind farm in Denmark[66], the results highlighted that all models have a tendency to overpredict the power level of turbines deep within the wind farm. One of the principal conclusions of the study was that turbulence is enhanced in arrays, sufficient to cause measurable increases in fatigue damage rates.

A series of full-scale experimental measurements have been undertaken at a number of European wind farms as part of recent CEC[3] JOULE programmes[93, 97]. The results from the research project indicate that the models predict centre-line velocity deficits, centre-line turbulence level and cross-wake profiles reasonably well. However, from the model validations, it becomes clear that the near wake input data influence the model results considerably and that an improvement in the calculation results requires a better description of the near wake.

[2]Tethered aerodynamically lifting anemometers

[3]Commission of the European Communities

### (b) Scale models and simulators

Many experimental studies investigating the aerodynamics of wind turbines have involved scale models and simulators. Experiments were designed to increase the amount of wake data as well as improve understanding of wake generation and decay. Simulators were practical for studying large arrays of turbines and later were used in studies of wind turbine wakes[27]. Simulators have been used in investigations of wake turbulence by Ross and Ainslie[83] who looked in detail at the wake structure of vane-type simulators with a laser doppler anemometer. The velocity and turbulence data obtained provided the foundations for empirical wake modelling. The results show a build up of turbulence between 2D−3D, beyond which the turbulence asymptotically decays to the ambient level.

The lack of realistic power extraction and uncharacteristic turbulence patterns produced by the vane-type simulators, led to the use of more refined models. Vermeulen[99] gives a summary of experimental results for models of size 0.2–0.3m in diameter. Possibly the most extensive investigation of wake turbulence using a scale model rotor was that conducted by Green[52]. The study involved the use of laser doppler anemometry on a modified aircraft propeller of diameter 0.15m. Analysis of velocity and turbulence profiles indicated that turbulence intensity does not vary greatly within the intermediate wake region while outside the wake the turbulence intensity rapidly decreases to the ambient level. Talmon[92] reported similar findings from wake traverses behind a 0.36m diameter model.

Laser anemometry was also used by Anderson *et al.*[13] to capture the wake flow behind a 3m machine. However, problems of poor signal to noise ratio and flow seeding were experienced. Condensation of seeding on the sides of the wind tunnel meant the workers had to resort to introducing the seeding into the measurement volume by a hand-held smoke wand. The results that were gathered pointed to rotor thrust coefficient as the principal parameter which characterises the rotor wake. Together with findings from Alfredsson[10], the results also indicated that turbulence decay is a function of ambient turbulence. As the ambient turbulence increases, the wake decays more rapidly. Baker *et al.*[17] proposed the near wake

decay is governed by the turbulence created by the turbine while the decay in the far wake is governed by the ambient turbulence level.

### (c) Numerical modelling

A number of numerical models of varying degrees of complexity have been developed to predict both mean velocities and turbulence intensities within wind turbine wakes. The earliest and simplest are semi-empirical, kinematic models based on previous parametric descriptions of co-flowing turbulent jets. The wind turbine wake is considered as a jet of lower momentum than the surrounding flow, being decayed by outer flow entrainment. The models are developed as far wake models and owe their simplicity to the similarity of velocity profiles in the far-wake region. The two-dimensional Lissaman model[67], provides the basis for all jet-analogy models. While the models are useful for estimating the effect of wake decay, they do not provide insight into the physical processes involved.

A more sophisticated approach to the problem is to use the Navier-Stokes equations to describe the flow. Although the equations cannot be solved directly, a combination of simplifying assumptions and existing computational fluid dynamics experience are used to derive approximate numerical solutions. Of the models that have been developed in this manner, the two that have found the most application are the eddy-viscosity and the k-$\varepsilon$ turbulence closure techniques.

Eddy-viscosity based models are able to predict the centreline velocity deficit and the cross-wind profiles in the wake reasonably well. In an eddy-viscosity closure scheme, the shear stresses in the wake region are related to the local velocity gradients via an eddy-viscosity. Further, the local eddy-viscosity is linked to other flow properties such as the wake width and velocity deficit. The first model of this type was formulated by Ainslie[7]. Good results were presented by Smith and Taylor[89]. Their turbulence modelling compared well with experimental data and a suitable choice of eddy-viscosity was obtained using detailed shear stress measurements. The k-$\varepsilon$ model for turbulence closure was formulated by

Crespo *et al.*[34] and refered to as the UPMWAKE code. The code includes more of the terms involved in the evolution of the wake than that used by Ainslie and produces a more detailed description of the wake. In theory it should provide more accurate results for mean velocity profiles and wake turbulence than the eddy-viscosity models. This is yet to be verified as few comparisons have been made with measured results.

The eddy-viscosity and k-$\varepsilon$ models are capable, at least in principle, of providing detailed information on mean and turbulent flow components in a turbine wake for a wide range of atmospheric conditions. However in practice, such approaches are subject to a number of limitations. The codes rely on near-wake input data which influence the results considerably. In addition, the influence of the rotor is neglected and the codes do not take into account the distorted pressure field around the rotor. Madsen *et al.*[70] has made some progess in this area by developing an integrated rotor and turbulent wake model. Lastly, such models are likely to be computationally expensive and are not suitable for direct application in array performance codes. At present, they are best suited to calibrating simple parametric models or to investigating a specific flow case in detail. One promising development is the multi-parametric wake modelling of Voutsinas *et al.*[103]. It takes into account rotor geometry using vortex methods in the near wake while preserving the simplicity of kinematic models by using similarity assumptions in the far wake.

The eddy-viscosity model and k-$\varepsilon$ turbulence scheme continue to be improved and extended under CEC JOULE initiatives[33]. As indicated by Zervos[108], a number of important phenomena still need to be understood including the turbulence characteristics within wakes and wind farms and the near wake structure and development.

### 1.2.4 Particle Image Velocimetry

The problems of poor signal to noise ratio and condensation of seeding in the wind tunnel experienced by LDA workers[13, 83] together with the desire to obtain simultaneous multi-point measurements with minimum disturbance to the flow caused by instrumentation, suggested the recently developed method of Particle Image Velocimetry (PIV) for studying flows behind wind turbine rotors.

PIV is a non-intrusive velocity measurement technique which allows complete two-dimensional flow fields to be captured at a single instant[49]. The basis of PIV is to stroboscopically illuminate a two-dimensional plane of flow containing small neutrally buoyant seeding particles by means of a sheet of pulsed light. A double (or multiple) exposure photograph of this plane is taken. The spacing between the images of each particle on the film gives the local velocity. This photograph is then analysed over a grid of points to determine the local flow velocities across the whole field. Further, the velocity information can also be processed to produce vorticity maps of the flow. The technique of PIV is addressed in detail in Chapter 2.

The technique of PIV was introduced to the field of wind turbine aerodynamics by Smith *et al.*[90] who conducted tests on a 0.9m Rutland Marlec wind turbine using pulsed lasers. The tests established the applicability and usefulness of the PIV technique as a velocimetry tool for wind turbines. However, the high slipstream velocities involved in wind tunnel testing meant that seeding particles separating at the trailing edge of the blades were dispersed out of the light sheet, causing problems of illuminating the wake structure. This limited the study but detailed profiles of bound circulation and the tip vortex were obtained by concentrating on the immediate vicinity of the blade. A second study included an attempt to apply the technique to a full-scale wind turbine in the field[59]. Outdoor seeding presented a further challenge due to the need to monitor changes in wind direction. To ensure reasonable energy density for the laser sheet, a small region of flow was captured around the leading edge of a blade section. The researchers propose to aquire more detailed data by using a twin-laser configuration in future experiments.

The Fluid Dynamics Unit of the University of Edinburgh has been using the technique of PIV in the study of fluid flows since 1987. The majority of studies have concerned the application of PIV to the measurement of velocity distributions under water waves in a purpose-built water channel[50].

## 1.3 Objectives of this Study

The objectives of this study can be stated as follows:

1. to use the PIV technique to record the flow behind a model wind turbine rotor placed in a water channel
2. to compare the PIV data with wake data from other experiments, including full-scale and wind tunnel tests, as well as comparing wake geometries with predictions from numerical codes
3. to gain an improved understanding of wake behaviour in order to evaluate some of the assumptions used in theoretical techniques
4. to assess the extent to which the results on the model turbine could be extrapolated to full-scale.

## 1.4 Summary

This thesis presents the results of an experimental study of the flow past a model wind turbine in a water channel using Particle Image Velocimetry (PIV). The thesis is solely concerned with the study of horizontal-axis wind turbines (HAWTs). The objective of the work was to use the PIV technique to obtain, for the first time, whole-field data in the near wake of a turbine and to establish an experimental database for wake velocities and structure.

The need to study the wake of a wind turbine arises for two reasons. Firstly, the wake structure determines the rotor inflow conditions and hence the forces on the blades. An accurate prediction of the wake structure is a dominant factor for reliable wind turbine aerodynamic prediction codes. Secondly, the turbulent downstream flow in wind turbine arrays is a limiting factor in terms of machine spacing. Better information on wake structure will provide insight into optimum array spacing.

Efforts to improve numerical models have intensified during recent years. With regard to wind turbine performance prediction, free wake vortex methods can be used to obtain a wake geometry which models the self-induced wake distortions. The computational costs, however, limit their use in rotor design calculations. On the other hand, simpler 2D theories such as blade-element/momentum theory (BEM) are only effective in a set range of operating conditions. Present performance methods need improvement, particularly in modelling the concentration of the trailing vorticity, the 'turbulent wake state' and the influence of viscous effects. Improvement in performance methods will allow industry to optimise rotor geometry and to more accurately assess the forces on the blade under all conditions.

Concerning the prediction of wind turbine wake characteristics in a windfarm, eddy-viscosity and turbulence closure schemes have been developed which provide detailed information on mean and turbulent flow components in a turbine wake for a wide range of atmospheric conditions. To date, the accuracy of the predictions has underlined the dependency of the numerical results on available data. The codes have particular trouble in modelling the near-wake region. This region cannot be treated by simple means. It is the most complex part of the flow with problems of wake deformation, blade-wake interactions, boundary layer effects and freestream turbulence. The models used remain inaccurate as many of the features of the flow are not yet fully understood or simply remain unknown.

The lack of detailed experimental data in the wake of a turbine, and the difficulty of obtaining it, is widely appreciated. Full-scale visualisation experiments are

difficult to perform and are limited by the problems of expense and non-repeatable conditions. Wind tunnel tests using laser velocimetry techniques have experienced problems with particle seeding and signal quality.

The work reported in this thesis represented an attempt to overcome these problems, by using the technique of PIV on small-scale models. The potential for the method is significant. In particular, it could provide information about those regions of flow where theoretical techniques give least satisfactory results.

# Chapter 2

**EXPERIMENTAL PROCEDURE**

**Overview**

In this chapter, the technique of Particle Image Velocimetry is documented, from its development as a flow visualisation and measurement tool to its implementation in the laboratories at Edinburgh University. The facilities used in the PIV experiments, both in the acquisition and analysis of PIV results, are detailed. Adapting the PIV method to the study of wind turbine wakes is described.

## 2.1 The Technique of PIV

### 2.1.1 An Introduction to PIV

With the introduction of the laser to the fields of science and engineering in the 1960s, a whole number of optical measurement techniques became available to researchers in the area of fluid dynamics. Laser Doppler Anemometry (LDA) became a prominent technique, providing precise multi-component velocity measurements at a single point in a fluid flow. However, rapid development in theoretical modelling of fluid flow due to the advances in computing capabilities promoted the need for multi-point measurements. Previously, essentially qualitative flow visual-

ization techniques (e.g. streak photography) had been the only option in providing flow information over an extended area. The enhancement of flow visualization techniques with new laser and computer technology has addressed the need for quantitative, instantaneous whole-field velocity measurements.

The most promising of the new techniques in terms of accuracy, resolution and reliability is that of Particle Image Velocimetry (PIV). The flow region of interest is illuminated by an intense, high powered, pulsed or continuous wave (CW) laser. The flow is seeded with particles which accurately follow the flow. Light scattered from the particles forms mutiple-images on photographic film due to stroboscopic illumination of the particles by the laser. The recorded images are subjected to a computer/optics based analysis that produces accurate simultaneous velocity data for the illuminated flow area.

Without question, the single most important contribution of PIV is its ability to make simultaneous measurements of the velocity vector at multiple points. This velocity vector map forms the basis of all subsequent analysis. The accuracy and spatial resolution of the map make it possible to compute vorticity and other components of the rate-of-strain tensor by direct differentiation of the velocity data. If the image data may be processed so that many frames of images are converted to vector maps, it is possible to carry out accurate statistical calculations.

PIV is now firmly established as a valuable tool for the measurement of unsteady fluid flow fields. Advances in both theory and technique have progressed PIV to a level whereby detailed information, previously inaccessible by other experimental methods, can be reliably obtained in complex fluid dynamics experiments. Below is an account of the evolution of PIV since its inception more than fifteen years ago. Good reviews are given by Adrian[2] and Gray[49].

### 2.1.2 The Development of PIV

#### (a) The origins of PIV

The PIV technique arose from investigations of applications of Scattered Light Speckle Photography (SLSP) to fluid dynamics in the late seventies. A surface was generated within the fluid by using an intense sheet of laser light to illuminate a heavily seeded flow. The random interference of scattered light produced a speckle field which was photographically recorded two or more times in order to generate a 'specklegram'[36, 20].

Quantitative analysis of a specklegram is possible either by point analysis with a narrow probe laser beam[28] or by a full-field spatial filtering technique[29]. The point analysis technique involves optical processing of small areas of the film. The speckle pattern displacement is assumed to be constant in each region. Passing a narrow laser beam through the film produces Young's fringes in the back focal plane of a lens. The periodicity and orientation of these fringes can then be related back to the recorded speckle displacement. Hence the motion of the object can be determined in each region. The full-field technique requires spatial filtering in the Fourier plane of the specklegram to reveal contours of equal displacement in the second image plane.

For a classical specklegram, small out-of-plane motion of the scattering particles between illuminating pulses results in decorrelation of the individual speckle patterns and loss of measurement at that point. This problem was solved by reducing the seeding density to produce a pattern of resolved particle images. These particles would then have to move completely out of the light sheet for total decorrelation to occur. In addition, this reduced the risk of altering the flow characteristics which was a cause for concern with the large seeding density required for the speckle patterns. Most fluid dynamic applications adopted this particle image mode of operation[78, 1], and the technique became known as Particle Image Velocimetry or PIV.

### (b) Advances in PIV technology

Many different aspects of PIV are reported in the literature aimed at improving the accuracy, resolution and applicability of the technique[3, 61]. The continual advance of computing and optical technologies has played a large part in the rapid development of PIV. This is illustrated in the following.

#### (i) Laser systems

The choice of laser system for PIV is influenced by the need to satisfy certain criteria. Sufficient light energy is required to record the particle images onto the photographic film. Factors affecting this are the size of flow field and the size and type of seeding material. In addition, a short and flexible time interval is desired. This ensures there is no acceleration of the flow in the pulse interval as well as matching the separation of images to the requirements of the analysis system.

The method of illumination in PIV defines two types of laser systems. Pulsed lasers, such as the Nd:Yag laser, are used in high speed applications such as flow in large wind tunnels. The laser beam is introduced to the fluid as a sheet of constant, usually sub-millimetre, thickness. The sheet forming optics expand the beam fan-like into the flow. Pulsing the beam illuminates each particle stroboscopically. Small glass spheres or dry inert powders are typical of types of seeding used for applications in air. In general, obtaining consistent seeding for experiments in air is a difficult process.

Continuous wave lasers such as the Argon-ion or Helium-Neon lasers are used in studying water flows or small areas of low speed airflows. The light sheet is created by either of two methods. In the expanding beam method, the beam is collimated with a plano-concave lens and expanded into the flow with a cylindrical lens. Alternatively, a *scanning-beam* system[51] may be employed. A scanning-beam is produced by light reflecting onto a parabolic mirror from a rotating mirror to form a psuedo light sheet. CW systems are more flexible than pulsed lasers with

an adjustable illumination interval as well as a multi-exposure option.

### (ii) Analysis systems

Automatic analysis systems have resulted in major improvements in PIV processing. Manual analyses of fringe patterns (from specklegrams or PIV negatives) are limited in terms of accuracy, resolution and speed. An automatic processing of Young's fringes gives a rapid and accurate evaluation of velocity information. Velocity measurements of high accuracy and resolution permit calculation of derivative quantities such as vorticity, streamfunction and rate of strain. Automatic analysis systems have been developed that are capable of point by point evaluation of a double exposure flow field record over thousands of points. These systems process the photographic flow record by a variety of different numerical processing techniques. Flow data may be obtained direct from the image plane using particle image data as well as using the Young's fringes approach in the Fourier plane of the film.

Yao & Adrian[107] measured particle displacements directly from particle image pairs by integrating the digitized image intensity distribution over a small local area of the PIV negative. The resulting records are numerically processed by correlation and Fourier transform methods to resolve the mean particle displacement components. The technique requires a reasonable amount of information per interrogation region and experiences difficulties for PIV negatives where there are low contrast images or decorrelation between images. In this case, a full 2-d autocorrelation of the local image plane intensity data is required. This is equivalent to a 2-d Fourier analysis of the fringe intensities[58]. The Young's fringe intensity pattern, detected in the back focal plane of a lens, is the power spectrum of the photographic density distribution of a region of film illuminated by a probe laser. The power spectrum and the autocorrelation function form Fourier transform pairs by the Weiner-Khintchine theorem[55].

With the large amount of information to be processed, computational time be-

comes the crucial feature of the PIV technique. Very high speed processing of PIV films can be achieved using purely optical techniques. Methods using non-linear optical media such as Bismuth Silicon Oxide (BSO) as a photorefractive material to realise the 2-d squared autocorrelation have been reported[31]. Optical correlation using spatial light modulators as frequency plane filters has proved a promising alternative to numerical methods. Research has been based on the use of both electrically-addressed[102] and optically-addressed[60] spatial light modulators. Optical techniques give a method of rapidly analyzing PIV flow records with the accuracy and reliability of the numerical autocorrelation approach to film analysis.

### (iii) Image shifting

From the autocorrelation of a PIV image, the magnitude and direction of the flow can be determined. However the autocorrelation function contains no information on the sense of the flow (i.e. positive or negative direction). Particle tracking[25] and fluorescent tracer techniques have the advantage of labelling the sign of the flow via coded illumination and tracer tails respectively. In PIV analysis, if the resulting vector map can resolve the velocity field sufficiently it is usually possible to reconstruct the correct directions. However for complex flows this is very difficult, if not impossible.

A solution to the problem was suggested by Ewan[39], whereby a translational velocity is imposed on the recorded image. Thus the largest negative velocity appears as the smallest positive velocity (or vice versa). As well as eliminating directional ambiguity, application of image shifting increases the dynamic range of the system. Particle images that could not be previously resolved because low flow velocities caused them to overlap, can be shifted into a range of displacements that suit the requirements of the analysis system. Image shifting is analagous to frequency shifting in Laser Doppler Anemometry where a phase shifter is used to superimpose a known positive velocity on all the measured velocities.

An alternative method to resolving problems of directional ambiguity is suggested by Coupland *et al.*[32]. The technique involves image plane holography to distinguish the first and second images in the flow. Illumination of the flow record with two independent reference beams reconstructs the first and second images separately. The two sets of particle image positions are then cross-correlated to determine an unambiguous particle displacement.

### (c) Current research on PIV

Recent advances[105, 104] in measuring sub-pixel displacements indicate that video resolution will improve to compete with photographic film. Direct video imaging will eventually replace photographic methods in the conventional PIV arrangement. The delay associated with chemical development of photographic media provides a bottleneck in the total turnaround time for PIV experiments. In addition, the mechanical film advance and shuttering limit the frame rate. Using a CCD camera reduces the time taken between recording the flow and obtaining results and employs a much higher frame rate. The capturing of 'on-line' PIV is referred to as Digital PIV or DPIV.

PIV research is also making advances in the area of three-dimensional PIV. The three-dimensionality that occurs in most flows is the main source of signal loss and uncertainty. Out-of plane motion carries particles in and out of the light sheet producing signal decorrelation and introducing errors into recorded displacements. Efforts have be made to extend 2-d planar light sheet PIV to measuring 3-d vectors on planes or in volumes by stereoscopic imaging[42] or holographic techiques[84]. Stereo PIV combines two 2-d vector data sets taken from two spatially separated positions using much the same arrangement as for conventional PIV. The third component is resolved by continuity of flow and simple trigonometry[15]. Holographic PIV (HPIV) uses a holographic medium to store the 3-d data. To obtain the three components, both the amplitude and phase of the scattered light need to be measured. Mixing the scattered light with a reference beam produces the 3-d image on the holographic plate. The particle field can then be reconstructed

from the hologram, detected by a CCD camera and analyzed to extract the 3-d displacements.

In order to perform the analysis of the large number of PIV frames required in cinematic PIV and holographic PIV, very fast interrogation rates of recorded images are required. It is possible to substantially increase the speed of interrogation by optical means (as mentioned previously) or by fast digital means. Using a parallel processor, interrogation rates by digital cross-correlation methods have approached 100 vectors per second. This is extremely encouraging for experiments involving a statistical analysis of turbulence. With these rates, it is not unrealistic to accumulate up to 1000 frames of 35mm film for the purpose of averaging the vector fields over each frame.

## 2.2 The Experimental Facilities at Edinburgh University

PIV studies at Edinburgh have been traditionally carried out in water channels, as there has been much study of breaking waves. The success of the PIV wave experiments at Edinburgh has been in contrast to the difficulties experienced by wind tunnel researchers, as discussed in the previous chapter. Therefore, despite the anomalies due to Reynolds number (discussed in Chapter 6), the present wind turbine experiments were undertaken in a water channel where advantage could be taken of the excellent PIV facilities.

### 2.2.1 Laboratory Equipment

#### (a) Water channel

Figure 2.2.1(i) depicts the water channel used for the experiments of this thesis. It consists of three bays of large panes of 12mm thick glass in a steel supporting frame. It is 9.770m long and 0.400m wide. The channel was designed by David Skyner, and features a high degree of dimensional accuracy. One inch diameter circular steel rails are mounted on top of the frame, to allow positioning and clamping of apparatus. The channel is equipped with both a wavemaker and a recirculating current pump. The frame was designed for maximum rigidity to minimize problems with vibration from current generation or impacting waves. Filling the tank to a depth of 0.75m results in approximately 3 tonnes of water to be supported. The glass panes and structural elements of the frame were chosen from stiffness criteria and deflection considerations.

Of the three bays, two are used for measurements. Parallel rails run beneath this area to support and permit traversal of the PIV illumination system. Glass panes form the base of the channel as well as the side walls. This allows optical access

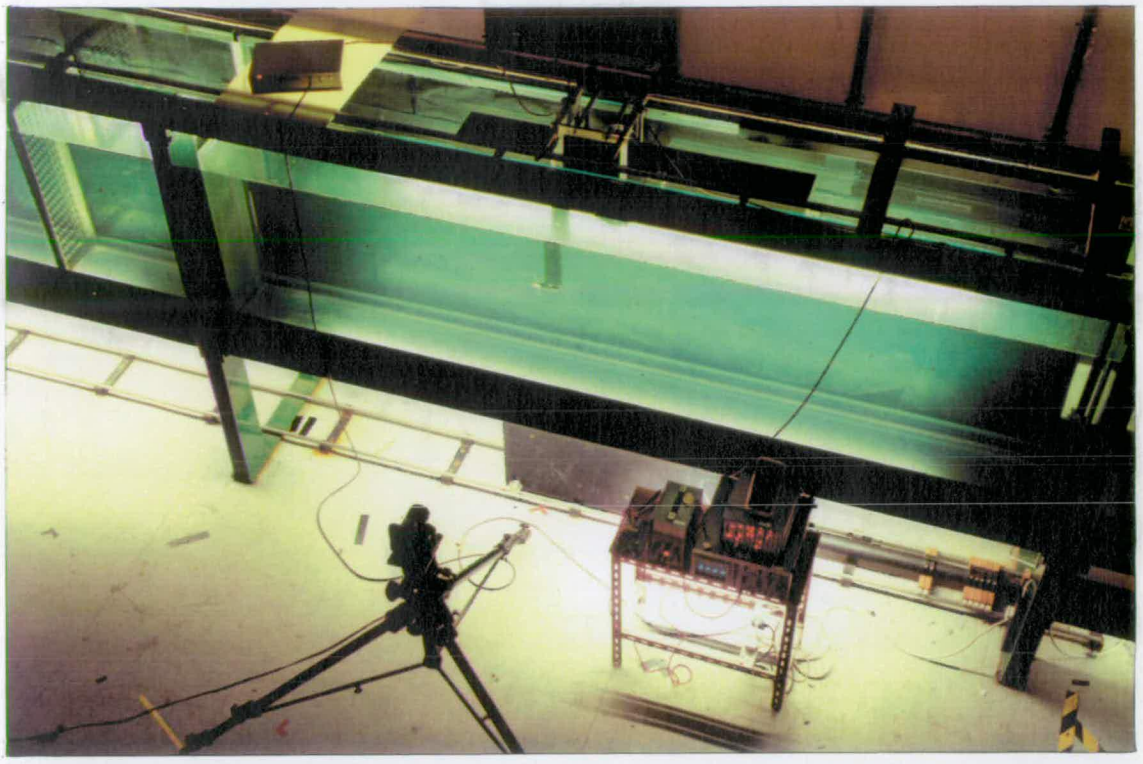

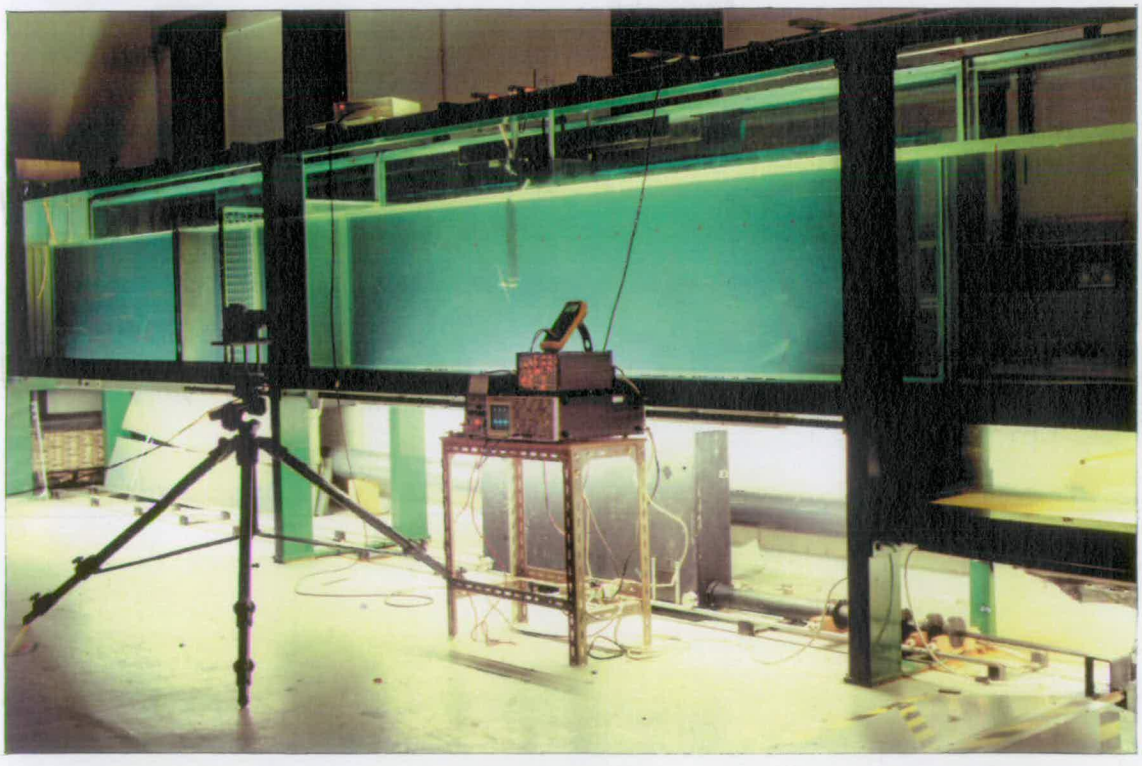

Figure 2.2.1(i) Photographs of the water channel at Edinburgh University.

of the pulsed light sheet produced from the illumination system. Finally, a line of reference crosses are placed across the side wall of the middle bay of the tank to act as registration points on the PIV negative.

### (b) Centrifugal pump

Behind the water channel is a centrifugal pump which supplies a recirculating current through the channel. A network of pipes connect the pump to the water flume and a series of four valves control the direction of the current and the overall flow rate. This is shown in the schematic diagram of Figure 2.2.1(ii). The pump can deliver up to 85 litres per second. Taking into account the impedance of the valves, this corresponds to a maximum flow rate of 0.25 m/s. By varying the arrangement of inlet/outlet valves, the direction of the current can be chosen.

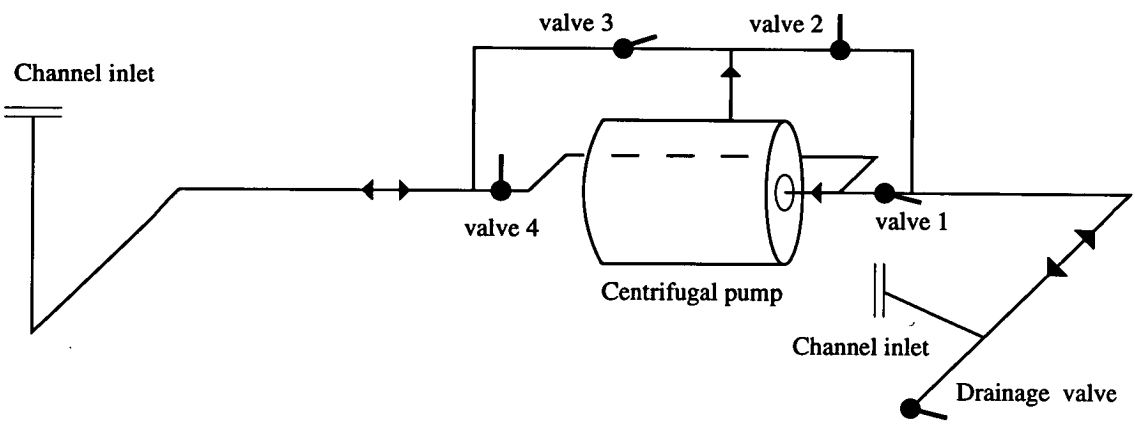


**Figure 2.2.1(ii)** Schematic diagram of pump and valve system supplying recirculating current to the water channel

In the present experiments, the current flowed through the tank towards the wavemaker (left to right in the photographs of Figure 2.2.1(i)). The current inlet leads to a settling chamber where meshes of skeletal foam (10 pores/inch) are used to reduce the turbulence and force the flow to become horizontal in the direction of the wavemaker. Turbulence manipulators were placed in the bay nearest the settling chamber to shape the upstream profile.

### (c) Turbulence manipulators

A number of turbulence manipulators were constructed and tested as a parallel system of baffles upstream of the rotor. An aluminium honeycomb section was used in conjunction with perforated plates and fine mesh screens. This is shown in Figure 2.2.1(iii).

The aluminium honeycomb section was a 0.39m $\times$ 0.8m $\times$ 0.075m rectangular prism composed of cells of diameter 5.5mm. Cut to the width of the channel, it was wound in strips of foam to protect the glass. It was placed furthest upstream of the rotor to act as a flow straightener, removing any components of swirl from the flow.

An aluminium perforated plate was supported in an aluminium frame of dimensions 0.4m $\times$ 0.82m $\times$ 0.05m. The plate was placed downstream of the honeycomb and held in position by an inflated inner tube, wrapped around the frame, pressing against the side walls of the channel. The perforated plate served to impose a particular profile on the upstream flow[68]. The shape of the profile was determined by the pitch and size of the perforations. For the PIV measurements reported in this thesis, a perforated plate of 32mm diameter holes with a regular pitch of 38mm was used.

Space is left in the tank, upstream of the rotor, to allow the turbulence introduced by the prescence of the plate and honeycomb to decay. Dissipation lengths were estimated based on the mesh-lengths of the turbulence manipulators, according to the laws of decay of turbulence behind grids[45]. Just before the rotor, final smoothing is provided by fine wire mesh screens (18 lines/inch). Aluminium frames are used to support the screens. At the section between the two bays, strips of metal are inserted into slots to act as keys upon which the frame can be slid in place.

The thickness, $l$, mesh length, $M$ and solidity, $\sigma$ (ratio of solid area to the total cross-sectional area) of the different turbulence manipulators are shown in

Table 2.2.1. The values of Reynolds number based on mesh size, $Re_M=(U_oM/\nu)$, pressure coefficient, $K$, and head loss, $\Delta h$, correspond to $U_o = 0.25$m/s.

| Manipulator | $l$(mm) | $M$(mm) | $\sigma$ | $Re_M$ | $K$ | $\Delta h$(mm) |
|---|---|---|---|---|---|---|
| Honeycomb | 75 | 5.5 | 0.63 | 1375 | 0.63 | 2.02 |
| P. Plate | 1.5 | 38 | 0.44 | 9500 | 0.43 | 1.40 |
| Screens | 0.5 | 1.18 | 0.31 | 294 | 0.62 | 2.00 |

**Table 2.2.1** Properties of the turbulence manipulators

### (d) Turbine rigs

The model turbine rig is depicted in the photograph of Figure 2.2.1(iv). The rig consists of a 14W d.c. electric motor/generator mounted on a platform. The platform is suspended above the water level by a frame supported on the steel rails on the top of the water channel. The nacelle of the turbine rig lies 0.39m below the surface of the water. Rotors can be attached to the turbine by means of a shaft which is connected to the electric motor by a toothed drive belt. The toothed belt is internal to an aluminium tube which acts effectively as an inverted 'tower'. The model rig was designed by Colin Anderson. The rig assembly drawings are displayed in Figure 2.2.1(v). The rig is placed across the tank, subjecting the rotor to a uniform current. Care is taken to make certain that the tower is perpendicular to the oncoming flow to ensure symmetric inflow conditions.

The speed and position of the rotor are measured by a tachogenerator and position encoder respectively, both connected to the electric motor. On the low-speed side of the motor gearbox, a HEDS 5540 3-channel encoder is attached to the motor shaft. It outputs an index pulse when the blade of the rotor reaches a predetermined azimuthal angle. On the high-speed side of the gearbox, output from the speed transducer is supplied to a simple analogue speed controller which adjusts the drive motor to allow precise values of blade passing frequency to be maintained.

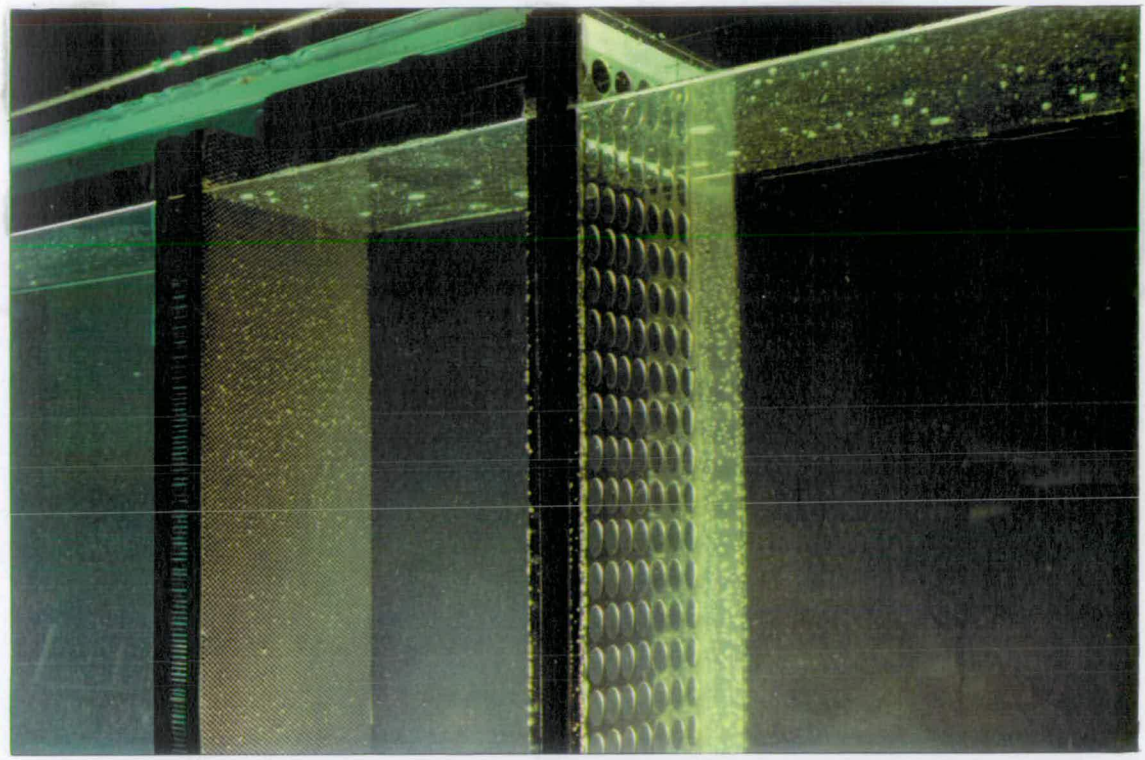

Figure 2.2.1(iii) Turbulence manipulators in the water channel.

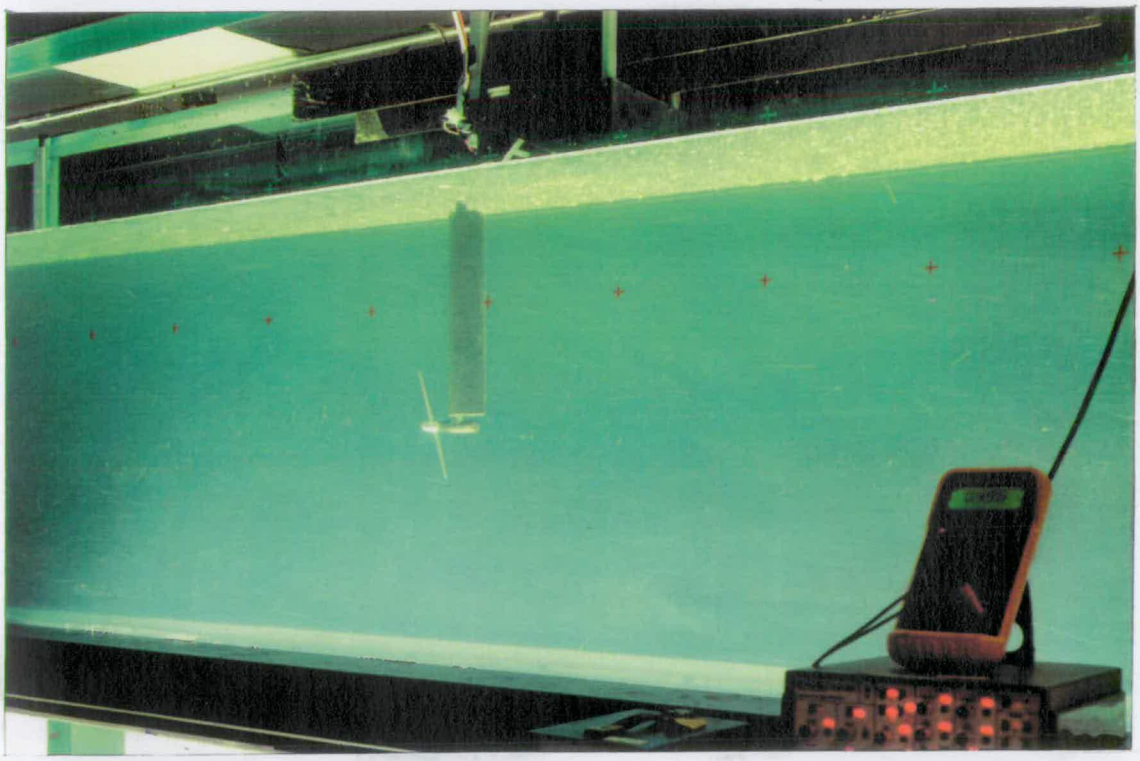

Figure 2.2.1(iv) The model wind turbine rig in the water channel.

### 2.2.2 Facilities for Recording PIV Images

#### (a) PIV illumination system

The PIV apparatus used for these experiments is basically that implemented by Gray[48] for water wave studies at Edinburgh. The illumination system consists of a high-powered laser, an arrangement of optical components to transmit the laser light toward the water channel and an optical system to produce a pulsed laser sheet.

A 15W continous wave (CW) Argon-ion laser is used to illuminate the flow. It is mounted on a trestle which is bolted to the concrete floor. For safety reasons, the laser is housed in a separate room adjoining the wave tank laboratory. Laser accessories, recirculating water, water conditioner and nitrogen gas supply, are stored with the laser.

The pulsed light sheet is produced by the scanning-beam system of illumination[51]. The scanning-beam system consists of a number of optical components housed within a 1.2m $\times$ 0.63m box (see Figure 2.2.2(i)). Steering mirrors are used to direct the laser beam into the box. As it enters, the beam is deflected upwards and passes through two matched lenses which narrow the beam. The beam is then collimated and reflected from an octagonal rotating mirror onto a parabolic recollimating dish. This is positioned beneath the centre of the channel and directs the beam vertically upwards through the glass base of the wave tank. As the octagonal mirror rotates, the beam scans over the parabolic mirror and the laser sweeps over the area of interest. This illuminates a vertical cross-section of the flow field.

Movement of the scanning-beam box along rails underneath the tank allows flexibility of the position of the light sheet within the water channel. An inverted channel made of black metal is placed along the top of the water channel, above the light sheet, to act as a beam stop and prevent any stray reflections. The scan rate of the system is controlled electronically and is continuously variable in the

range 0.5–8ms. The illuminated cross-section of the flow, extending from the bed of the channel to the surface of the water, is 1m wide and roughly 2mm thick.

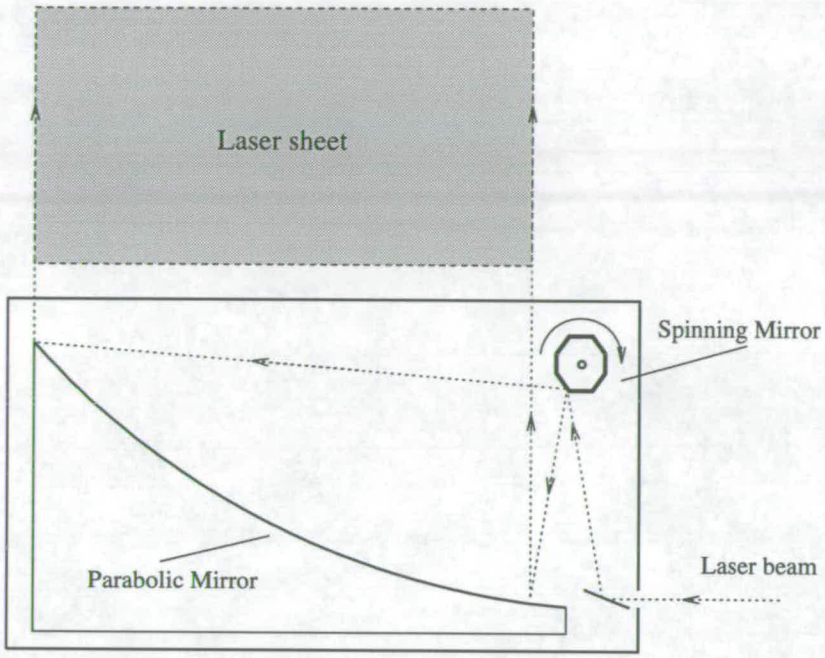


**Figure 2.2.2(i)** Schematic diagram of the scanning-beam illumination system

A light sheet produced in this way is susceptible to some variation in intensity. Slight perturbations in the parabolic dish lead to problems of eveness of light across the sheet. However, the sheet produced from the parabolic mirror used for the experiments can be regarded as flat to within 3mm. Chopping the CW beam is an inefficient use of laser light. Losses in light intensity due to the rotating octagonal mirror, the parabolic mirror and the base of the wave channel are significant with transmission coefficients of 80%, 73% and 80% respectively. Errors incurred during the PIV experiments are described in detail in Chapter 6.

### (b) Camera

For PIV experiments, a high quality camera with a flat focus lens is essential in order to minimize image plane distortions. Hasselblad cameras were used for the majority of the experiments. The choice of focal length of lens can reduce the

effect of out-of-plane motions and improve the imaged region of the flow. The lens used for these experiments had a focal length of 80mm.

The timing aspects of the camera rely on mechanical devices and need to be calibrated. The delay time between triggering the camera and its shutter opening can be checked by passing a low-powered laser beam through the lens of the camera and detecting the signal using a photodiode. The trigger delay was found to be 30ms if the lens was already cocked and 78ms otherwise. Recording actual shutter times is important to predict the number of particle exposures accurately. For the 80mm lens, the difference between recorded shutter times and nominal times was significant in some cases but resulted in only a small change in the number of images recorded[88].

### (c) Film

Using high resolution film is vital in the PIV process. High contrast, black and white, negative film is desirable. Kodak TMAX 400 ASA−120 was used for most of the experiments.

### (d) Seeding

The criteria required for seeding in PIV is that it is neutrally bouyant and small enough to follow the flow with sufficient accuracy but large enough to scatter light effectively. For these experiments, conifer pollen was used as seeding. The pollen has an average diameter of 70$\mu$m and concentrations were maintained at a level to ensure a high density of non-overlapping particles on the resulting film record. The accuracy with which the conifer pollen follows the flow is examined in Chapter 6.

### (e) Image-shifting system

The advantages of image-shifting while recording in PIV have been outlined in Section 2.1.2. For these experiments, image-shifting was needed as much to resolve small velocities in the flow as to eliminate directional ambiguity. The image-shifting was performed by a *rotating mirror* system[80]. The system was designed by Jean-Baptiste Richon (Optical Flow Systems) and Tim Campbell (Neat Systems). A schematic diagram of the rotating mirror system is shown in Figure 2.2.2(ii). The image-shifting system is described below in terms of its hardware, software and the sequence of events in the shifting procedure.

#### (i) Hardware

The system is composed of three main items :-

1. **Rotation stage**

   An accurate rotation stage is fitted with position encoder and tachometer and powered by a DC motor.

2. **Control module**

   A control module provides closed-loop position control and motion scheduling of the rotation stage. The module also includes a power drive for the rotation stage DC motor.

3. **Computer**

   A PC is used to communicate with the control module and supervise the shifting sequence.

### (ii) Software

Parameter values are passed to the control module via the PC and are specific to the photographic hardware and the experiment being performed.

### (iii) Shifting sequence

The mirror starts from a home position. The camera is in a fixed position with respect to the rotating assembly. In the PIV experiments, the camera is aligned parallel to the laser sheet and the mirror must reach an angle of $45^{o}$, with respect to the camera, halfway through the shutter opening time. Before the start of the mirror motion, the control module receives an index pulse from an external source. The delay between the pulse and the start of the mirror motion can be programmed by the user to provide synchronization of the shifting system with the external event. In these PIV experiments, the shifting sequence is synchronized with an index pulse emitted from the position encoder connected to the turbine motor. By programming the correct delay time, the blade azimuthal angle can be predetermined when the photo is taken. Thus, a number of PIV exposures can be taken with the blade in the same azimuthal position and averaging processes employed in analysis.

Once the delay time has elapsed, the mirror accelerates rapidly to the selected angular velocity. The time during which the shift velocity is sustained is determined by the time it takes for the camera shutter to open in full, expose the film and then shut again. The system sends a TTL pulse to the camera to trigger the shutter opening at a time computed in advance. After the constant shift velocity period, the mirror decelerates and returns to its home position. Figure 2.2.2(iii) shows the timing diagram for the rotating mirror system.

### 2.2.3 PIV Analysis System

The Optical Flow Systems (OFS) analysis system has been developed at Edinburgh to extract velocity information from the PIV photographic flow record. This automated method was first implemented at Edinburgh by Callum Gray[48]. The Fourier method was chosen to deal with flows requiring high-seeding density.

The analysis procedure consists of scanning a small part of the negative at a time with a probe laser to produce an interference pattern from the multiple particle images in that area. The beam intensity can be adjusted using a polariser in front of the laser. A spatial filter and recollimating lens are used to improve beam illumination over the interrogation spot. An aperture is used to crop the beam diameter to 1mm, while a 45° mirror steers the laser onto the negative. It is assumed that the particle images correspond to a near constant velocity within the interrogation area of the probe laser. The interference fringes are imaged onto a CCD array camera and digitized rapidly using a video digitiser (frame grabber) interfaced to the PC. A fast fourier analysis can then be performed by the PC to transform the fringes to the autocorrelation plane where the mean particle image displacements are calculated.

## 2.3 Conducting PIV Experiments

One noticeable feature of the technique of Particle Image Velocimetry in practice is that it can involve a day's work to set-up the experiment while perhaps only minutes to take the film. This contrast makes it frustrating for the experimenter if, at the end of the whole process, nothing comes out on the film. It is therefore vital, that the experiments have good preparation before the acquisition of PIV images.

### 2.3.1 Preparation

#### (a) Water channel

Prior to each test series, the whole tank was drained and cleaned, flushing any rust sediment out in the process. A pump attached to the drainage valve was used to speed this process. Two taps at each end of the tank supply jets of water for filling the tank. Filling the tank with 3 cubic metres of water took about 1.5 hours.

Cleaning the glass of the channel is important to ensure no marks are left on the glass when the photographs are taken. Household washing-up liquid was used for the cleaning and lint-free dust cloths to wipe the area of glass to be included in the negative.

#### (b) Camera alignment

The tripod legs were extended and spread out evenly before levelling the tripod in the vicinity of the proposed camera position. The baseplate of the rotating mirror system was attached, ensuring the mirror was perpendicular to the plate and the plate was parallel to the channel. The camera was then mounted and the mirror rotated to 45° with respect to the axis of the camera. This was verified by checking that the reflection of the camera lens in the mirror was in the centre of the camera's viewfinder.

#### (c) Choice of parameters

The PIV negatives must be in a suitable form in order to obtain valid data. Particle images on film must be in good focus, of suitable size and in good contrast with the background. They must be of sufficient number (at least two) but not

excessive. Table 2.3.1(i) summarises the requirements, within each interrogation area on the film, for obtaining high quality flow maps[88].

| *Setting* | *Range* |
|---|---|
| Number of images for each particle | $3 < N < 6$ |
| Number of separate particles | $> 10$ |
| Particle image size | $20\mu$m |
| Particle image displacements | $20\mu\text{m} < \delta < 250\mu\text{m}$ |
| Displacement gradient | $< 3\%$ |
| Change of displacements over measured time | $< 3\%$ |

**Table 2.3.1(i)** PIV settings for valid data

The choice of parameter settings in PIV is a difficult process due to the interdependence of the parameters. Obtaining good PIV images on film can be a case of trial and error. A number of test films are usually taken first before iterating towards the optimum parameters for the particular flow. One guide, however, is to work backwards from the PIV analysis stage. For successful PIV analysis, particle displacements must be in a range suited to the requirements of the analysis system. In terms of resolution, particle images on film must be separated by at least one particle diameter and not be further apart than one quarter of the diameter of the interrogation beam[48]. For the analysis rig at Edinburgh and the seeding used in these experiments, this gives a range of displacements,

$$20\mu\text{m} < \delta < 250\mu\text{m} \tag{2.1}$$

Parameters are then chosen to record displacements on the film within this range.

With a fixed camera position and an estimate of the dynamic range of the flow, a choice of illumination interval sets the particle displacement according to the relation

$$\delta = mVT \tag{2.2}$$

where $m$ is the image/object magnification, $V$ is the flow velocity and $T$ is the illumination interval. Given an illumination interval, the shutter speed of the

camera can then be chosen to give the desired number of particle images on the film. Once a test film is taken, it may be necessary to modify the illumination interval or the magnification factor. Changing the scan rate, however, will affect the amount of light captured on the film. Hence, other parameters affecting exposure have to be varied accordingly. Table 2.3.1(ii) shows typical values for these parameters and how they affect exposure.

| *Parameter* | *Typical Value* | *Exposure dependence (exponent of proportionality)* |
|---|---|---|
| laser power | 15W | 1 |
| illumination interval | 2ms | 1 |
| camera distance | 1m | -2 |
| focal length of lens | 80mm | 0 |
| aperture (f-number) | f4 | -2 |
| film speed(ASA) | 100 | 1 |
| laser sheet length | 1m | -1 |
| laser sheet thickness | 2mm | -1 |
| particle diameter | 70$\mu$m | 3 |

**Table 2.3.1(ii)** Exposure dependence of PIV parameters

### 2.3.2 Acquisition

The recirculating pump was switched on and seeding introduced to the flow. Uniformity of the seeding is desirable. The conifer pollen was poured via a funnel through a vertical plastic pipe weighted at the bottom of the water channel. The pipe had evenly spaced holes to disperse the seeding evenly from top to bottom of the channel. Periodic mixing of the pollen was required to maintain uniformity of the seeding. Once the scanning mirror was activated, the laser was powered to produce the light sheet. A signal from the pulsed light sheet was recorded by photo-diode. This was then stored on oscilloscope to determine the illumination interval.

Large variations in the quality of the images arise from slight variations in focus setting. A number of options were thus initially recorded in order to determine the focus setting. The mirror of the camera was then locked away to allow rapid successive exposures and to reduce vibration during the taking of the photographs. Spherical aberration effects need to be balanced with point diffraction limits of the lens[48]. One f-number below the maximum aperture offered the best compromise and made focussing easier.

The actual photography was performed in darkness and the execution mostly automated with the mirror shifting and camera triggering computer controlled. There was little manual intervention, apart from altering the focus, shutter speed and aperture in between photographs. If the scan rate or apparatus position needed to adjusted, the attenuator of the laser was closed and a beam stop placed in the beam path. Space was left on the film to record a calibration photograph. A calibration grid of known gridsize was placed in the water channel, in the measurement plane. It was lit by ordinary fluorescent light and captured on film. In this way, the image/object magnification was calculated for each new lens or camera position.

The film was unloaded in subdued light and stored in the refrigerator until it was developed. Kodak TMAX developer was used in accordance with the times and temperatures recommended. Films can be developed for longer than recommended if the exposure is likely to be low and PIV films are often push-processed in this way, to heighten contrast of the images with the background. AMFIX fixer was used to halt the development process. The magnification factor was calculated from the negative of the calibration grid. The darkroom enlarger was used to make measurement of grid squares easier. An indication of the success of the experiment was quickly obtained by passing a low-powered laser beam through the film. The appearance of the fringe patterns produced with the probe laser revealed whether high quality images were captured on film.

### 2.3.3 Analysis

The negative was cut to size and placed in a film frame holder. The OFS software OFSANAL was invoked in order to define the grid of points required in analysis of the negative. This could be done both in terms of co-ordinates on the film and in the reference frame of the tank, providing details were supplied of the magnification and scan rate used in the experiments. These were entered in a defaults file of parameters along with details of the grid in terms of stepsize and range in both horizontal and vertical directions. Conversion between reference frames was possible via rotation and translation transformations. Finally, the film and film frame number of the negative were recorded in the list of parameters.

A polarised 2mW He-Ne laser was used to pass a coherent beam of 1mm diameter through the photographic negative. The film was moved relative to the probing beam by means of a two-component translation stage. The OFSANAL software allowed manual interaction to move the film so that the beam rested at a reference point; usually a stable feature of the flow such as a piece of apparatus. In the case of the turbine on film, the reference point was chosen to be the hub of the rotor. This provided an origin for the grid.

### 2.3.4 Development of the PIV method for Rotor Measurements

Experimentation with the techniques and facilities outlined in this chapter produced a method suited to the study of wind turbine wakes using PIV. In a set of preliminary tests, optimal values for the PIV parameters were sought, and the influence of the tower and blade type on the flow observed behind the rig was considered.

In initial testing, PIV was used to examine the wake behind a small model aircraft propeller. The propeller was a 2-bladed model of 175mm diameter and was run

in reverse in order that its twist and chord distributions approximated those of a wind turbine rotor. Figure 2.3.4(i) depicts a PIV flow record taken with the model propeller. Figure 2.3.4(ii) displays the corresponding velocity vector map of the propeller operating at a tip speed ratio of $\lambda = 4$. Low-quality vectors have been filtered from the map at the PIV analysis stage. Although the map contains some evidence of vortex structure, it is affected by interference in the upper half of the wake. This is caused by turbulence shed in the wake by the tower of the rig, which acts as a bluff body. A wide range of velocities were observed in the tank in these early tests from the undisturbed upstream flow to a region of almost stagnant fluid immediately behind the rotor, especially at high tip speed ratios. This region contained flow velocities too small to be analysed by the PIV system, as is revealed in Figure 2.3.4(ii).

A second set of tests was required in order to address these problems. The propeller was not an ideal turbine model as its aerofoil section operated trailing edge first, and it was replaced by flat-plate blades. This was considered the simplest way of generating a more realistic wind turbine simulator. Steps were taken to enhance the quality of the measurement data. Firstly, the tower of the rig was streamlined with a foam plastic shroud in order to limit its wake interfering with the top half of the wake structure. Figure 2.2.1(iv) shows the model rig equipped with the shroud. Secondly, the rotating mirror image-shifting system was used to impose a translational velocity on the recorded image to resolve velocities immediately behind the rotor. The effects of these changes are illustrated in Figure 2.3.4(iii) in the form of vector maps of flow past the flat-plate blades. The blades are operating at tip speed ratios of $\lambda = 2.9$ and $\lambda = 6.4$. The image-shift velocity has been subtracted from each flow record. Figure 2.3.4(iii) shows the image-shifting to be succesful in improving the amount of high-quality data captured in the PIV experiments.

To extract the vortex structure in the wake from the superposed turbulence, a process of averaging of PIV velocity vector maps was employed. Figure 2.3.4(iv) shows the result of averaging six PIV vector maps with the flat-plate blades operating at tip speed ratios of $\lambda = 2.9$ and $\lambda = 6.4$. The photographs were taken

without the aid of a timing device so that the blades were captured at arbitrary azimuthal angles. The averaging led to further improvement in the quality of the data both at the low and high tip speed ratio. However, averaging flow records of different wake phases led to a 'smearing' of the vortex structure. The corresponding vorticity contour maps to the vector maps of Figure 2.3.4(iv) are displayed in Figure 2.3.4(v) By synchronizing the flow recording with the image-shifting system, photographs could be taken of the blades in the same azimuthal position. Preliminary tests with blade synchronization using a speed controller showed that an azimuthal position could be repeated with an accuracy of less than 1%, even at the highest speeds. Averaging of these PIV maps served to highlight the vortex structure as well as enhancing the data quality. This is shown in the velocity vector maps and vorticity contour plots of Figures 2.3.4(vi) and 2.3.4(vii).

The experimental method was completed by compensating for the image-shifting distortions incurred during the acquisition of PIV data. In order to separate the effects of image-shifting from the flow recording of the wake, a number of PIV photographs were taken of still-water in the tank. The seeding was stirred so that the particles were well distributed and then the flow was allowed to settle. In order to have no correlation of the flow in successive negatives, a reasonable time was allowed to elapse between still-water shots. A photograph was then taken before the seeding dispersed from the laser sheet. After averaging a number of still-water records, the results were then subtracted pointwise from the PIV datafiles of the turbine wakes in order to correct for shift velocities. This is shown in the PIV vector maps of Figure 2.3.4(viii).

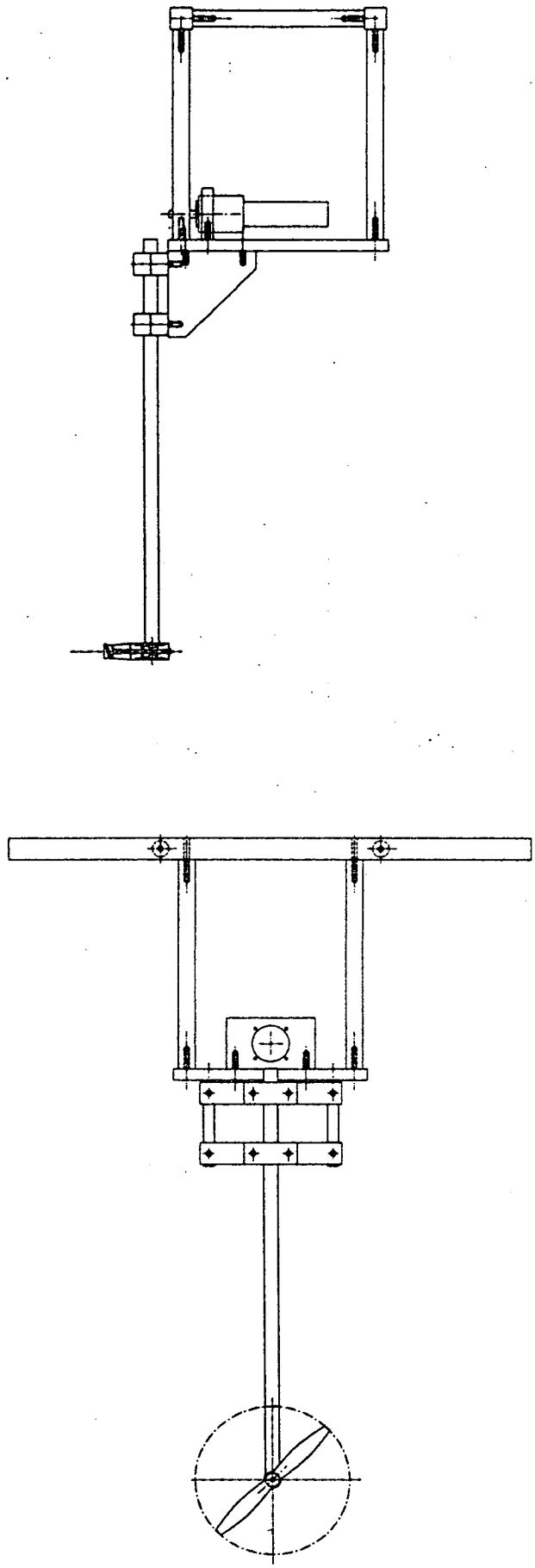

Figure 2.2.1(v) Assembly drawings of the model wind turbine rig.

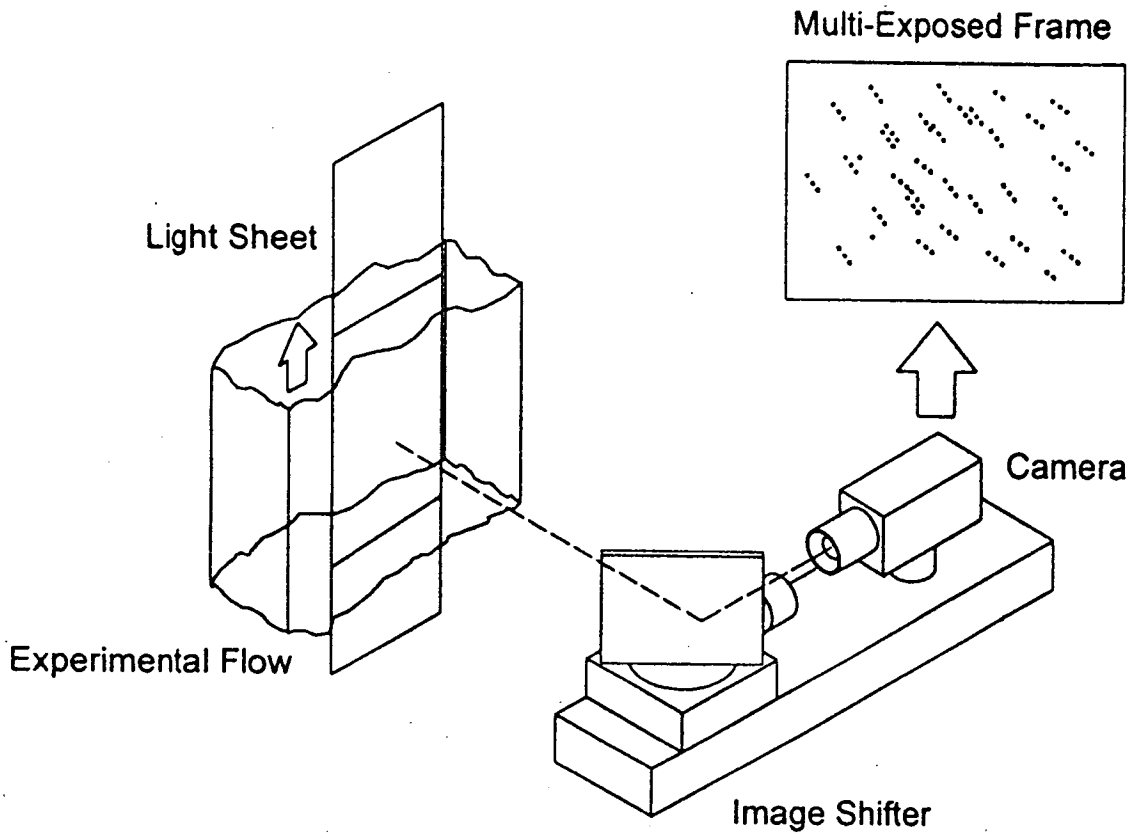


Figure 2.2.2(ii) Schematic diagram of the image-shifting system.

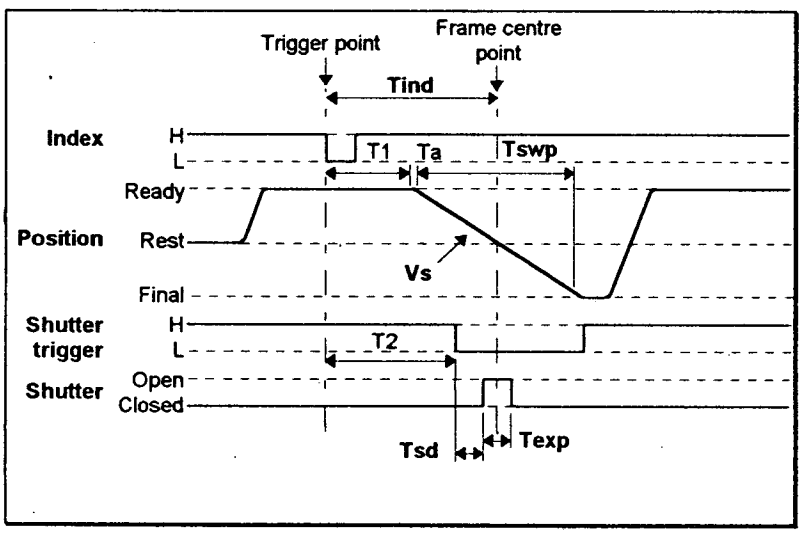


Figure 2.2.2(iii) Timing delays for the image-shifting system.

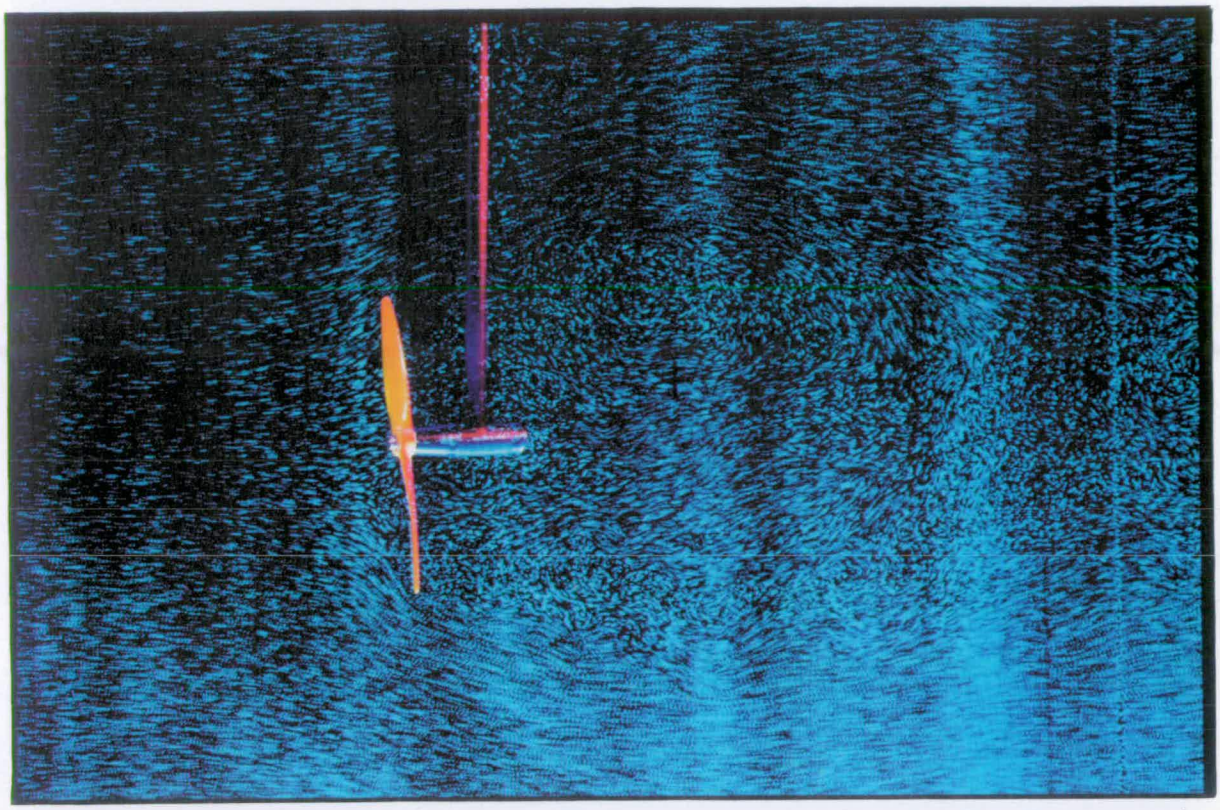

Figure 2.3.4(i) PIV photographic flow record of a model propeller in the water channel (no image shifting).

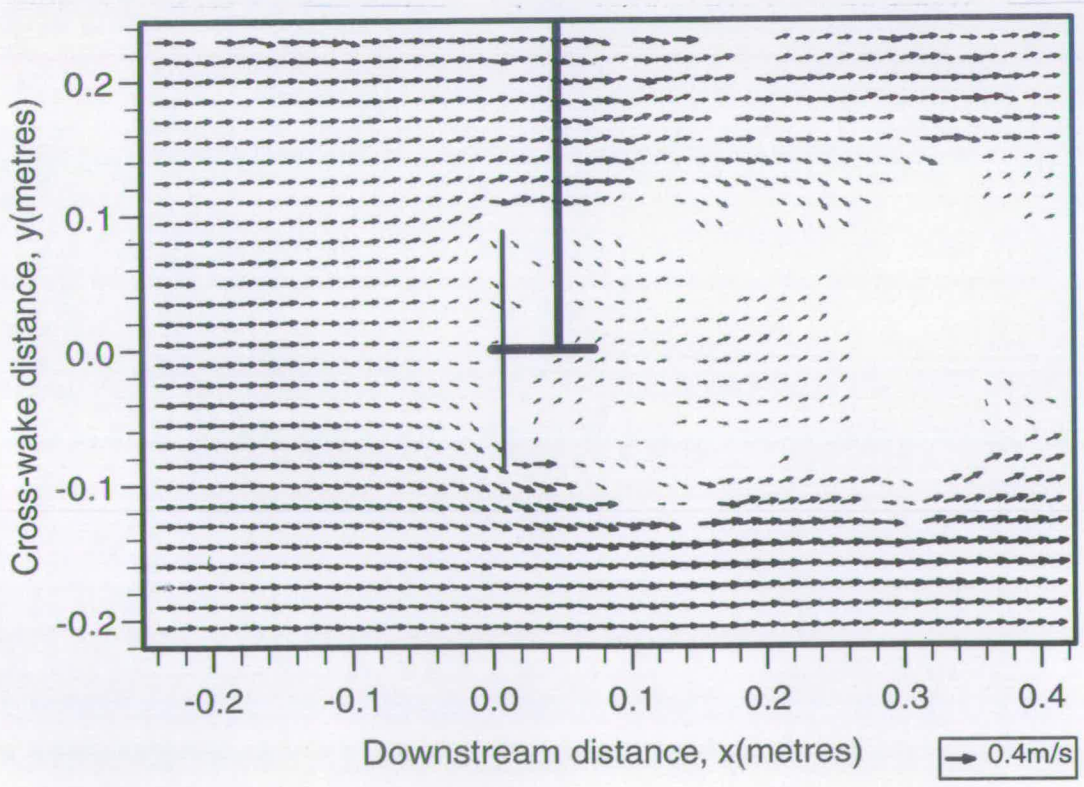


Figure 2.3.4(ii) PIV velocity vector map corresponding to the flow record of Figure 2.3.4(i).

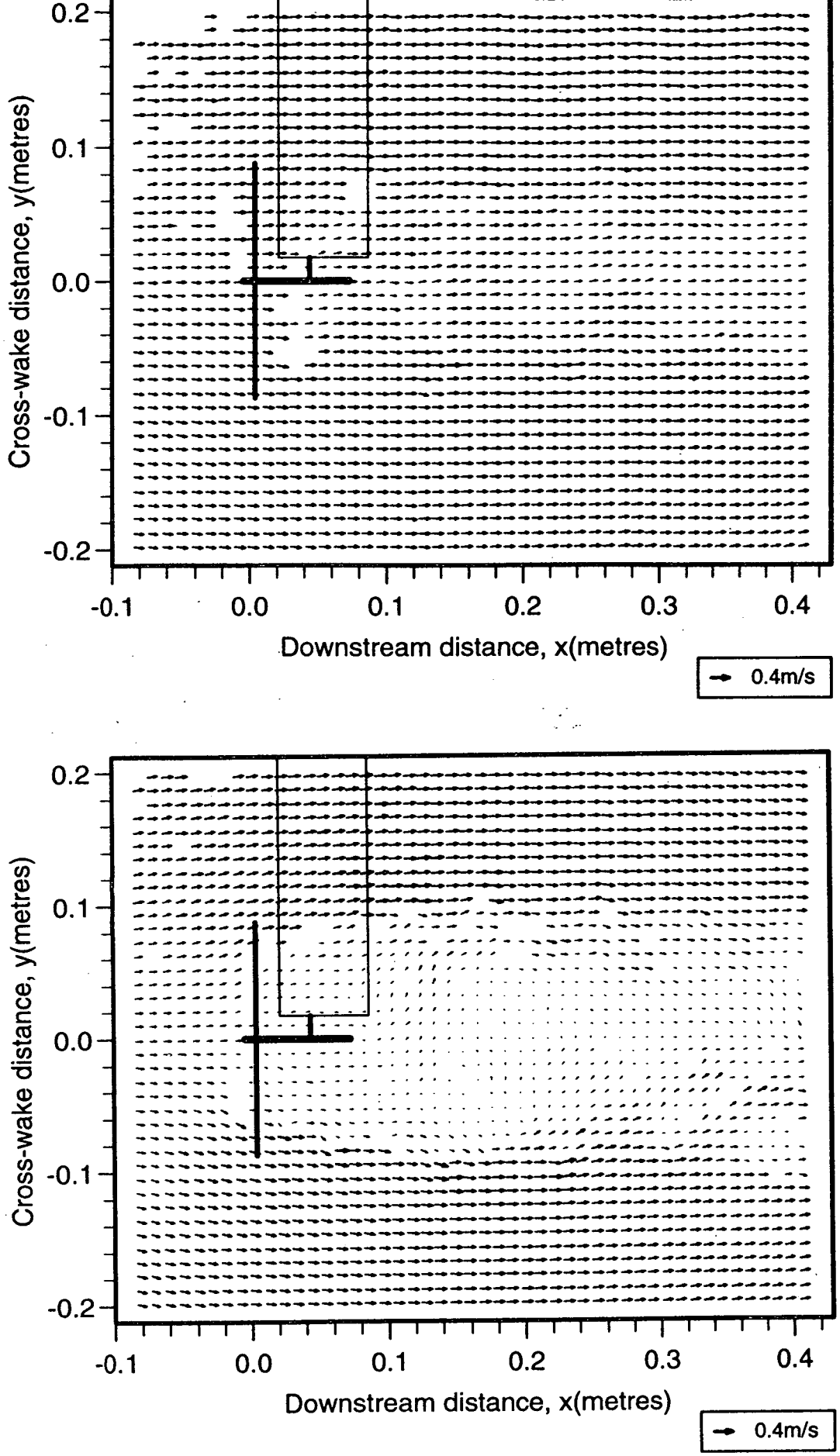


Figure 2.3.4(iii) PIV velocity vector maps of the wake of the 2-blade rotor operating at $\lambda = 2.9$ (above) and $\lambda = 6.4$ (below).

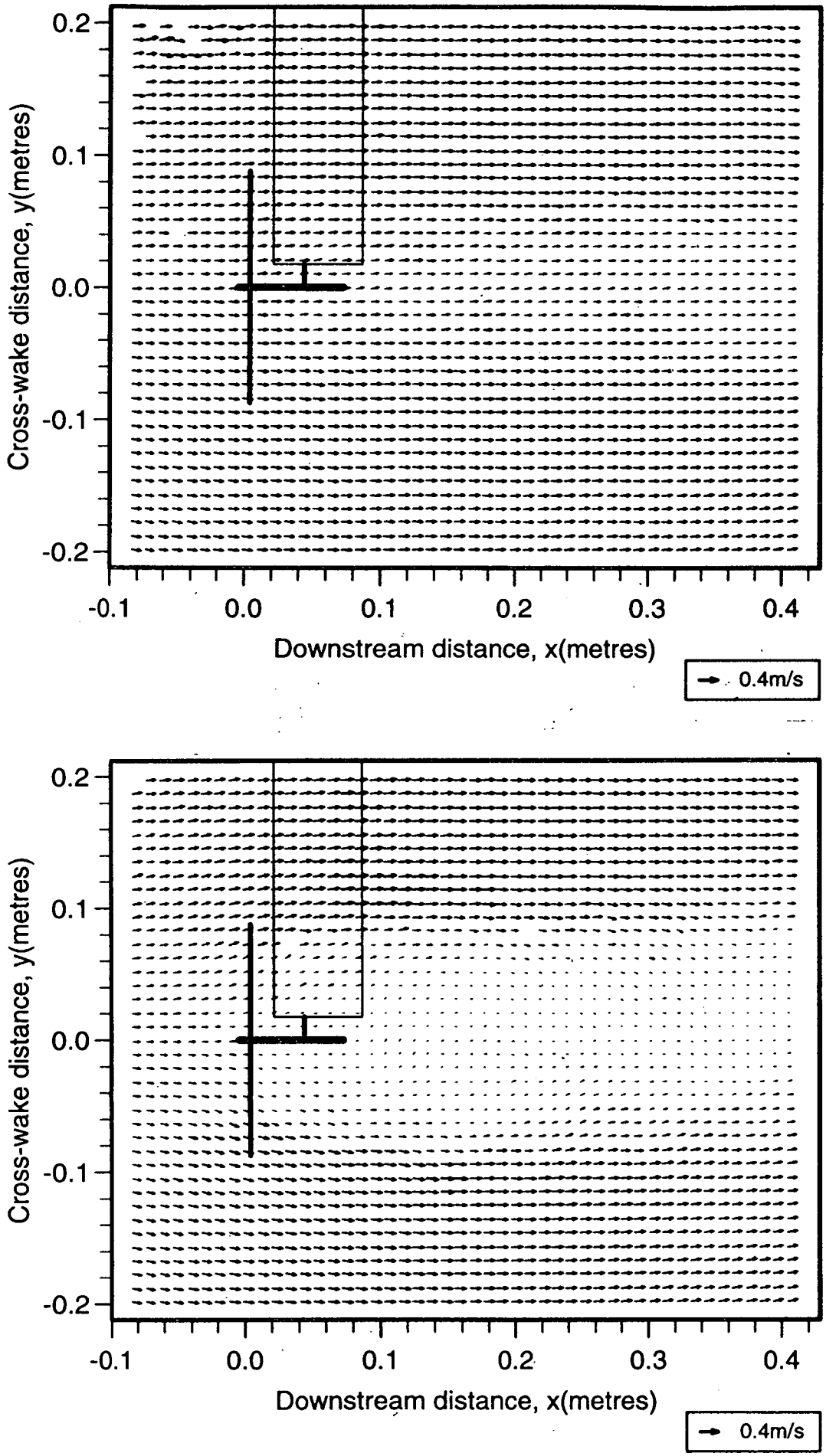


Figure 2.3.4(iv) Averaged PIV velocity vector maps of the wake of the 2-blade rotor at $\lambda = 2.9$ (above) and $\lambda = 6.4$ (below).

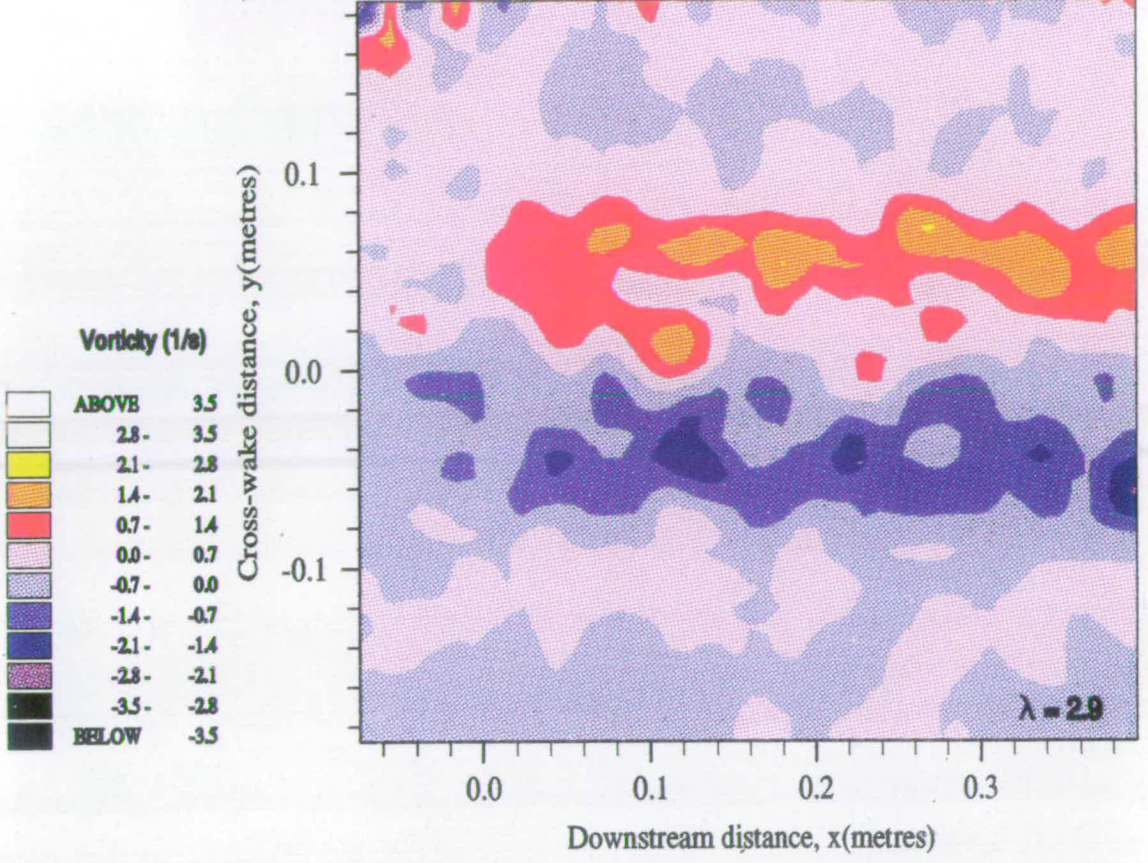


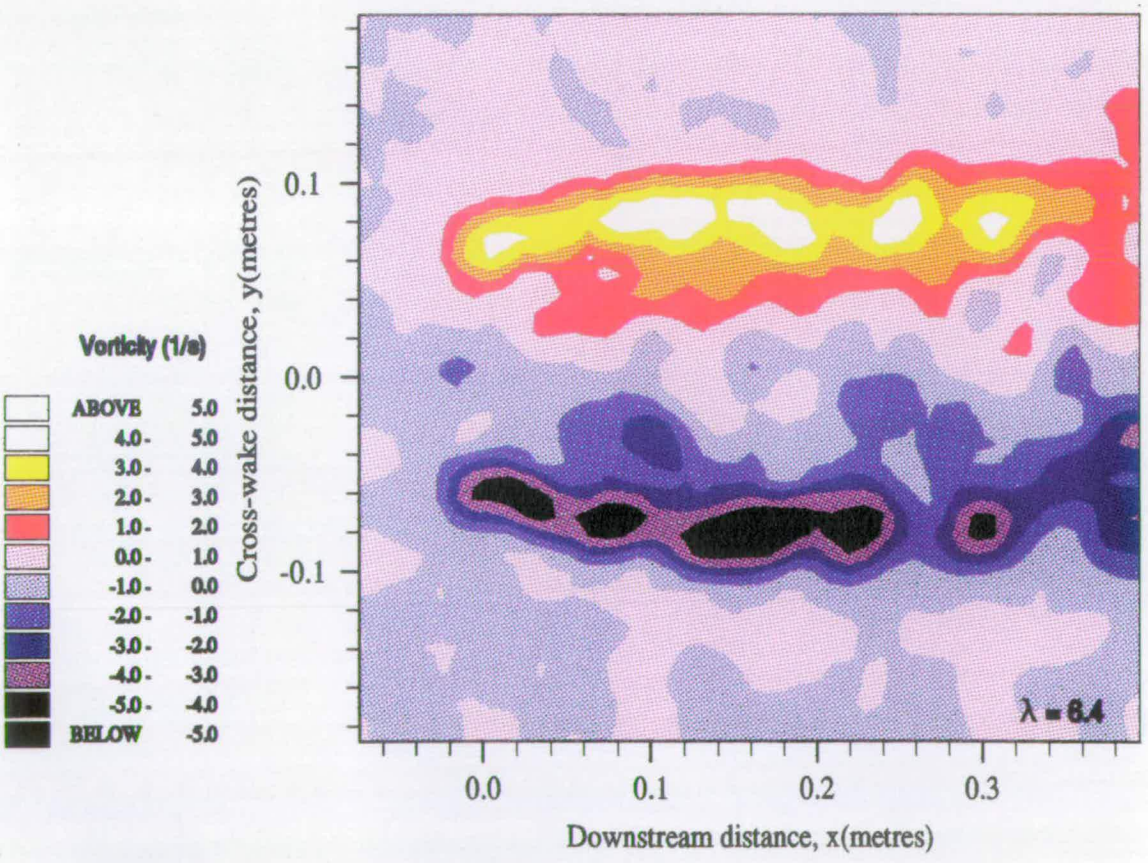


Figure 2.3.4(v) PIV vorticity contour plots corresponding to Figure 2.3.4(iv) at $\lambda = 2.9$ (above) and $\lambda = 6.4$ (below).

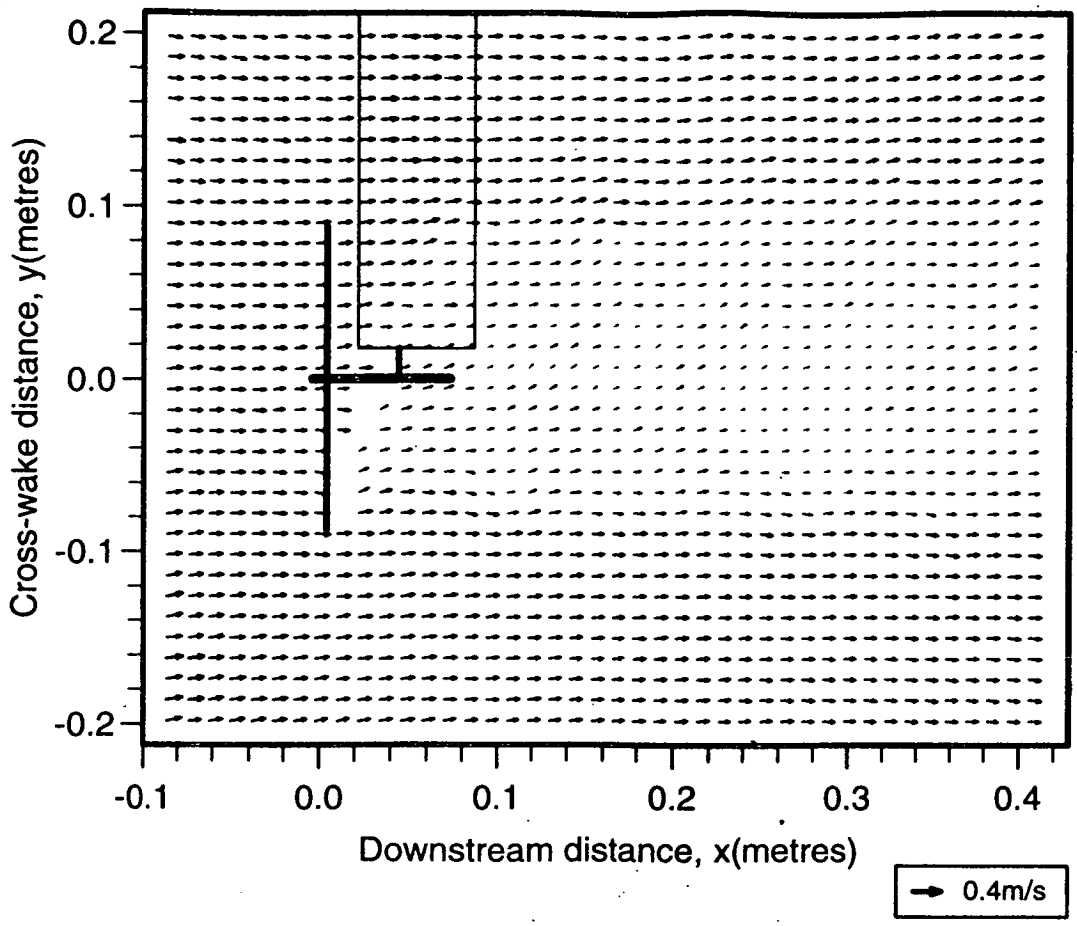


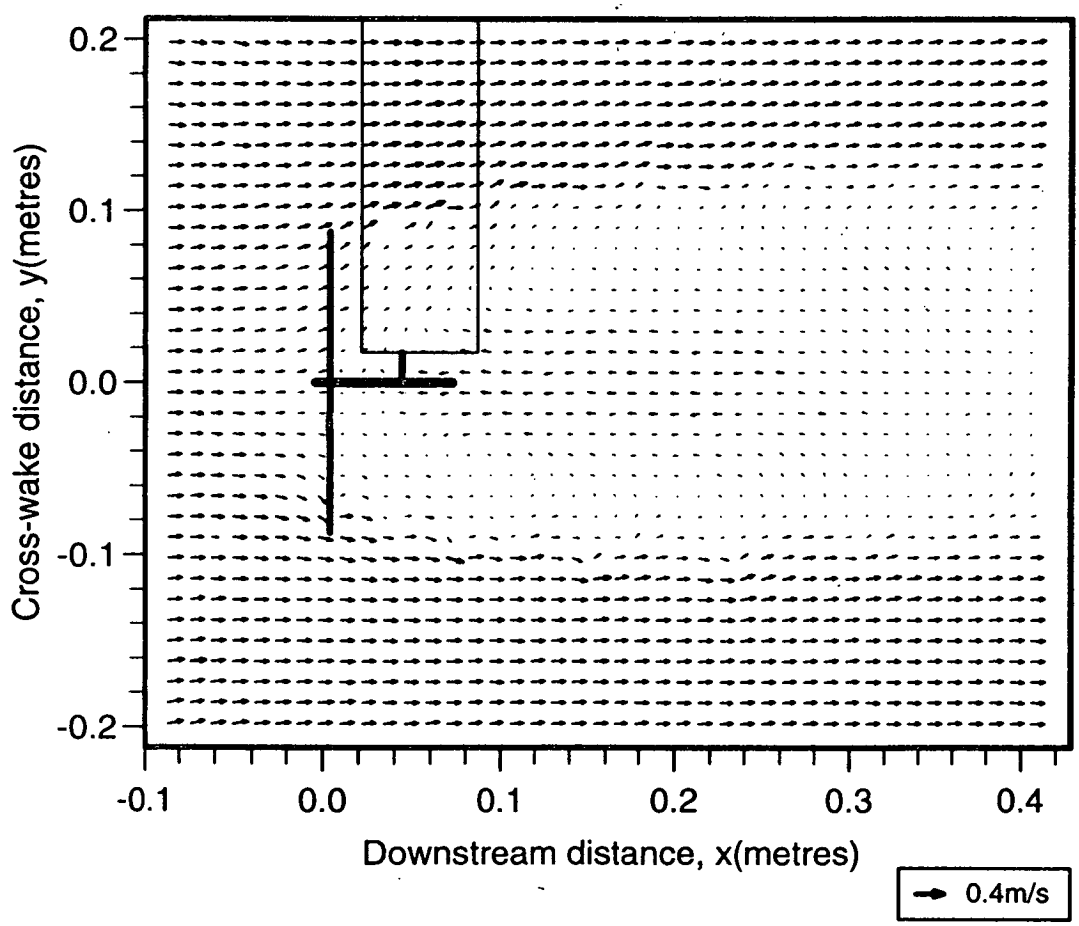


Figure 2.3.4(vi) Synchronised PIV velocity vector maps of the wake of the 2-blade rotor at $\lambda = 2.9$ (above) and $\lambda = 6.4$ (below).

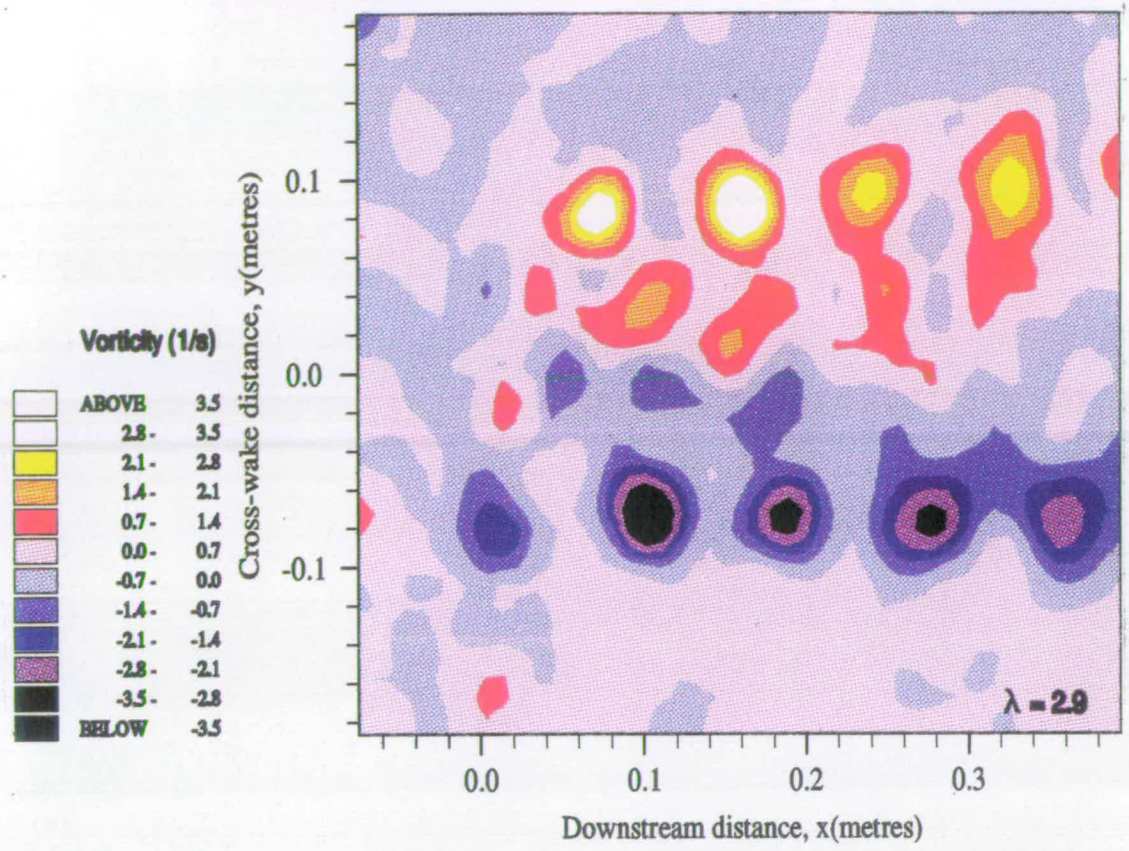


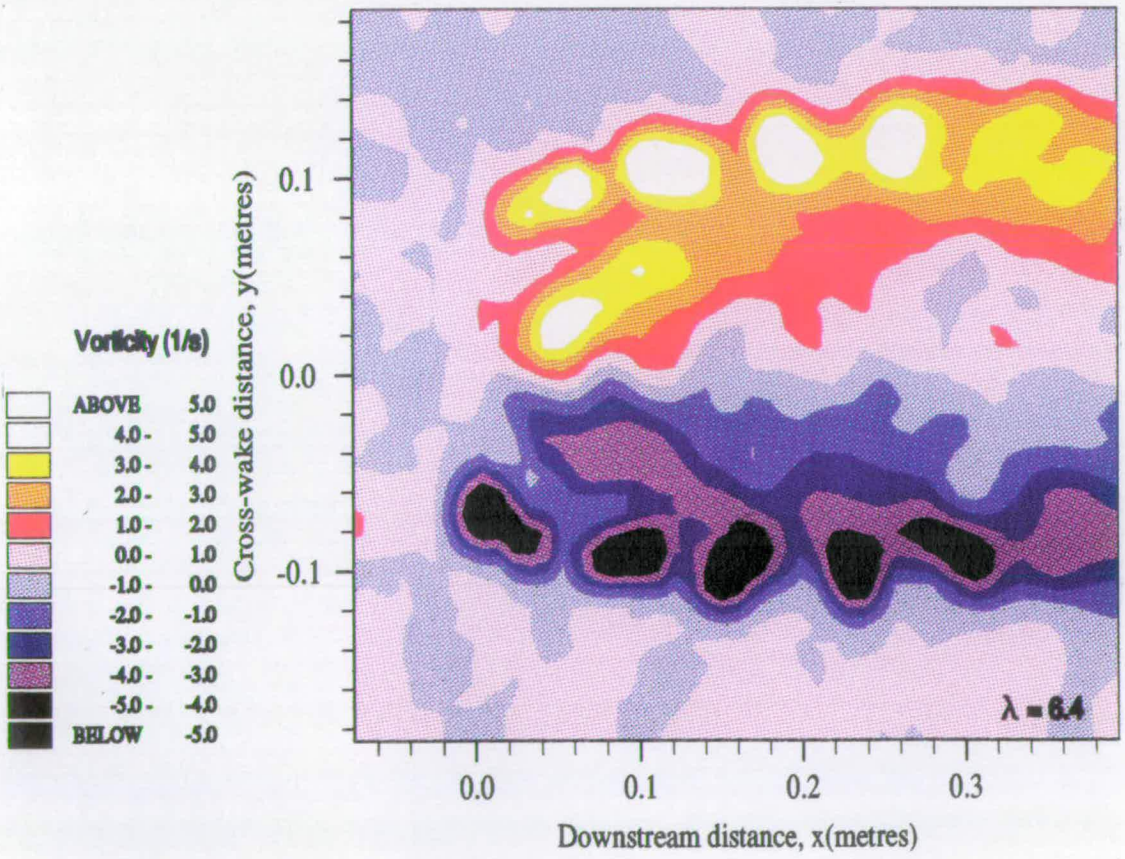


Figure 2.3.4(vii) PIV vorticity contour plots corresponding to Figure 2.3.4(vi) at $\lambda = 2.9$ (above) and $\lambda = 6.4$ (below).

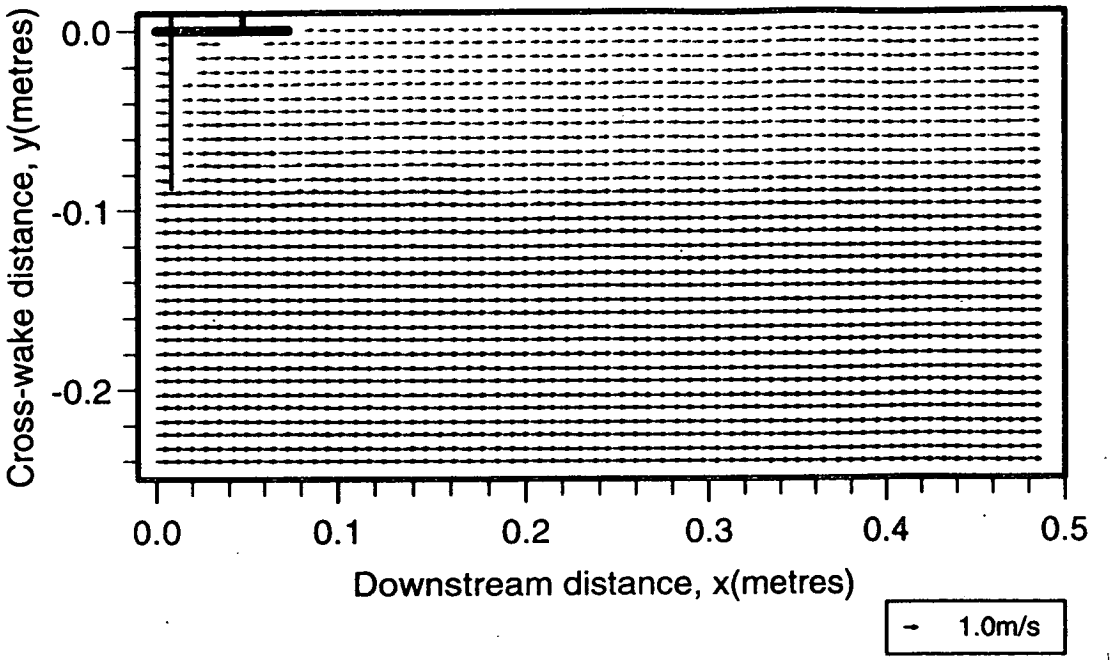


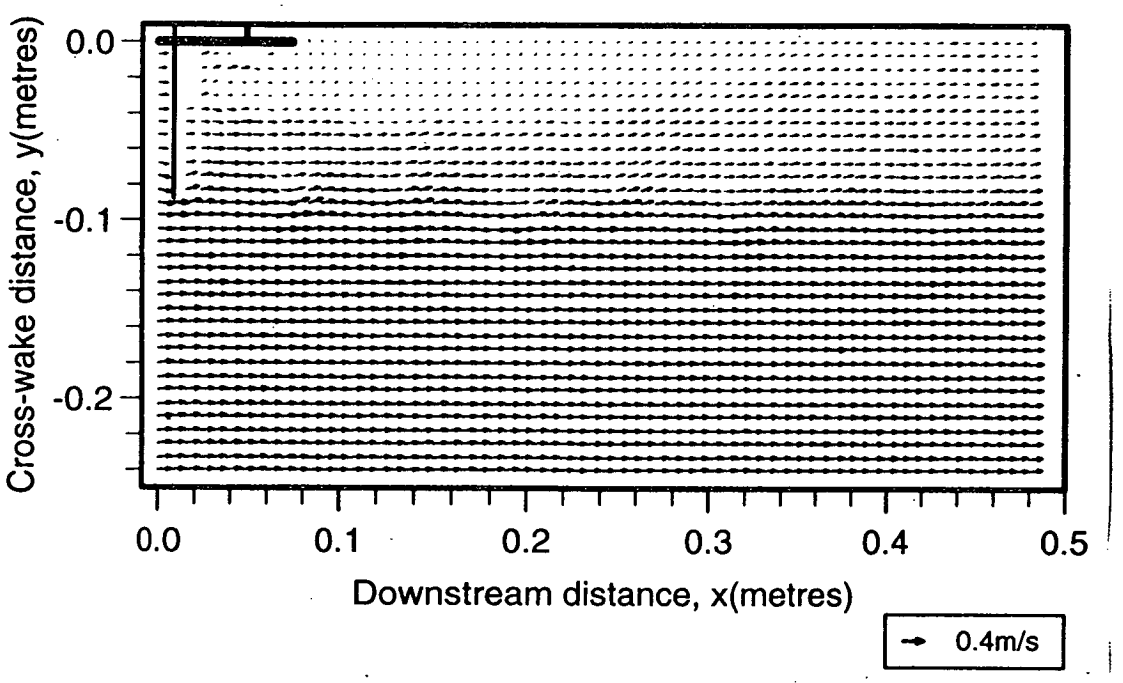


Figure 2.3.4(viii) PIV velocity vector map of the lower half of the wake of the 2-blade rotor (above) which is then corrected for shifted velocities (below).

# Chapter 3

## TESTS AND RESULTS

### Overview

In this chapter, tests on a 2-blade and a 3-blade model rotor are described. The major analytic goals of the experiments are outlined. The equipment and test parameters are listed in detail. The results of the tests are presented in the form of PIV velocity vector maps and the structure of the rotor wakes evident from the maps is discussed.

## 3.1 Objectives of the Tests

The objectives of the PIV tests on the model rotors are listed as follows:

1. **Obtain full-field velocity data**

   The first objective of the tests with the model rotors was to capture detailed velocity data across the full field of the near wake of the models. The resulting PIV velocity vectors maps would then form the basis of all subsequent analysis.

2. **Obtain full-field vorticity data**

   Experiments with a two-bladed rotor aimed to capture vorticity recently shed from the blade as it passed through the laser sheet. The PIV velocity maps could then be converted into vorticity contour plots, in order to compare results with vortex wake codes. This is detailed in Chapter 5.

3. **Investigate the turbulent structure of the wake**

   Experiments with a three-bladed model rotor aimed to simulate a full scale experimental campaign on the Greek Island of Samos in 1991 by researchers from the University of Athens. Mean wake velocities and turbulent velocity values could be then obtained by a process of averaging PIV records and contrasted with full-scale measurements. Chapter 4 contains further details of the Samos Island campaign of 1991 and the analysis of the data for subsequent comparison with the PIV results.

4. **Investigating the influence of scale**

   An important feature of the work was to establish whether tests on a rotor at model scale could yield valid data regarding the performance of full-scale wind turbines. In replicating as accurately as possible the conditions pertaining to the full-scale measurements on Samos Island, any discrepancies between the full-scale measurements and those obtained from PIV tests could be attributed mainly to scale effects. This is discussed in Chapter 6.

## 3.2 General Experimental Procedures

### 3.2.1 Set-up of Laboratory Equipment

#### (a) Turbine rig position

In positioning the 2-blade rotor it was intended to capture cross-sections of the helical vortex filaments while avoiding interference of the blade in the laser light.

The nacelle of the rig was thus placed slightly offset from the position of the laser sheet in the centre of the water channel. Vortex filaments shed from the trailing edge were then captured in the laser sheet. Variation in the component of vorticity perpendicular to the light sheet, due to offset from the centreline, was assumed negligible.

The 3-blade rotor was positioned so that the laser sheet intersected the blade at a location corresponding to the height of the downstream anemometer unit at full-scale. This was equivalent to an offset distance of 0.42R from the rotor centreline to the laser sheet. Assuming an axially symmetric wake, data were thus recorded at an equivalent offset position from the centre of the wake to the readings taken at full scale.

Values for the rig position in each case can be found later in the chapter, in Tables 3.3.2 and 3.4.2.

### (b) Turbine rig operation

The speed of the electric motor of the turbine rig was altered to change the blade tip speed in order to achieve the desired tip speed ratio. This also had the effect of altering the Reynolds number of the flow over the blade. The Reynolds number is proportional to the ratio of inertial to viscous forces on the fluid. In wind turbine studies, it is conventional to define a *blade* Reynolds number based on the relative velocity (W) and the chord (c) at a point on the blade. Thus,

$$Re = \frac{Wc}{\nu} \tag{3.1}$$

where $\nu$ is the kinematic viscosity of the fluid. The influence of Reynolds number on the PIV experiments is addressed in Chapter 6.

Values for the tip speed ratios and blade Reynolds numbers in both the 2-blade and 3-blade experiments are shown in Tables 3.3.2 and 3.4.2.

### (c) Flow rate

The valves controlling the flowrate from the centrifugal pump were set to allow maximum current recirculating through the water channel. The current velocity was initially estimated by tracing pollen particles over a section of the wave flume, but final current values were derived from the PIV analysis.

### (d) Configuration of turbulence manipulators

An arrangement of honeycomb section, perforated plate and fine mesh screen were used as turbulence manipulators upstream of the rotor. From the Samos experiments, it was concluded that the wind speed and turbulence intensity were fairly constant through the rotor disk. At full-scale, the mean upstream turbulent intensity was 6%[56]. Thus, the turbulence manipulators in the water tank were arranged to produce a uniform upstream profile with low turbulence[68]. Values for the spacing of the manipulators for each set of experiments are given in Tables 3.3.2 and 3.4.2.

### (e) Camera position

The rotating mirror shift system was used. The tripod supports camera and mirror, mounted on a baseplate. The camera was raised until the nacelle of the rig was centred in the viewfinder with respect to the height of the film frame. The hub of the blades were situated at one-sixth of the frame length from the left-hand edge, with the remainder of the frame to capture the wake image. This camera position allowed a global picture of the wake to be captured, focussing on the near wake. With the camera in the same position, a series of still-flow recordings were taken in order to establish corrections for shift velocities.

### (f) Synchronization

The shifting system was synchronized to capture the 2-bladed rotor in a vertical position, parallel to the tower of the rig. This captured cross-sections of trailing vortex filaments while avoiding interference of the blade in the sheet. Six frames were taken of 5 tip speed ratios, each with the flat-plate blade in the vertical position.

For the 3-bladed rotor, a different form of synchronization was required. Since the full-scale results were based on time-averaged recordings, while the PIV technique produced instantaneous wake images, it was necessary to repeat each PIV test several times, with the image synchronised to a different rotor position. A numerical average was then taken of the resulting vector maps. Six exposures were taken of the rotor at each tip speed ratio. The rotor and the image-recording system were synchronized to capture the blade in six different azimuthal positions at 20 degree intervals. For a 3-bladed rotor, this discretizes one whole revolution. Averaging the velocities in the wake recorded in these six phases introduces a concept of temporal averaging akin to the full-scale experiments.

## 3.2.2 PIV Procedures

### (a) PIV parameters

The same PIV parameters were used for both the 2-blade and 3-blade experiments and are outlined on the next page in Table 3.2.2.

A shutter speed of 8ms allows 3 images for each particle to be captured on film. The arc swept by the 2-blade rotor during this shutter time is less than 10 degrees at the highest tip speed ratio tested. The arc swept by the 3-blades during this time is between 2–6 degrees over the range of tip speed ratios tested.

| | | |
|---|---|---|
| camera | aperture | 2.8 |
| | exposure time | 8ms |
| | shutter delay time | 30ms |
| laser | power | 14W |
| | scan time | 2.5ms |
| mirror | rotation | 20°/s |
| | sweep time | 500ms |

**Table 3.2.2** Parameters for PIV acquisition.

### (b) Analysis parameters

The PIV negatives of the 2-blade rotor were analyzed using two separate numerical grids. A small He-Ne laser was used to probe areas on the film of ≈1mm diameter at a time. In physical units, this corresponded to examining a total area in the water channel of 0.6m × 0.6m. Grid spacings are the same in both cross-wake and downstream directions with a stepsize of 12mm. Analysing on a finer grid of 7.5mm spacings highlighted a lower part of the wake corresponding to an area in the channel of 0.5m × 0.26m.

The PIV negatives for the 3-blade rotor were analysed on a grid of 2550 points. Analysis over an area of 0.6m × 0.588m (in physical units) with stepsize 12mm produced a 'global' picture of the near wake.

Similar regions were analysed for the still-water negatives and the resulting datafiles were averaged together to form files of correction data for the PIV rotor flow records.

### 3.2.3 Post-analysis Processing

The datafiles from the still-water tests were averaged and subtracted from each datafile of the 2-blade and 3-blade rotor results. The resulting datafiles were averaged with respect to tip speed ratio. Averaging of instantaneous wake images extracts the coherent structure of the trailing vortex filaments from the superposed turbulence. In the 2-blade experiments, the synchronisation process captured the wake in the same phase whereas in the 3-blade experiments, the wake was recorded at discrete phase increments. For clarity, the averaged images from the 2-blade tests shall be referred to as 'frozen' wakes and the 3-blade images simply as 'averaged' wakes.

Statistical analysis of the averaged files produced values for the mean axial velocity upstream of the rotor for each tip speed ratio. These quantities were calculated from the first three columns of the averaged files. This avoided possible errors associated with taking values only from the first column, due to signal dropout at the edge of the film. This procedure was also repeated for each of the raw datafiles, to separate the effect of averaging from possible trends in the results. Figure 3.2.3(i) shows the mean upstream velocity statistics for both the 2-blade and the 3-blade rotor measurements. The datapoints for the 2-blade results are seen to be distributed fairly evenly around 0.25m/s, the rated value for the re-circulating flow. The 3-blade raw data are more scattered and the results appear to be strongly affected by blade speed. The value for the mean axial upstream velocity can be found from results at lowest blade rotation rate where the effect of the rotor is assumed to be negligible. Since the sample size of raw data is small, a reasonable an estimate of the upstream velocity from the 3-blade measurements is the rated current value, 0.25m/s.

Information about turbulence parameters was extracted in the averaging process. At each grid point,

$$s^2 = \frac{n}{n-1}\left(\frac{\sum_{i=1}^{n} x_i^2}{n} - \overline{x}^2\right) \tag{3.2}$$

was used as an unbiased estimate of the velocity fluctuations, $\sigma^2$, where $n$ is small.

Values for the ambient turbulence in terms of longitudinal fluctuations were taken from mean variations upstream of the rotor. Figure 3.2.3(ii) plots values of the upstream turbulence intensity against blade rotation rate for the 2-blade and 3-blade results. The value for the ambient turbulence can be found from results at the lowest rotation rate where the effect of the rotor on the upstream flow can be assumed to be negligible. Due to the small sample size, the relationship between upstream turbulence and rotation rate is estimated by first approximation. A line of regression is plotted through the datapoints for the 2-blade and 3-blade results. From Figure 3.2.3(ii), a value for the ambient turbulence intensity is selected as $\sigma/Uo = 4\%$ in both cases.

## 3.3 Two-blade Rotor Tests

### 3.3.1 Description of the Model

The two-blade model rotor was made using flat-plate blades. The blades were chosen for their simplicity of construction and for reasons of comparison with theory, since the blades represent a very fundamental case. The blades were cut from sheet aluminium to a diameter of 175mm. Figure 3.3.1(i) shows a photograph of the flat-plate model. The solidity of the rotor is 9.1%. The blades have a thickness of 1.26mm and a hub chord of 15mm, with a linear taper to a tip chord of 10mm. Finally, the leading edge was smoothed and the trailing edge sharpened in the workshop. Details of the blade dimensions are shown in Figure 3.3.1(ii).

### 3.3.2 Test Parameters

The test parameters for the two-blade experiments are summarised in Table 3.3.2. The table gives values for the placing of the turbulence manipulators as distances upstream of the rotor blades. The rig position is the offset distance of the nacelle

from the laser sheet and the camera height is measured from the floor to the middle of the lens. The blade Reynolds (Re) number is based on chord length measured at 70% blade span.

| | | |
|---|---|---|
| rig position | | 10mm |
| turbulence manipulators | honeycomb | 2.48m |
| | perforated plate | 2.08m |
| | mesh screen | 1.3m |
| camera | height | 1.24m |
| | optical distance | 0.88m |
| | magnification | 0.085 |
| tip speed ratios | | 3, 4, 5, 6, 8 |
| range of Re numbers | | $6.4 \times 10^3 - 1.6 \times 10^4$ |

**Table 3.3.2** Test parameters for the 2-blade rotor experiments.

### 3.3.3 Results and Comments

Velocity vector maps in order of increasing tip speed ratio are displayed in Figures 3.3.3(i)-(iii). At the lowest tip speed ratio, $\lambda = 3$, the wake appears as an area of reduced velocity behind the turbine model which recovers to the freestream velocity with downstream distance. There is evidence of a sinusoidal pattern at the boundary of the wake which can be attributed to the presence of vorticity shed from the blades. Velocity vector maps of the lower half of the wake highlight the sinusoidal pattern of the wake boundary, as shown in Figures 3.3.3(iv)-(vi).

As the tip speed ratio increases, the wake becomes more evident, growing in width and containing greater velocity deficits and a stronger sinusoidal pattern at the edge of the wake. At $\lambda = 6$, the velocity deficits have increased to such an extent that the region of flow immediately behind the nacelle appears to be almost stagnant. Together with this stagnant wake core and the outer wake containing strong vortex structure, a third region of wake flow becomes clearer from the

vector maps at high tip speed ratios. Immediately behind the rotor, an 'inner wake' is evident: a region of shear velocities that divides the outer freestream from the wake core.

At the highest tip speed ratio, $\lambda = 8$, the wake is still increasing in width and the flow in the inner wake is observed to move under the influence of wake expansion. Areas of recirculating flow can be observed within the wake and the wake boundary has started to contract at a downstream distance of around 0.4m. This is consistent with the flat-plate blades operating in a 'turbulent wake state', as defined by Eggleston & Stoddard[38]. The structure of the wake is discussed in more depth in Chapters 4 and 5.

## 3.4 Three-blade Rotor Tests

### 3.4.1 Description of the Model

The model rotor was a 1/100th scale replica of the 3-bladed Vestas (formerly Windmatic) WM-19S. Figure 3.4.1(i) displays a photograph of the model. The blades were manufactured[1] from rigid plastic, using a numerically controlled cutter. Despite the small scale, the model blades were accurately profiled with a NACA-632XX section, with twist, chord and thickness distributions based on the manufacturers' original drawings (see Figures 3.4.1(ii)-(iv)). The 3-blade model rotor has a solidity of 7.8%.

[1] courtesy of Angus Modelmakers, Glasgow

### 3.4.2 Test Parameters

The test parameters for the three-blade experiments are summarised in Table 3.4.2.

| | | |
|---|---|---|
| rig position | | 37mm |
| turbulence manipulators | honeycomb | 2.5m |
| | perforated plate | 2m |
| | mesh screen | 1.2m |
| camera | height | 1.24m |
| | optical distance | 0.89m |
| | magnification | 0.084 |
| tip speed ratios | | 1.6, 2.7, 3.2, 4.2, 4.8 |
| range of Re numbers | | $2.6 \times 10^3 - 6.0 \times 10^3$ |

**Table 3.4.2** Test parameters for the 3-blade rotor experiments.

### 3.4.3 Results and Comments

Velocity vector maps in order of increasing tip speed ratio are displayed in Figures 3.4.3(i)-(iii). For the low tip speed ratios of $\lambda = 1.6, 2.7$ and 3.2, there is little discernible effect behind the rotor. At $\lambda = 4.2$ the wake becomes more obvious as an area of reduced velocity forming behind the rotor, recovering to the freestream value with downstream distance. At the highest tip speed ratio tested, $\lambda = 4.8$, the region directly behind the rotor contains larger wake deficits. In addition, there is slight wake expansion and slower recovery with downstream distance.

## 3.5 Summary and Discussion

PIV tests were undertaken on two different model rotors. A 2-blade model was constructed of flat-plate blades while a 3-blade model was manufactured by a

professional modelmaker as a replica of a full-scale machine from the windpark on the Greek island of Samos. While both sets of tests aimed to record detailed wake velocities, the flat-plate tests were specifically designed to capture vortex structure in the wake, in order to compare with vortex wake codes. The 3-blade tests were designed for comparison with measurements of mean and turbulence properties of the wake of the Samos Island machine.

The equipment and parameters used in the tests are listed in detail. In addition to the experiments with the rotors, PIV experiments were also carried out for still water in the channel. Post-analysis processing of PIV data involved subtracting the still water results from the model rotor results in order to calibrate for image-shifting errors. Phase averaging of PIV flow records produced maps of 'frozen wakes'. Capturing the blade at different azimuthal positions discretized one rotor revolution, and map averaging introduced a concept of 'time-averaged' wakes.

A statistical analysis of the PIV data produced values for the mean upstream axial velocity and ambient turbulence. There was a general trend of increasing upstream turbulence with increasing blade rotation. This suggested that the rotor exerted an influence over upstream flow at higher rotation speeds. This may be attributed to diversion of the flow by the rotor. The upstream flow approaches the turbine and at high rotation rates is forced outwards, around the edges of the area swept by the rotor.

The results of the tests are presented in the form of velocity vector maps. A brief comment upon the results is given from inspection of the maps. The maps show the wake flow to be divided into 3 distinct regions; a wake core with high velocity deficits, an inner wake with sheared flow and an outer wake containing strong vortex structure. Further analysis of the wake structure is detailed in Chapters 4 and 5.

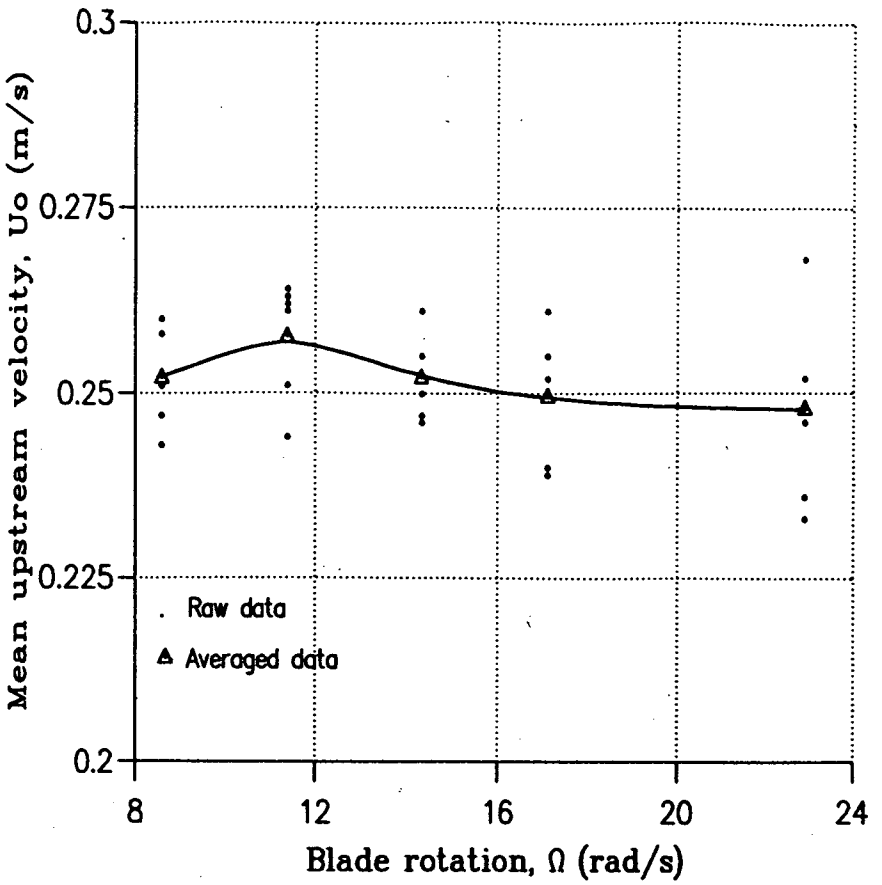


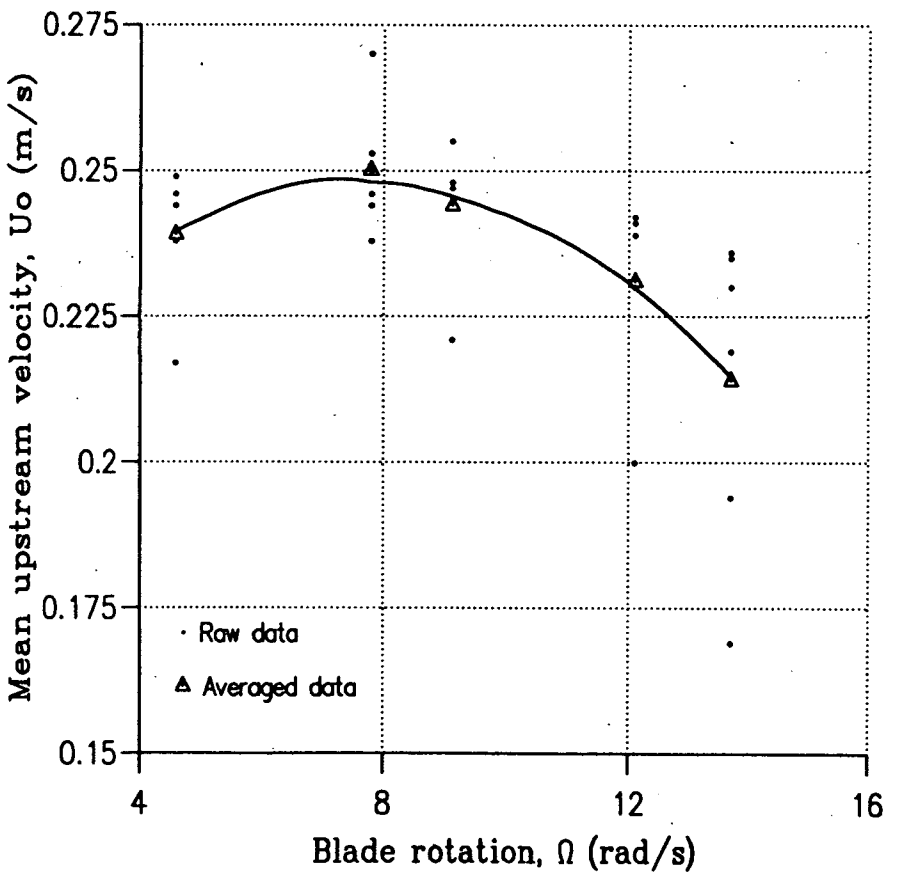


Figure 3.2.3(i) Mean upstream velocity statistics for the 2-blade rotor (above) and the 3-blade rotor (below).

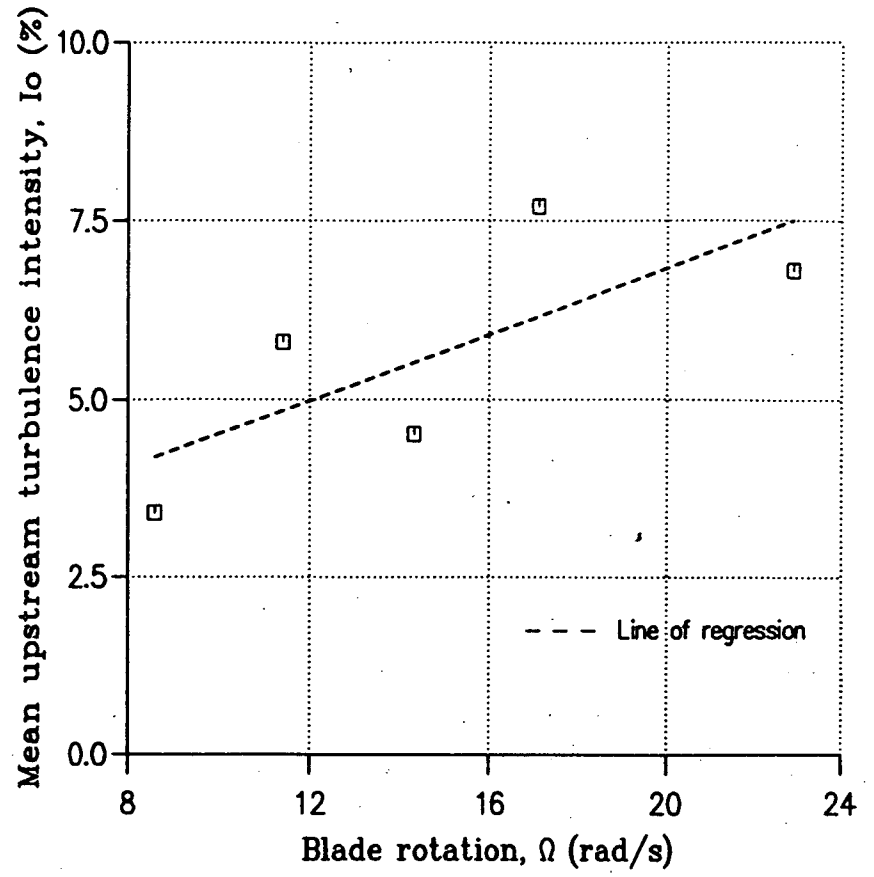


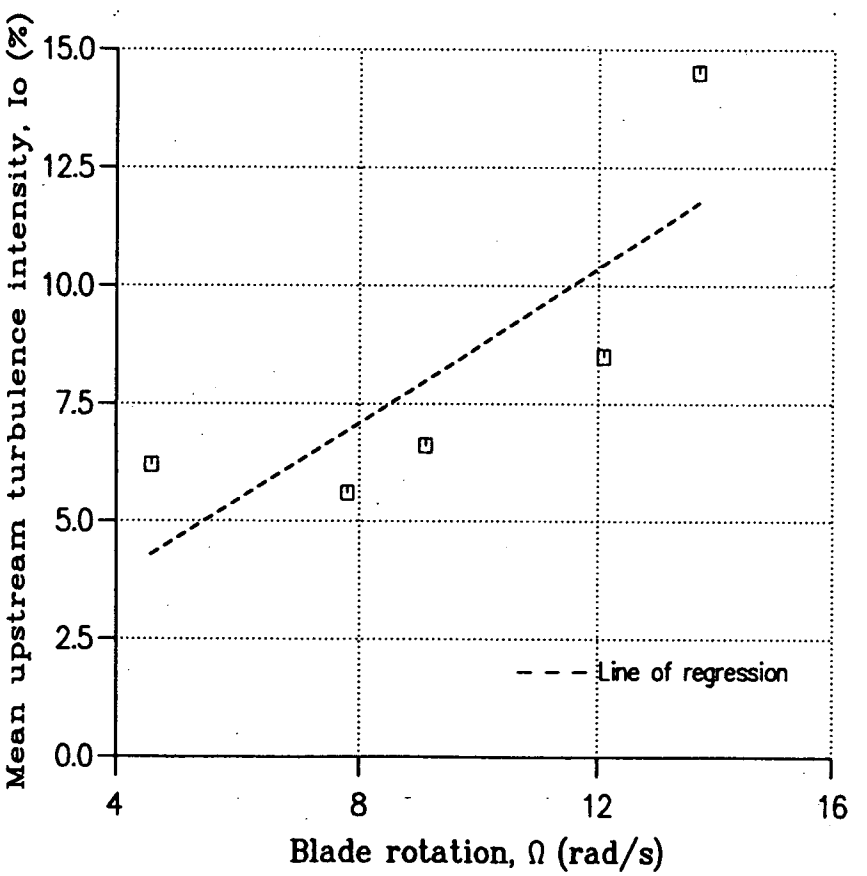


Figure 3.2.3(ii) Mean upstream turbulence statistics for the 2-blade rotor (above) and the 3-blade rotor (below).

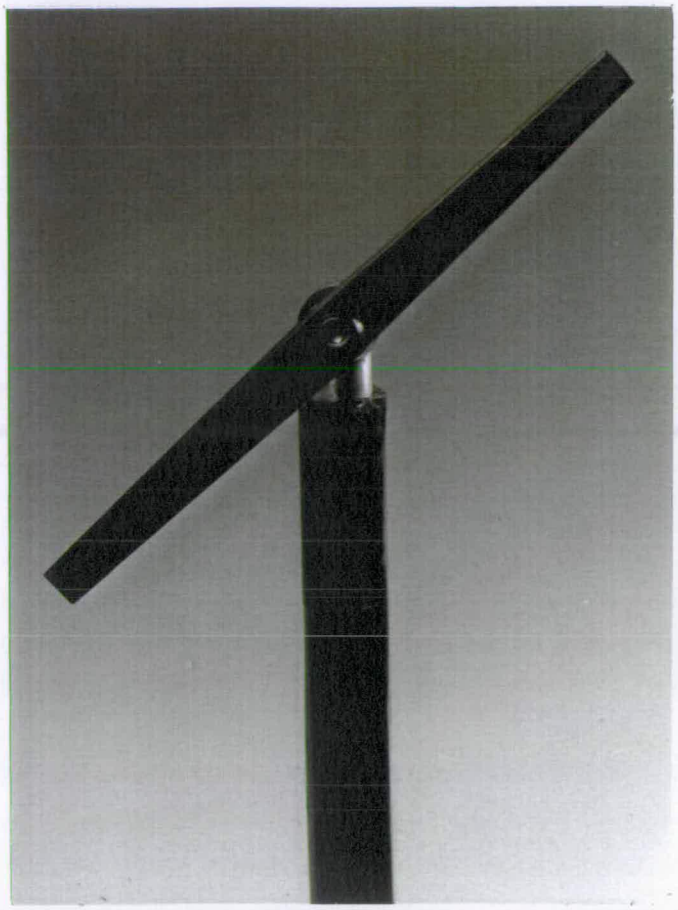

Figure 3.3.1(i) Photograph of the 2-blade flat-plate rotor.

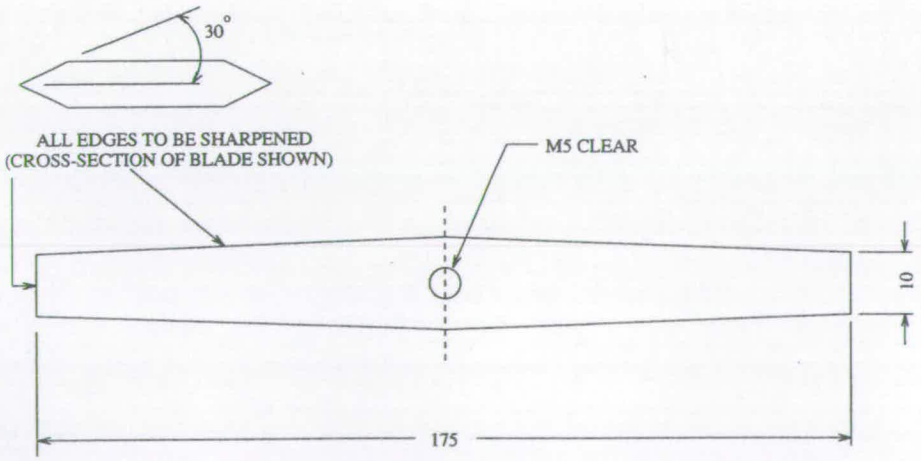


Figure 3.3.1(ii) Dimensions of the flat-plate blades.

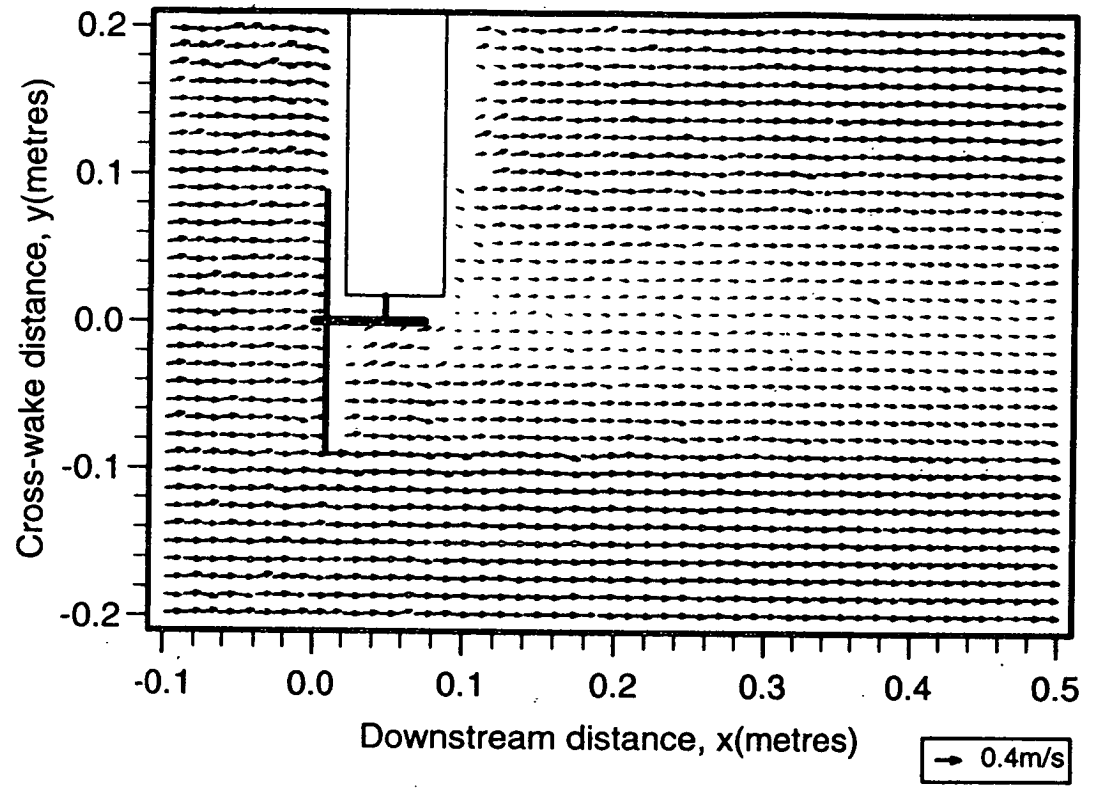


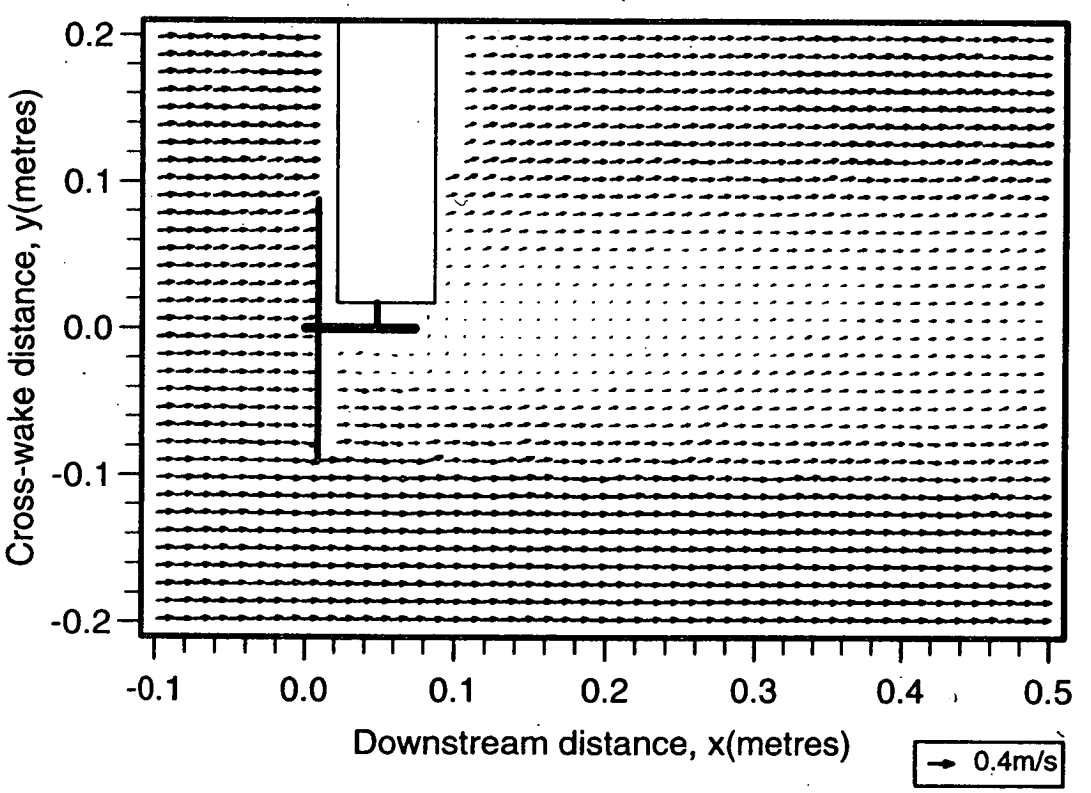


Figure 3.3.3(i) PIV velocity vector maps of the wake behind 2-blade rotor at $\lambda = 3$ (above) and $\lambda = 4$ (below).

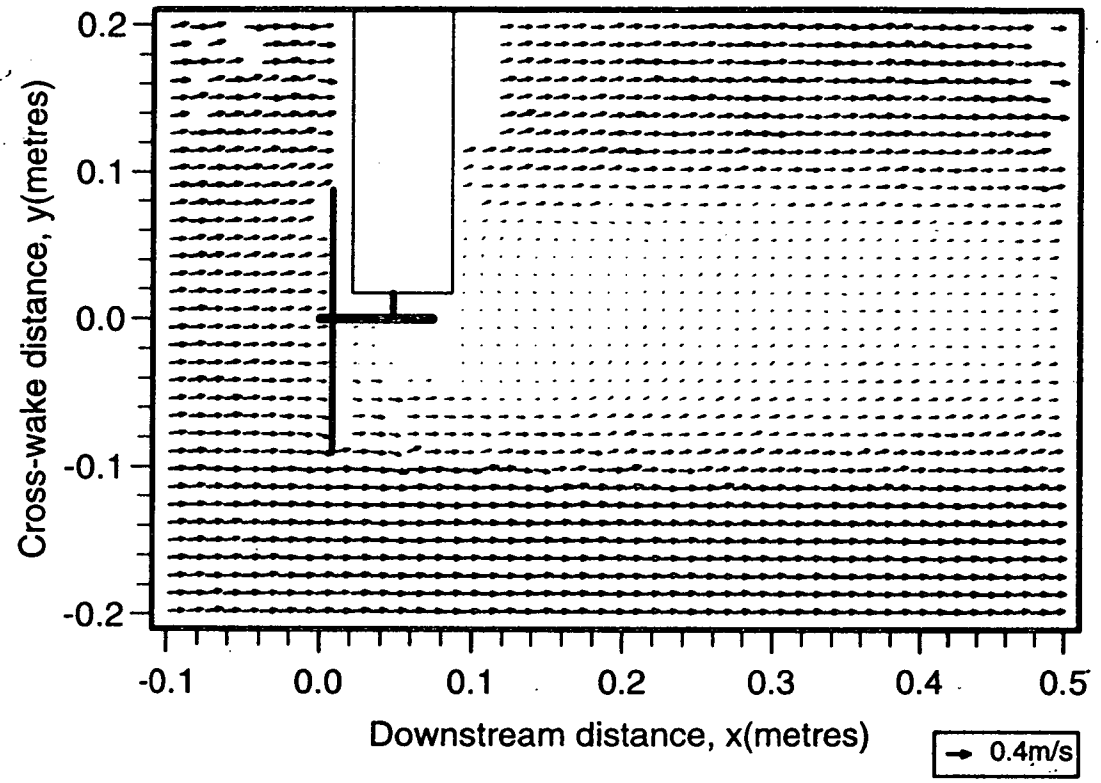


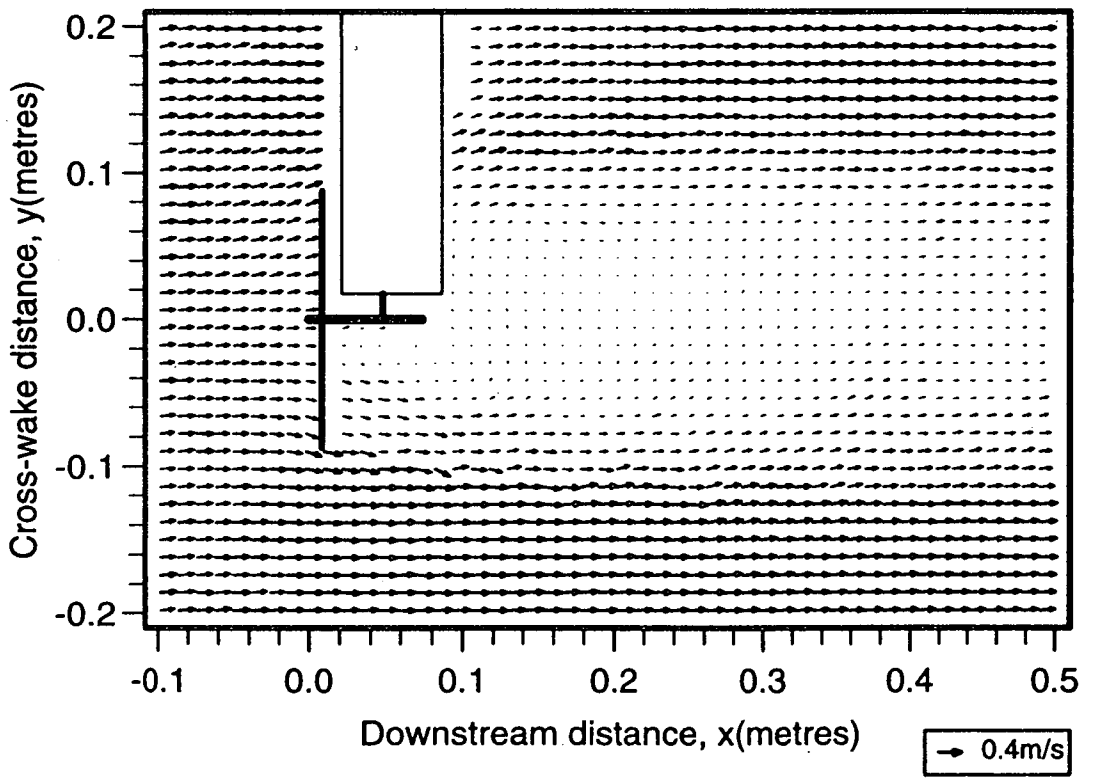


Figure 3.3.3(ii) PIV velocity vector maps of the wake behind 2-blade rotor at $\lambda = 5$ (above) and $\lambda = 6$ (below).

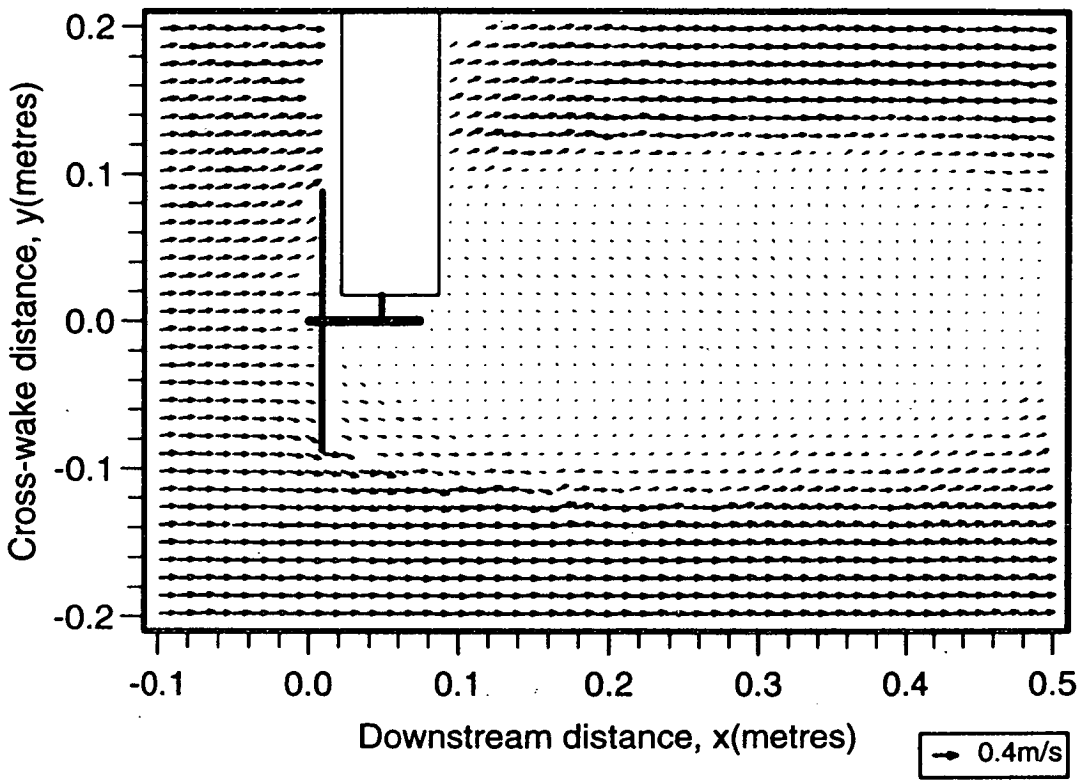


Figure 3.3.3(iii) PIV velocity vector map of the wake behind 2-blade rotor at $\lambda = 8$.

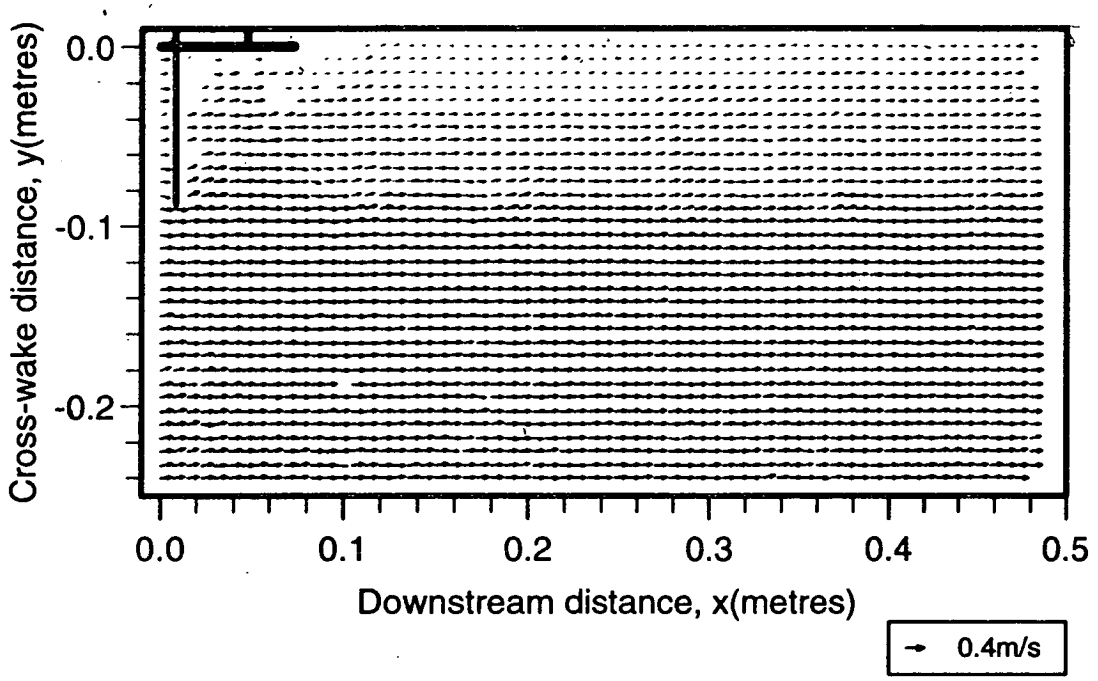


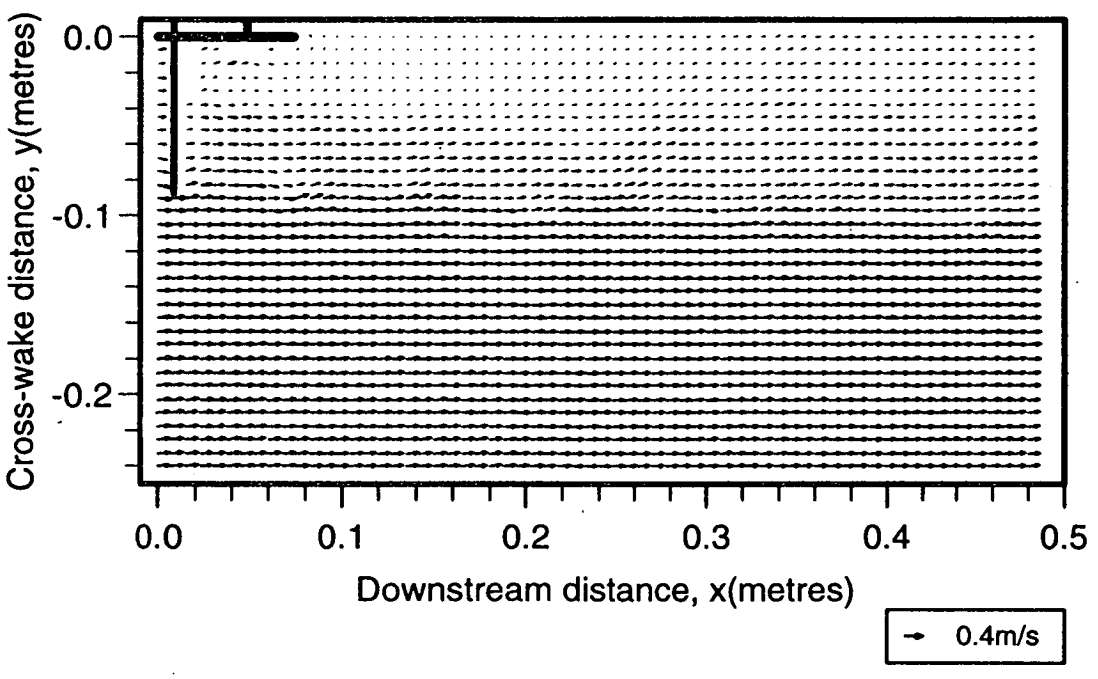


Figure 3.3.3(iv) PIV velocity vector maps of the lower half of the wake behind 2-blade rotor at $\lambda = 3$ (above) and $\lambda = 4$ (below).

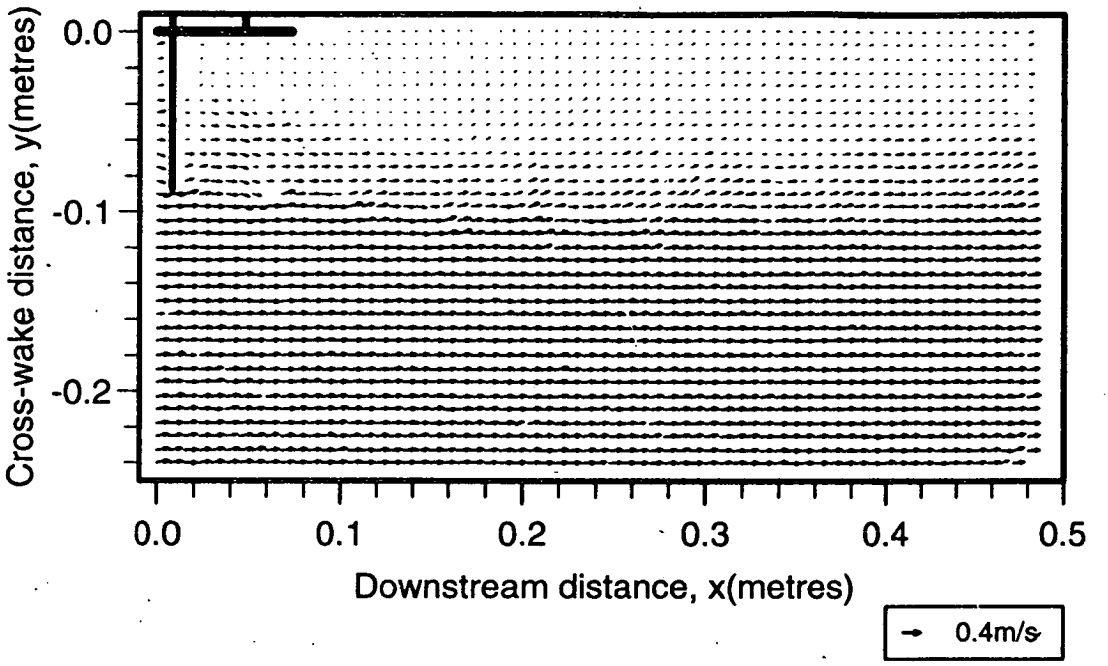


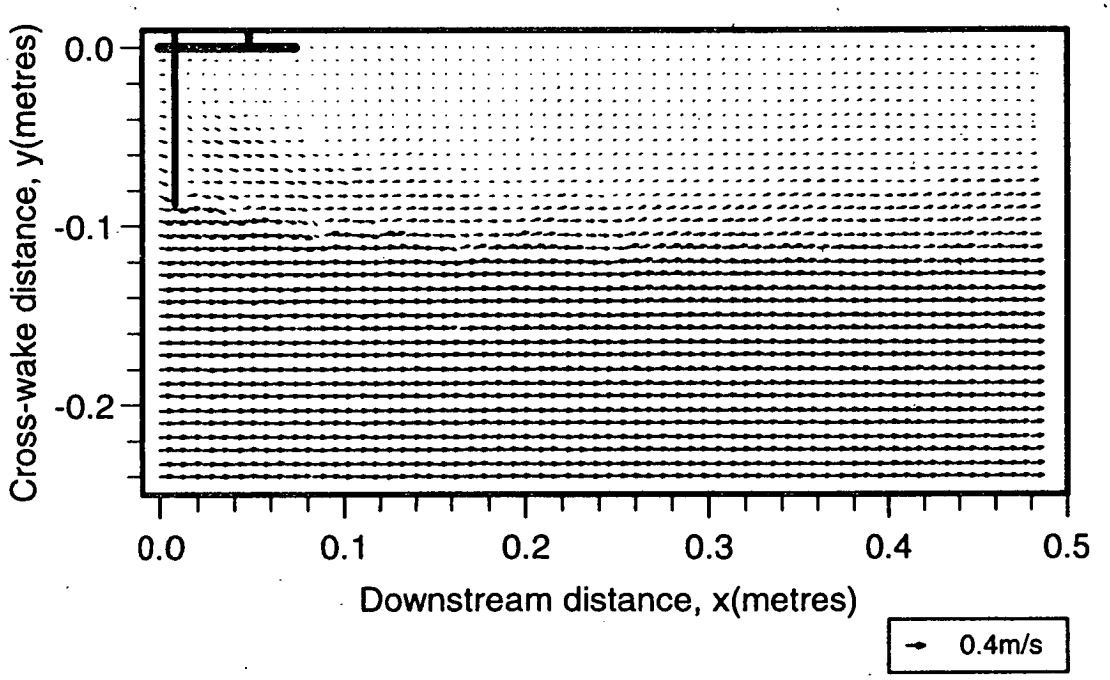


Figure 3.3.3(v) PIV velocity vector maps of the lower half of the wake behind 2-blade rotor at $\lambda = 5$ (above) and $\lambda = 6$ (below).

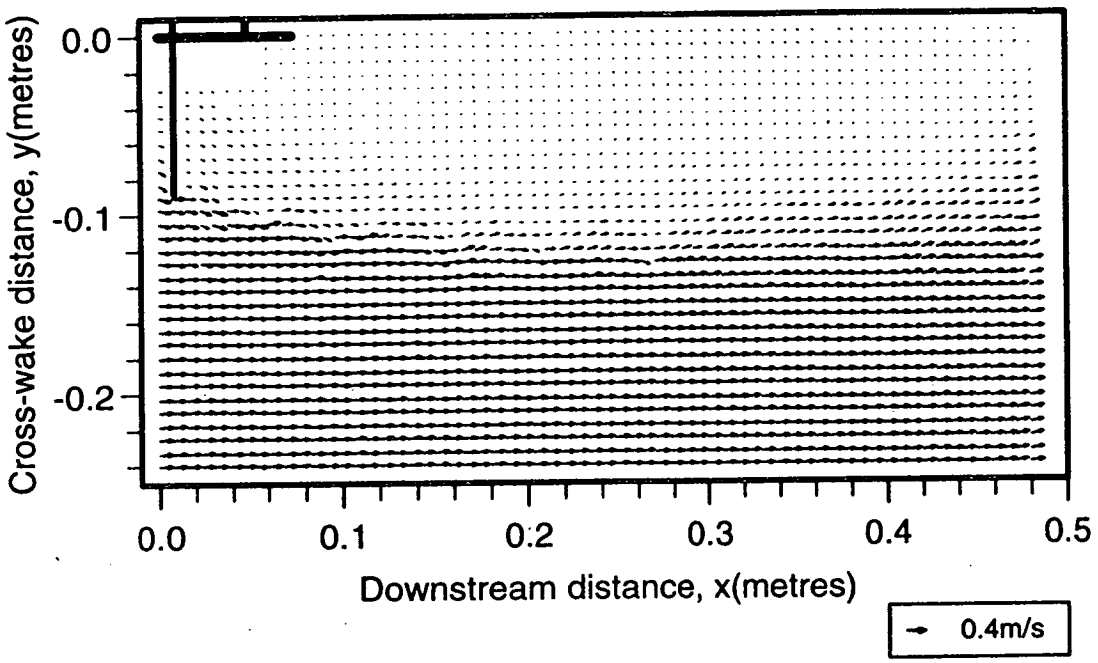


Figure 3.3.3(vi) PIV velocity vector maps of the lower half of the wake behind 2-blade rotor at $\lambda = 8$.

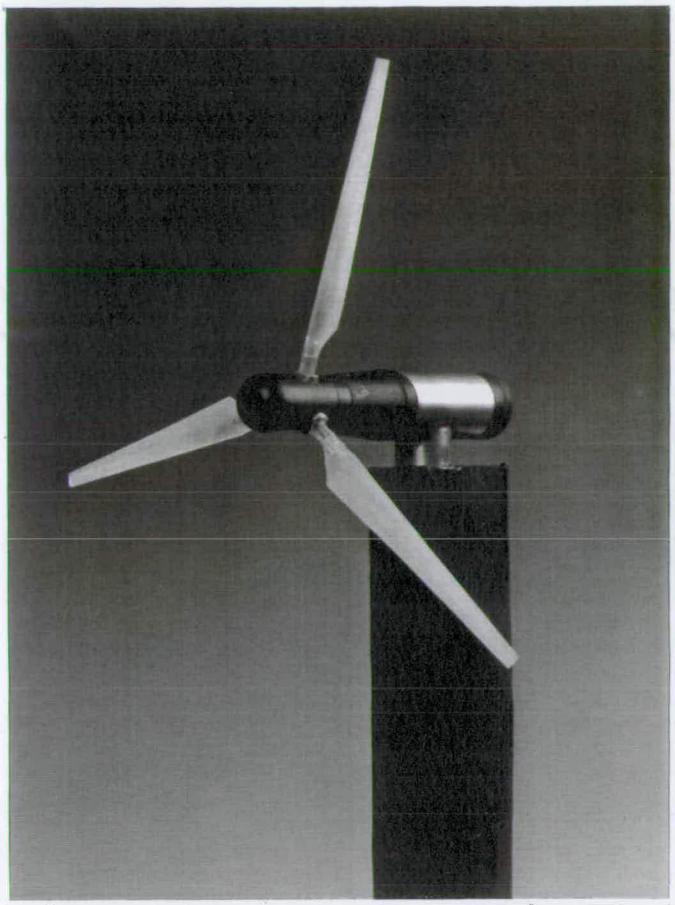

Figure 3.4.1(i) Photograph of the 3-blade WM19S Vestas replica.

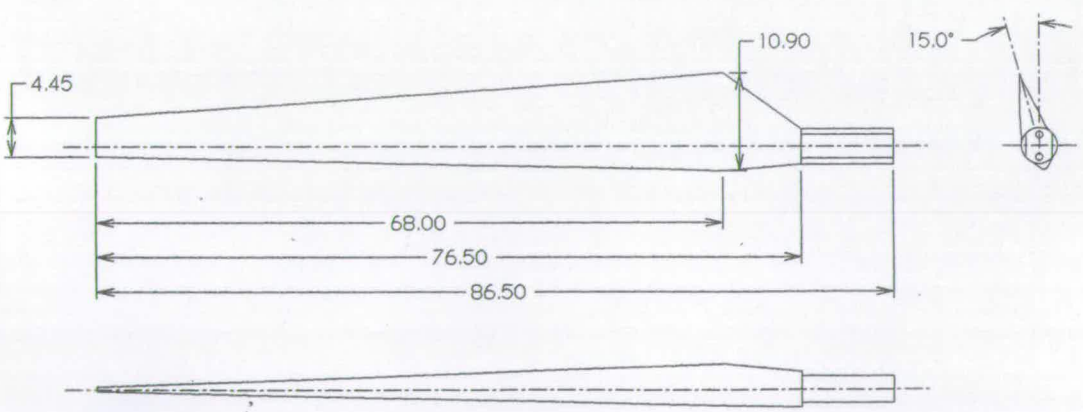


Figure 3.4.1.(ii) Dimensions of the Vestas replica blades.

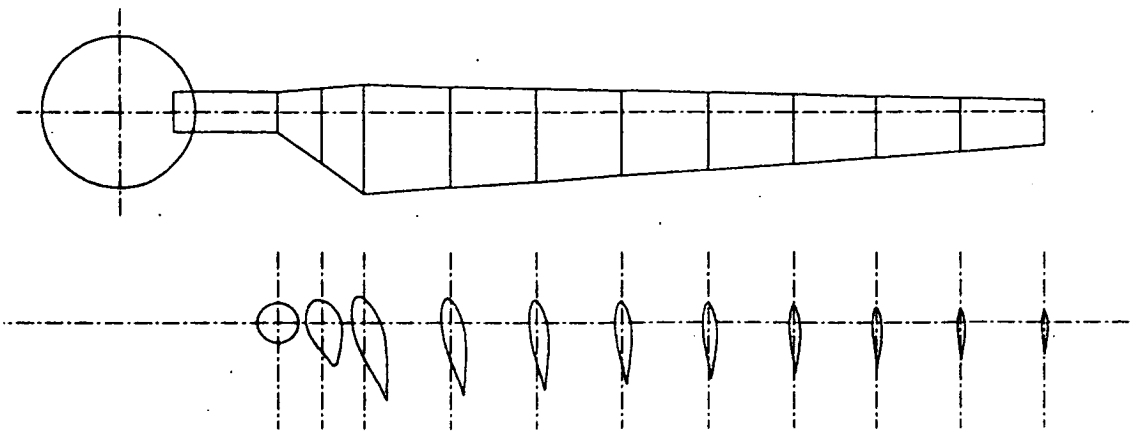

Figure 3.4.1(iii) Spanwise twist distributions used in the manufacture of the replica.

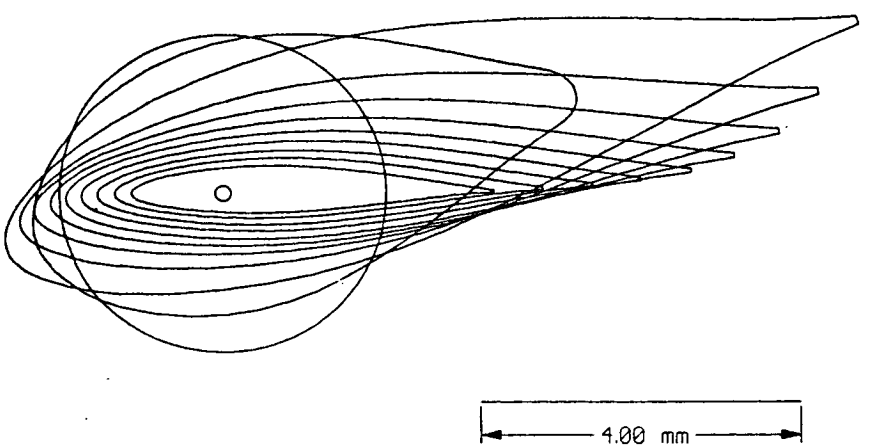


Figure 3.4.1(iv) Superposition of segments showing the spanwise change in pitch and chord for the replica.

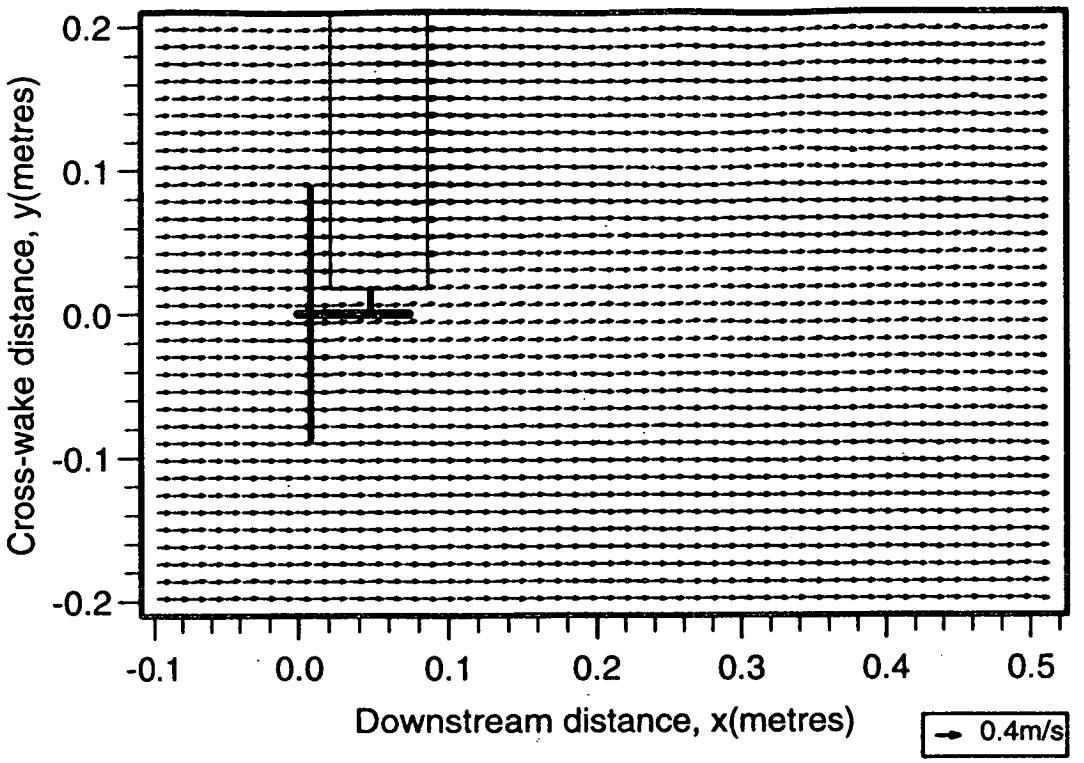


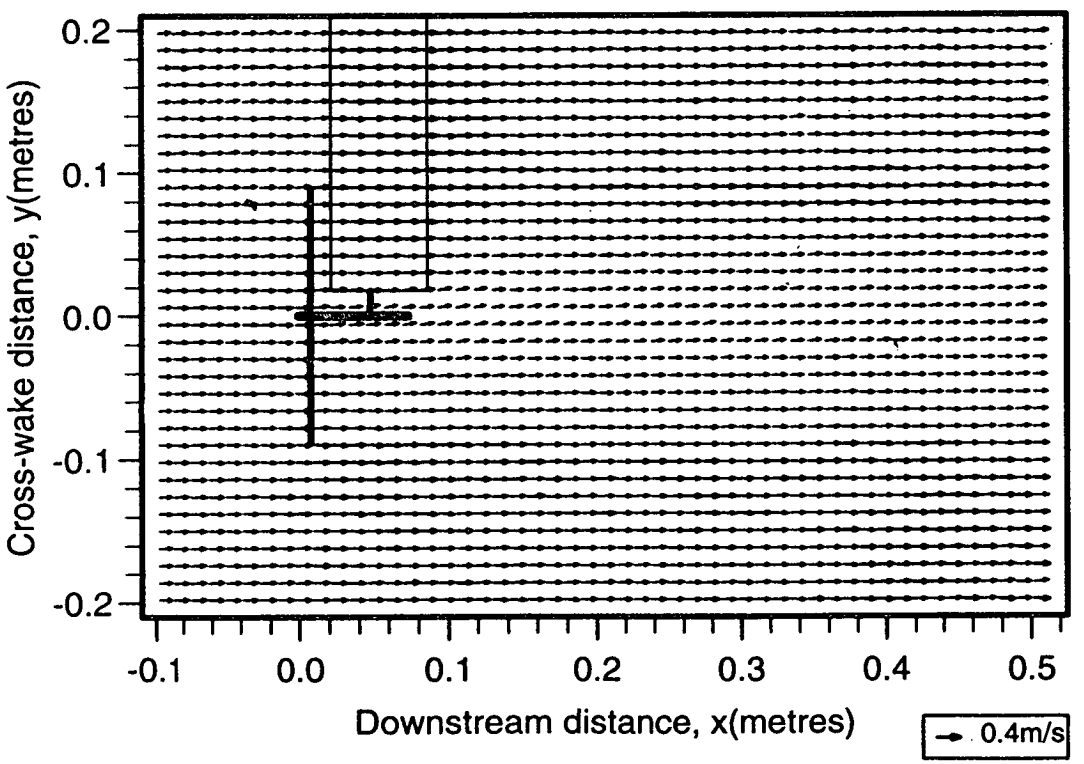


Figure 3.4.3(i) PIV velocity vector maps of the wake behind 3-blade rotor at $\lambda = 1.6$ (above) and $\lambda = 2.7$ (below).

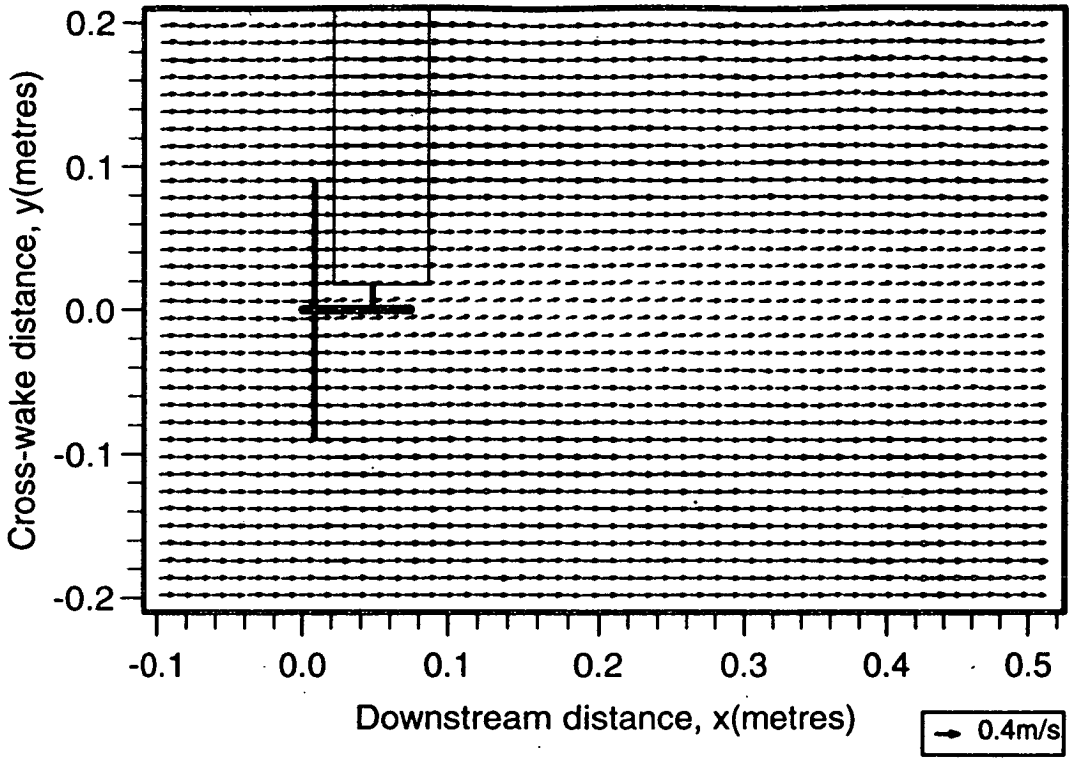


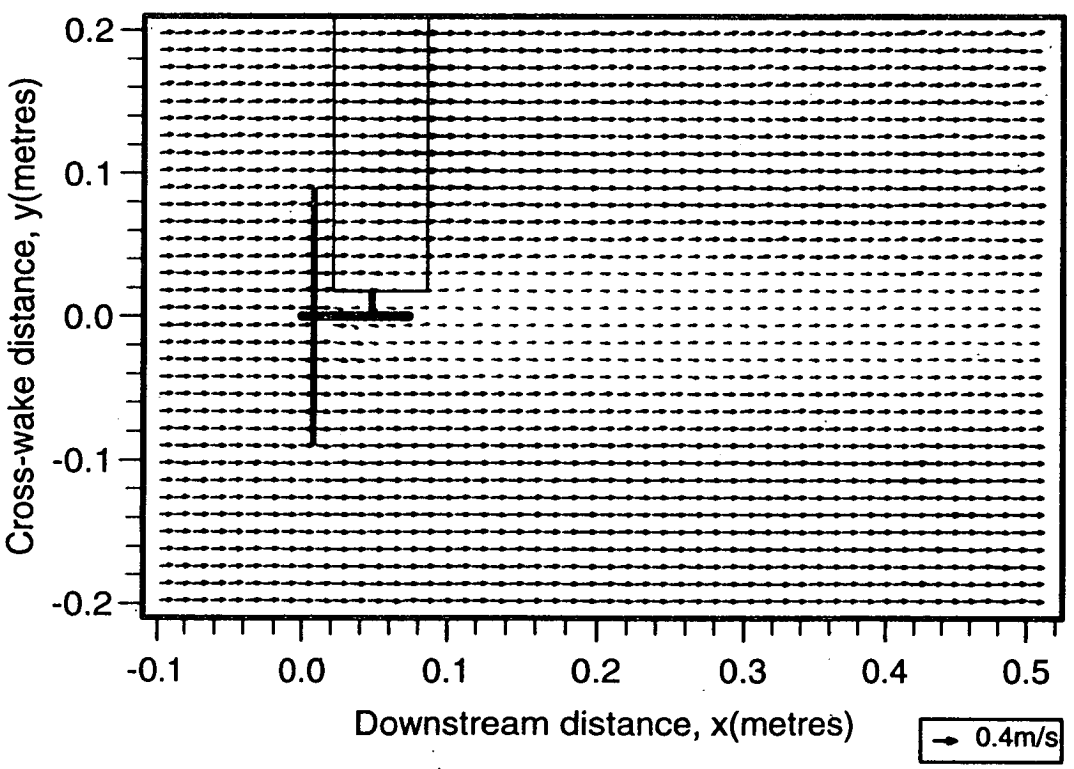


Figure 3.4.3(ii) PIV velocity vector maps of the wake behind 3-blade rotor at $\lambda = 3.2$ (above) and $\lambda = 4.2$ (below).

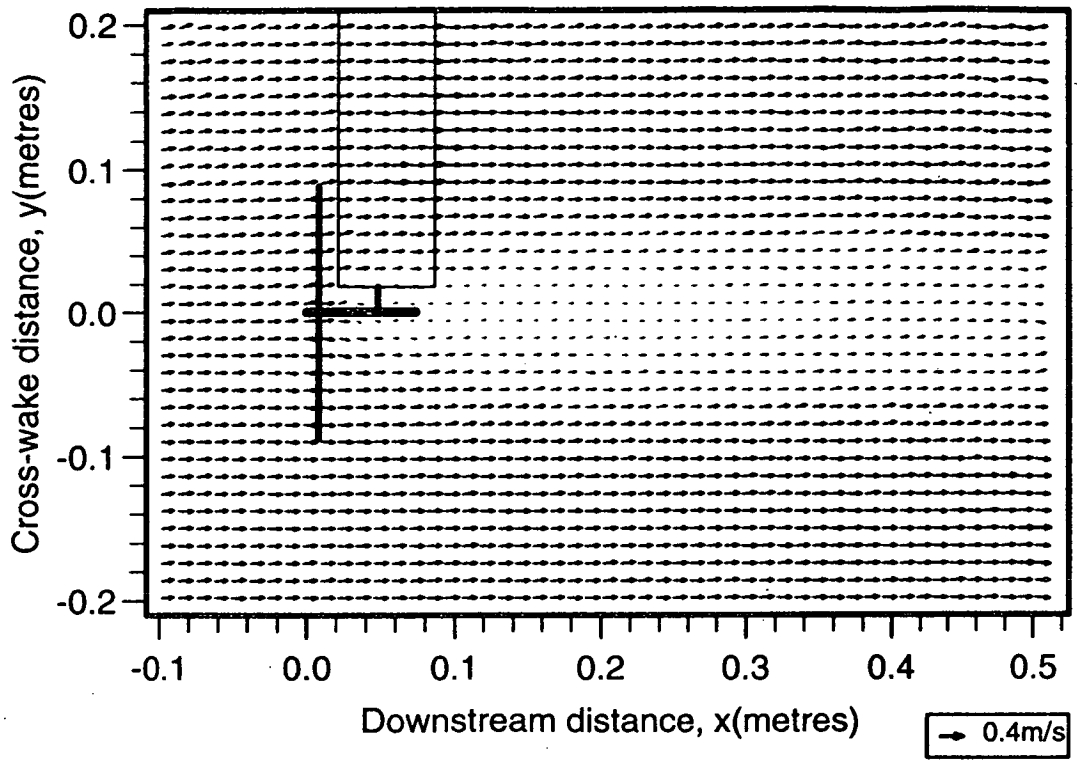


Figure 3.4.3(iii) PIV velocity vector map of the wake behind 3-blade rotor at $\lambda = 4.8$.

# Chapter 4

## WAKE VELOCITY STRUCTURE

### Overview

In this chapter the use of PIV velocity vector maps to obtain wake velocity and turbulence profiles is described. Data are presented from measurements on both a 2-blade and a 3-blade rotor model. The data is reduced to a normalised form which allows features of the wake to be readily identified and compared with the results of other surveys. These include full-scale measurement campaigns at Samos Island, Greece, as well as the Nibe site and The Risø Test Station for Windmills in Denmark. Comparisons are made with wind tunnel tests conducted at Loughborough University and at the Marchwood Engineering Laboratories.

## 4.1 PIV Analytic Procedures

### 4.1.1 Extracting Velocity and Turbulence Information

#### (a) Mean velocity

The PIV technique provides a complete velocity map in the wake of the model, giving access to cross-wake profiles at any downstream location in the photographic

plane. Mean axial velocity profiles are computed by analysing a single column of vectors in each PIV vector map corresponding to the appropriate distance from the rotor. Results are expressed as a function of $\lambda$ with cross-wake distance plotted against mean axial velocity ratio. The velocity ratio is calculated as a ratio of the local axial velocity at a point to the freestream velocity

$$u' = \frac{u}{U_0} \tag{4.1}$$

**(b) Turbulence**

Turbulent velocity profiles are calculated at a particular downstream station with cross-wake distance plotted against turbulent velocity ratio for each tip speed ratio. Plots of local turbulence velocity are preferred to local turbulence intensity in order to highlight vortex structure within the turbulence profiles. In addition, as far as fatigue damage to full-scale machines is concerned, it is the magnitude of the turbulent fluctuations which is important. For wind turbine loading and performance calculations, information on only the longitudinal component of turbulence is required.

Normalized turbulent velocity is defined as

$$\sigma_u' = \frac{\sigma_u}{U_0} \tag{4.2}$$

where $\sigma_u$ is the standard deviation of the wake velocities at a point in the wake and $U_0$ is the freestream velocity.

The increase in turbulence in the wake of the rotor is also considered and is referred to as *added* turbulence. This is defined as

$$\Delta\sigma_u' = \frac{\sqrt{\sigma_u^2 - \sigma_0^2}}{U_0} \tag{4.3}$$

where $\sigma_0$ is the mean variation of velocity in the freestream.

### (c) Standard error

Six data values are used to calculate the mean axial velocity at each point in the wake. Since the sample size is small, the Student's t-distribution is chosen to mathematically model the random variable, Z, describing the mean axial velocity at a point.

The standard error, S(Z), associated with estimating the mean axial velocity using a sample of six datapoints is

$$S(Z) = z_\alpha \frac{\sigma}{\sqrt{5}} \tag{4.4}$$

where $P(Z > z_\alpha) = \alpha$.

## 4.1.2 Results for 2-blade rotor (frozen wake)

### (a) Mean velocity

Mean velocity profiles from the 2-blade results are shown in Figures 4.1.2(i)-(iii) as a function of $\lambda$ with mean axial velocity ratio plotted against cross-wake distance. The cross-wake profiles are calculated at 0.5D, 1.0D, 1.5D, 2.0D and 2.5D downstream of the rotor for each tip speed ratio. In the presentation of the data, the first profile ($x/D = 0.5$) is correctly positioned on the horizontal axis, while the remaining profiles are offset by multiples of 0.25. Although each profile is based on a single line of vectors from the PIV vector map, their variation in shape with respect to downstream distance can provide information about the development of the wake.

Firstly, it is noted that, in all the figures, there is an asymmetry in the profiles about the wake centreline. This is due to the presence of turbulence in the upper part of the wake introduced by the tower of the turbine and its streamlined shroud. This is most prominent just behind the rotor at 0.5D; the profiles are highlighted using dotted lines.

As $\lambda$ increases, the profiles become smoother with greater velocity deficit and wake expansion just behind the rotor. As the wake recovers, the profiles lose their depth and develop flat central sections by 2.5D downstream. At the higher tip speed ratios the transition to 'square' profiles occurs closer to the rotor.

Plotting the centreline velocity ratios against downstream distance illustrates the wake recovery process more clearly. Figure 4.1.2(iv) shows the slow-up, the velocity 'jump' across the rotor and the gradual return to freestream values of the flow for each tip speed ratio. The speed of recovery is inversely related to the tip speed ratio, as expected. The curves $\lambda = 3$ and $\lambda = 8$ stand out as the cases with the quickest and slowest recovery in centreline velocity, respectively. By 2.5D downstream the magnitude of the axial velocity is 65.6% of the freestream for $\lambda = 3$, while only 4.1% for $\lambda = 8$. There is some scatter immediately behind the rotor in the case of $\lambda = 3$. Separated flow from heavily stalled blades could provide the explanation for this. It is more likely, however, that the scatter is the result of missing data due to the presence of the tower shroud in the light sheet. For the other values of $\lambda$, Figure 4.1.2(iv) shows the velocity to be constant across the rotor disk. This again is likely to be due to missing data values (and the limitations of the graphics package). In the $\lambda = 8$ case, downstream axial velocity ratios are less than zero for a considerable part of the wake centreline, indicating a large amount of recirculating flow behind the rotor.

### (b) Turbulence

Turbulent velocity profiles are displayed in Figure 4.1.2(v) for two locations in the wake, 0.5D and 2.5D downstream. Turbulent velocity ratio is plotted against cross-wake distance for each tip speed ratio. In the presentation of the data, the first profile ($\lambda = 3$) corresponds to the vertical axis, while the remaining profiles are offset by multiples of 0.25.

Comparing the plots, the low-$\lambda$ cases reveal higher turbulence levels at an axial distance of 0.5D than further downstream at 2.5D. At higher tip speed ratios,

the reverse appears to be true. In addition, the turbulence at 2.5D appears less scattered than that at 0.5D. The $\lambda = 6$ curves of the figure display a strong double-peaked structure associated with vortices at the tips of the blades. The curve furthest downstream exhibits broader peaks suggesting wake expansion together with an increase in turbulence across the wake. The turbulence peaks seen outside the rotor circumference (specifically $y/R > 1$) may be due to the wake of the supporting 'tower'.

Turbulent velocity ratios on the wake centreline at 0.5D, 1.0D, 1.5D, 2.0D and 2.5D are plotted in Figure 4.1.2(vi). In general, the turbulence at each downstream station appears to increase for the range $\lambda = 3-5$, reach a maximum around $\lambda = 5$ and then decrease with increasing $\lambda$. The notable exception is at the 2.5D downstream station. There, the turbulence steadily increases with increased rotor speed and for the highest tip speed ratio case, $\lambda = 8$, turbulence in the wake reaches a level 4.2 times the ambient level at 2.5D downstream. The curves again reflect the reversal in trends with respect to turbulence at downstream locations as $\lambda$ increases. At low-$\lambda$, the highest levels of turbulence in the wake exist at the station closest to the rotor whilst at higher $\lambda$, the greatest levels can be found at the furthest downstream station.

### 4.1.3 Results for 3-blade rotor (averaged wake)

#### (a) Mean velocity

Mean velocity profiles from the 3-blade results are shown in Figures 4.1.3(i)-(iii) as a function of $\lambda$ with mean axial velocity ratio plotted against cross-wake distance. The cross-wake profiles are calculated at 0.5D, 1.0D, 1.5D, 2.0D and 2.5D downstream of the rotor for each tip speed ratio. In the presentation of the data, the first profile ($x/D = 0.5$) is correctly positioned on the horizontal axis, while the remaining profiles are offset by multiples of 0.25.

As in the 2-blade profiles, there is a certain amount of asymmetry displayed in

the results. In addition to disturbance produced by tower interference, there is asymmetry in the wake core, which is more pronounced at low tip speed ratios (Figure 4.1.3(i)). This could be the influence of a stalled rotor.

As $\lambda$ increases, the wake profiles become smoother and more closely resemble a Gaussian distribution although there is evidence of 'square' profiles, referred to in Section 4.1.2, at 2.5D downstream for $\lambda = 4.2$ and $\lambda = 4.8$. An increase in velocity deficit is associated with the increase in tip speed ratio. Velocity ratios from the centre of the off-axis plane, although difficult to compare with the 2-blade centreline results, are still of interest. Figure 4.1.3(iv) displays the recovery of the wake with each tip speed ratio. At 2.5D, the velocity for the $\lambda = 1.6$ and the $\lambda = 4.8$ cases have recovered to 91.5% and 49.5% of the freestream, respectively.

### (b) Turbulence

Turbulent velocity profiles are displayed in Figure 4.1.3(v) for two locations in the wake, 0.5D and 2.5D downstream. Turbulent velocity ratio is plotted against cross-wake distance for each tip speed ratio. In the presentation of the data, the first profile ($\lambda = 3$) corresponds to the vertical axis, while the remaining profiles are offset by multiples of 0.1.

The plots display a general increase in turbulence levels with tip speed ratio. The turbulence is less structured than for the 2-blade data due to the 'time-averaging' of measurements. Vorticity at the blade tips, an expected source of high turbulence, was not captured by the laser light due to the discretisation of the rotor's revolution during the measurements.

Turbulent velocity ratios along the centre of the off-axis plane are plotted at downstream stations of 0.5D, 1.0D, 1.5D, 2.0D and 2.5D in Figure 4.1.3(vi). The figure shows a general increase in turbulence at each station over the tip speed ratio range $\lambda = 3-5$, a pattern observed from the 2-blade results. At lower tip speed ratios, high levels of turbulence are noted at 0.5D and 1.0D. At 2.5D, the

highest levels of turbulence in the wake are witnessed, roughly 4 times the ambient turbulence, at $\lambda = 4.8$.

## 4.2 Comparisons with Full-scale Data

Direct comparison of field data is difficult due to significant differences in operating conditions. However, data sets which offer the closest agreement in terms of tip speed ratio, measurement plane and ambient turbulence intensity have been chosen for comparison. The comparison with data from Samos Island, the result of a two-year programme of research with the University of Athens, is covered in the most depth and the following section details the preparation of the full-scale data prior to comparison.

### 4.2.1 Vestas WM19S, Samos Island

#### (a) Description of full-scale experiments

The full-scale tests were carried out on Samos Island, which lies in the eastern region of the Aegean Sea. The wind farm on Samos is located 390m above mean sea level (MSL) on a saddle confined by the island's two major mountain ranges. The wind park is shown in the photographs of Figure 4.2.1(i) and comprises nine three-bladed, horizontal axis, Vestas WM19S wind turbines. Each machine has a rotor diameter of 19m, a solidity of 7.8%. and a hub-height of 25m. The output rating of the WM19S is 100kW.

The WM19S is stall-regulated, with rated power achieved at a windspeed of 13m/s. The cut-in and cut-out wind speeds are 3m/s and 27m/s, respectively. The blades' rotational speed is 48 r.p.m., and the maximum power coefficient $C_{pmax} = 0.38$, is attained in the windspeed range 8−10m/s. The prevailing conditions during

the experiments were quite windy, with wind speeds exceeding 9m/s and reaching 27m/s. The mean upstream turbulent intensity was 6%.

Measurements were made on a single wind turbine, using two anemometers, one upwind (0.8D) and one downwind (1.1D) of the machine. The data to be compared refer to two cup anemometers, mounted at 12m and 29m above ground level, on the upwind and downwind masts, respectively. The anemometers were sampled at a rate of 1Hz. At the given elevation (29m) the downstream unit was above the centreline of the rotor, well clear of the influence of downstream tower shadow. The experimental layout is described fully by Helmis *et al.*[56]. The measurements were made over the period 16–24/8/91.

The wake velocity was expressed as the ratio of downstream to upstream windspeed. In doing this, it was necessary to compensate for influences other than the wind turbine wake: these were principally windshear, non-uniform inflow conditions due to the local terrain, and downstream tower shadow (as noted above, however, the last of these was effectively removed by analysing data at a downstream elevation in the upper half of the wake). Measurements were therefore taken with the turbine in operation (the wake data set) and stationary (the non-wake data set). The results in the latter case were used to establish two correction curves (for low and high winds) for non-wake effects.

### (b) Analysis of full-scale data

A preliminary analysis of the non-wake data set was used to establish the background correction to be applied to operational data. The importance of this procedure is seen from previous results described by Helmis *et al.*, who highlight the uncertainty introduced by estimating wake velocity deficits by comparing upstream and downstream measurements using data recorded only with the turbine in operation.

The background correction is particularly important when dealing with the near-

wake region. In complex topography this is due to terrain inhomogenities; below hub-height the effects of nacelle and tower shadow are also important[93].

The non-wake velocity ratio was found to vary significantly with wind direction, but to be relatively independent of windspeed (Figure 4.2.1(ii)). Data for all windspeeds were therefore averaged to yield two correction curves, which gave the non-wake velocity ratio as a function of wind direction only. This was then used to provide correction factors for the data obtained during operation of the turbine: a given velocity ratio obtained with the turbine running was divided by the non-wake ratio corresponding to the same incident wind direction. In this way the data was treated to compensate for the effects of topography and windshear.

It should also be said that by expressing the velocity ratio as the ratio of the downstream to upstream anemometer readings (suitably corrected), it is implied that the upstream values of wind speed and ambient turbulence are considered representative of the flow which intersects the rotor. In fact, separate analysis verified that the wind speed and turbulence intensity were fairly constant across the rotor disk. The observed ranges for wind speed and turbulence intensity were 9–27m/s and 3–16% respectively, based on 1-minute averages.

The corrected wake data, ie. with the turbine operational, are shown for a range of windspeeds in Figure 4.2.1(iii). The data are plotted against incident wind direction: on the assumption that the wind turbine yaw system tracks the wind direction accurately over long periods, the data can be re-interpreted as velocity profiles obtained by a horizontal traverse behind, and parallel to, the rotor.

Although full wake profiles are not available, due to a shortage of data, the results show a clear dependence on windspeed, with the wake ratio increasing as a function of tip speed ratio. Assuming that the wake centreline corresponds with the 350° wind direction, for which the wind turbine is directly upwind of the 29m measuring anemometer, centreline velocity ratios may be derived directly from the data in Figure 4.2.1(iii).

The given wake profiles are based on 1-min averages. Based on longitudinal and lateral coherence considerations[93] the relatively short averaging time is appropriate. Analysis of corresponding 15-minute samples give almost identical results, though with a somewhat more 'spiky' appearance: this was attributed to changes in rotor orientation during the 15-minute period due to operation of the yaw system. The graphs based on 1-minute data are nonetheless fairly smooth. The statistical significance of the results may be assumed greatest for the more extended wake data sets.

Note that the wake profiles thus obtained are inherently averaged with respect to short-term variations of incident wind direction. It is assumed that on average the rotor was aligned with the incident upstream wind direction throughout the measurements (no turbine yaw information was available); it is to be expected, however, that rotor alignment lags behind changes in incident wind direction. The measured standard deviation of wind direction was $\approx 5-6°$, implying a maximum cross-wake smoothing over $\pm 5\%$ D.

### (c) Results of comparison

PIV experiments were carried out using a model replica of the Vestas WM-19S machines of Samos Island (see Section 3.4). The cross-wake profile at 1.1D downstream of the model rotor was found by averaging the four columns of vectors in each PIV velocity vector map corresponding to distances $1-1.2$D behind the rotor, to account for any uncertainty in downstream position. The results are shown in Figure 4.2.1(iv), as velocity ratio plotted against cross-wake distance for each tip speed ratio. In calculating the velocity ratio for each location, a single averaged value of the upstream velocity was assumed.

The vertical scales for the wake profiles have been shifted to separate them. The profile for the case $\lambda = 4.8$ is positioned correctly with respect to the graph axes while the remaining profiles are offset by multiples of 0.1. The influence of tip speed ratio can be clearly seen from Figure 4.2.1(iv), with the downstream velocity

ratio increasing with increasing $\lambda$. Profile asymmetry is detectable, especially at low tip speed ratios. This is caused by wake interference by the tower structure as mentioned previously. Small increases in the velocity ratio above 1.0 are displayed at the inner edge of the wake.

From the given wake profiles, velocity ratios from the centreline of the off-axis measurement plane may be obtained. As noted above, the wake ratios measured at full scale (Figure 4.2.1(ii)) incorporate directional smoothing, due to the variation in incident wind direction during the averaging period. To account for this at model scale, the 'centreline' velocity at 1.1D downstream was averaged over a cross-wake distance based on the variance of the wind direction in the full scale tests. In practice, this involved averaging together the velocity vectors either side of the 'centreline' i.e. two adjacent (cross-wake) values at 1.1D downstream.

The resulting 'centreline' velocity ratios from the model tests are shown as a function of tip speed ratio in Figure 4.2.1(v), together with the corresponding data from the Samos Island measurements. Error bars are plotted for the PIV data using confidence intervals based on the standard error of estimating the centreline velocity ratio (see Section 4.1.1). For low tip speed ratios, the comparison is promising. However the curves diverge from each other as $\lambda$ increases. At $\lambda = 2$, the data from the curves agree to within 3% while at $\lambda = 4$, the curves agree to within 33%.

A number of factors may account for the discrepancy. It is hoped that greater insight may be found by direct comparison of full-scale and model wake data in the form of wake profiles at similar tip speed ratios. Figures 4.2.1(vi) and 4.2.1(vii) show that the shapes of the model and full-scale wake are different. The full-scale wake is wide and has a homogeneous central portion, implying significant cross-wake mixing. In addition, the minima of the curves very often does not coincide with the machine alignment of 350°, suggesting that wake meandering may affect the full-scale results. Figure 4.2.1(iii) shows that at $\lambda = 4.4$, the minimum velocity ratio for the full-scale data is about 0.68 at a cross-wake position of 340°. Figure 4.2.1(iv) shows this is very close to the result for the model at a

similar tip speed ratio.

Figure 4.2.1(viii) displays the cross-wake turbulence velocity profiles at 1.1D for various tip speed ratios from both the full-scale and the laboratory experiments. The turbulent velocity profiles from the PIV tests have been separated for clarity. The profile for the case $\lambda = 1.6$ is correctly positioned on the axes and the other profiles are offset by multiples of 0.04. In general, the PIV profiles show an increase in turbulent velocity as the tip speed ratio increases, with maximum turbulence in the region of the wake centreline. This same behaviour can also be observed from study of the standard error involved in the cross-wake averaging (Fig. 4.2.1(v)). The size of the standard error bars reflects the level of turbulence existing at the location of interest in each case. There is also some evidence that the wake turbulence does not increase indefinitely with increasing $\lambda$, but goes through a minimum at an intermediate value close to $\lambda = 3$. The full-scale results also reveal an increase of wake turbulence towards high tip speed ratio, with a minimum in between (at $\lambda = 3.3$). The flat profiles of the Samos Island results for the case $\lambda = 3$ and $\lambda = 3.3$ probably reflect the wake meandering and cross-wake smoothing of full-scale data.

Centreline turbulent velocity ratios are taken from the PIV profiles and plotted together with the corresponding full-scale ratios in Figure 4.2.1(ix). The two curves are notable for displaying similar trends in turbulence levels with respect to tip speed ratio. This is discussed is Section 5.4. Comparison of turbulence intensity profiles at similar tip speed ratios is plotted in Figure 4.2.1(x). The results again suggest that the full-scale data may be affected by wake meandering.

### 4.2.2 Vestas V20/100, Risø Test Station

#### (a) Description of full-scale measurements

Measurements were undertaken in 1988 at Risø's National Laboratory, 30km west of Copenhagen[76]. The Vestas V20/100 is a 3-bladed machine with 19.93m rotor

diameter and a hub-height of 24.25m. The rotor solidity is 5.5%. It is rated at 100kW, is stall-regulated and operates at a rotor speed of 45.5RPM. A photograph of the machine is reproduced in Figure 4.2.2(i).

Measurements were made using meteorological masts arranged in a line in the direction 285° North. PIV data is compared with readings taken from masts placed 0.68D upstream and 1.5D downstream. Anemometers were arranged on top of the masts at hub-height.

Data was sampled at a frequency of 2Hz. Run statistics were calculated using 10-minute averages. Incident wind speeds and ambient turbulent intensities were recorded at a location 2.5D upstream. Windspeeds between 8.25m/s and 8.75m/s yield the most suitable tip speed ratios for comparison with the PIV data, corresponding to $5.4 < \lambda < 5.9$. Ambient turbulence intensity was on average between 5−10% over the wind speed range.

### (b) Results of comparison

The 3-blade model replica of the WM-19S has a geometry that is very similar to the V20 machine. A velocity profile from PIV tests on the model rotor for the case $\lambda = 4.8$ is compared to Risø data at 1.5D downstream. The Risø data, recorded at hub-height, is adjusted so that comparisons may be made with the PIV data, recorded in a plane offset from the wake centreline. Assuming the wake is axisymmetric, the Risø data is subjected to spline interpolation, before a geometric translation of the data onto an equivalent offset plane. The results are displayed in Figure 4.2.2(ii) where mean velocity ratio has been plotted against wind direction and corresponding cross-wake distance.

The Risø data and PIV measurements compare reasonably well. The centreline velocity deficit (the difference of the velocity ratio from unity) of the Risø data is 89% of the PIV deficit. The full-scale profile is slightly wider and is notable for velocity ratios greater than 1.0 at the extremes of the profile.

### 4.2.3 Nibe 'B' Wind Turbine

#### (a) Description of the full-scale measurements

The two turbines, Nibe 'A' and 'B', are located 200m apart on a flat, coastal site in Jutland, Denmark. Both have 3-bladed, 40m diameter rotors of similar aerodynamic design mounted at a hub-height of 45m. Each machine is electrically rated at 630kW, with rated power achieved at a windspeed of 13m/s. The cut-in and cut-out wind speeds are 6m/s and 25m/s respectively. The 'A' rotor is intended to operate in stall-regulated mode while turbine 'B' is operated with full-span pitch control. The rotor speed is approximately 34 RPM. Figure 4.2.3(i) shows the twin-turbine site at Nibe.

Measurements were made in the period June 1982–July 1987. The data examined here corresponded to the 'B' turbine operating alone in southerly winds. A well-instrumented meteorological mast was situated 2.5D downstream of the turbine. The non-operating turbine 'A' lies a further 2.5D downstream with additional masts placed at 4D, 6D and 7.5D downstream of turbine 'B'. The data to be compared was collected by a cup anemometer mounted at 56m above ground level. This provides the closest equivalent offset position from the centre of the wake to readings taken at laboratory scale.

Long-term statistical data have been collected in the form of 1-minute means and standard deviations whenever the incident wind direction was within $\pm 30^{\circ}$ of the inter-machine axis (magnetic bearing 188°). The sampling rate was 2Hz. No direct measurement is available of the incident wind speed nor ambient turbulence intensity since all measurement masts lie in the wake of the 'B' turbine. Instead, data records have been selected which fall within a specified range of electrical power output from Nibe 'B'. The corresponding incident wind speeds at hub-height have then been estimated using the measured power curve.

In this way, data is selected that is most suitable for comparison with the operating conditions of the scale model tests. With the Nibe 'B' machine operating

in the 550−605kW power range, a range of tip-speed ratios is covered between 5.3−6. Ambient turbulence intensity is estimated as 10−15% by collecting readings measured at 3m on the downstream mast in the assumption that they are not influenced by the rotor.

### (b) Results of comparison

A velocity profile from PIV tests at $\lambda = 4.8$ is compared to Nibe data at 2.5D downstream. Mean velocity ratio has been plotted against wind direction and corresponding cross-wake distance (Figure 4.2.3(ii)). The trough of the PIV profile is seen to be deeper than the Nibe profile. The centreline velocity deficit of the Nibe data is 52% of that of the PIV data. Both sets of measurements have velocity ratios greater than 1.0 at the extremes of the profiles. In the case of the PIV data, this appears to be due to interference from the turbine 'tower'.

Turbulent velocity data are compared with measurements from the Nibe experiments at distances corresponding to 2.5D downstream of the model and full-scale machine. Turbulent velocity ratio is plotted against cross-wake distance and the corresponding wind-direction in the field in Figure 4.2.3(iii). The agreement between the two sets of data is very good with respect to the level of turbulence in the wake, despite the differences in ambient turbulence for the two sets of experiments. Alfredsson[10] proposed that as the ambient turbulence increases the wake decays more rapidly. It is possible that the PIV and Nibe data are contrasted at a station sufficiently far downstream such that, under the influence of high ambient turbulence, the turbulence in the wake of the Nibe 'B' machine has decayed to the level present in the PIV experiments. The centreline turbulent velocity ratio of the Nibe data is 97% of the PIV ratio. The maximum level of turbulence for the two sets of data agree to within 5%. It is noted, however, that both sets of turbulence data vary considerably around the centreline and emphasis must not be placed on these percentages.

The high amount of activity displayed by the PIV data at the edges of the wake

could be due to large eddies in the wake at 2.5D, formed when the rotor enters the 'turbulent wake state'. There may be a transfer of energy from the boundary of the wake to the inner core. According to Ainslie[8], large scale turbulence is generated in the annular shear layer of the intermediate wake, which spreads into the core of the wake. Thus, it is possible that the boundary of the near wake and the intermediate wake exists around 2.5D.

## 4.3 Comparisons with Wind-tunnel Data

### 4.3.1 Loughborough University

#### (a) Description of wind-tunnel tests

The data used for these comparisons were the results of experiments carried out in the large closed circuit wind tunnel at the Department of Mechanical Engineering at Loughborough University of Technology during the period 1983–85. Green conducted tests on a small modified aircraft propeller of 150mm diameter[52]. Laser doppler anemometry was used to record the flow in the wake of the 2-blade model with smoke as a seeding agent.

The data examined here correspond to the model operating at a tip speed ratio of $\lambda = 3.98$. The mean hub-height velocity of the incident flow was 5.91m/s with a mean hub-height turbulence intensity of 4.7%. Measurements were made of axial, radial and swirl components of velocity and turbulence both at the rotor and up to 7D downstream. The data most suitable for comparison are axial components from the horizontal plane at hub-height at 1D and 2D downstream of the rotor. The 2-blade PIV results are chosen for comparison since, under the assumption of an axisymmetric wake, measurements on the centreline correspond to horizontal hub-height readings.

### (b) Results of comparison

PIV velocity and turbulence profiles are compared with Green's data at 1D and 2D downstream. There is a considerable difference in the shape of the velocity profiles at 1D. Figure 4.3.1(i) shows that Green's profile has a wider and flatter trough and is asymmetric. The PIV profile is smoother with a narrow deep deficit. The centreline velocity deficit for Green's data is 49% of that of the PIV profile. The PIV data contains velocity ratios greater than unity at the wake boundary in the lower half of the wake whereas Green's data contains no velocity ratios greater than unity. At 2D downstream, the velocity profiles compare more favourably. From Figure 4.3.1(ii), it is seen that the centreline velocity deficit of Green's data is now 83% of that of the PIV profile. However, the differences in wake width and wake boundary values become more apparent.

At 1D, the turbulent velocity profiles match well at the wake boundary due to similarities in ambient turbulence conditions. However, across the wake core, Green's turbulence profile dominates, as displayed in Figure 4.3.1(iii). Large peaks in turbulence are witnessed at the blade tips and may be attributed to the presence of tip vortices. The PIV data does not display such recognizable structure. The maximum peak in turbulence of the PIV data is 59% of that of Green's profile while the centreline turbulent velocity ratio is 38% of Green's.

At 2D, the tip vortices are even more prominent in Green's profile. In Figure 4.3.1(iv), the PIV data displays signs of some structure with small peaks in turbulence appearing at the blade tips. However, the maximum peak in turbulence occurs inboard at around 40% blade span. The maximum turbulence of the PIV data has dropped to 39% of that of Green's profile. On the other hand, the centreline turbulent velocity has increased to 56% of that of Green's value.

### 4.3.2 Marchwood Engineering Laboratories

#### (a) Description of the wind-tunnel tests

Experiments were carried out in the CEGB[1] Marchwood Engineering Laboratories (MEL) wind tunnel, reported by Hassan[54]. Three-bladed, rotating wind turbine models with rotors of 0.27m diameter and 14% solidity were used. The models were operated in a 1:300 scale atmospheric boundary layer simulation. The hub-height wind speed was 4m/s and the turbulence intensity was 9%. Wake surveys were performed using hot-wire anemometers. Data were recorded at hub-height at a number of downstream positions over the range 2D−25D for the turbine operating at tip speed ratios of 2.9, 4.0 and 5.1. Mean velocity, turbulence and shear stress profiles were obtained in the vertical, transverse and streamwise directions.

PIV data are compared with MEL wake profiles at 2.5D downstream. Horizontal profiles from the wind tunnel measurements were chosen for comparison in preference to vertical profiles to avoid effects of the simulated boundary layer. The 2-blade PIV results are preferred for comparison because they were recorded with the nacelle in-line with the laser sheet and effectively correspond to 'hub-height' measurements. In addition the 2-blade rotor had a solidity that matched that of the wind tunnel model more closely than the 3-blade rotor. Similarity of number of blades is a secondary consideration and the 3-blade results are also used for interest. Under the assumption of an axisymmetric distribution of velocities in the wake, geometrical arguments are used to translate the 3-blade data onto the centreline. The off-axis recording means that there are missing values for an inner core of the wake. For the 3-blade measurements there is no data for $-0.42 < r/R < 0.42$.

[1]Central Electricity Generating Board

### (b) Results of comparison

PIV velocity and turbulence profiles are compared with MEL data at 2.5D downstream with the turbines operating at a tip speed ratio of around $\lambda = 4$. In Figure 4.3.2(i), the velocity profiles compare well, particularly the 2-blade results in terms of profile shape and width. The centreline velocity deficit of the PIV data is 90% of that of the MEL data. There are again discrepancies in wake boundary values with ratios from PIV data rising above unity. Mean velocity ratios for the MEL data are all below unity.

Centreline velocity ratios are compared across the tip speed ratio range in Figure 4.3.2(ii). Cross-wake and streamwise averaging are employed in calculation of the ratios. Although the data is sparse, the figure seems to indicate a favourable comparison as the tip speed ratio increased from low- to mid-$\lambda$. The 2-blade PIV data is plotted together with error bars based on the standard error of the velocity ratios (see Section 4.1.1). The error bars reflect the amount of turbulence in the wake centre at 2.5D downstream. The size of the error bars increases dramatically as tip speed ratio increases.

Turbulent velocity profiles at 2.5D are compared in Figure 4.3.2(iii). The PIV data displays lower turbulence values than the MEL data with the PIV centreline and maximum values being 48% and 64% of the corresponding MEL values, respectively. The MEL data reveals an approximately symmetric double-peak structure, consistent with the presence of tip vortices. The PIV data is more scattered. There are peaks in turbulence values just outboard of the tip but also significant peaks inboard at 44% blade span in the lower wake and 56% blade span in the upper wake.

The 5% difference in ambient turbulence intensities for the two experiments is an obvious factor to explain the difference in magnitudes of the turbulence datasets. The *added* turbulence in the wake, as defined in Section 4.1.1, may be a more suitable parameter with which to compare the datasets. However, the MEL results as reported by Hassan, indicate that the concept of added turbulence is not ap-

propriate over the whole wake. As a result, turbulence on the wake centre only is considered, where the mean turbulence intensity upstream is used as an estimate of hub-height intensity. The resulting plot is shown in Figure 4.3.2(iv). Negative values of $\Delta\sigma'_u$ in the graph indicate that the wake turbulence is lower than the freestream value. The two datasets show a more favourable comparison than the previous plot. However, the PIV data is considerably more sensitive to tip speed ratio. The data look to agree more closely as tip speed ratio is increased from low $\lambda$ to medium values of $\lambda$.

## 4.4 Summary and Discussion

Mean velocity and turbulent velocity profiles from the 2-blade and 3-blade models have been evaluated at separate locations in the near wake for a range of tip speed ratios. In addition, velocity and turbulence ratios on the wake centreline and along the centre of an off-axis plane have been plotted with downstream distance. The results were compared to measurements from Samos Island, Risø and Nibe at 1.1D, 1.5D and 2.5D downstream respectively. Mean and turbulent velocity ratio has been plotted against wind direction and corresponding cross-wake distance in each case. Comparisons were also made with wind tunnel results from Loughborough University (1D, 2D) and from the Marchwood Engineering Laboratories (2.5D).

### (a) Mean wake properties

Asymmetry in the PIV velocity profiles was noticeable for both the 2-blade and the 3-blade results. This was due to disturbance of the upper half of the wake by the supporting 'tower' of the model. The 2-blade results were especially prone to wake interference since the tower was in the plane of the laser sheet during the recording of the measurements. Profile asymmetry in the near wake has been noted by Green in the wind tunnel tests at Loughborough University but in that case a non-uniform upstream profile was imposed and the asymmetry was likely

to be the presence of swirl in the wake.

The shape of the PIV profiles differed in significant areas from the full-scale measurements. In general, the PIV results produced narrow, deep profiles. Although the full-scale data is not as dense as the PIV data, it would appear that measurements from the field produced wider profiles. Data from the Samos Island experiments yielded profiles with homogeneous central portions. This could imply significant cross-wake mixing. Complex terrain may also be a factor in explaining the shape of the profiles from the Samos data. Despite attempts at similarity, the scales of the turbulence in the atmosphere may have been different from those in the water tank and have varied according to stability. Large scale inhomogeneities of the terrain impose energetic turbulent motions with characteristic scales of the size of the wake (and even larger), leading to a smearing of velocity gradients in the centre of the wake.

In wind tunnel tests, Green commented upon the observation of 'square' profiles at the boundary of the near wake region, as the profiles decay to a self-similar form. This has also been noted at full-scale from measurements made on the Nibe turbines[94]. In the the PIV results, profiles with flat central sections also occured at the edge of the near wake region and were especially noticeable at high $\lambda$. The change in velocity profile is similar to flow entering a converging channel. This is consistent with wake contraction, characteristic of the turbulent wake state experienced by the flow at high tip speed ratios. The description of wake flow by Ainslie (see Section 1.2.1), however, suggests that large scale turbulence from the shear layer of the wake spreads to the wake core and reaches the centreline at around 3–5D downstream. The square profiles at 2.5D could be the first signs of this process, where the turbulent mixing process has not yet penetrated the whole of the wake cross-section.

With the exception of the Risø comparison, the PIV wake deficits (given by the difference of the centreline velocity ratios from unity) were found to be much greater than the corresponding full-scale deficits. This was particularly noticeable in the comparison with the Nibe data. In the comparisons with the WM19S on

Samos Island, the centreline velocity ratios of the PIV results were more sensitive to changes in $\lambda$. The largest discrepancies occured at very high $\lambda$ where the PIV data yielded negative values of centreline velocity ratio, indicating areas of recirculating flow in the wake. The difference in scale is the most likely reason for the discrepancies observed, particularly the difference in Reynolds number of the flow. It is likely that the boundary layer flow on the model blades will differ from that at full-scale, particularly regarding the stall angle and the transition to turbulence[41]. Blockage in the water channel could also be a factor in explaining the differences in velocity deficits between full-scale and the model tests. However, it is noted that uncertanties pertaining to the field measurements could be significant. Cross-wake smoothing of full-scale data has already been discussed. In the results from Samos Island, wake meandering is also suggested as a reason for displacement of the full-scale and laboratory profiles. Scale effects are further addressed in Chapter 6.

Comparisons of centreline velocity ratios from the PIV measurements and wind tunnel tests were more favourable. The 2-blade results were used for the majority of comparisons with wind tunnel measurements. It is noted that, whereas a high degree of geometric similarity existed between the 3-blade rotor and the full-scale machines of Samos and Risø, the 2-blade rotor differed greatly compared to the geometry of the wind tunnel models. This suggests the importance of scale effect in the comparison of the PIV work with other measurement campaigns. The results indicated that the comparisons in centreline velocity improved with downstream distance. This may be attributed to the very high blockage caused by the flat-plate in contrast to the wind tunnel models, in particularly near the root of the blade. This causes an almost stagnant region of flow immediately behind the blades which recovers further downstream.

The full-scale measurements produced velocity ratios greater than unity at the extremes of the profile. Taylor[94] queried whether increases in wind speed ratio above unity were due to errors in calculating the wind velocity from the turbine power output. Far outside the periphery of the wake, the ratios must decrease to 1.0 as the velocity returns to that of the freestream value. This suggests a

region of accelerated flow between the freestream and the wake. The PIV profile of Figure 4.3.2(i) is also consistent with a region of accelerated flow. At experimental scale, this tendency may be exaggerated by blockage in the tank, but it is clear from Figures 4.2.1(vi), 4.2.2(ii) and 4.2.3(ii) that it also occurs at full-scale.

A simple explanation for the region of accelerated flow is that the rotor partially obstructs the airflow, as a solid object would. In order to conserve mass flow (at constant pressure), the air must speed up around the obstacle. Alternatively, as the air in the wake slows down and expands, so the air outside it must speed up to flow through a more confined space. The effect is consistent with the idea of a helical vortex structure in the wake, which retards the air inside it, but accelerates the air outside, with respect to the freestream.

### (b) Turbulence properties in the wake

A significant increase in turbulence was observed from the PIV turbulent velocity profiles as tip speed ratio increased. Maximum values of turbulence occured in the region of the wake centreline. Plotting values of the turbulent velocity ratio in the centre of the wake versus $\lambda$ yielded more information about the location of turbulence in the wake. The 3-blade results suggested that at $\lambda = 1.6$, the greatest turbulence was contained in a region immediately behind the rotor. At around $\lambda = 3$, the turbulence reached a minimum value before levels began to increase with increasing $\lambda$. The 2-blade results suggested that at $\lambda = 8$, the highest levels of turbulence existed further downstream, at around 2.5D.

An explanation for this may be that at low tip speed ratio the rotor is heavily stalled, and the turbulence is due to the separated flow behind the individual blades of the model rotor; this may be referred to as 'local' turbulence. At high tip speed ratio, the blades are likely to be largely unstalled, with smooth (unseparated) flow over their surfaces. However, in this case, the wake itself is highly turbulent on a large scale, due to the strong vorticity being transmitted into it from the rotor. As the rotor enters the turbulent wake state, large areas of re-

circulating flow form downstream of the rotor. At some intermediate value of tip speed ratio, the blades may be operating out of stall, but with a relatively weak vortex pattern in the wake. Comparison of centreline turbulent velocity ratios between the 3-blade PIV results and the full-scale results from Samos Island at 1.1D revealed similar trends in turbulence levels with tip speed ratio. This result is very encouraging, given the effect terrain may have on the stability of the full-scale flow.

Care must be taken in comparing the turbulence results from the 2-blade and 3-blade rotor, due to the difference in the averaging processes employed for each set of results. In particular, the 3-blade data was averaged over different wake phases and it is not straightforward to separate the effects of turbulence from the effects of vortex wake structure.

The PIV results demonstrate a large growth in turbulent energy in the centre of the wake with increasing $\lambda$. This appears to be due to the strong tip vortex structure. The turbulence peaks seen at low $\lambda$ outside the rotor circumference may be due to the wake of the supporting 'tower'. The phase-averaging involved in producing the 'frozen'-wake results is seen to reveal more evidence of tip vortex structure. The wind tunnel results, with which the 2-blade data is compared, display higher levels of turbulence and stronger tip vortex structure. In the case of Green's experiments, the large twist on the modified aircraft propeller may explain the high turbulence. When contrasted to a flat-plate blade, the decrease in angle of attack at each radial station results in the twisted blade operating at the equivalent of a higher local tip speed ratio for a given angle of incidence. This may explain the higher levels of wake turbulence of Green's results. For the MEL data, the higher ambient turbulence could be an important factor explaining the difference in results.

## 4.5 Conclusions

A wake velocity analysis of the PIV results and a comparison with both full-scale and wind-tunnel experiments has been undertaken. The most important findings of this chapter may be listed as follows:

1. The shape of the PIV velocity profiles differed in significant respects from full-scale measurements. In general, the PIV data yielded narrow, deep velocity profiles whereas measurements from the field produced wider profiles with homogeneous central portions.

2. Large discrepancies in centreline velocity deficit between the full-scale and PIV data and the full-scale results occurred at high tip speed ratio. Uncertainties in full-scale measurements, however, must be taken into consideration. In the Samos Island experiments, the complex terrain of the wake farm may produce large scale inhomogeneities which affect the wake properties.

3. The PIV data revealed that the highest levels of turbulence occured at the highest $\lambda$ and existed at around 2.5D downstream. The model rotor may have been operating in a turbulent wake state, causing large areas of recirculating flow, downstream of the rotor.

4. The PIV analysis revealed the presence of 'square' profiles at 2.5D, especially at high $\lambda$. These occured during the transition from a highly structured to a turbulent wake. The shape of the profile may indicate that the turbulent mixing process has not yet penetrated the whole of the wake core.

5. The PIV results showed favourable comparison with the wind tunnel tests, particularly with increasing downstream distance. One explanation for this trend could be that, far downstream, the effects of high blockage at the root stations of the flat-plate blade become less important.

6. Of the comparisons with full-scale measurements, those taken from full-scale machines in flat terrain showed most promise, specifically the comparison of velocity profiles with Risø data and the comparison of turbulent velocity profiles with the Nibe data.

7. Scale effects are the most likely reasons for dissimilarity between the PIV results and results from other surveys.

It would be unwise to draw too many firm conclusions at this stage, especially from the turbulence results, since the sample size was very small. The difficulty of comparison with other experiments must be taken into account. The choice for comparison was dictated by the availability of a reasonable amount of cross-wake data from the full-scale set, and the proximity of parameters such as tip speed ratio and ambient turbulence in each case. Where possible, measures were taken via cross-wake and streamwise averaging, to ensure that results did not rely on a single column of vectors or a single vector.

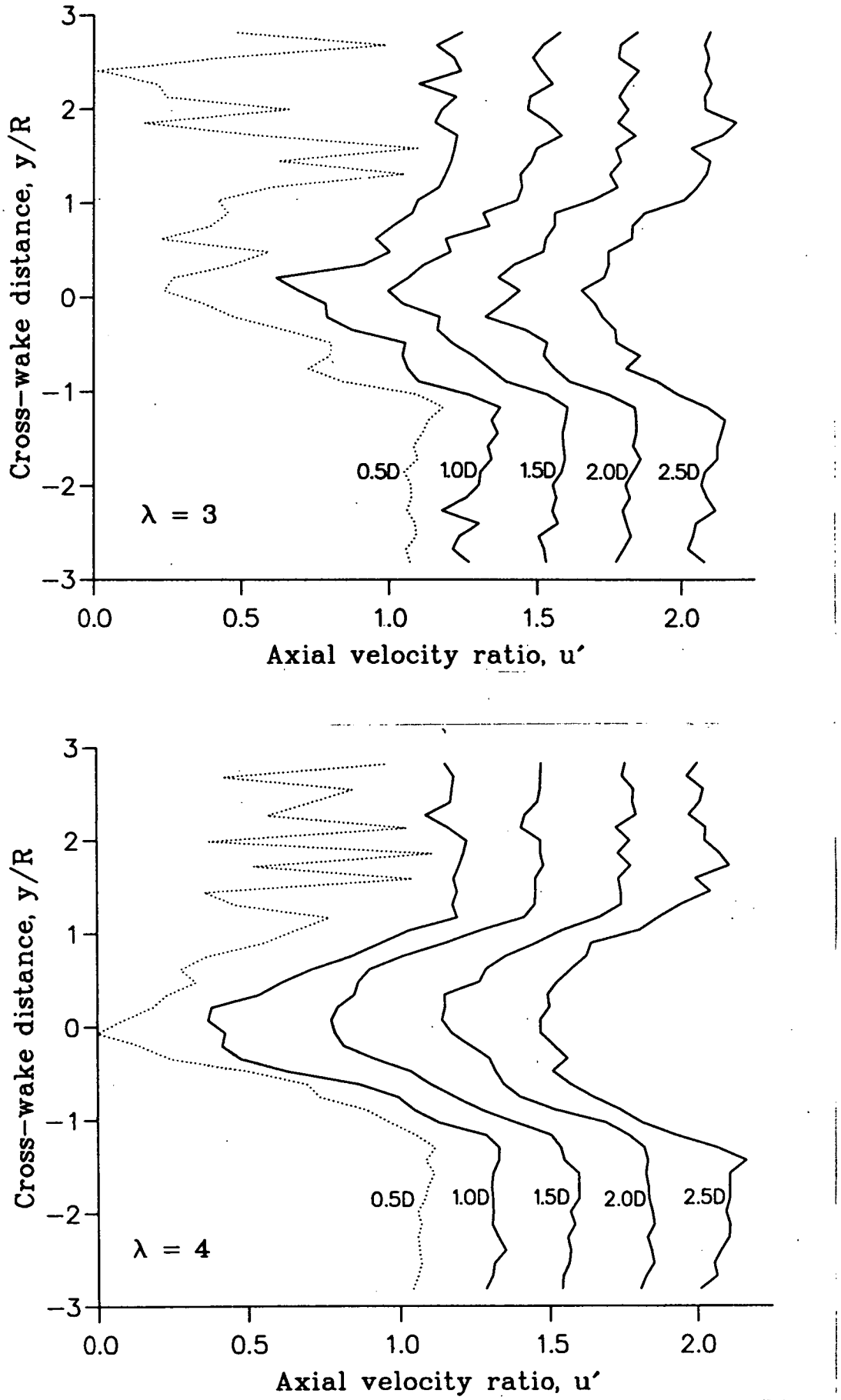


Figure 4.1.2(i) PIV velocity profiles downstream of the 2-blade rotor for $\lambda = 3$ (above) and $\lambda = 4$ (below).

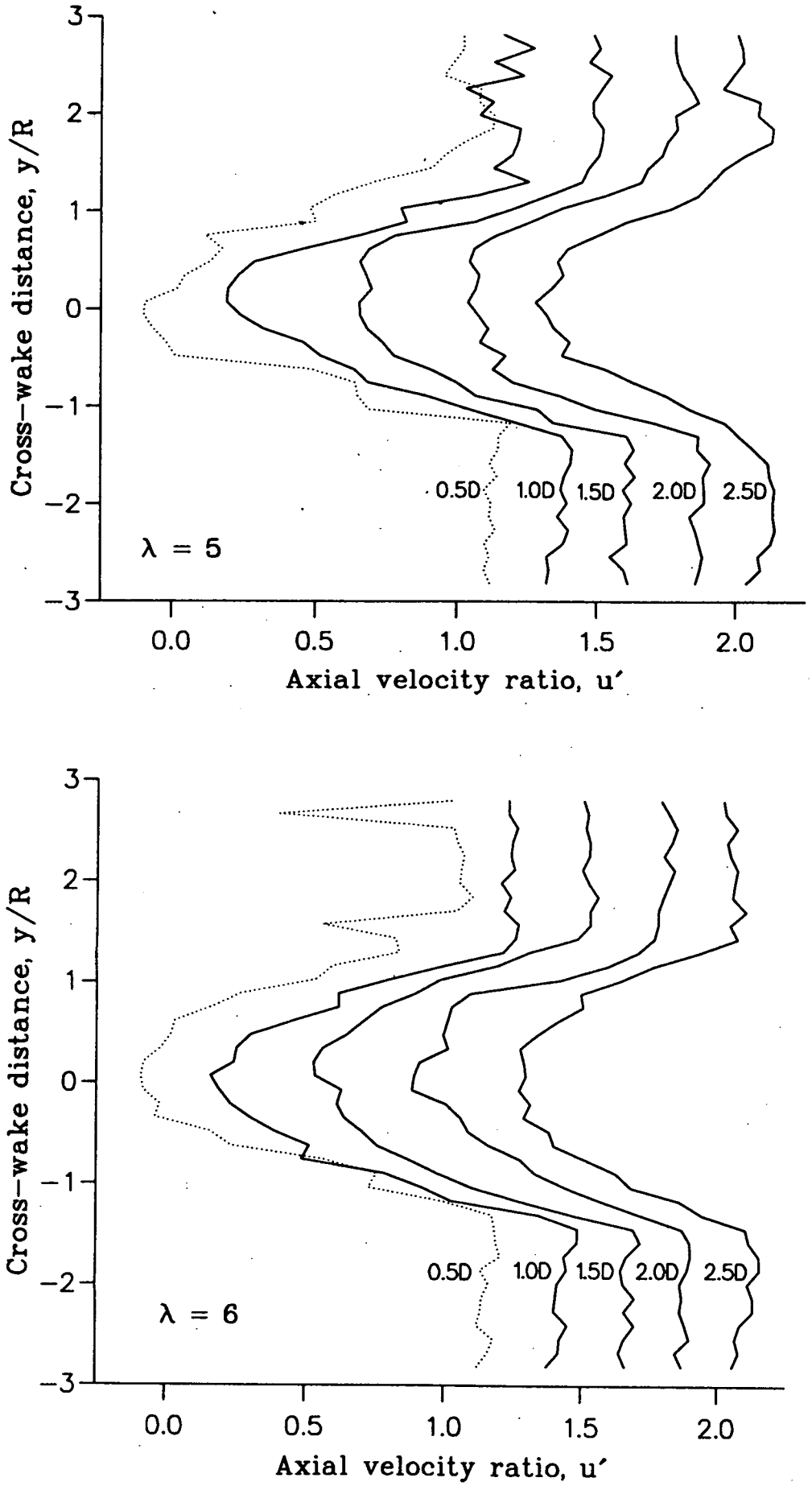


Figure 4.1.2(ii) PIV velocity profiles downstream of the 2-blade rotor for $\lambda = 5$ (above) and $\lambda = 6$ (below).

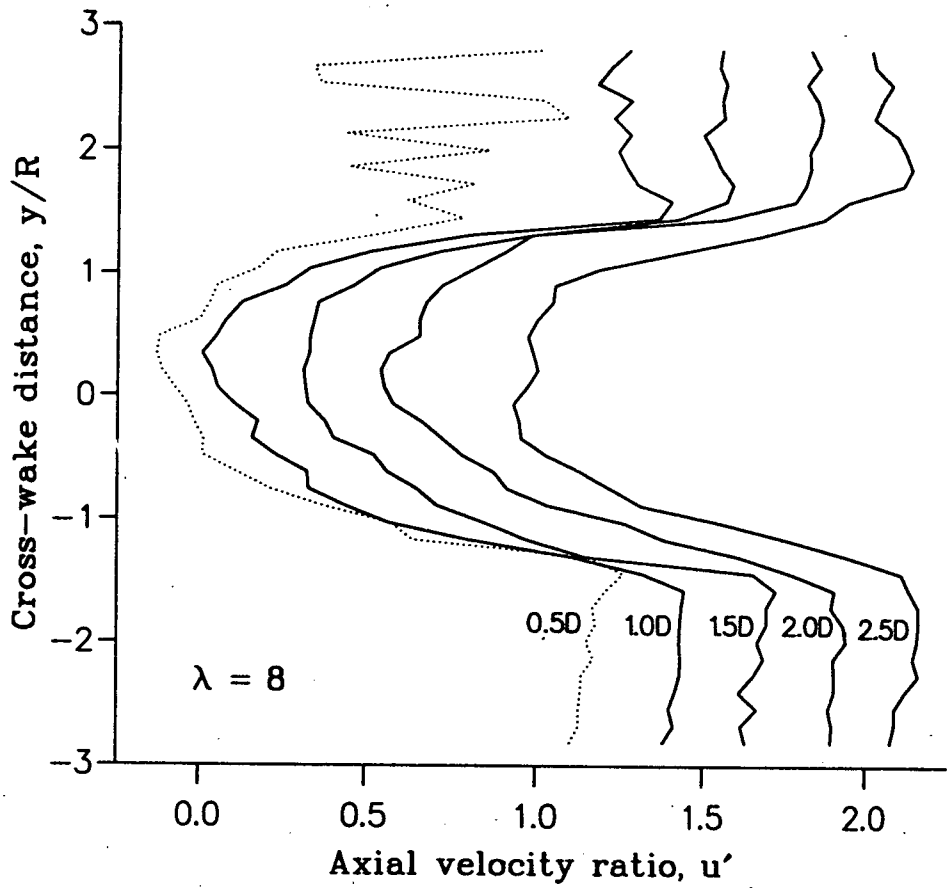


Figure 4.1.2(iii) PIV velocity profiles downstream of the 2-blade rotor for $\lambda = 8$.

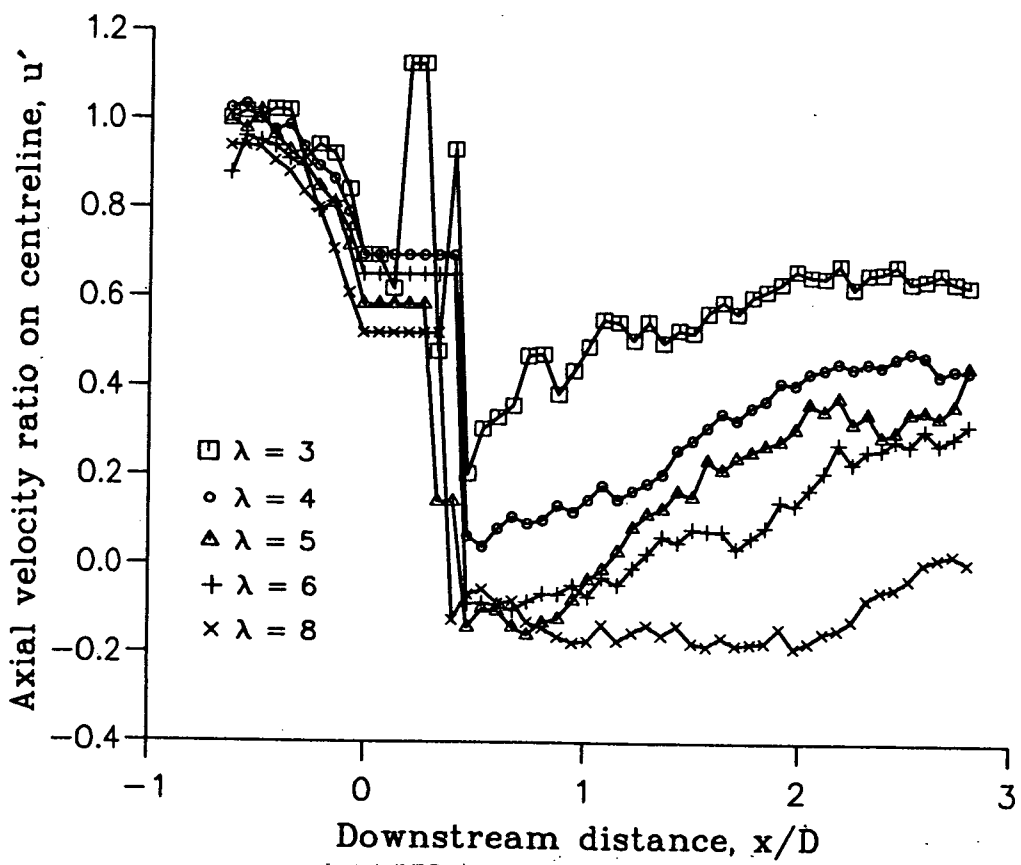


Figure 4.1.2(iv) Centreline velocity ratios in the wake of the 2-blade rotor.

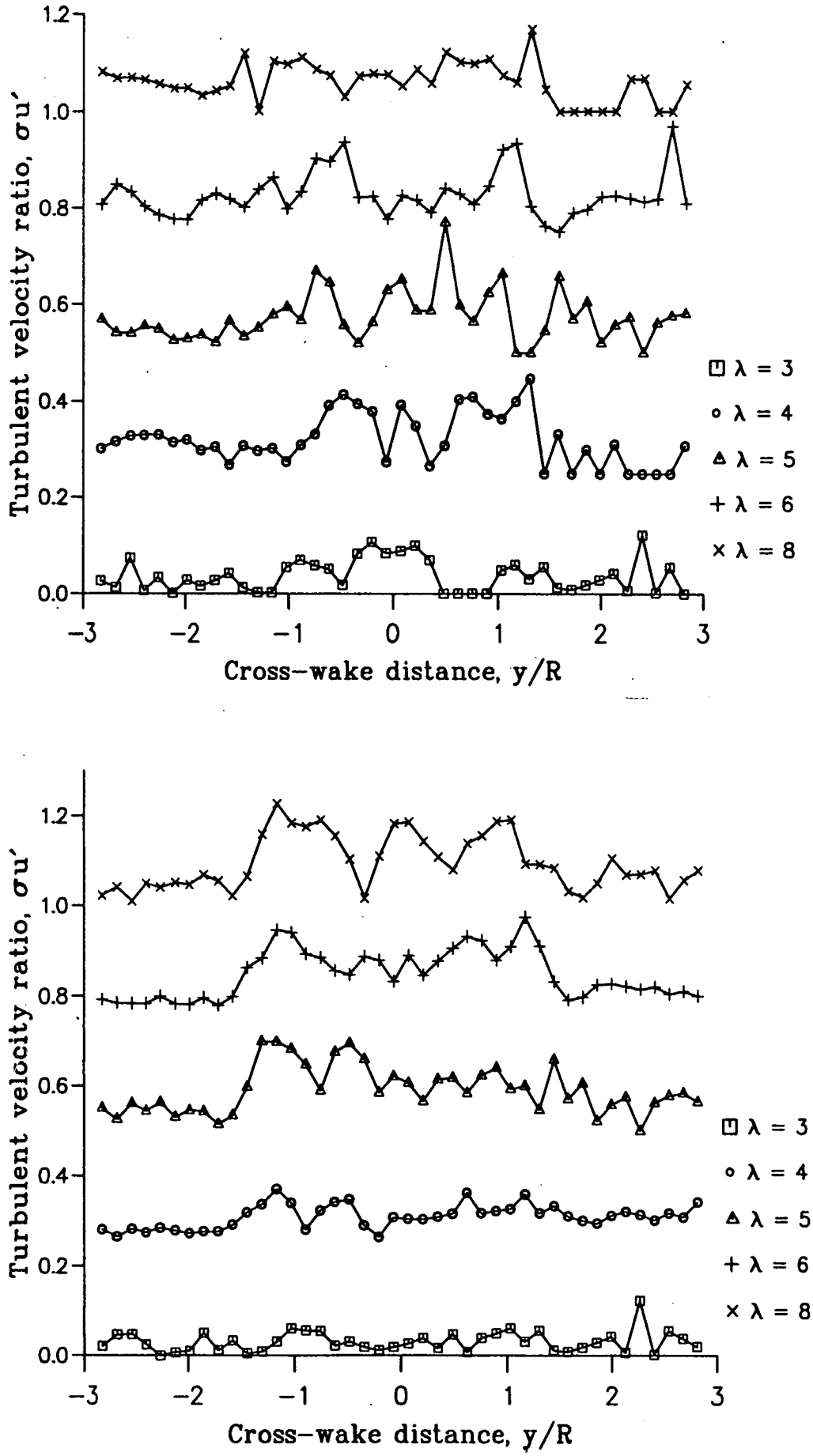


Figure 4.1.2(v) PIV turbulent velocity profiles downstream of the 2-blade rotor at $x/D = 0.5$ (above) and $x/D = 2.5$ (below).

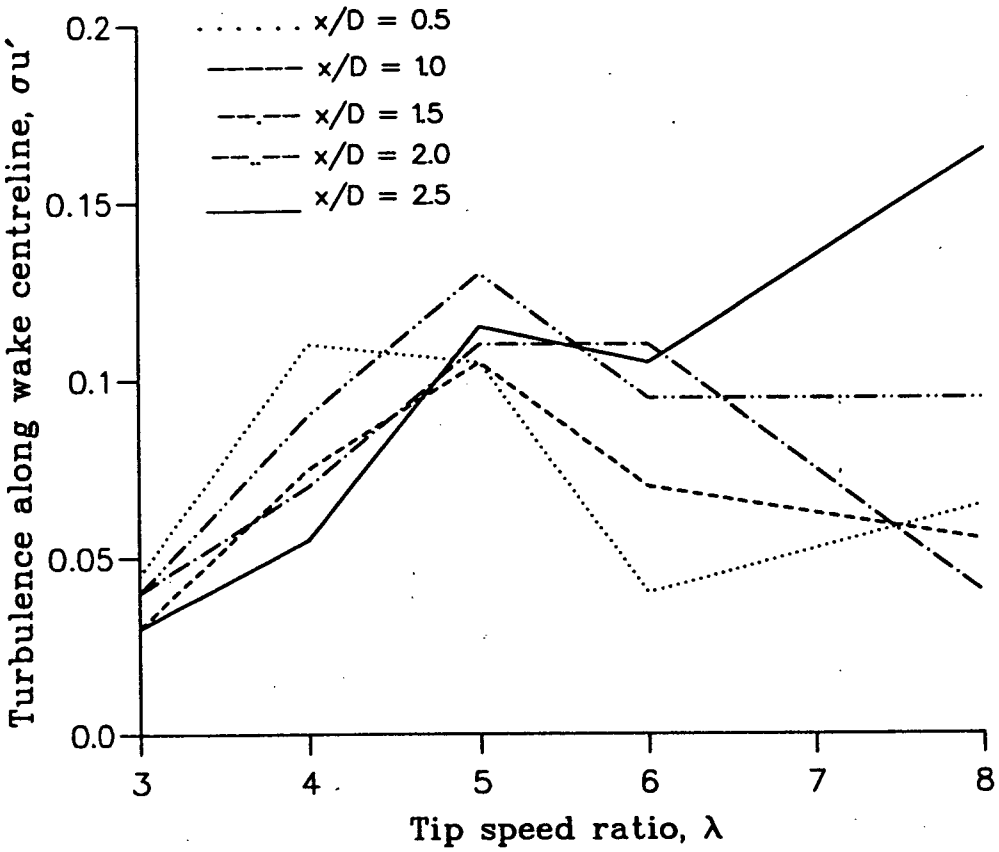


Figure 4.1.2(vi) Centreline turbulent velocity ratios in the wake of the 2-blade rotor.

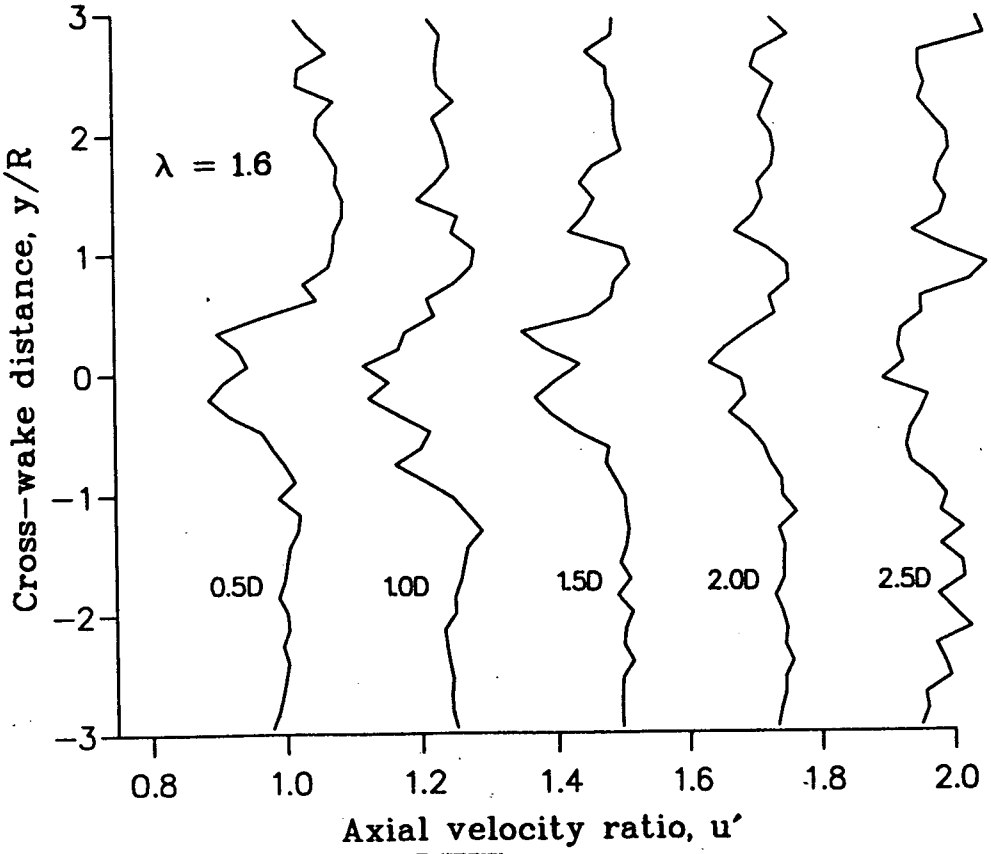


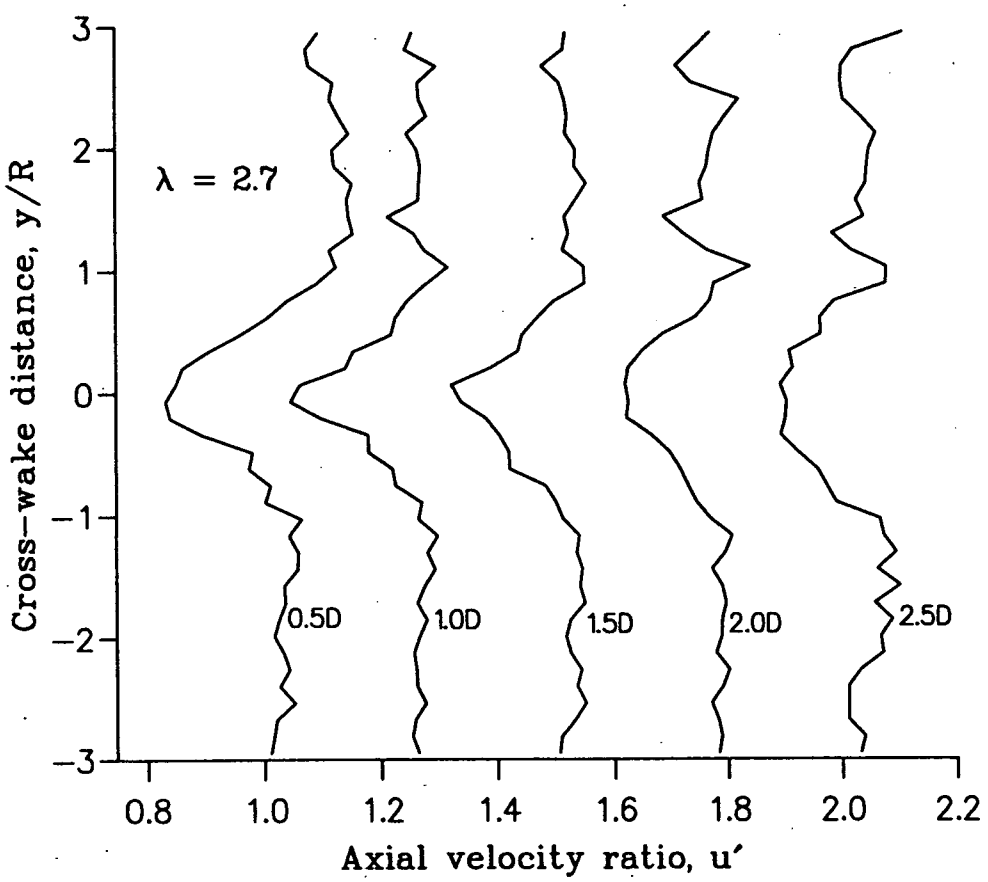


Figure 4.1.3(i) PIV velocity profiles downstream of the 3-blade rotor for $\lambda = 1.6$ (above) and $\lambda = 2.7$ (below).

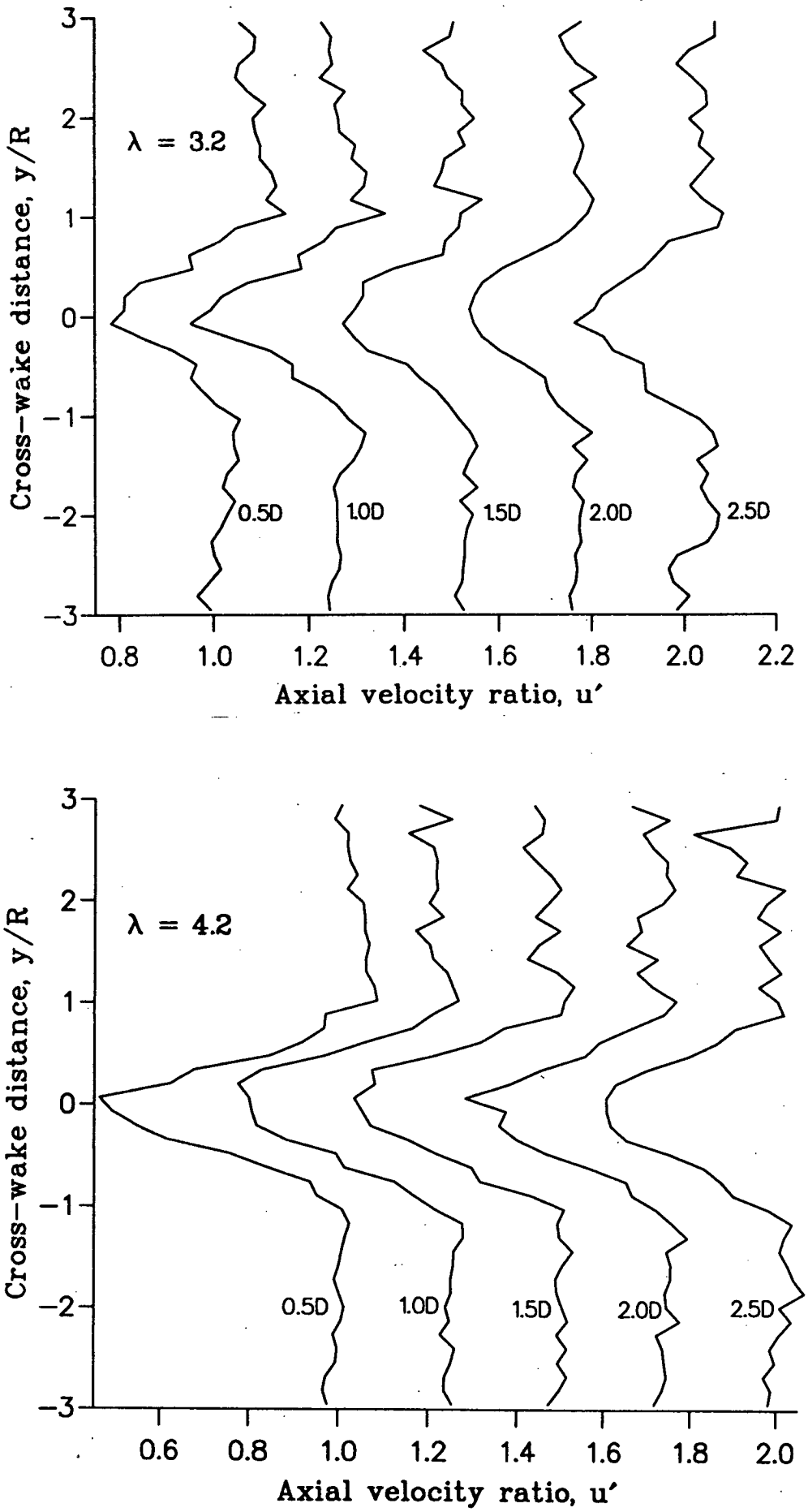


Figure 4.1.3(ii) PIV velocity profiles downstream of the 3-blade rotor for $\lambda = 3.2$ (above) and $\lambda = 4.2$ (below).

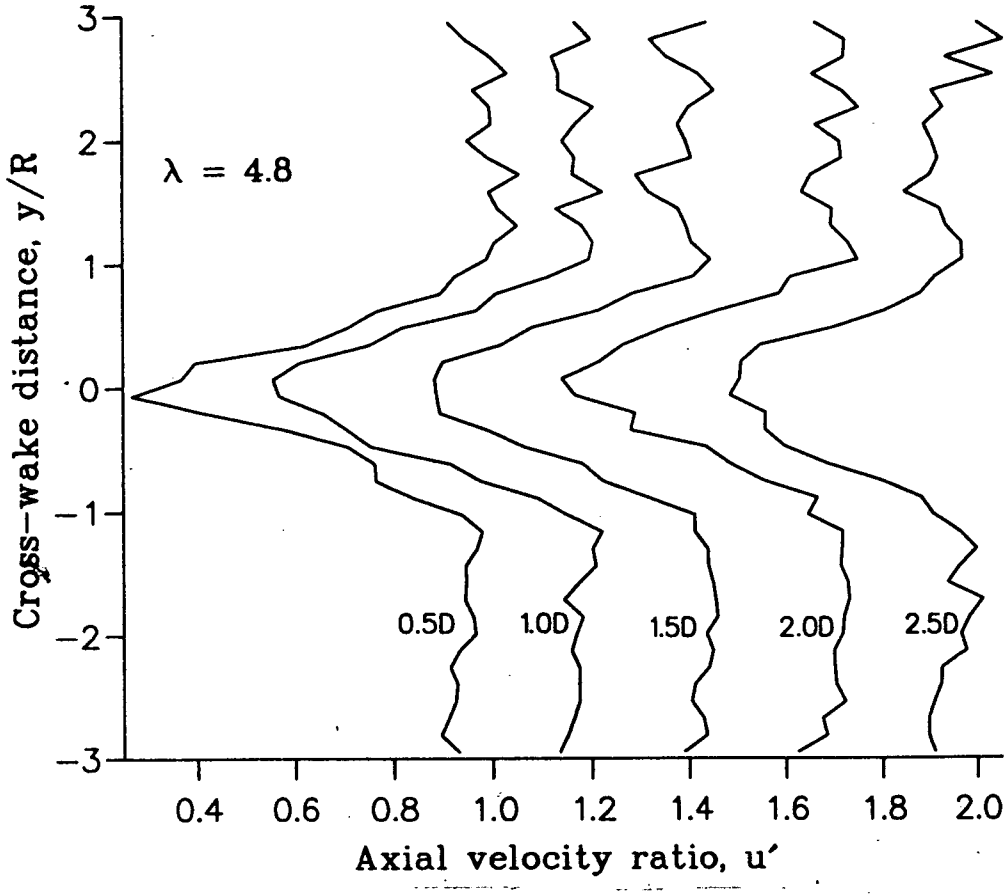


Figure 4.1.3(iii) PIV velocity profiles downstream of the 3-blade rotor for $\lambda = 4.8$.

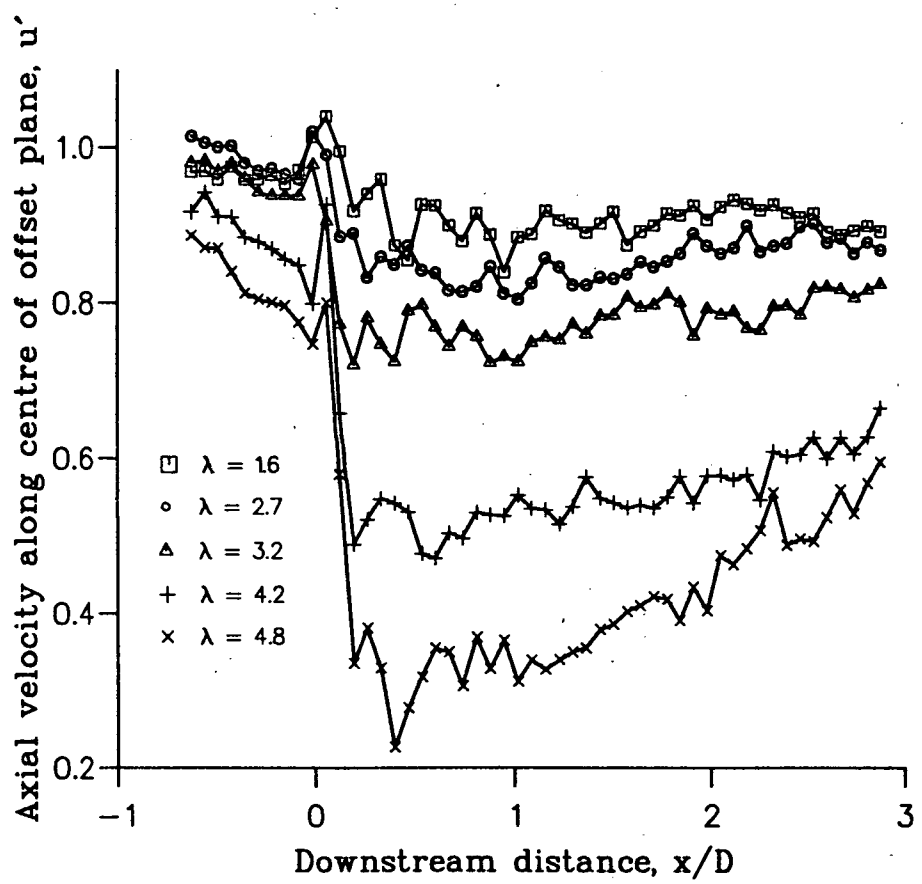


Figure 4.1.3(iv) Velocity ratios along the centreline of the measurement plane in the wake of the 3-blade rotor.

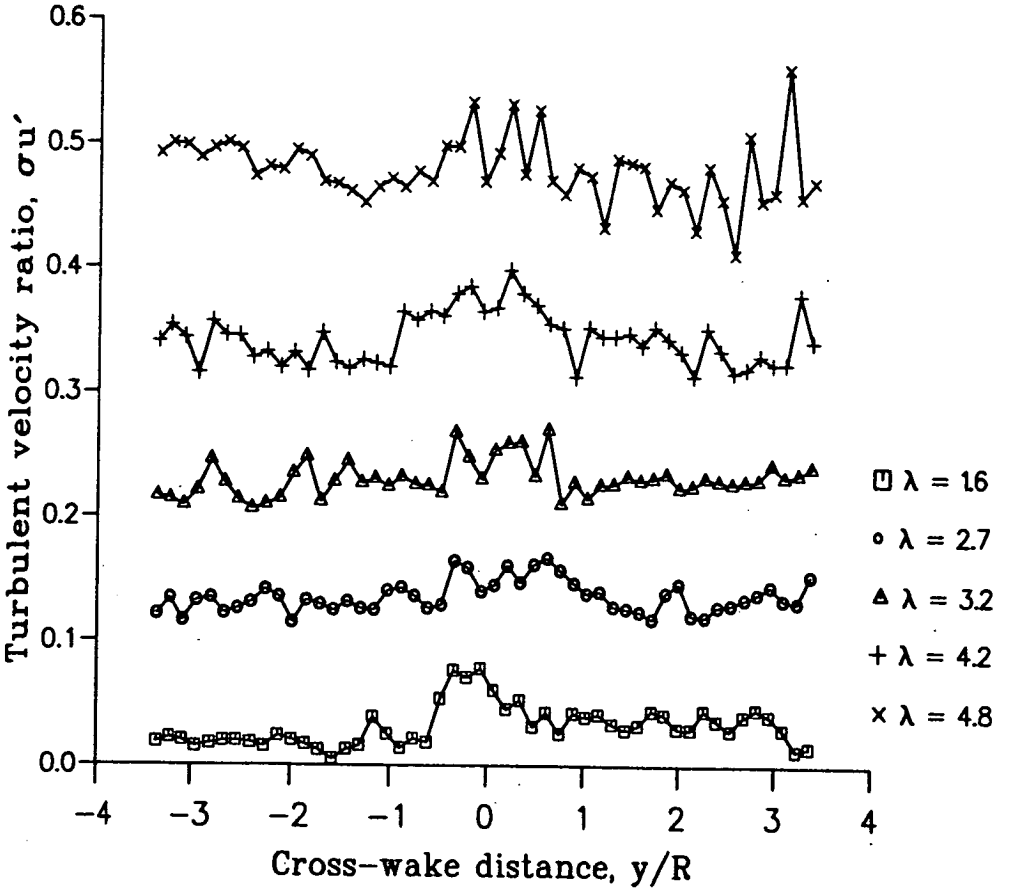


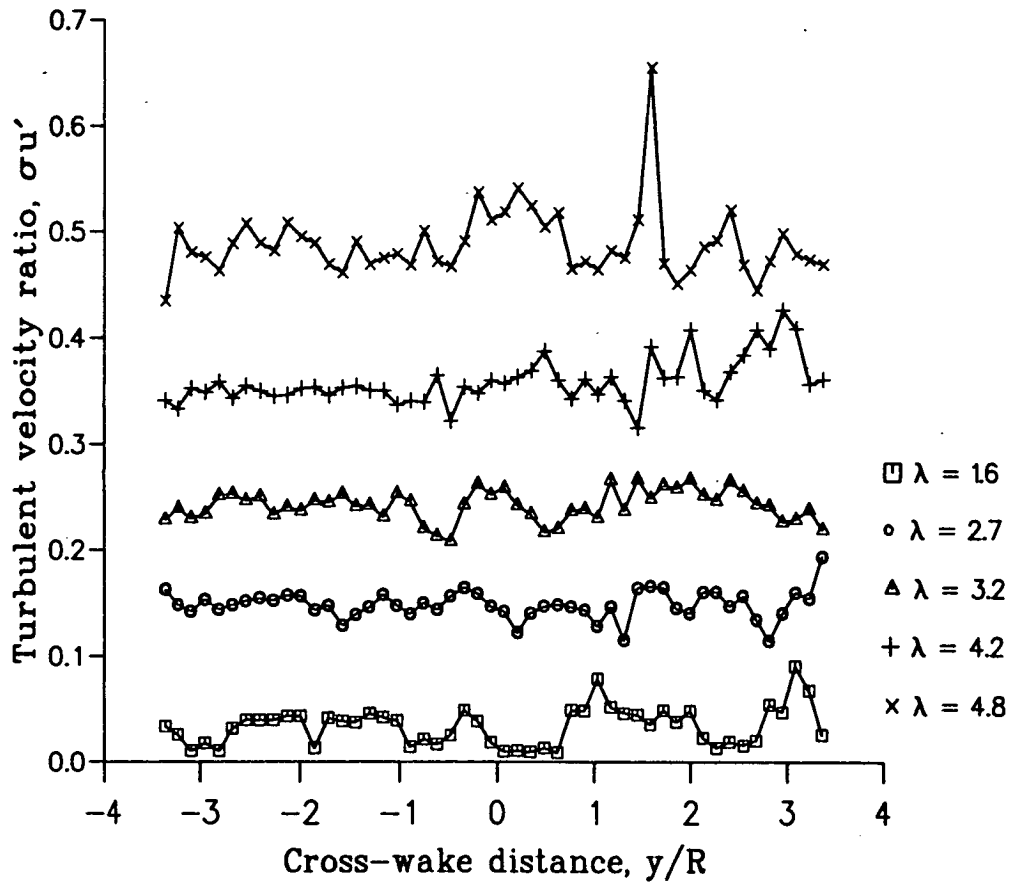


Figure 4.1.3(v) PIV turbulent velocity profiles downstream of the 3-blade rotor at $x/D = 0.5$ (above) and $x/D = 2.5$ (below).

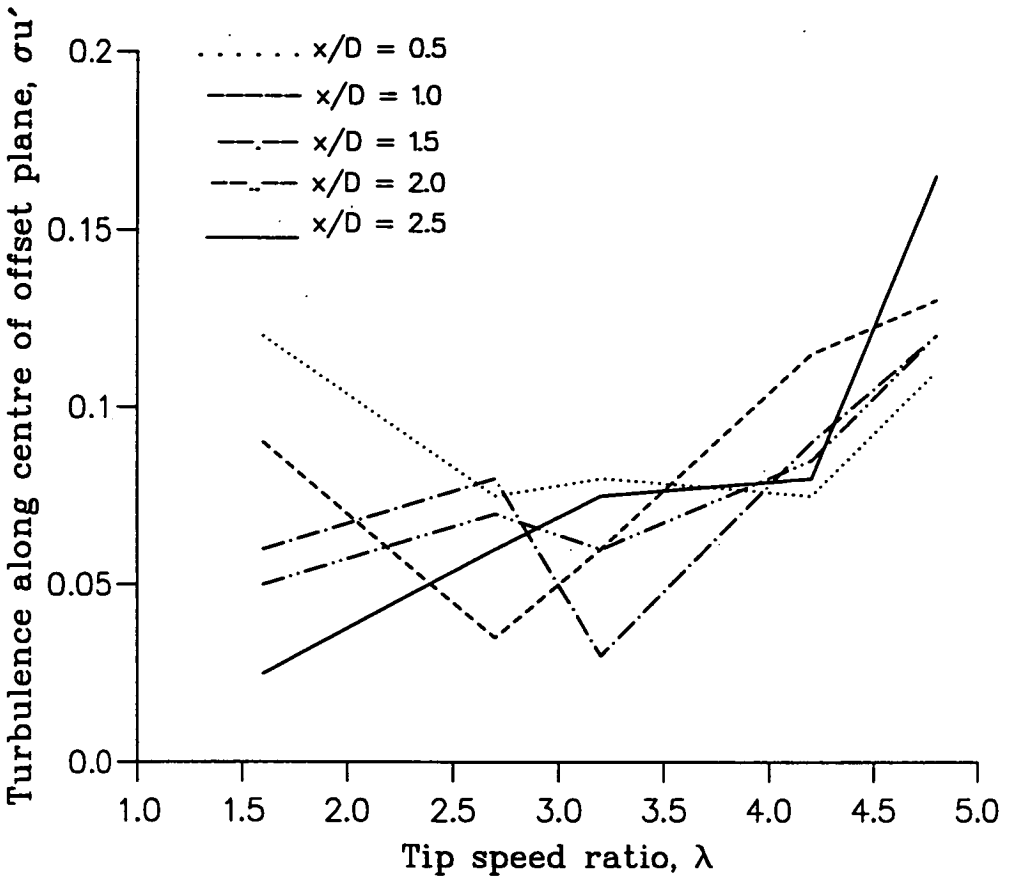


Figure 4.1.3(vi) Turbulent velocity ratios along the centreline of the measurement plane in the wake of the 3-blade rotor.

Figure 4.2.1(i) Vestas WM19S wind turbines on Samos Island, Greece.

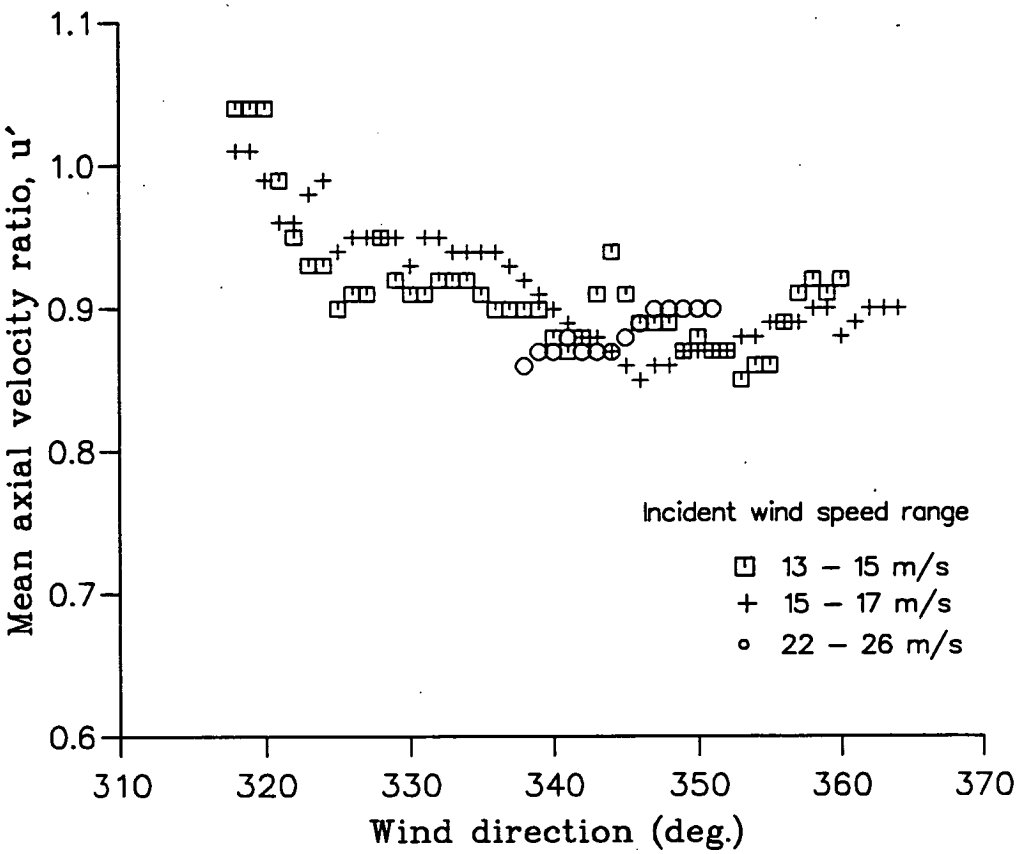


Figure 4.2.1.(ii) Non-wake velocity ratios at 1.1D for the WM19S turbine (rotor stationary), as a function of upstream windspeed.

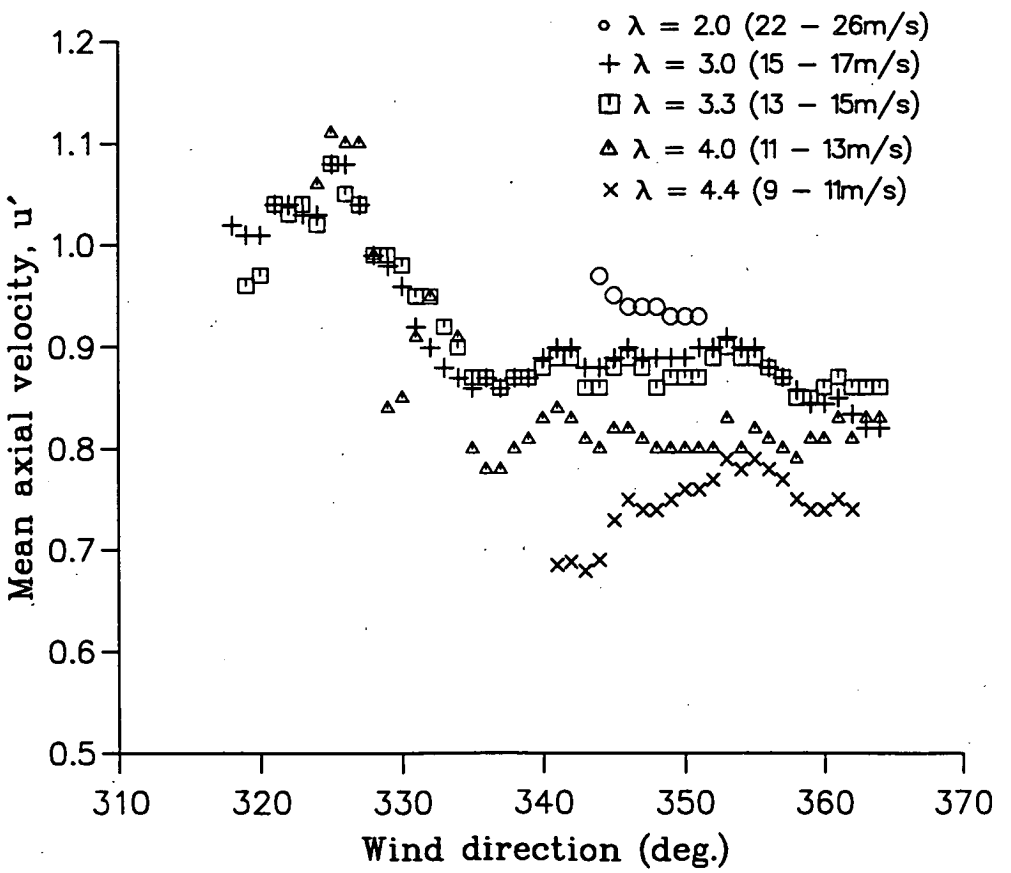


Figure 4.2.1(iii) Wake velocity ratios at 1.1D for the WM19S wind turbine, corrected for non-uniform inflow conditions.

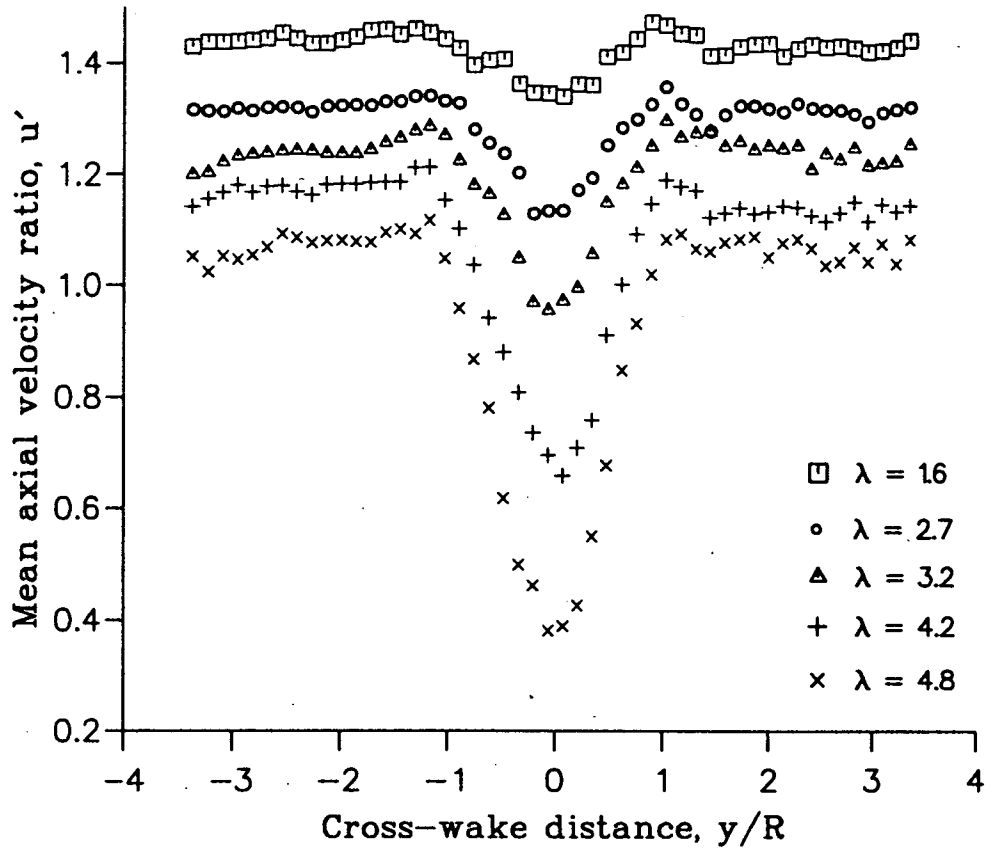


Figure 4.2.1(iv) Wake velocity profiles at 1.1D for the 3-blade WM19S replica used in the PIV experiments.

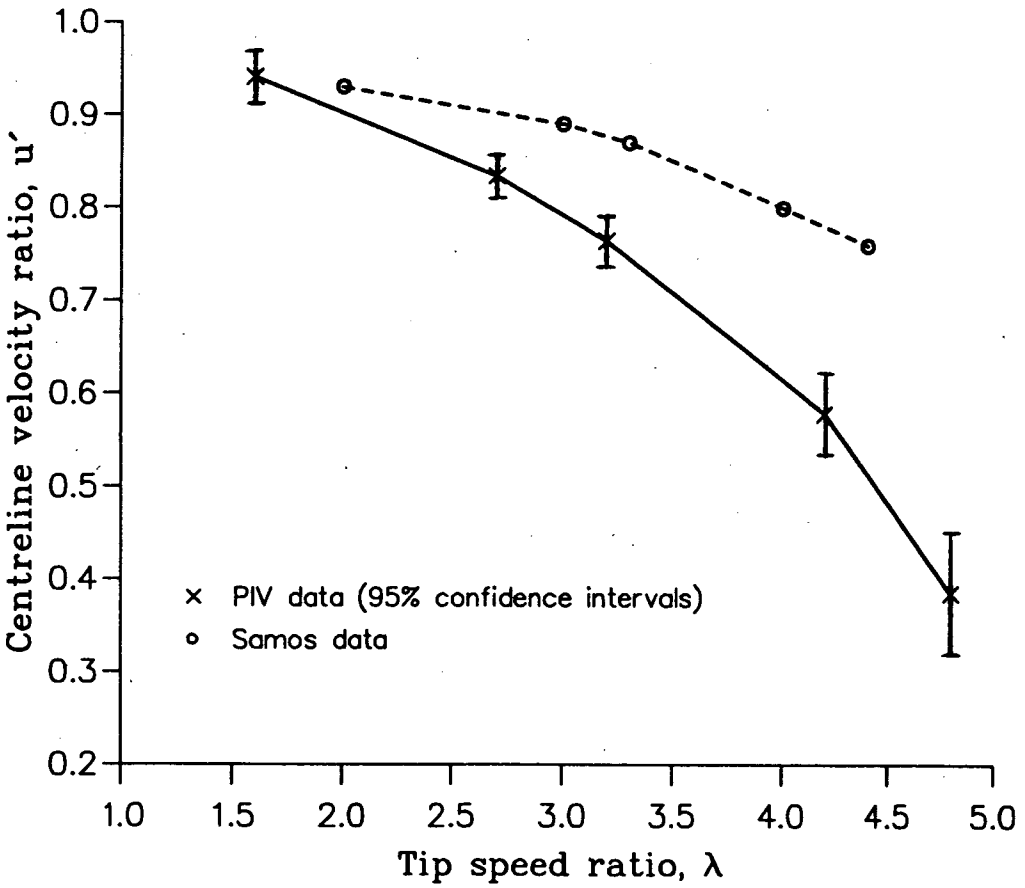


Figure 4.2.1(v) Centreline velocity ratios at 1.1D for the WM19S rotor, comparing PIV and full-scale data.

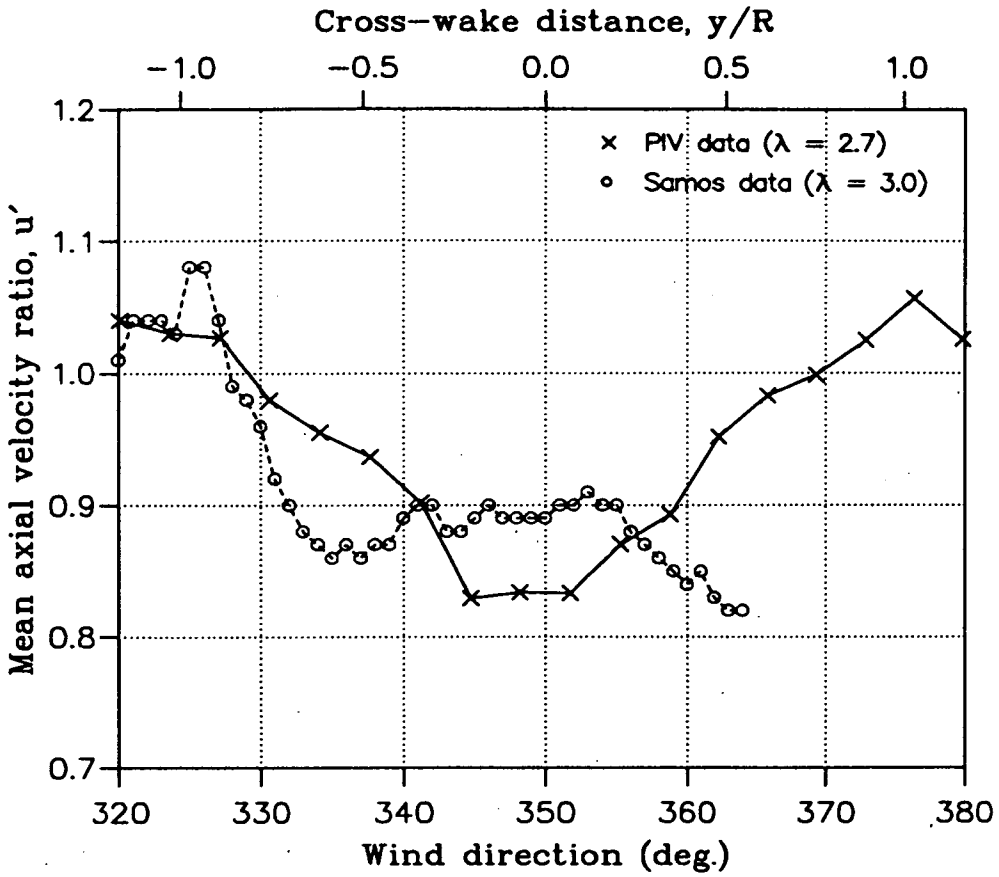


Figure 4.2.1(vi) Velocity profiles at 1.1D for the WM19S rotor, comparing PIV data ($\lambda = 2.7$) and full-scale data ($\lambda = 3.0$).

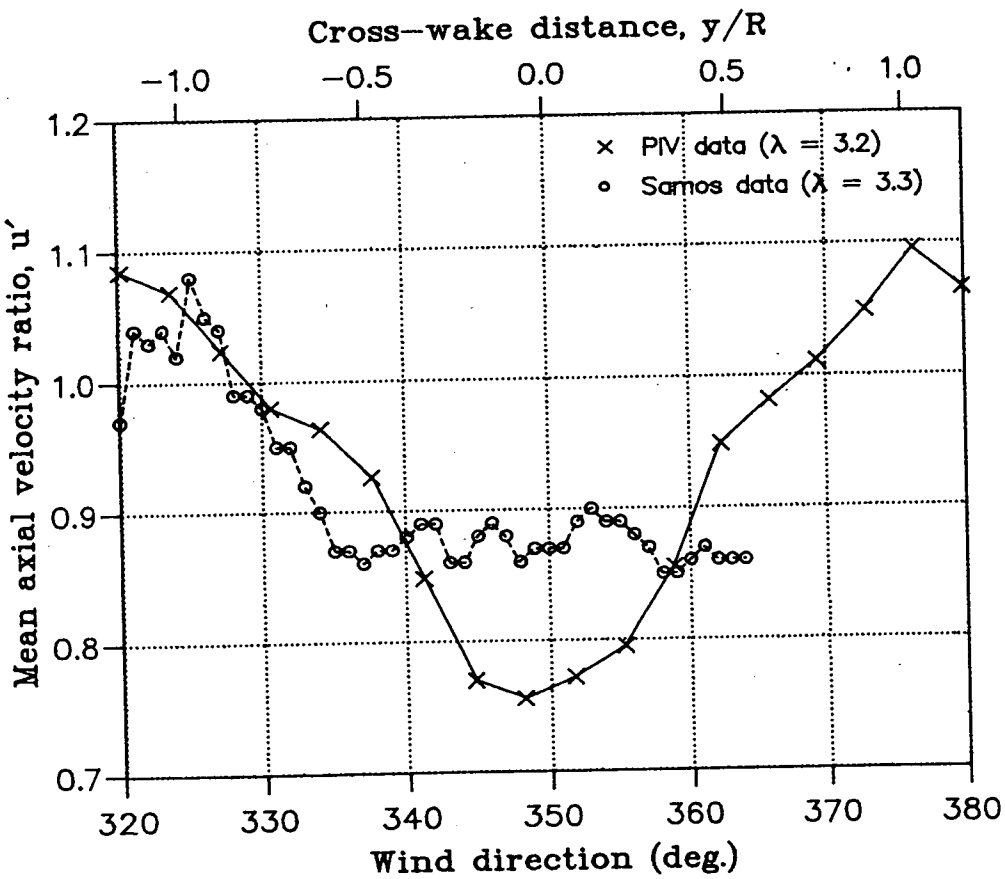


Figure 4.2.1(vii) Velocity profiles at 1.1D for the WM19S rotor, comparing PIV data ($\lambda = 3.2$) and full-scale data ($\lambda = 3.3$).

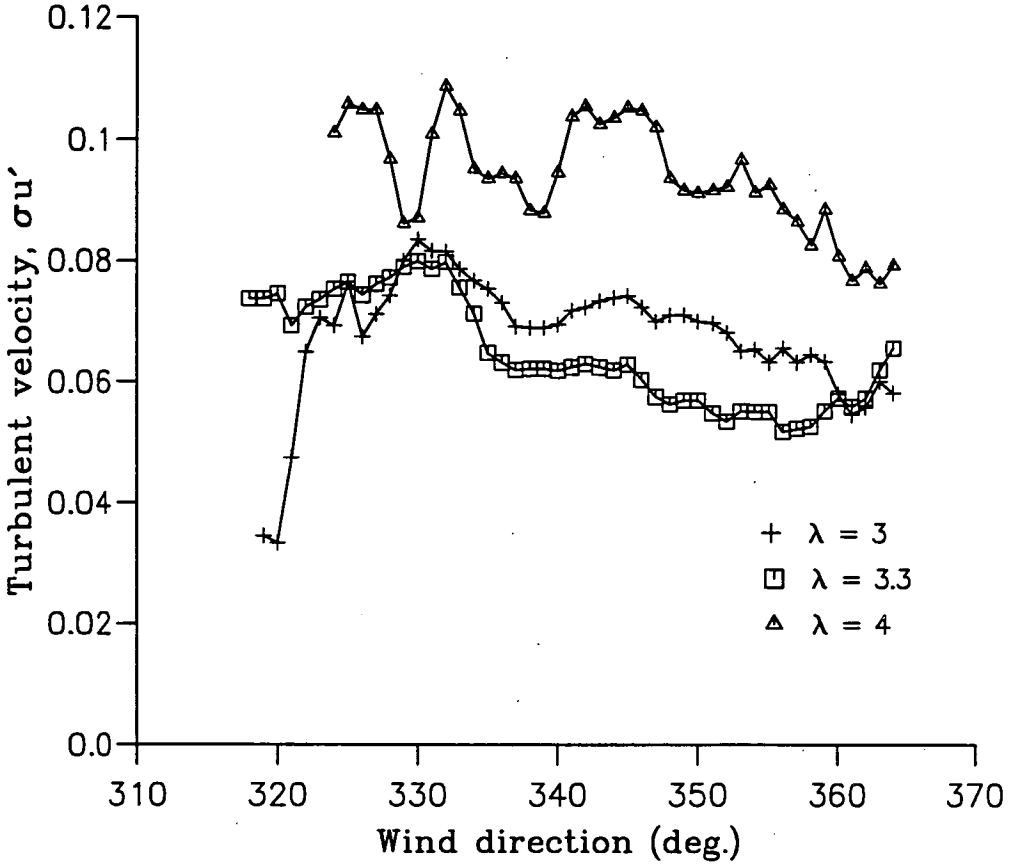


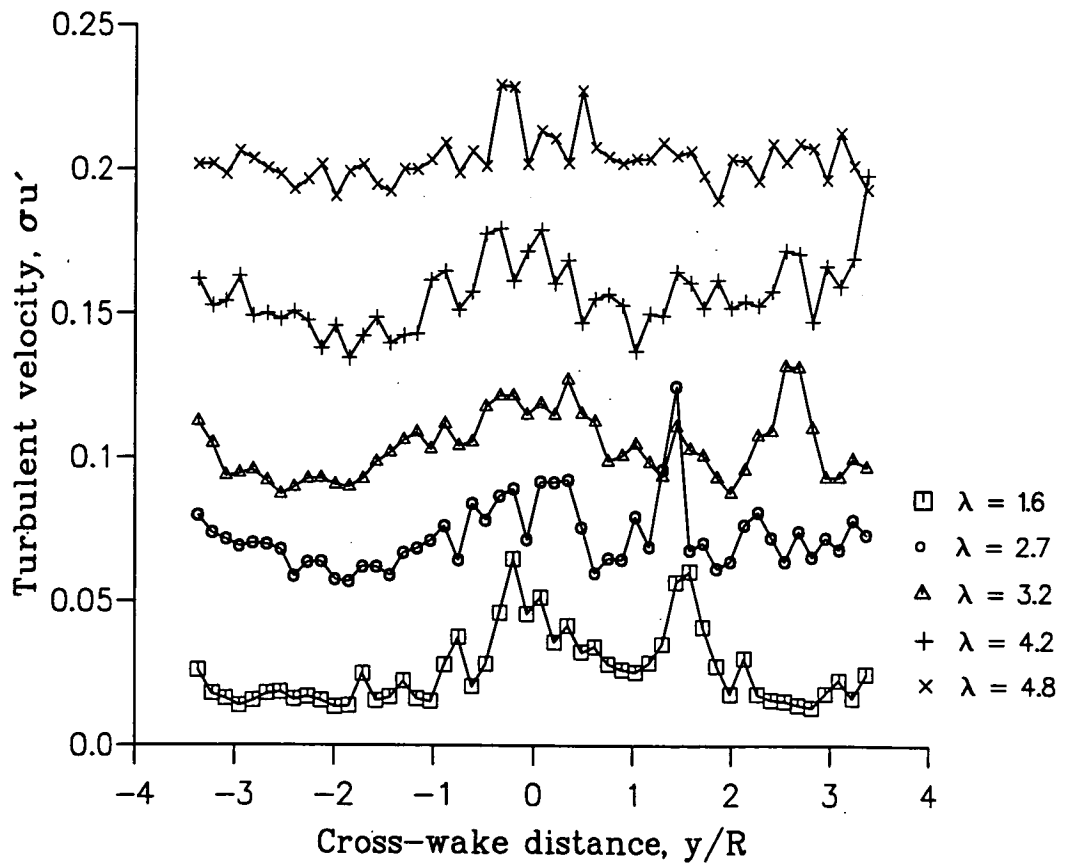


Figure 4.2.1(viii) Turbulent velocity profiles at 1.1D for the WM19S rotor, comparing full-scale data (above) and PIV data (below).

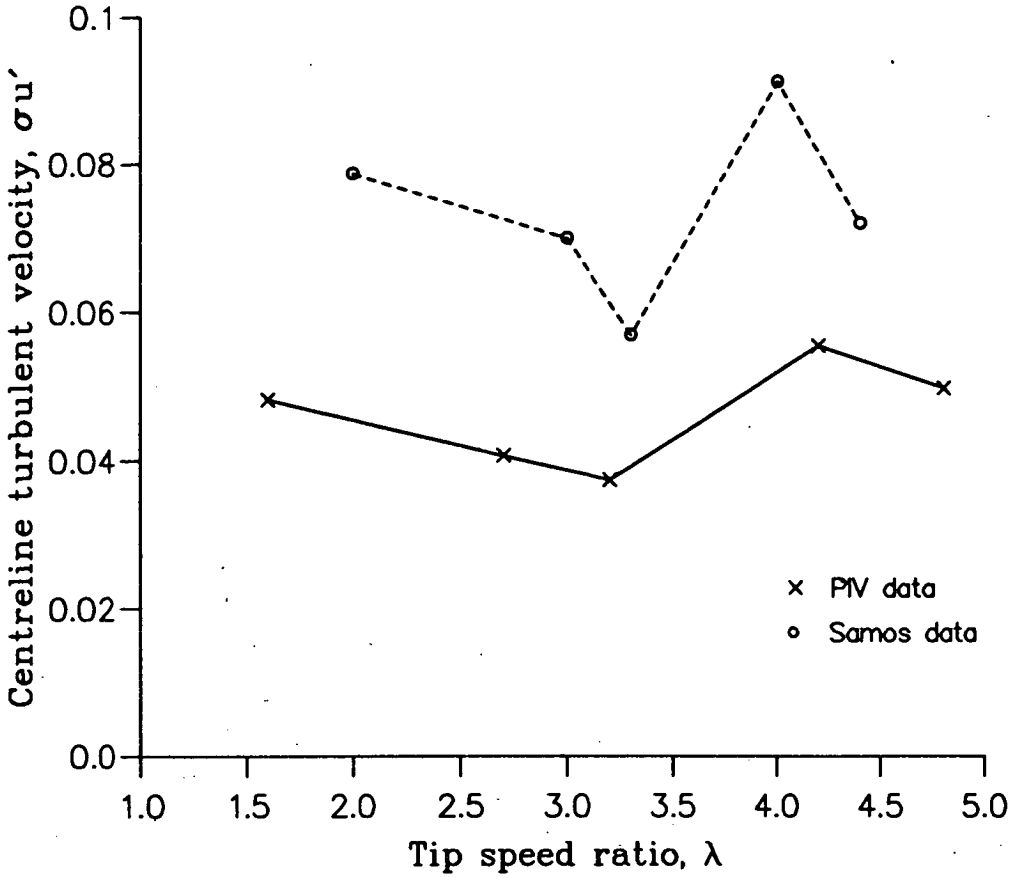


Figure 4.2.1(ix) Centreline turbulent velocity ratios at 1.1D for the WM19S rotor, comparing PIV and full-scale data.

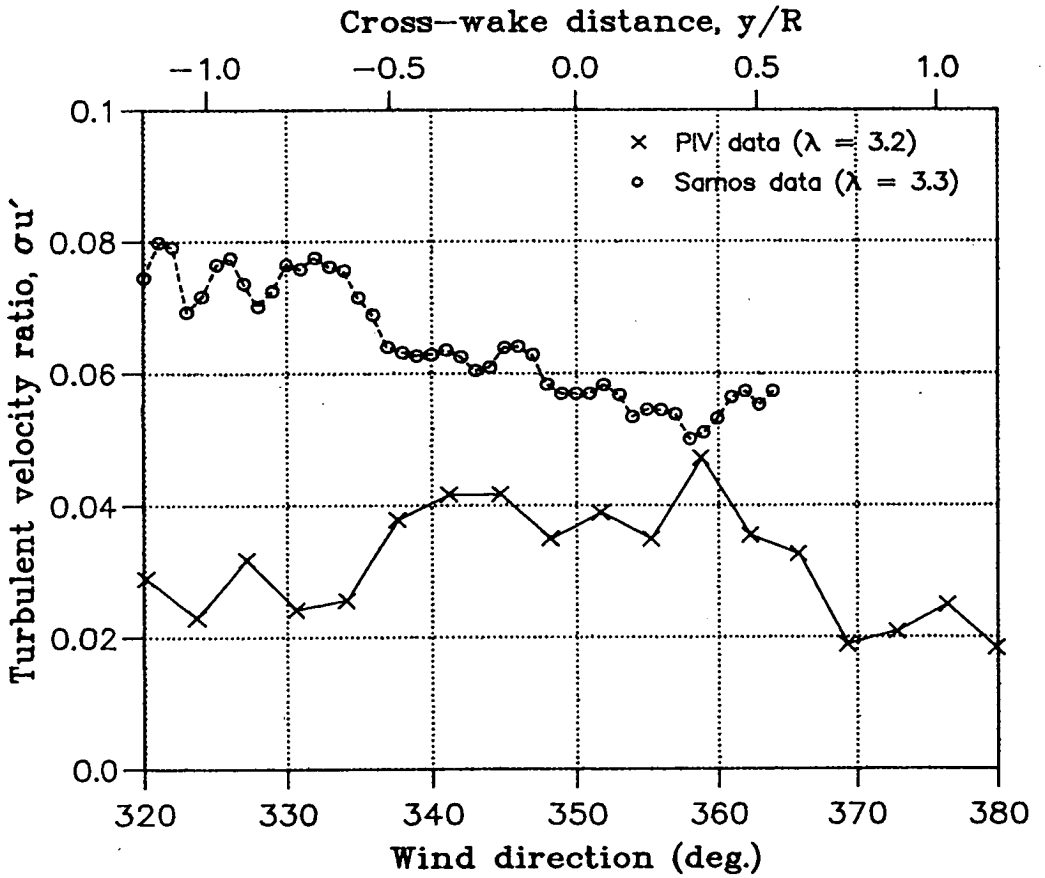


Figure 4.2.1(x) Turbulent velocity profiles at 1.1D for the WM19S rotor, comparing PIV data ($\lambda = 3.2$) and full-scale data ($\lambda = 3.3$).

Figure 4.2.2(i) Vestas V20/100 wind turbine at the Test Station for Windmills, Risø, Denmark.

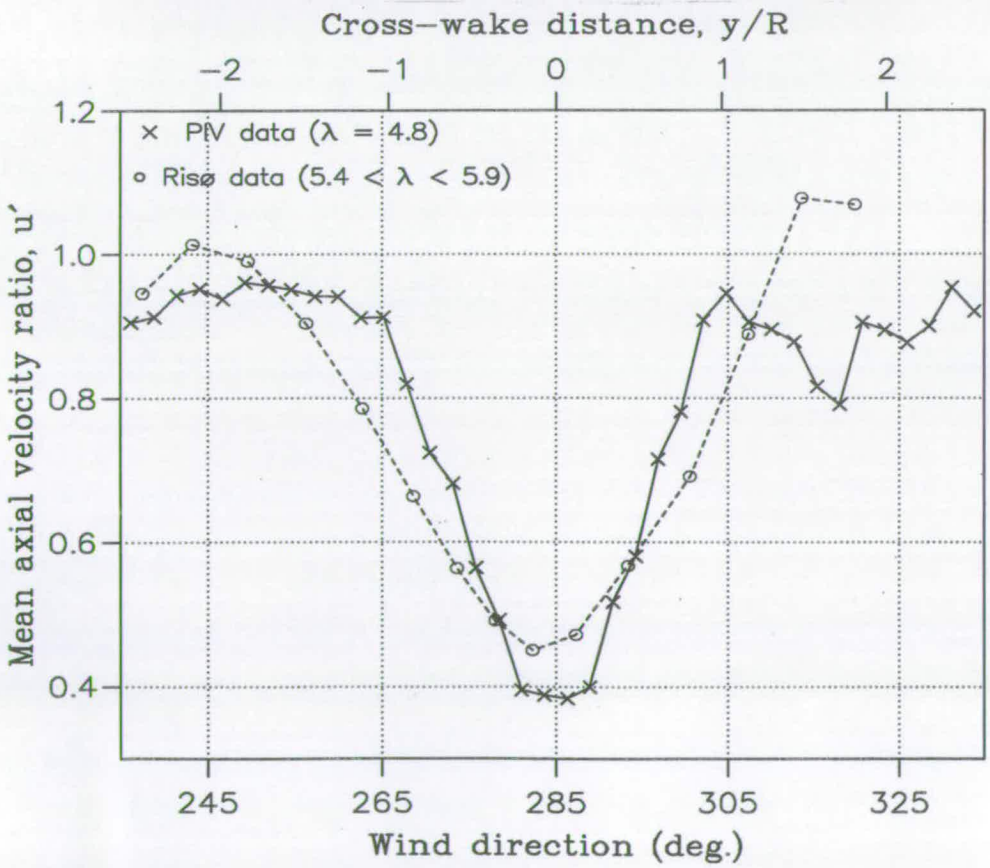


Figure 4.2.2(ii) Comparison of PIV wake velocity profile at 1.5D ($\lambda = 4.8$) with full-scale measurements from the V20/100 at Risø ($\lambda \sim 5.6$).

Figure 4.2.3(i) The Nibe 'A' and 'B' twin-turbines from Jutland, Denmark. The Nibe 'B' machine is featured in the background of the photograph.

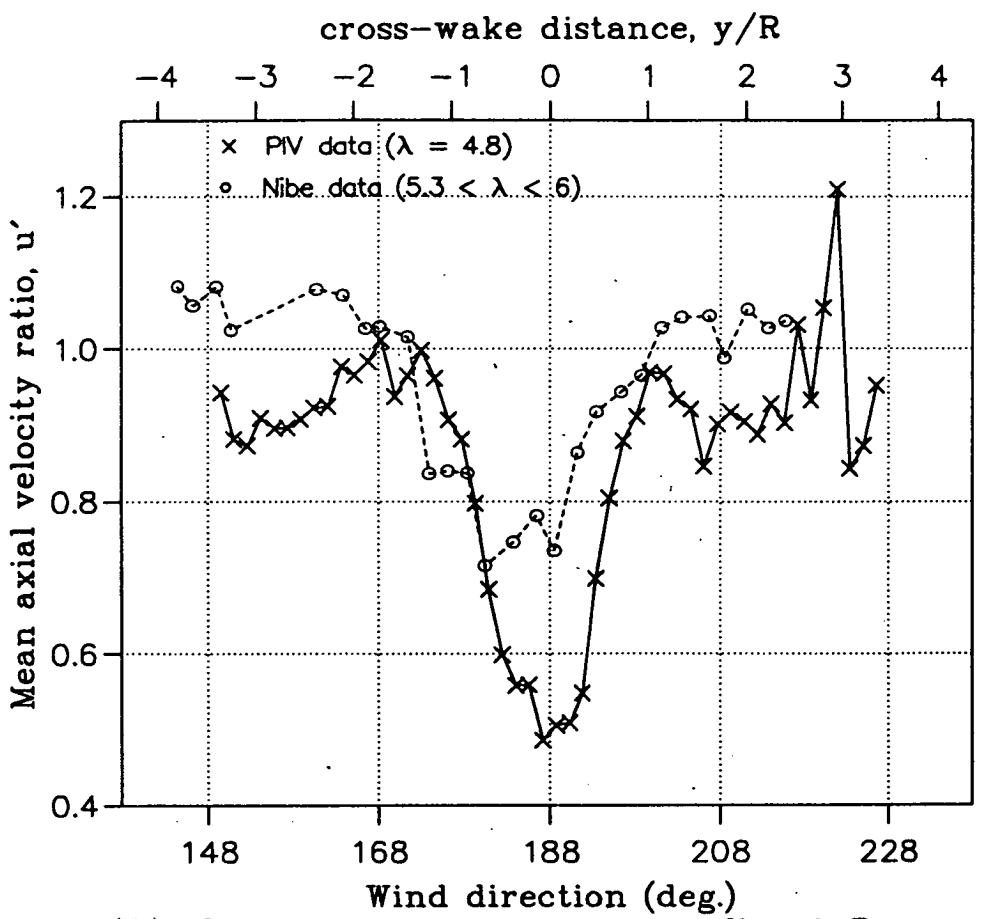


Figure 4.2.2(iii) Comparison of PIV wake velocity profile at 2.5D with full-scale measurements from the Nibe 'B' wind turbine.

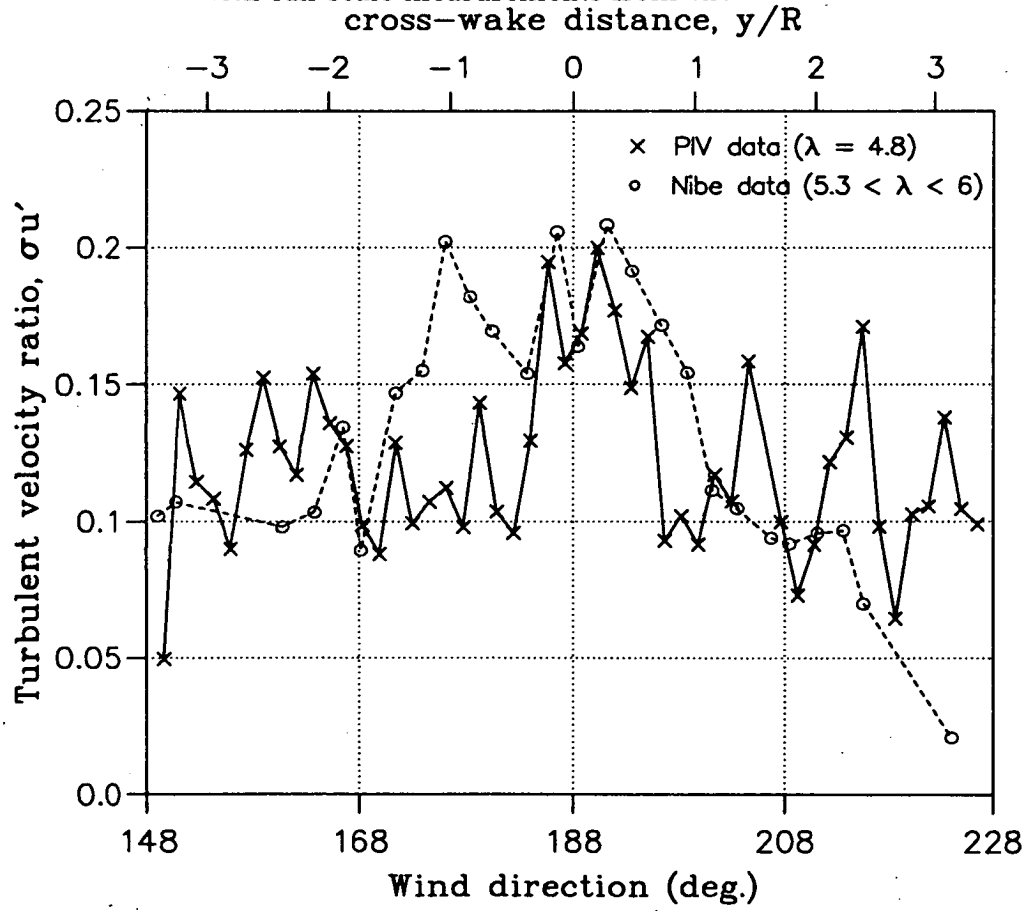


Figure 4.2.2(iv) Comparison of PIV turbulent velocity profile at 2.5D with full-scale measurements from the Nibe 'B' wind turbine.

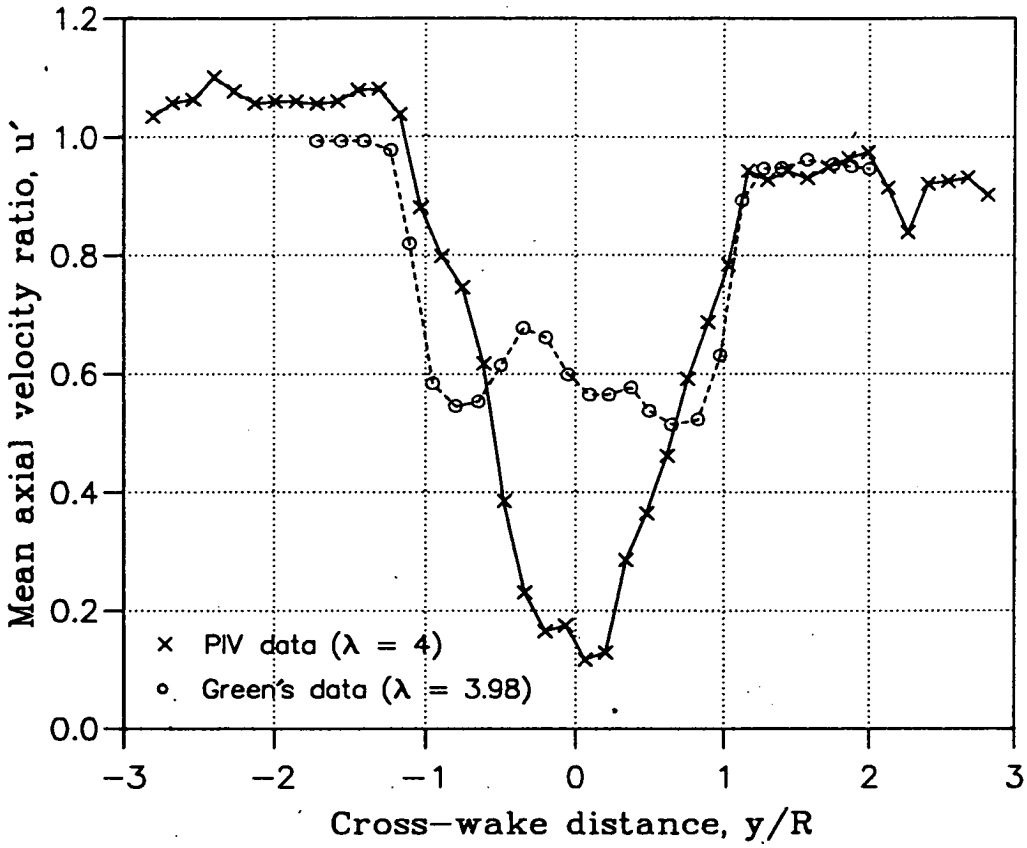


Figure 4.3.1(i) Comparison of PIV wake velocity profile at 1.0D with wind-tunnel measurements from Loughborough University.

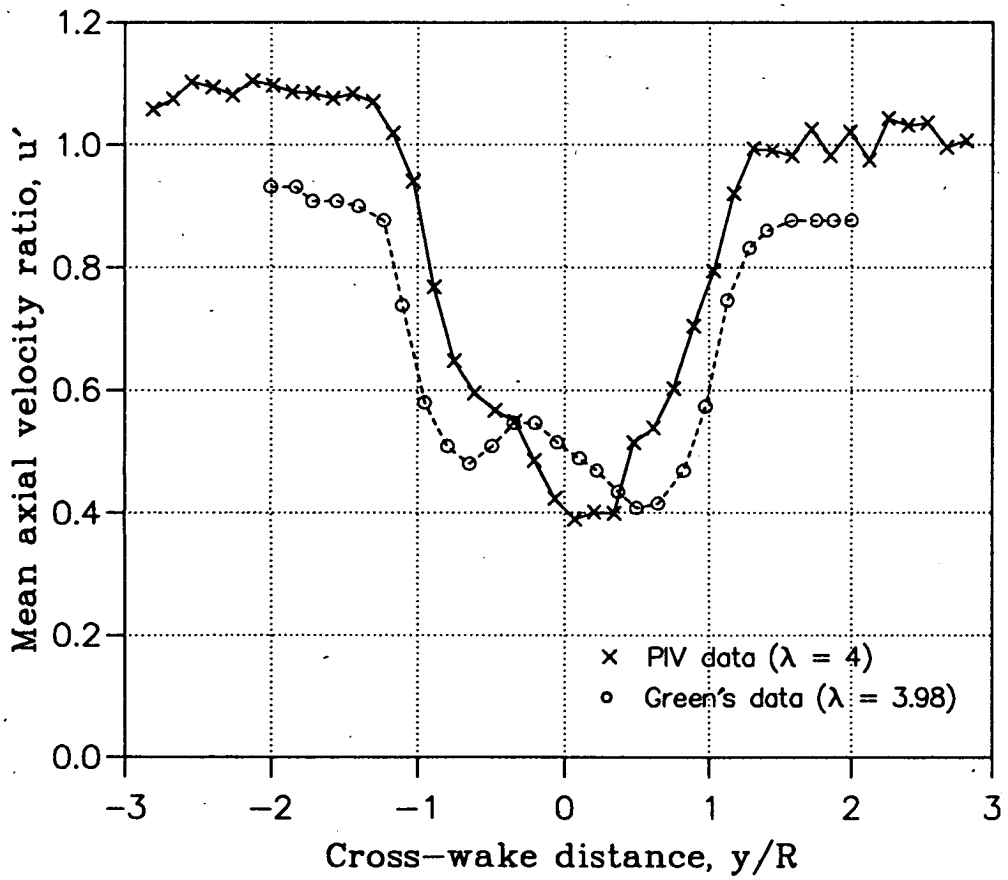


Figure 4.3.1(ii) Comparison of PIV wake velocity profile at 2.0D with wind-tunnel measurements from Loughborough University.

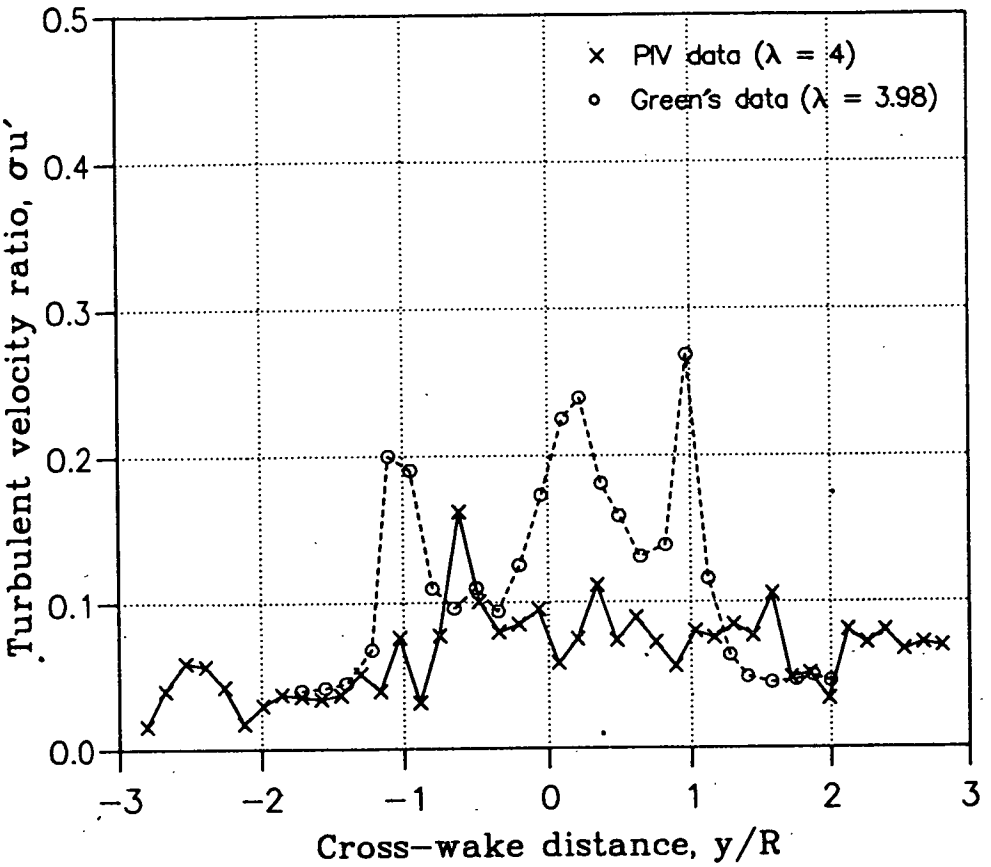


Figure 4.3.1(iii) Comparison of PIV turbulent velocity profile at 1.0D with wind-tunnel measurements from Loughborough University.

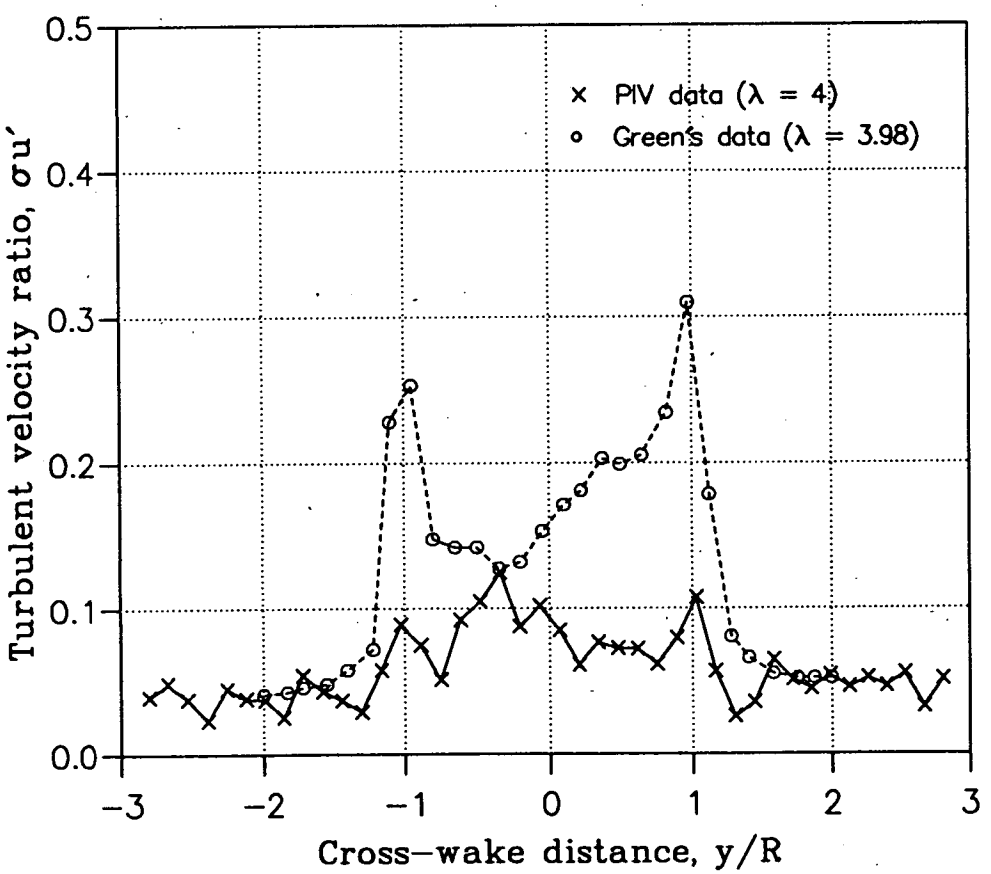


Figure 4.3.1(iv) Comparison of PIV turbulent velocity profile at 2.0D with wind-tunnel measurements from Loughborough University.

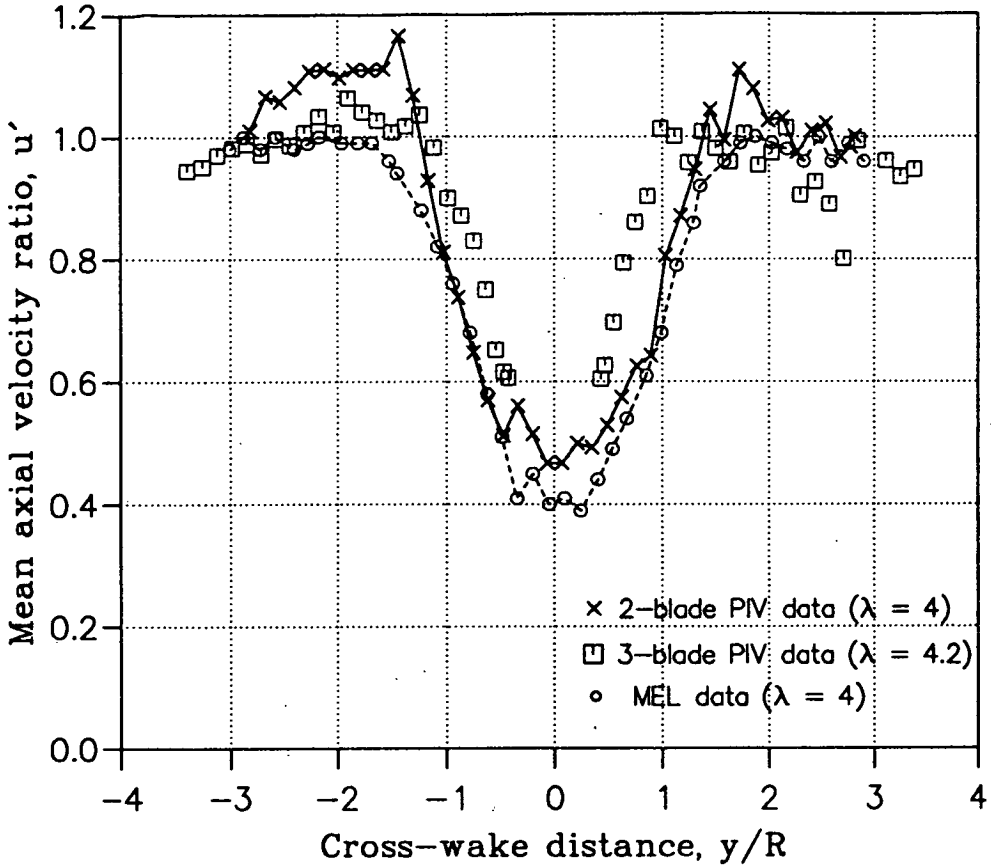


Figure 4.3.2(i) Comparison of PIV wake velocity profiles at 2.5D with wind-tunnel measurements from Marchwood Engineering Laboratories.

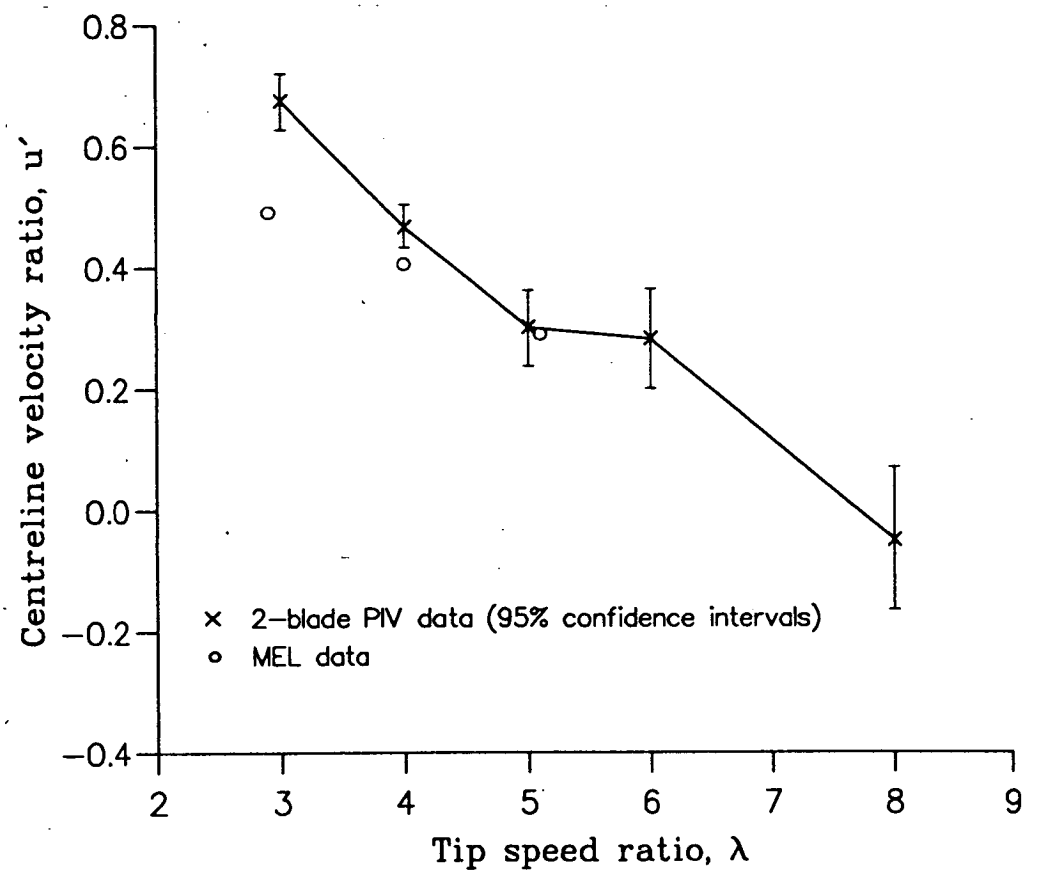


Figure 4.3.2(ii) Centreline velocity ratios at 2.5D, comparing PIV data with wind-tunnel measurements from Marchwood Engineering Laboratories.

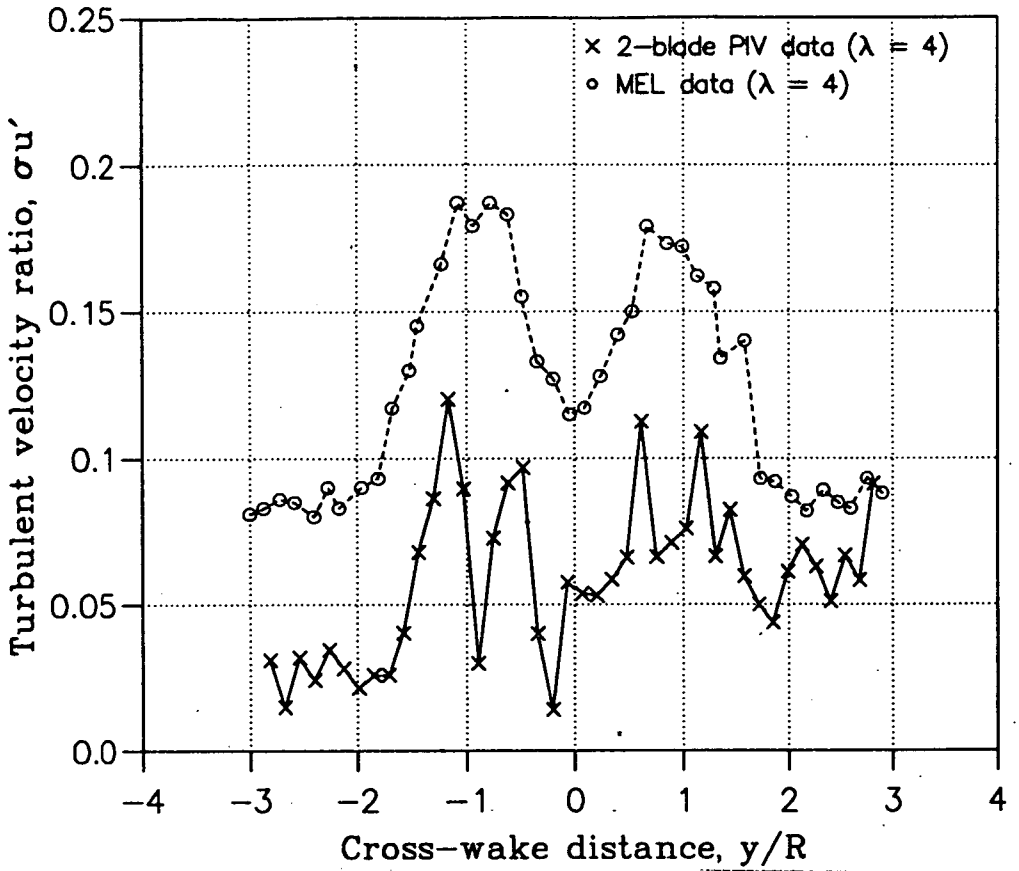


Figure 4.3.2(iii) Comparison of PIV turbulent velocity profile at 2.5D with wind-tunnel measurements from Marchwood Engineering Laboratories.

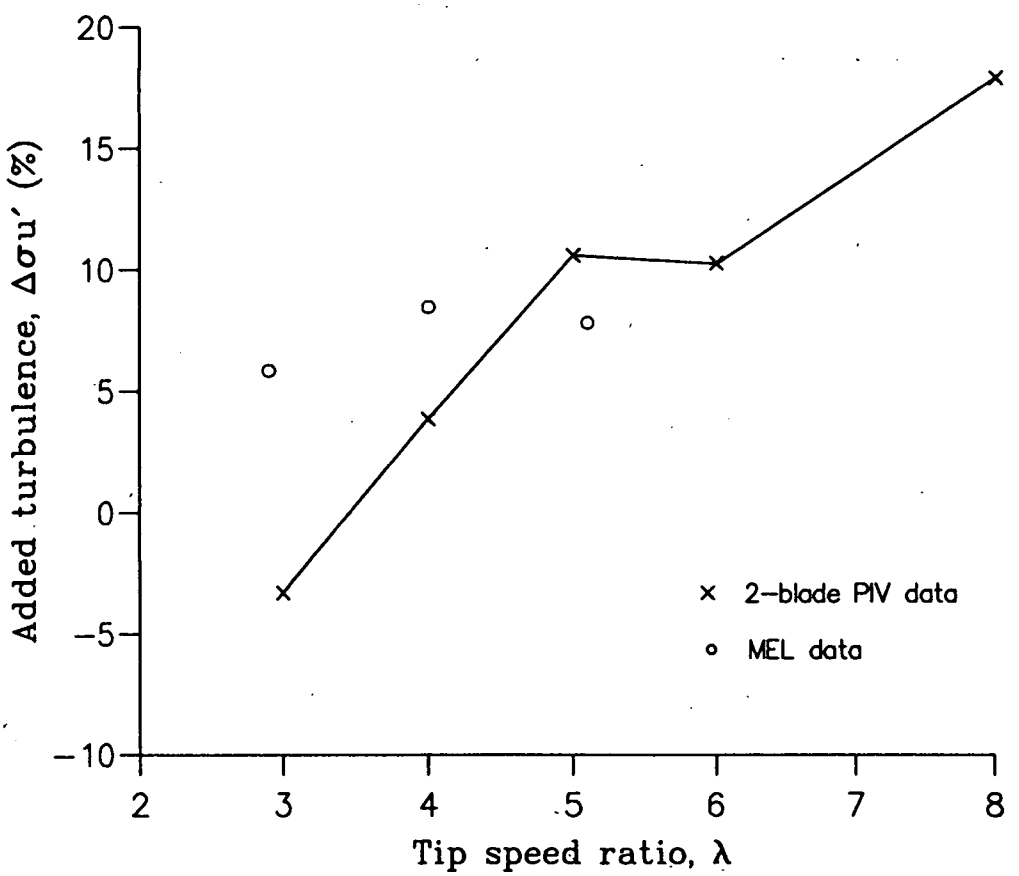


Figure 4.3.2(iv) Added turbulence on the wake centre at 2.5D, comparing PIV data with wind-tunnel data from Marchwood Engineering Laboratories.

# Chapter 5

## WAKE VORTICITY STRUCTURE

### Overview

In this chapter PIV vector maps are used to obtain information about the vorticity shed into the wake of the model rotors. Vorticity contour plots are presented from measurements on both a 2-blade and a 3-blade model. The study focuses on the 2-blade data since the phase-averaged wakes and measurements from the centreline are more useful in revealing the vortex structure. The shape, transport, dissipation and instabilities of the vortex structure are investigated. Comparisons of the PIV vorticity measurements are made with simulations from a sophisticated free wake vortex code developed at the University of Stuttgart.

## 5.1 PIV Analytic Procedures

### 5.1.1 Extracting Vorticity Information

For each point (x,y,u,v) of the PIV velocity vector map, the vorticity at that point is calculated according to the equation

$$\zeta = \frac{\partial u}{\partial y} - \frac{\partial v}{\partial x} \tag{5.1}$$

using the convention that a clockwise circulation in the flow is a source of positive vorticity. A fifth order polynomial is used to approximate the terms $\frac{du}{dy}$ and $\frac{dv}{dx}$ with a routine that searches for the four nearest neighbours to the point in each of the directions, x and y, in order to perform the discretization. The resulting PIV vorticity data is then normalised using the relation

$$\zeta' = \frac{\zeta d}{U_0} \tag{5.2}$$

where $d$ is the diameter of the search routine area and $U_0$ is the freestream velocity. The data is then used as input to a contour plotting package. If the PIV data contains missing vectors then the data is input as an irregular grid and the contour package uses a spline interpolation scheme to account for the missing values.

For the 3-blade experiments the nacelle of the model was offset from the measurement plane. In some analyses, a transformation based on simple geometrical considerations was used to translate the observed vorticity of each fluid element onto the centreline. Thus,

$$\zeta_c = \zeta \sin\theta \tag{5.3}$$

where $\sin\theta = \frac{y}{r}$ and $r$ and $y$ dictate the radial and cross-wake positions of the fluid element, respectively. The wake was assumed to have an axisymmetric distribution of vorticity.

Assuming the wake also has an axisymmetric distribution of axial velocity, the quantity $\phi = u\zeta$ was integrated over concentric annuli at each downstream location to estimate a value for the flux of vorticity in the wake with respect to downstream distance. This was given by discretisation of the equation

$$\Phi = 2\pi \int \phi r dr \tag{5.4}$$

This is converted to a dimensionless quantity using the relation

$$\Phi' = \frac{\Phi}{U_0^2 R} \tag{5.5}$$

where $U_0$ is the freestream velocity and $R$ is the radius of the rotor blades.

### 5.1.2 Results for 2-blade rotor (frozen wake)

Direct conversion of the velocity vector maps of the 2-blade rotor (Figures 3.3.3(i)-(iii)) for the tip speed ratios of $\lambda = 3$, 4, 5, 6 and 8, produces vorticity data which is displayed in the contour plots of Figures 5.1.2(i)-(iii). The vorticity contour plots are presented using the same scale for the purposes of comparison. However, it is possible to change the contrast of the plots to highlight interesting aspects of the flow. Figure 5.1.2(iv) replots the vorticity data for the $\lambda = 3$ case using a different scale.

#### (a) Tip vortices

A number of trends are seen from examination of the figures. At the tip speed ratios of $\lambda = 3$ and $\lambda = 4$, there is slight wake expansion immediately behind the rotor which continues downstream. As the tip speed ratio increases, the initial expansion is more obvious and in addition the boundary of the wake is subject to contraction some way downstream. This can be seen in the cases $\lambda = 5$, 6 and 8. With increasing tip speed ratio, the point of contraction of the wake boundary moves closer to the rotor.

The upper half of the wake is seen to be clearly affected by the shroud and the tower of the support structure. Cosequently, the lower half of the wake is used for futher analysis of the 2-blade vorticity data. Plotting the position of maximum vorticity for each tip vortex gives an indication of the shape of the wake boundary as tip speed ratio is increased (see Figure 5.1.2(v)). The points corresponding to $\lambda = 5$ are correctly positioned on the graph with respect to the vertical axis. The other curves are offset by multiples of 0.5. The curve for the case $\lambda = 8$ is particularly noticeable and could suggest large contraction in the wake. Care must be taken, however, since the appearance of large wake contraction is based on only one datapoint. It can be seen that there are discrepancies in the shape of the wake boundary given by the position of tip vortices shed from different blades. This can be attributed to slight differences in the geometry of the individual blades

of the 2-blade rotor and the blades are labelled as blade 1 and blade 2. Blade 1 is identified as the blade responsible for shedding the vortex closest to the rotor plane in the vorticity plots of Figures 5.1.2(i)-(iii).

Figure 5.1.2(vi) is a plot of axial distance downstream of the rotor for each tip vortex. The spacing of tip vortices from the 2-blade PIV results is not consistent with an asymptotic slow-down of the wake, corresponding to the ideas of conservation of mass in both blade element/momentum and induction theory. These theories predict a densely-packed helical vortex system in the wake. From the Figures 5.1.2(i)-(iii), the packed helical vortex appears as a temporary phenomenon immediately behind the rotor. Further downstream, the helix angle appears to increase and we observe a more loosely packed vortex spiral. This behaviour has been commented upon previously by Montgomerie[74], with reference to smoke tests in a wind tunnel by Alfredsson and Dahlberg[9]. In general, the spacing between tip vortices immediately formed behind the 2-blade rotor decreases with tip speed ratio, as expected. The points plotted for $\lambda = 8$ clearly do not match the trend in the graph. This is discussed further in Section 5.3.

The vorticity contour plots reveal that the strength and size of the tip vortices increase with tip speed ratio. The point of maximum vorticity within the tip vortex is plotted as a dimensionless quantity for the 2-blade rotor in Figure 5.1.2(vii). The two blades are treated separately since, as noted above, the vortices shed from each display differing behaviour. It can be seen from the plot that vortices shed from the rotor when operating in the mid-$\lambda$ range persist longer. This has also been witnessed at full-scale by Pedersen & Antoniou[77]. At low $\lambda$, the tip vortex of the PIV results is very weak and decays by about 1.0D downstream. At high $\lambda$, the tip vortex is strong but, as seen from the graph, decays very quickly and persists up to 1.5D downstream. A number of factors may influence the strength and lifetime of the tip vortices and care must be taken when isolating the effect of tip speed ratio alone on vortex decay. This is discussed further in Section 5.3.

The transport of vorticity in the whole of the wake is studied by plotting the flux of vorticity, $\Phi'$, versus downstream distance for each tip speed ratio in the

separate graphs of Figure 5.1.2(viii). The frequency and amplitude of oscillations in vorticity flux correspond to the position and strength of tip vortices in the wake. The vorticity transport curves illustrate the more loosely packed tip vortices further downstream. The behaviour of flux of vorticity in the wake with tip speed ratio is further addressed in Section 5.2.2.

**(b) Inboard vorticity**

The contour plots reveal a second source of vorticity, in addition to the tip vortices, inboard of the tip. Figure 5.1.2(iv) replots the vorticity data, for $\lambda = 3$, on a scale which highlights this 'inboard' vorticity, compared to Figure 5.1.2(i). The region of concentrated vorticity has its origins very close behind the blade but not close enough to the hub, nor of the correct sign, to be labelled as a root vortex. The inboard vorticity moves under the influence of the flow behind the rotor and clearly indicates the effects of wake expansion with tip speed ratio. At high tip speed ratio, this second source of vorticity moves outward until it merges with the helical tip vortex system. For the case $\lambda = 8$ (see Figure 5.1.2(iii)), this results in an increase in the maximum vorticity within the tip vortex system at that point. The source of the inboard vorticity is discussed in Section 5.3.

### 5.1.3 Results for 3-blade rotor (averaged wake)

Data obtained from tests with the 3-blade rotor are presented as vorticity contour plots in Figures 5.1.3(i)-(v). The data was captured off-axis and averaged over six different rotor positions in order that the measurements were more suitable for comparison with the time-averaged recordings of full-scale results from Samos Island (see Section 3.2.1). Averaging of data with the helical vortex system in different phases results in a loss of all time-dependent vortex structure and the plots displayed in Figures 5.1.3(i)-(iv) show less distinct vortex patterns than the 2-blade contour plots. However, averaged vorticity maps yield a steady-state axisymmetric vortex pattern and as such, can provide vorticity data which is directly

comparable with the assumptions of actuator disk models. General observations concerning the relative vortex stengths and structure are made for each of the operating states $\lambda = 1.6$, 2.7, 3.2, 4.2 and 4.8.

At $\lambda = 1.6$, isolated regions of concentrated vorticity are displayed in the contour plot of Figure 5.1.3(i). The wake is divided into regions of positive and negative vorticity, lying on either side of the centreline. This is the expected pattern from the cross-section of a helical vortex. As $\lambda$ increases, the wake width increases as does the strength of the vorticity contained within it. The sinusoidal pattern imposed on the boundary of the wake in Figure 5.1.3(iii) is consistent with the presence of trailing tip vortices. The figure also shows two sources of concentrated vorticity lying very close to, and either side of the centreline. They appear to be stronger, though of the same sign as the corresponding tip vortices. As $\lambda$ increases, the strength and size of this inboard vorticity increases relative to the vorticity at the periphery of the wake. Figure 5.1.3(v)($\lambda = 4.8$) is notable for signs of wake contraction around 2.5D downstream.

To compensate for the offset factor in the 3-blade measurements, vorticity 'corrections' are applied to the results. This problem was overcome in the 2-blade measurements by conducting experiments with the nacelle of the rig in the plane of the laser sheet. Under the assumption of an axisymmetric wake, the 3-blade vorticity data is translated onto the centreline plane to yield absolute values of vortex position and strength for each tip speed ratio. As an example, the corrected vorticity data for $\lambda = 3.2$ is plotted as a contour plot in Figure 5.1.3(vi). The position of the vortices at the boundary of the wake is consistent with vorticity shed from the tip of the blades, as expected. The contour plot reveals that the vorticity corrections have the disadvantage of an absence of data from the inner 42% of the blade. The strong inboard vorticity, in comparison with the vorticity shed by the tips of the blade, may be a property of the mathematical translation. However, the strong inboard vorticity appears to emanate from a spanwise position of around 0.5R. This coincides with a position on the blade that was captured on film intersecting the laser sheet. This suggests the possibility of large circulation around the WM19S replica blades at a spanwise station of 0.5R, and

this blade-bound circulation is then captured in the laser sheet. Futher discussion on the source of the inboard vorticity is presented in Section 5.3.

## 5.2 Comparison with a Vortex Wake Model

This section presents a comparison between the PIV results and a sophisticated vortex wake code developed at the Institut für Aerodynamik und Gasdynamik (IAG), Universität of Stuttgart. The comparison is based on the 2-blade results since flow past the flat-plate blades is a fundamental study and offers simplicity in modelling the rotor. In particular, extreme operating states of the blades are investigated. These correspond to regions of flow where current theoretical techniques give least satisfactory results.

### 5.2.1 The ROVLM code

The **RO**tor **V**ortex **L**attice **M**ethod code[19, 18] is a modular free-wake code for the calculation of loads and flow field properties of wind turbines. The ROVLM code has been developed at IAG over the past four years and extends a lattice method[24] to simulate the effects of vortex shedding and roll-up in the wake. It is able to predict the wake geometry and the strength of the vorticity on the rotor blades and in the field. The input consists of the blade geometry and the flow conditions. No prior assumptions concerning the shape of the wake are necessary.

In the simulation, the blades start their rotation in the first time step and in every subsequent time step a new portion of the wake is shed from the trailing edge of the blades. A steady state solution develops after a few revolutions depending on the loading of the rotor and the oncoming flow.

### (a) Theory

The method is based on the solution of the Laplace equation assuming an inviscid and irrotational flow. Solutions take the form of elementary singularities representing vortices, sources or dipoles. These singularities are used to model the flow field. Within the current method, dipoles are placed at the blades and in the wake. This corresponds to simulating the lift forces on the rotor. Blade thickness is neglected.

### (b) Discretization

The rotor blades have to be discretized into a set of quadrilateral panels covering the camber line of the local blade profiles along the radius. Sensitivity studies have shown that the main features of the solutions can be retained by using only one panel in chordwise direction, although the code is able to treat more. In the radial direction 10 panels are used. Each panel contains a dipole of constant strength which is equivalent to vortex filaments defined by the corner points of the panel. (See Figure 5.2.1(i)).

### (c) Procedure

In the centre of each panel, a control point is declared at which the singularity strength is specified. The singularity distribution across the blade panels is determined by applying the kinematic boundary condition in external Neumann form so that the velocity component normal to each panel vanishes. Vorticity is shed into the wake as a row of wake panels, evolving from the trailing edge. The amount of shed vorticity is determined by the Kutta condition. The presence of the wake panels affects the induced velocities at the blades and the singularity distribution has to be re-calculated. Repeating this procedure for each time step results in a growing wake. To reduce the computation involved in the free-wake calculations, a simplified model is incorporated for far wake transport.

### (d) Flow field calculations

A post-processer is used to read in the geometry and the singularity strengths of the blades together with their wakes and calculate velocities at desired points in the flow field. The wake velocities are determined using the Biot-Savart law. The vorticity is assumed to be concentrated within the filaments. Therefore, if a field point is very close to an inducing vortex filament an unrealistic high value of the velocity will be achieved. In order to overcome this problem a core radius has to be assumed for that case. Once the velocities are known, the vorticity components normal to the field plane are calculated from the central differences of the neighbouring points.

### (e) Simulations

Blade geometry, operating states of the rotor and size and location of the measurement area in the flume were used as input to the ROVLM code in order to simulate the PIV measurements.

Figure 5.2.1(ii) shows a typical result of the ROVLM calculations. Depicted is the discretized rotor together with the resulting wake. The flow is in the positive z-direction of the diagram. A two-dimensional region is depicted, corresponding to the laser sheet in the PIV set-up, from which wake velocities are extracted for the purpose of comparison with the PIV data.

In a typical simulation by the ROVLM code, 140 iterations would be performed, corresponding to about 10 hours computational time.

## 5.2.2 Results of Comparison with the ROVLM Model

Wake velocities from the 2-blade PIV experiments and the ROVLM simulations are analysed to produce vorticity contour plots for the purpose of comparison of

results. Only velocities in the lower half of the wake are used since the upper half of the wake of the PIV data is affected by 'tower' shadow. The comparisons are displayed in Figures 5.2.2(i)-(v) for tip speed ratios of $\lambda = 3, 4, 5, 6$ and 8. The plots highlight important differences and similarities between the two sets of results.

### (a) Tip vortices

Firstly, the results compare reasonably well in terms of the overall shape of the wake; the ROVLM simulations model the contraction of the wake at high $\lambda$ with some success. Figure 5.2.2(vi) compares the width of the wake for the two cases. The shape of the wake boundary is estimated by studying the position of maximum vorticity within the tip vortices. The maximum and minimum location of this point are plotted versus tip speed ratio to consider the extent of wake expansion and wake contraction. Figure 5.2.2(vi) reveals that the shape of the wake boundary for the PIV data is more sensitive to $\lambda$ than the ROVLM data. This is particularly evident at high $\lambda$ where large initial wake expansion is followed by marked contraction.

The average tip vortex spacing for each tip speed ratio for the 2-blade PIV results is calculated from the slope of the points in Figure 5.1.2(vi) and is contrasted with the ROVLM results in Figure 5.2.2(vii). The two curves can be seen to agree quite closely at low $\lambda$, but deviate at higher tip speed ratios. As tip speed ratio increases, the two curves exhibit a trend of decreasing tip vortex spacing, consistent with the shedding of a vortex system of decreasing helix angle. The rate of decrease in this vortex angle becomes less at higher $\lambda$. The highest tip speed ratio, $\lambda = 8$, produces the largest discrepancy between the PIV and the ROVLM results. Again, care must be exercised when interpreting this result as the observation is based on only one datapoint.

The strength of tip vortices for the PIV and ROVLM results are compared in Figure 5.2.2(viii). The two blades of the flat-plate rotor are treated separately

since differences in the vortex shedding properties of the blades were discovered (see Section 5.1.2). The graphs of Figure 5.2.2(viii) show the maximum value of vorticity in the vortex closest to each blade (see Figures 5.2.2(i)-(v)) as a function of tip speed ratio. In the PIV aquisition and the ROVLM simulations, this corresponds to the vortex most recently shed from the blade. Figure 5.2.2(viii) shows that the strength of the vortex for the ROVLM data is relatively constant compared to the PIV results. Although the results display some agreement at low tip speed ratios, the ROVLM simulations do not match the strength of the vortices produced in the PIV experiments at high $\lambda$. The PIV data from blade 1 at $\lambda = 5$ may be spurious but, in general, the PIV data appears to be more sensitive to $\lambda$ than the ROVLM data and shows an increase in magnitude of the vortex strength as $\lambda$ increases. This is consistent with the notion of more energy introduced into the trailing vortices at higher $\lambda$. There is a slight decrease in the magnitude of the vortex strength for the ROVLM curve. Comparing the graphs of Figure 5.2.2(viii), there is little difference in the ROVLM results for the two separate blades, as expected for a numerical simulation. The PIV results confirm that the individual blades of the 2-blade rotor have different properties in terms of vortex shedding. This may be attributed to differences in geometry between the two blades.

Analysis of Figure 5.2.2(viii) yields an average vorticity flux which is plotted together with the corresponding ROVLM values in Figure 5.2.2(ix). Both curves display trends which suggest there is a transport of vorticity away from the rotor which increases as tip speed ratio increases. Values for this flux of vorticity for the PIV results are shown to be larger than for the ROVLM results.

### (b) Inboard vorticity

The ROVLM results display no signs of the 'inboard' vorticity apparent in the PIV contour plots. In the PIV plots of Figures 5.2.2(iii) and 5.2.2(iv) ($\lambda = 5$ and $\lambda = 6$), it is noted that interaction between successive tip vortices occurs once the inboard source of vorticity has merged with the tip vortex spiral. There is some

evidence from the plots that the vortices dissociate at 2.5D downstream. The PIV plots also show that the inboard vorticity is distinct from the root vorticity. Evidence of root vorticity can be seen in the top left hand corner of the PIV contour plots. It is not as strong as the vorticity of the tip vortex system and is seen to disperse within one blade revolution. In contrast, the root vorticity of the ROVLM contour plots is very pronounced. The inviscid assumptions of the ROVLM code mean that large angles of attack near the hub in the IAG simulations lead to large circulation around the root of the blade instead of separated flow, as would occur in experiments, corresponding to blade stall. Thus the root vortices are very strong and in addition not subject to viscous dissipation. The IAG contour plots reveal a breakdown in the vortex structure downstream of the rotor. This appears to be have its origins in interaction of root vortices shed from separate blades. This breakdown of vortex structure occurs closer to the rotor at higher tip speed ratios.

## 5.3 Summary and Discussions

The vorticity in the near wake of a 2-blade and 3-blade model has been examined for a range of tip speed ratios with the aid of contour plots. Vorticity data has been analysed to gain information about the geometry, strength and stability of the vortex system. Comparisons are made with an advanced free-wake code (ROVLM), developed at the University of Stuttgart. The ROVLM code was configured to simulate the same conditions, in terms of rotor geometry and tip speed ratio, as those obtained in the 2-blade PIV tests.

The vorticity contour plots for both the 2-blade and 3-blade PIV tests revealed structures that were consistent with the expected pattern of a cross-section of a helical vortex spiral. At low tip speed ratios, mild wake expansion was observed. This pattern concurs with simple wake theory. For both the 2-blade and 3-blade results, tip speed ratios of around $\lambda = 5$ and higher displayed signs of contraction in the wake downstream of the rotor. This has been observed to precede the

breakdown of the structured wake into a highly turbulent state.

The contraction in the wake may be explained as follows. At high tip speed ratios the model behaves like a circular disc placed perpendicular to the flow, forcing the fluid around it. The resulting large slipstream expansion, turbulence and recirculation in the wake are characteristic of a wind turbine rotor operating in the turbulent wake state. The areas of recirculation produced downstream of the rotor reduce the velocities in the core of the wake. The law of conservation of mass flux then explains the contraction of the wake boundary. As tip speed ratio is increased the width of the low pressure region of fluid behind the turbine increases and the point of contraction of the wake occurs closer to the rotor. In the extreme case, areas of recirculating flow are established in the rotor plane. This is referred to as the vortex ring state[38].

Areas of recirculation within the wake could also encourage re-entrainment of the free -stream into the wake and thus would be expected to have an effect on the velocities of the tip vortices. The 2-blade PIV results confirmed that the spacing of the vortices was not consistent with an asymptotic slow down of the wake, as assumed by BEM theory. The same finding was reported by Björn Montgomerie at an IEA symposium in 1990. He referred to wind tunnel tests carried out by The Aeronautical Research Institute of Sweden (FFA) in 1979, when smoke studies on model turbine rotors revealed strong acceleration of the wake spirals, following an initial deceleration. This was noted to coincide with strong mixing of the freestream and the wake, again in contradiction to basic BEM theory. Figure 5.2.2(vii) of the PIV results appears to show a dramatic increase in tip vortex spacing at $\lambda = 8$. It is plausible that there is a wake acceleration due to re-entrainment which uncoils the densely packed helical spiral. However, the PIV contour maps at high $\lambda$ (Figures 5.2.2(iii) and 5.2.2(iv)) displayed signs of vortex pairing in the tip vortex system. For $\lambda = 8$, Figure 5.2.2(v) showed the downstream wake appearing as large well-spaced vortices. Each of these vortices may actually be two vortices coalesced into one. This vortex interaction would lead to an uncertainty in determining the spacing of the vortices, with the result that they may appear to be accelerating.

The PIV contour plots revealed a second region of concentrated vorticity in the wake of the model, inboard of the tip. The 'inboard' vorticity was not of the correct sign to be attributed to root vorticity and although the 3-blade results suggested it may be due to blade-bound circulation in the laser sheet, its size and strength relative to the tip vorticity and its persistence downstream cast some doubt over this theory.

Close study of the PIV velocity vector maps of Section 4.1.3 may give some insight into the source of the inboard vorticity. A PIV velocity vector map of the 2-blade rotor at $\lambda = 8$ is reproduced in Figure 5.3. The map identifies three distinct regions of flow in the wake. Firstly a *wake core*, containing very small velocities. At very high $\lambda$, the flow immediately behind the rotor is almost stagnant, while further downstream areas of turbulence and recirculating flow establish themselves. The second region is the *outer wake*, comprising the tip vortex structure while the third region is an *inner wake* moving under the influence of rapidly expanding flow. The inner wake may well contain sections of vortex filaments shed from the blades. This matches Glauerts description of the wake as a vortex system comprising an intense tip-vortex outer region and a weakly-diffused vortex sheet inner region. The velocity gradients across the inner wake result in a shear layer of vorticity. The stretching of smoke traces in tests by Pedersen & Antoniou give credit to the existence of this shear layer at full-scale.

The vortex structure in the shear layer was found to move under the influence of rapid expansion. As tip speed ratio increased, this led to an interaction of the vorticity in the shear layer and the tip vortices. At $\lambda = 5$ and $\lambda = 6$, this caused instability to the tip vortex system resulting in the coalition of adjacent vortices. This 'pairing process' has been commented upon previously in separate studies by Alfredsson[10] and Green[52]. In Figure 5.2.2(iv), the preceeding vortex appeared to roll-up over the top of its neighbour to produce a single vortex by 1.5D downstream. Green estimates the distance for the pairing vortices to become indistinguishable as 2.0D downstream. At $\lambda = 8$, the shear layer merged with the tip vortex system to produce an area of concentrated vorticity of thickness of the order of the rotor radius. The area of influence of the tip vortex system thus

extended to more than twice the swept area of the rotor. At full-scale, Pedersen & Antoniou recorded the area of influence to be close to 40% of the swept area.

The 2-blade PIV results were compared with simulations from ROVLM, a sophisticated vortex wake code. Detailed comparisons with the numerical data are of less interest than the overall conclusions, since the code was inviscid. The generation of vorticity on the physical model is due to the boundary layer on the blades and hence the dependence of the PIV results on Reynolds number is inevitable. This is discussed further in Chapter 6.

The PIV and ROVLM simulations compared reasonably well in terms of overall wake geometry. The numerical results modelled wake contraction with some success although the wake contraction of the 2-blade PIV results was more sensitive to tip speed ratio. As tip speed ratio was increased, the PIV results displayed a corresponding increase in both the size and strength of the tip vortices. The turbulent wake preserves the energy within the trailing vortex filaments to produce a very strong vortex pattern. Although the PIV and ROVLM results show some agreement at low $\lambda$, the tip vortices shed at higher $\lambda$ were much stronger for the case of the PIV results.

The size and strength of tip vortices were more sensitive to changes in $\lambda$ in the case of the PIV experiments. Vortices shed from the rotor when it was operating at medium $\lambda$ appeared to travel further downstream before dissipation. The tendency for tip vortices to persist in moderate wind conditions has also been witnessed at full-scale by Pedersen & Antoniou. The PIV results indicate that in the mid-$\lambda$ range, the tip vortices do not persist more than two diameters downstream. This is in accordance with observations made at full-scale by Savino & Nyland.

Care must be taken before drawing conclusions on the effect of tip speed ratio alone on the properties of the vorticity shed into the wake for the PIV experiments. It has been noted above that the PIV results were very sensitive to changes in $\lambda$, yet in the PIV experiments different tip speed ratios were achieved by running the rotor at different speeds. Thus the blade Reynolds number would also vary from

one test to another. This is addressed further in Chapter 7.

The root vortices were more pronounced in the results of the ROVLM simulations. Due to inviscid assumptions, there is large circulation but no separated flow despite large angles of attack near the hub. Thus the root vortices were very strong and not subject to dissipation. In contrast, the PIV data revealed that, due to stall near the hub, the root vortices were not as large as those of the ROVLM simulations. The root vortices in the experiments were subject to dissipation due to the influence of viscosity. The PIV vorticity contour plots revealed that the root vortices were dissipated within a blade revolution. This was consistent with observations from full-scale by Pedersen & Antoniou. The numerical simulations revealed that, with no viscous damping, the strong presence of the root vortices resulted in an interaction of vortices from separate blades leading to instability in the vortex structure.

## 5.4 Conclusions

A wake vorticity analysis of the PIV results and a comparison with the ROVLM code has revealed behaviour in the wake of the models which influences the structure of the vortex system shed from the blades. The most important findings of this chapter may be listed as follows:

1. The PIV and ROVLM results both predict wake contraction after initial expansion, at high tip speed ratios. This is contrary to simple BEM/actuator disk models. Areas of recirculation, established in the wake at high $\lambda$, may be responsible for the wake contraction.

2. The PIV contour plots revealed a second region of concentrated vorticity in the wake of the model, attributed to a shear layer between the tip vortex system and the retarded inner wake. This inboard vorticity moved under the influence of rapid wake expansion to merge with the helical tip vortex spiral. In some cases this leads to instability of the tip vortex system.

3. The ROVLM simulations did not display evidence of inboard vorticity. The inboard vorticity may be due to the tests having been carried out at low Reynolds numbers, but this is unproven. The phenomenon may be a fundamental property of HAWT near wakes at all scales. The ROVLM needs to be modified to incorporate Reynolds number as a variable parameter within the code.

4. At high $\lambda$, both the PIV and ROVLM results indicated a breakdown of the vortex structure into large-scale turbulence at 2D–3D downstream. For the PIV results, this may coincide with the rotor operating in the turbulent wake state. In the ROVLM case, this may be due to interaction of strong, persistent root vortices. Wake breakdown is, however, absent from most rotor codes, of either BEM or vortex-wake type.

5. The ROVLM code needs to be capable of modelling the case of stalled flow at the blades. This is an important case and an area where current prediction codes give the poorest results. At present, the ROVLM modelling of the inboard sections (at high incidence) will be significantly in error, and the root-vortex strength will be over-predicted.

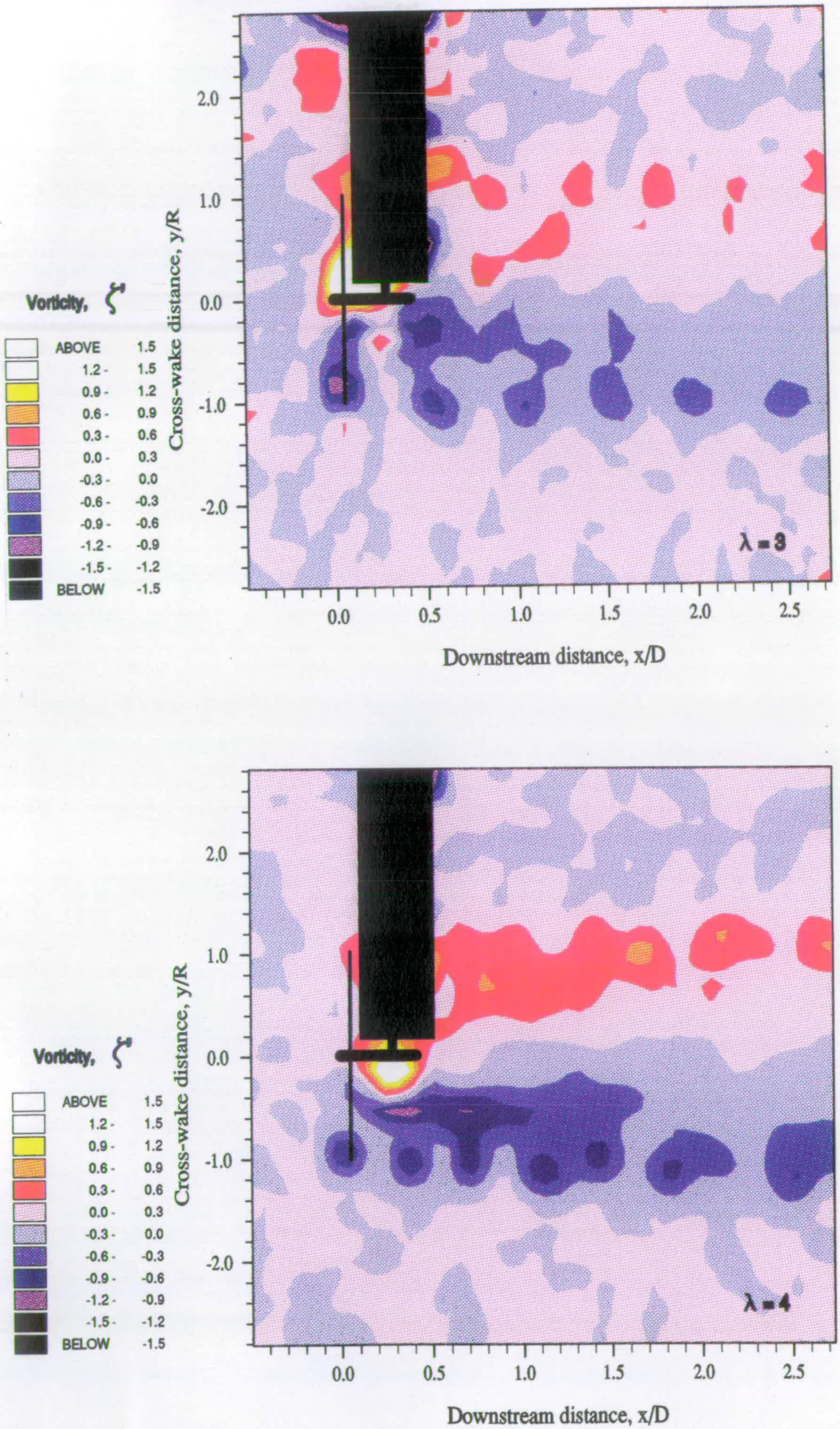


Figure 5.1.2(i) PIV vorticity contour plot for the 2-blade rotor at $\lambda = 3$ (above) and $\lambda = 4$ (below).

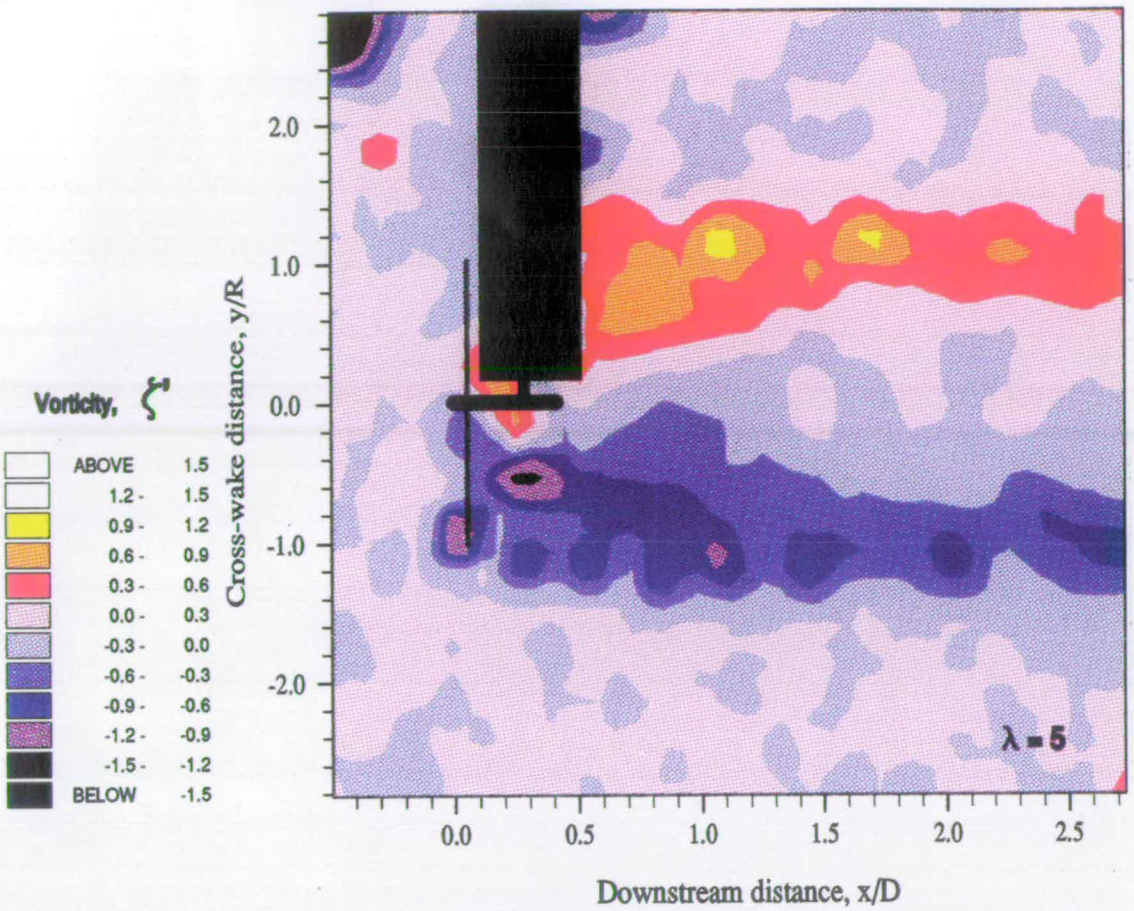


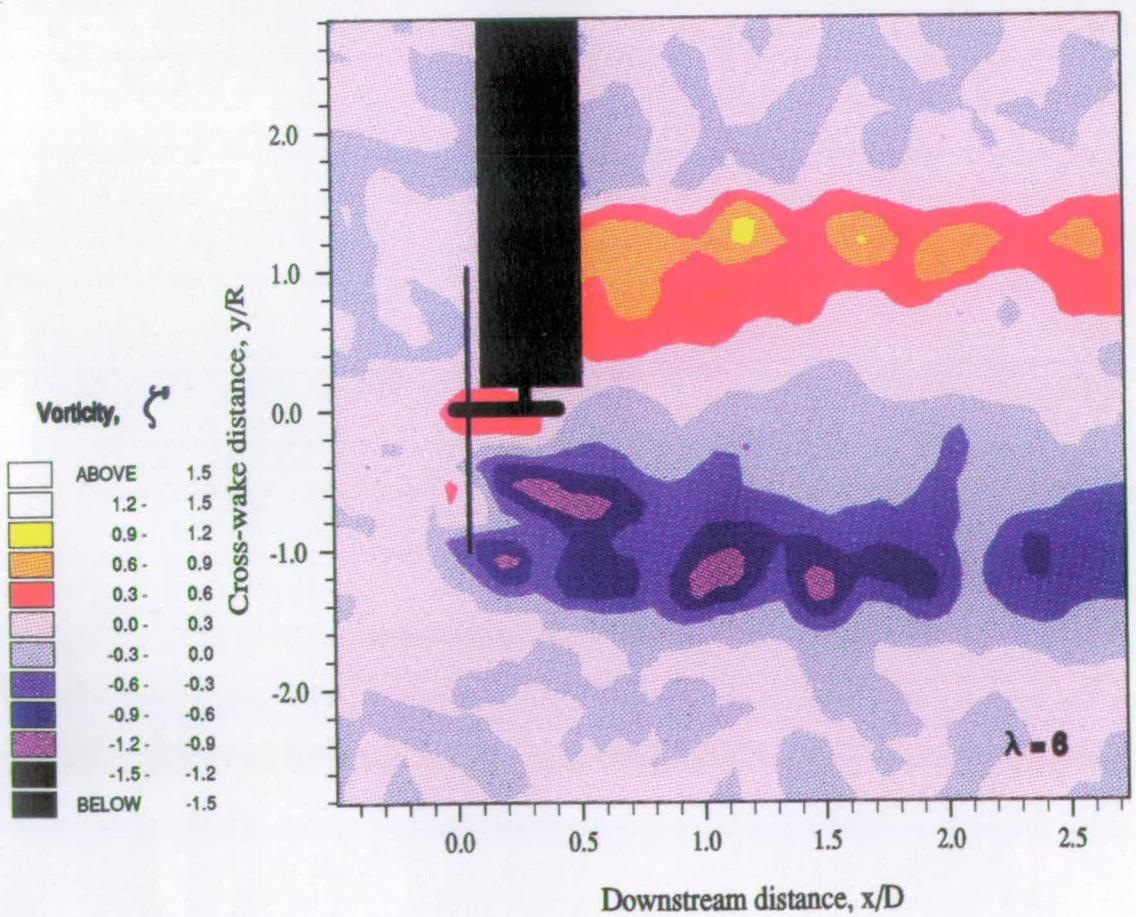


Figure 5.1.2(ii) PIV vorticity contour plot for the 2-blade rotor at $\lambda = 5$ (above) and $\lambda = 6$ (below).

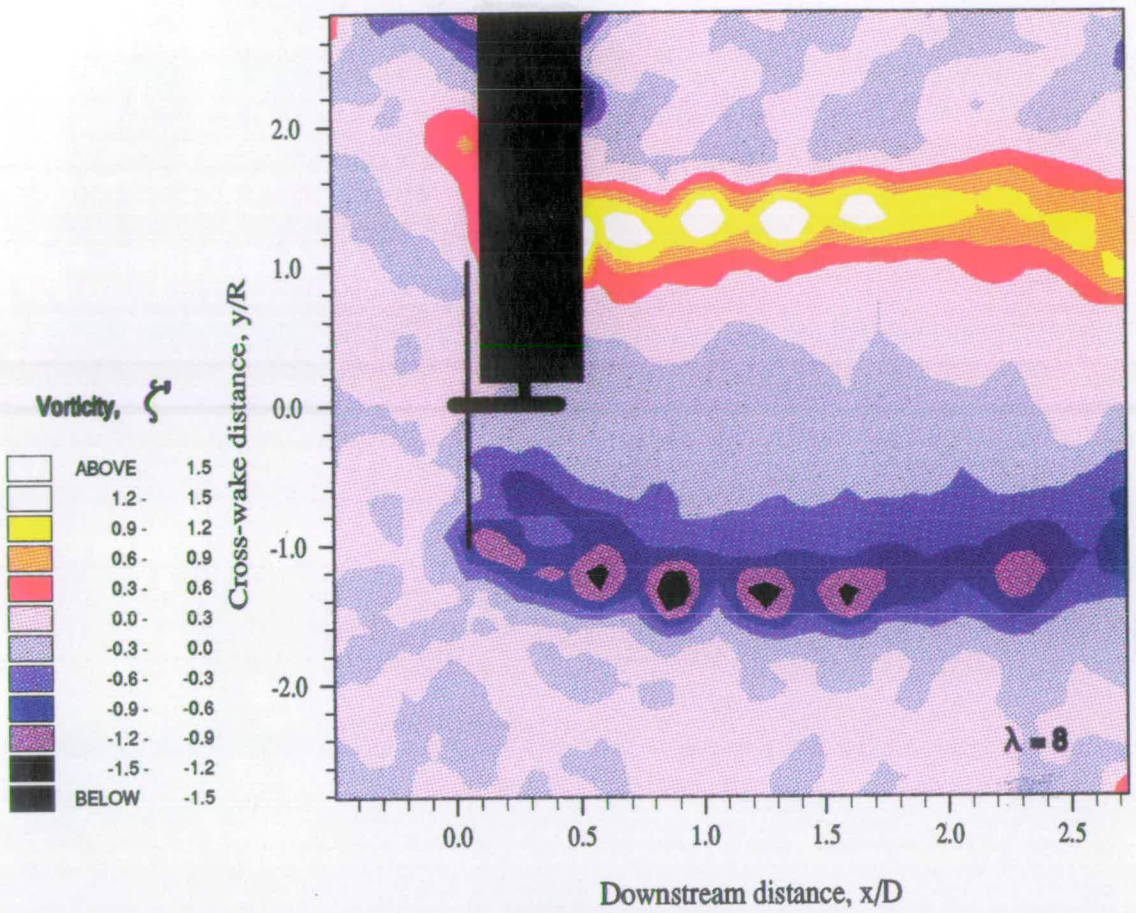


Figure 5.1.2(iii) PIV vorticity contour plot for the 2-blade rotor at $\lambda = 8$.

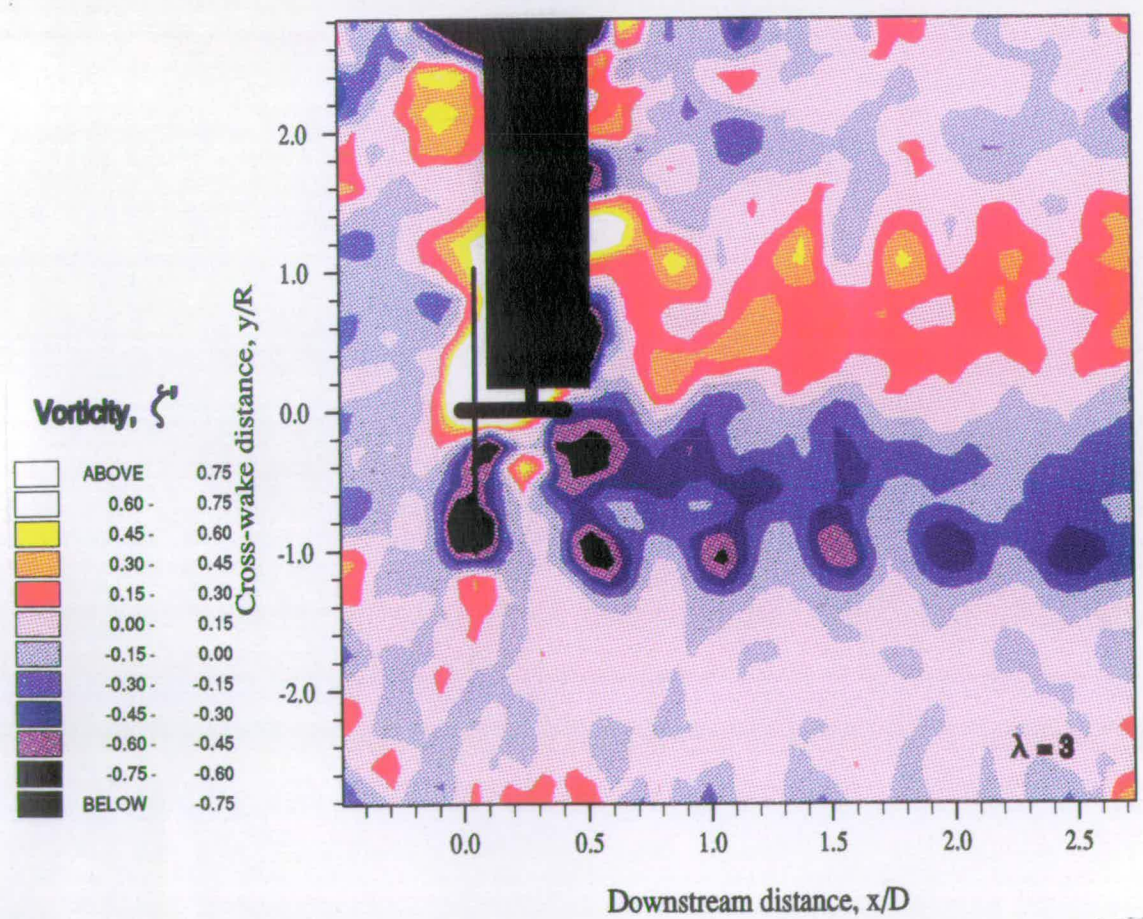


Figure 5.1.2(iv) PIV vorticity contour plot for the 2-blade rotor at $\lambda = 3$, with alternative contrast setting.

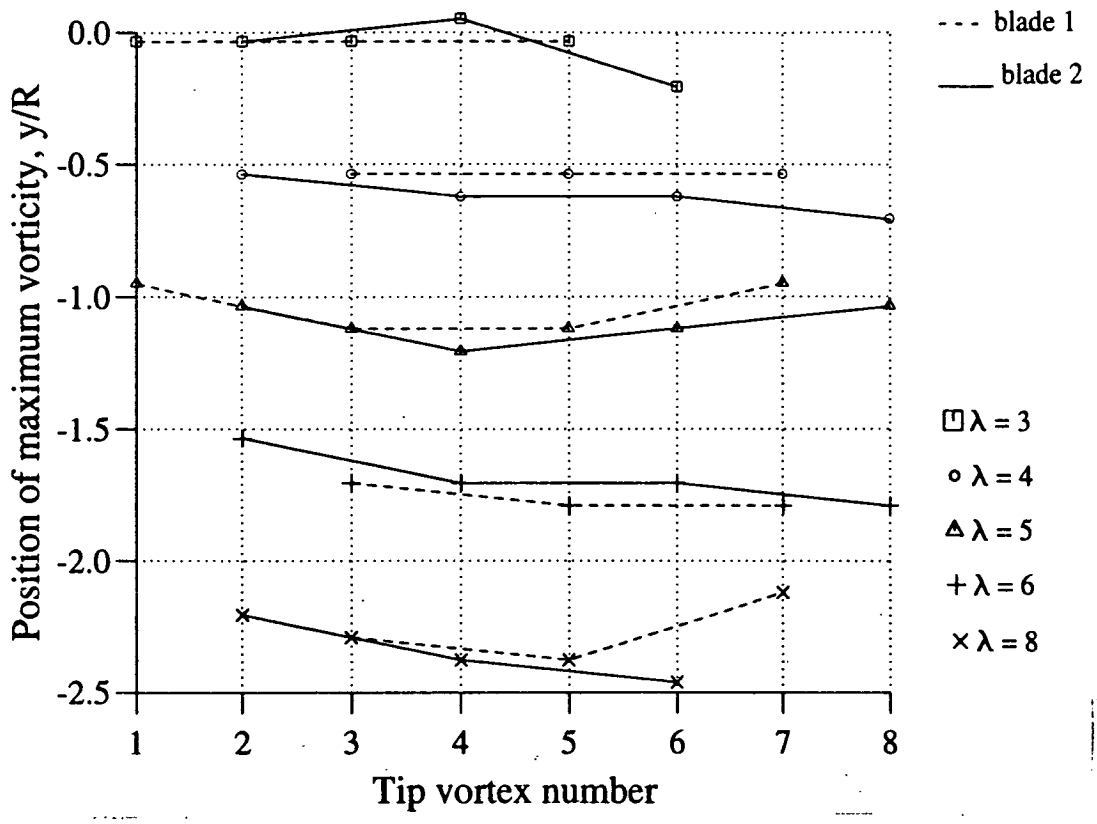


Figure 5.1.2(v) Cross-wake locations of the tip vortices in the lower wake of the PIV images. Each blade of the 2-blade rotor is treated separately.

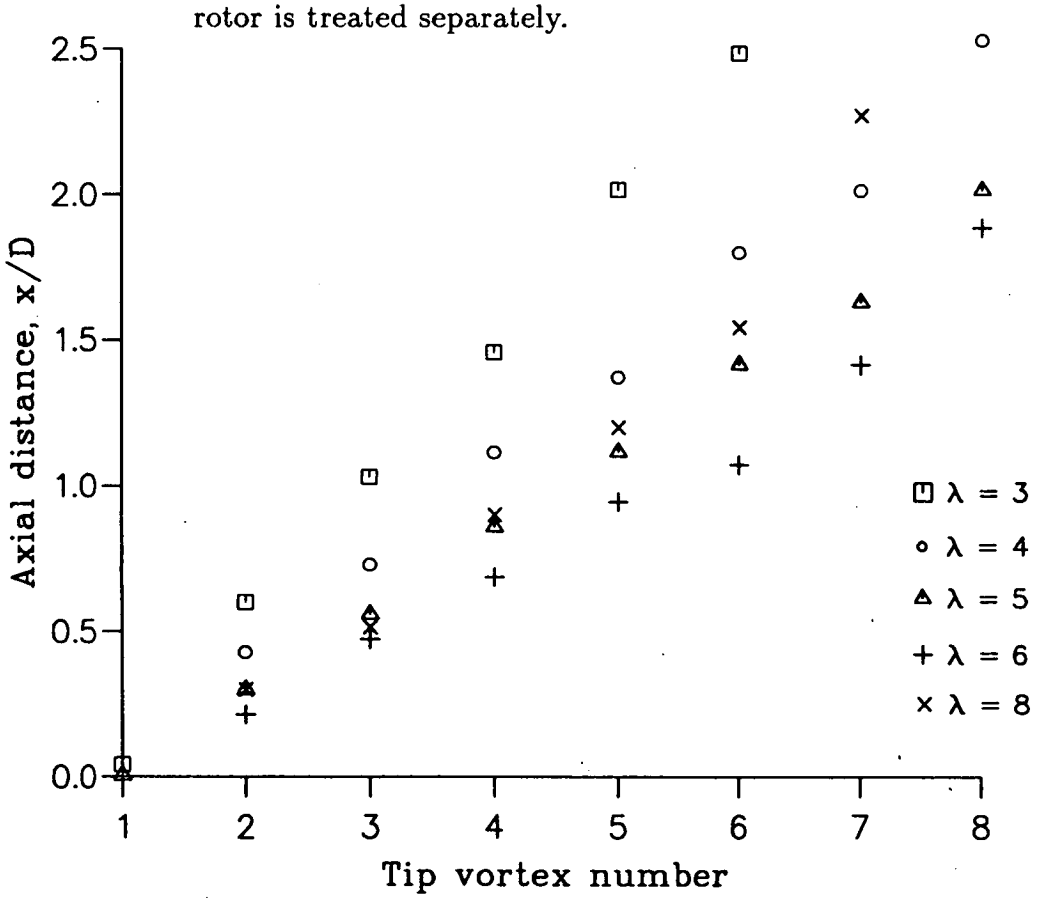


Figure 5.1.2(vi) Axial distance of the tip vortices, downstream of the 2-blade rotor, in the lower wake of the PIV images.

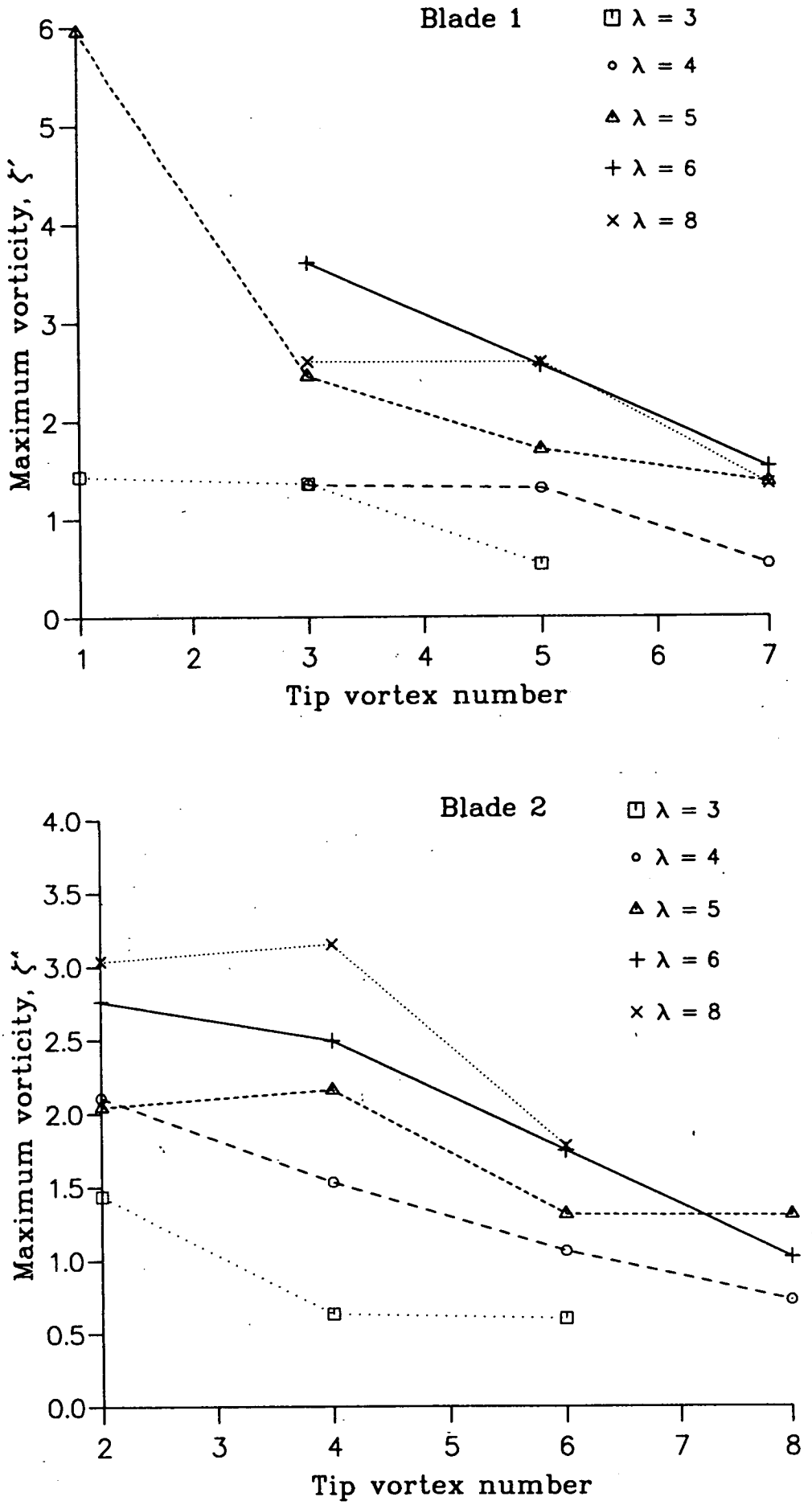


Figure 5.1.2(vii) Strength of the tip vortices in the lower wake of the PIV images for blade 1 (above) and blade 2 (below) of the 2-blade rotor.

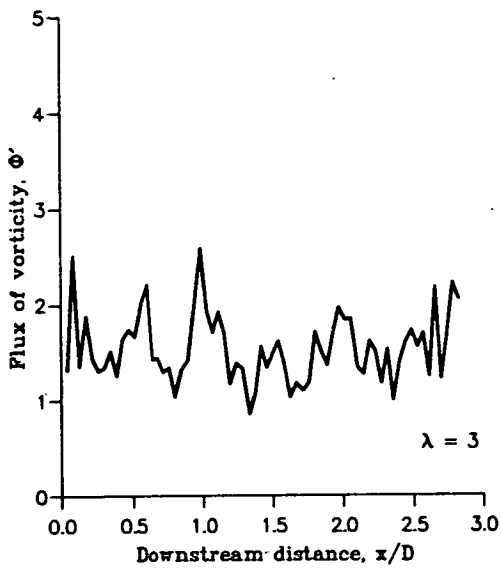


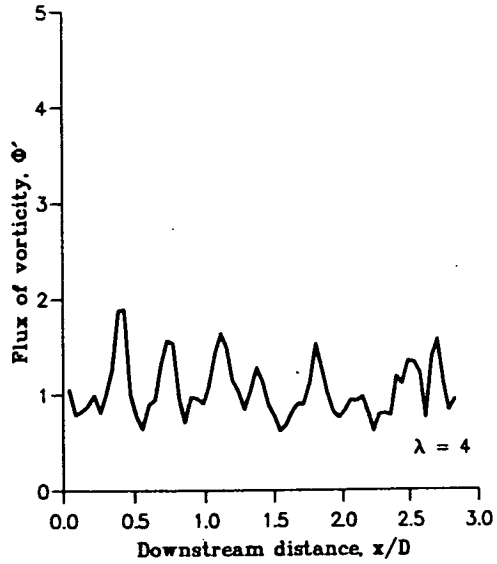


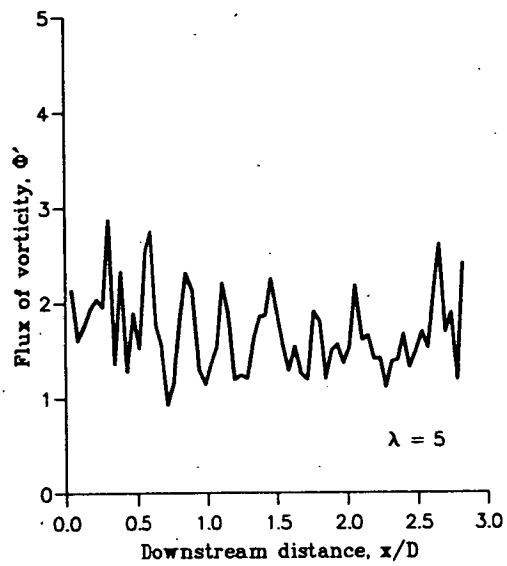


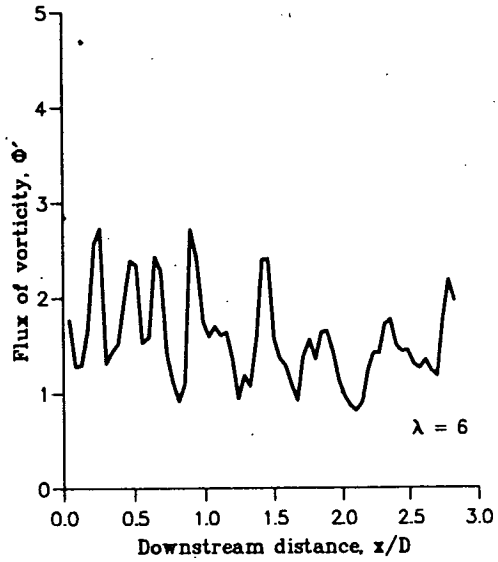


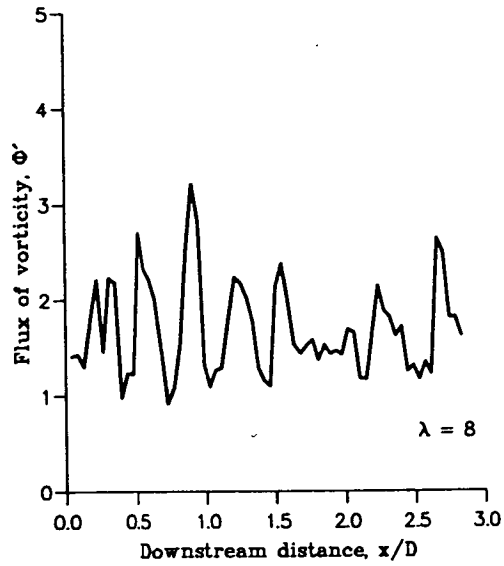


Figure 5.1.2(viii) Flux of vorticity in the wake of the 2-blade rotor. The separate graphs display results for different values of tip speed ratio.

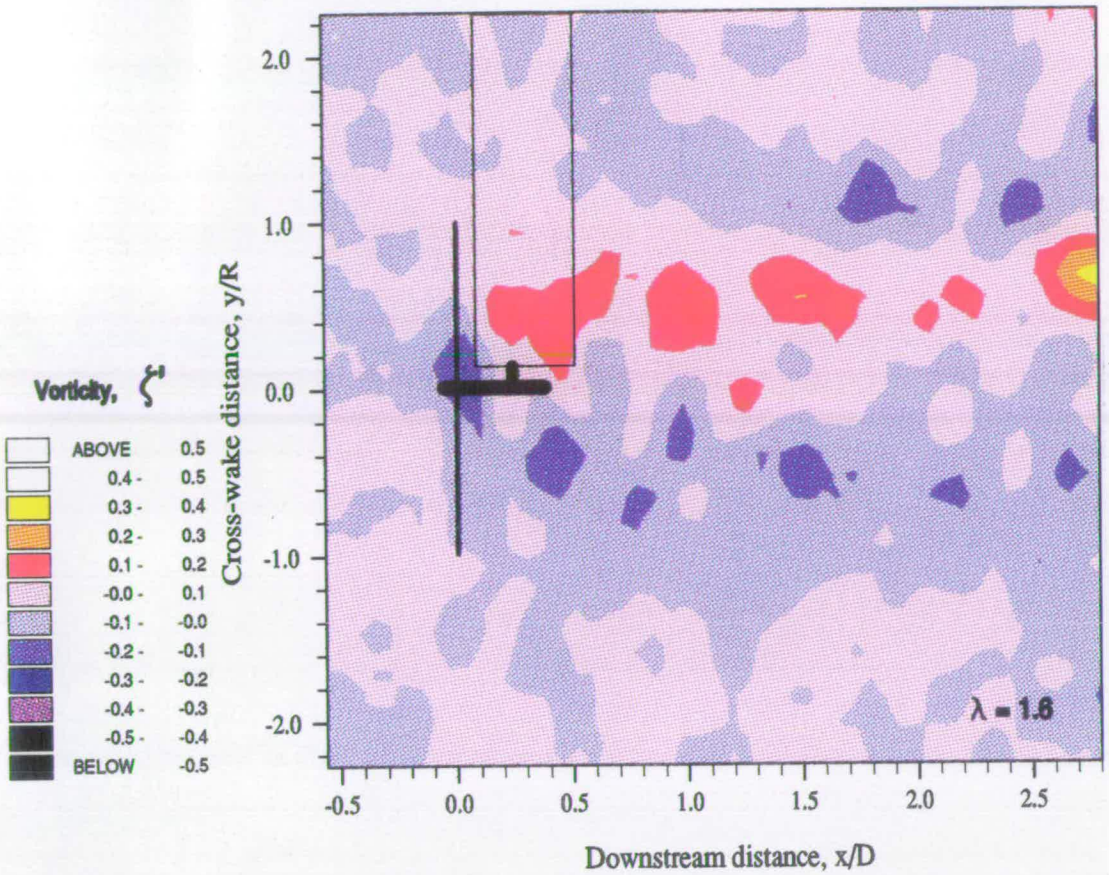


Figure 5.1.3(i) PIV vorticity contour plot for the 3-blade rotor at $\lambda = 1.6$.

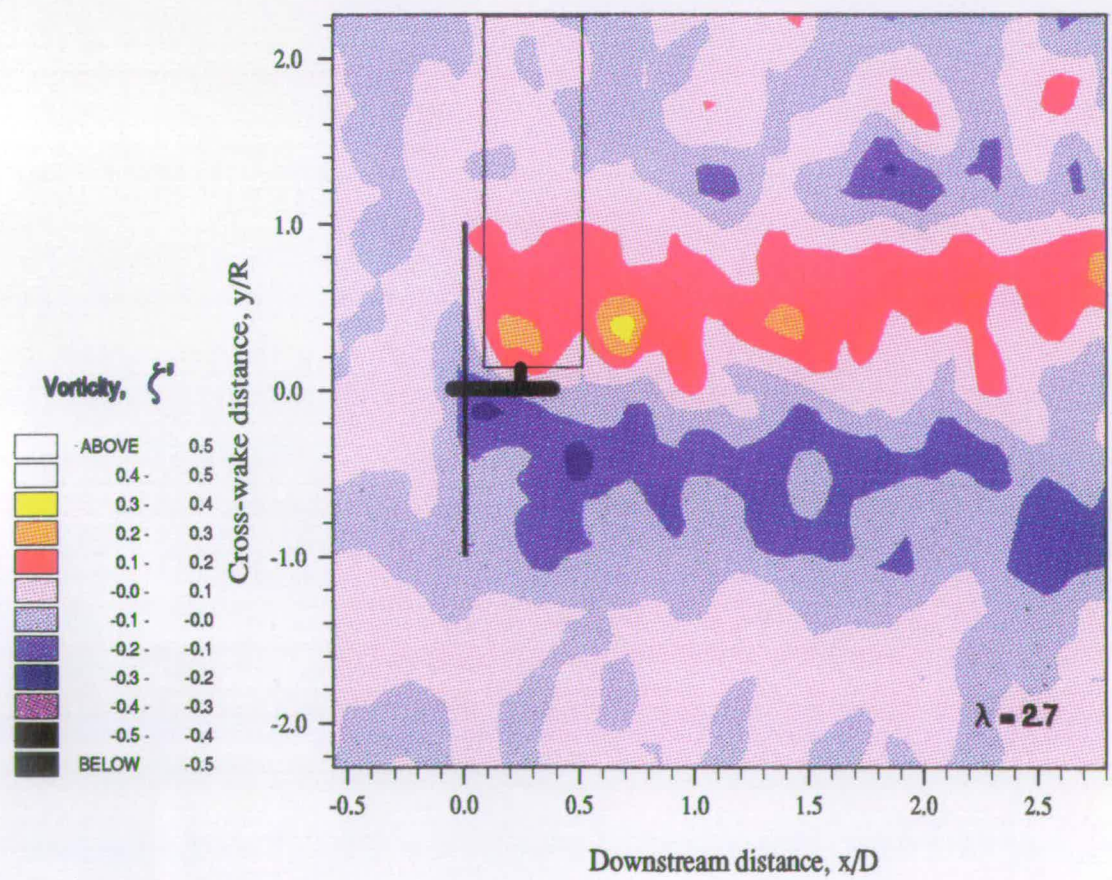


Figure 5.1.3(ii) PIV vorticity contour plot for the 3-blade rotor at $\lambda = 2.7$.

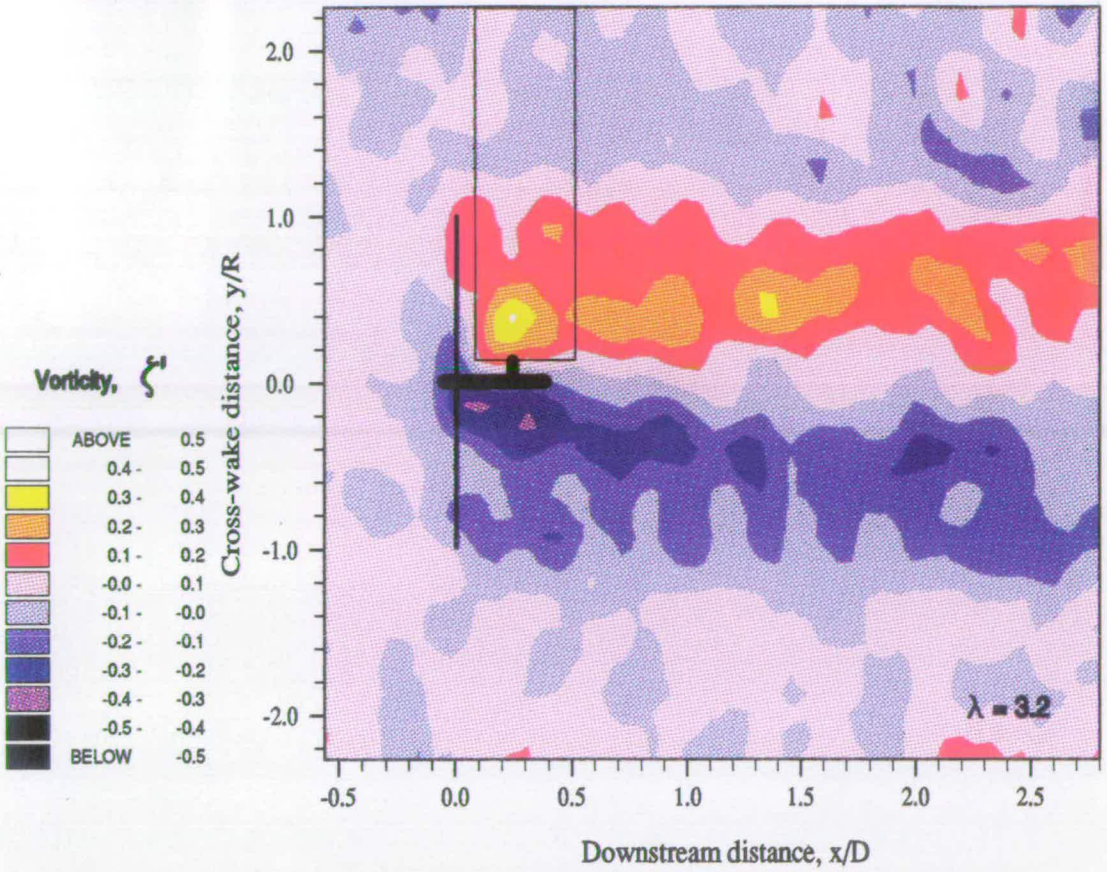


Figure 5.1.3(iii) PIV vorticity contour plot for the 3-blade rotor at $\lambda = 3.2$.

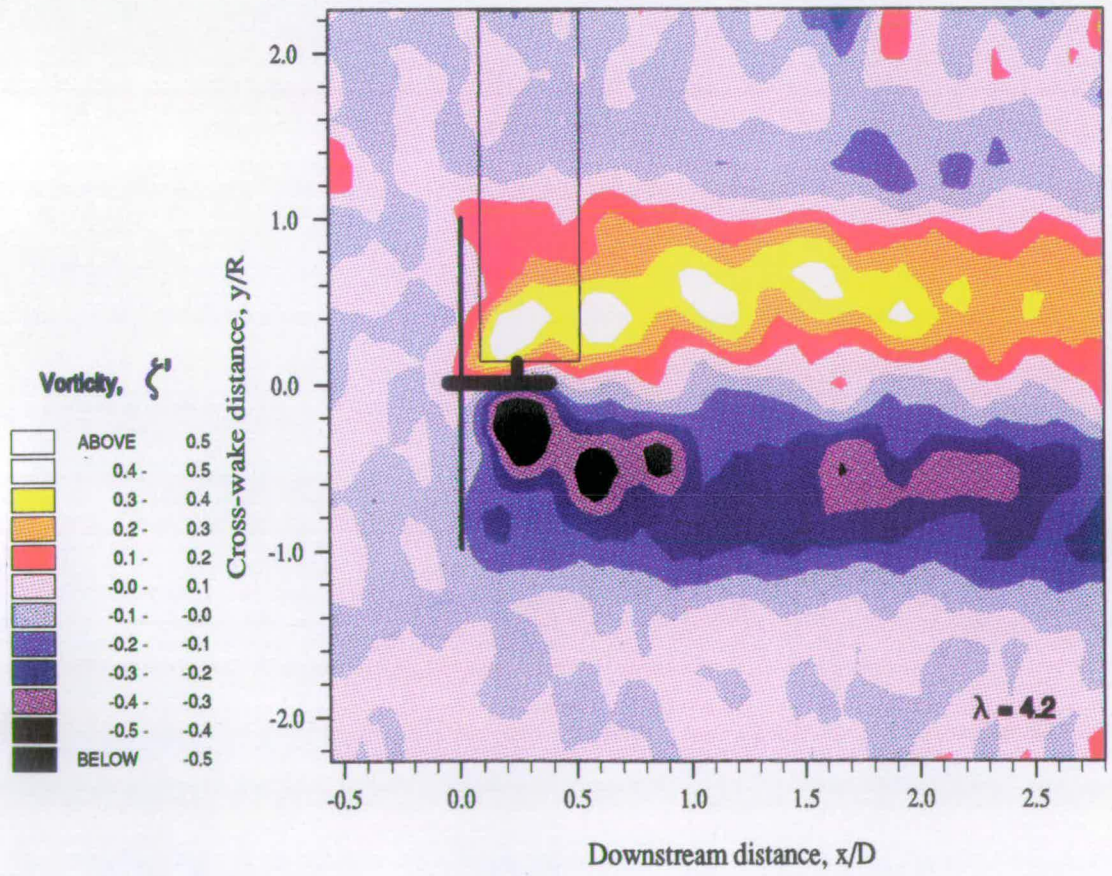


Figure 5.1.3(iv) PIV vorticity contour plot for the 3-blade rotor at $\lambda = 4.2$.

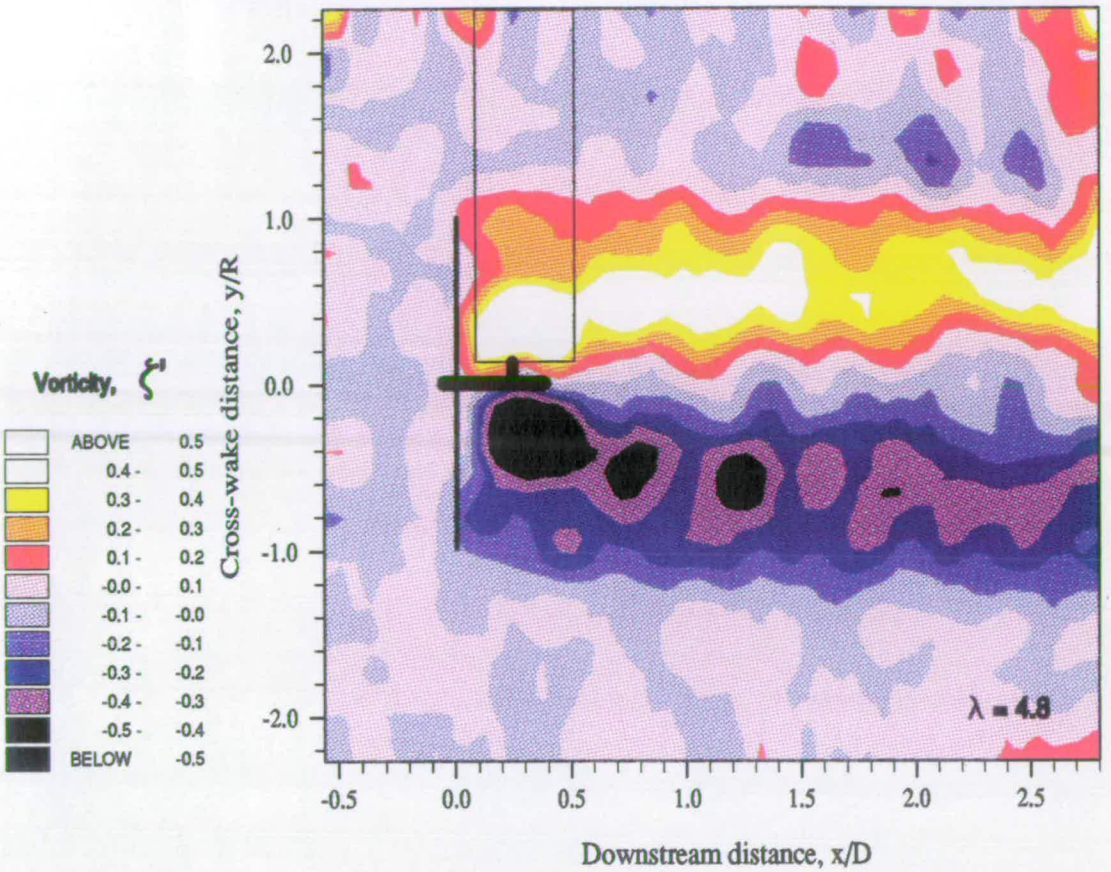


Figure 5.1.3(v) PIV vorticity contour plot for the 3-blade rotor at $\lambda = 4.8$.

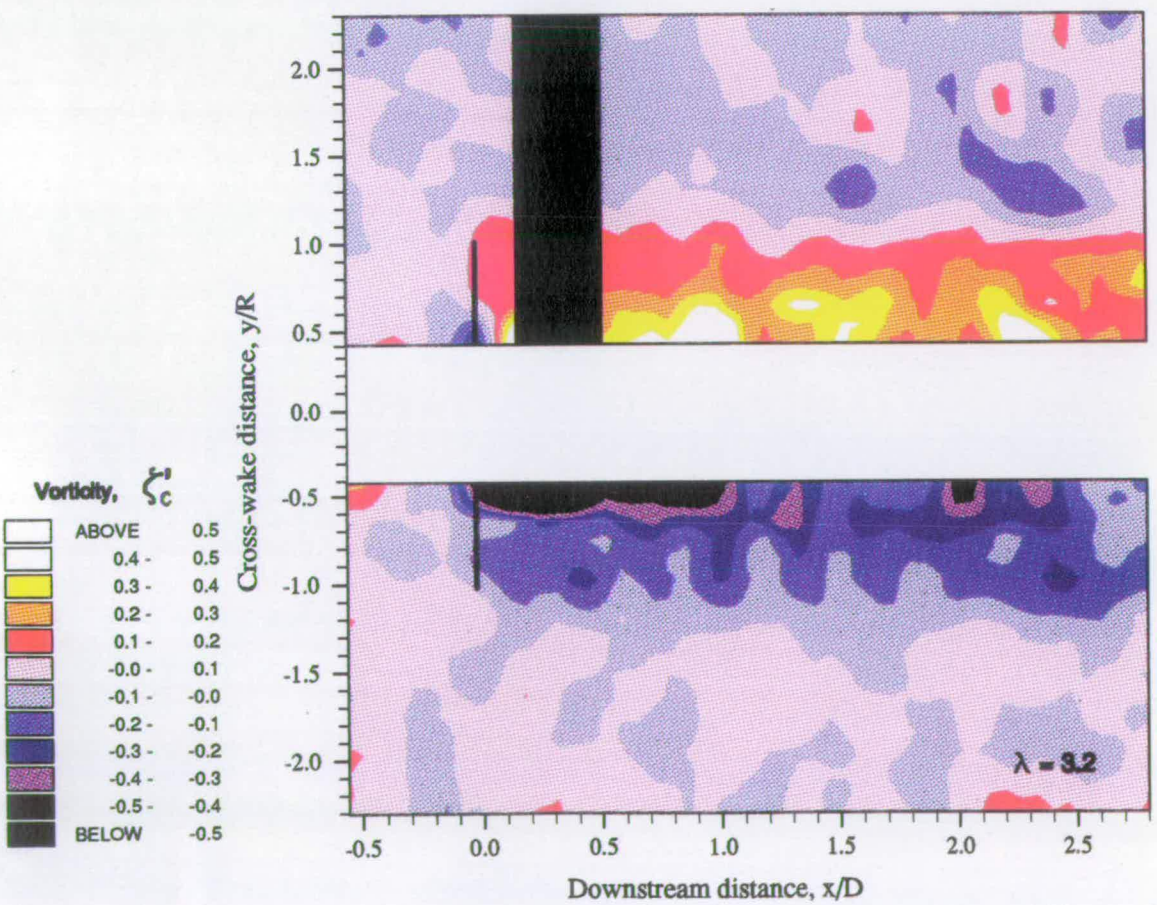


Figure 5.1.3(vi) PIV vorticity contour plot for the 3-blade rotor at $\lambda = 3.2$, corrected for the offset factor in the 3-blade PIV measurements.

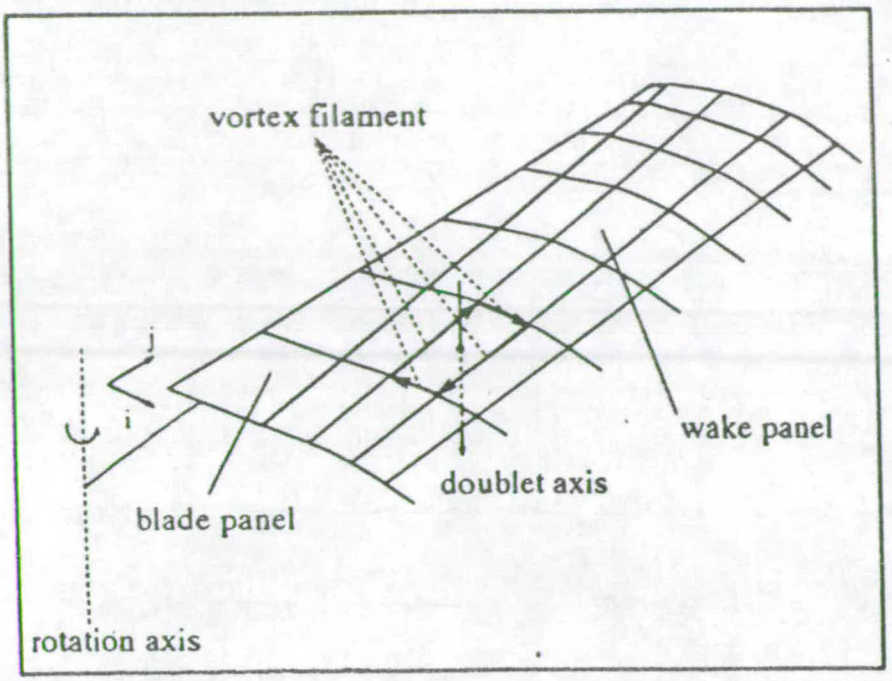


Figure 5.2.1(i) Discretisation of the blade and wake in the ROVLM vortex-wake code.

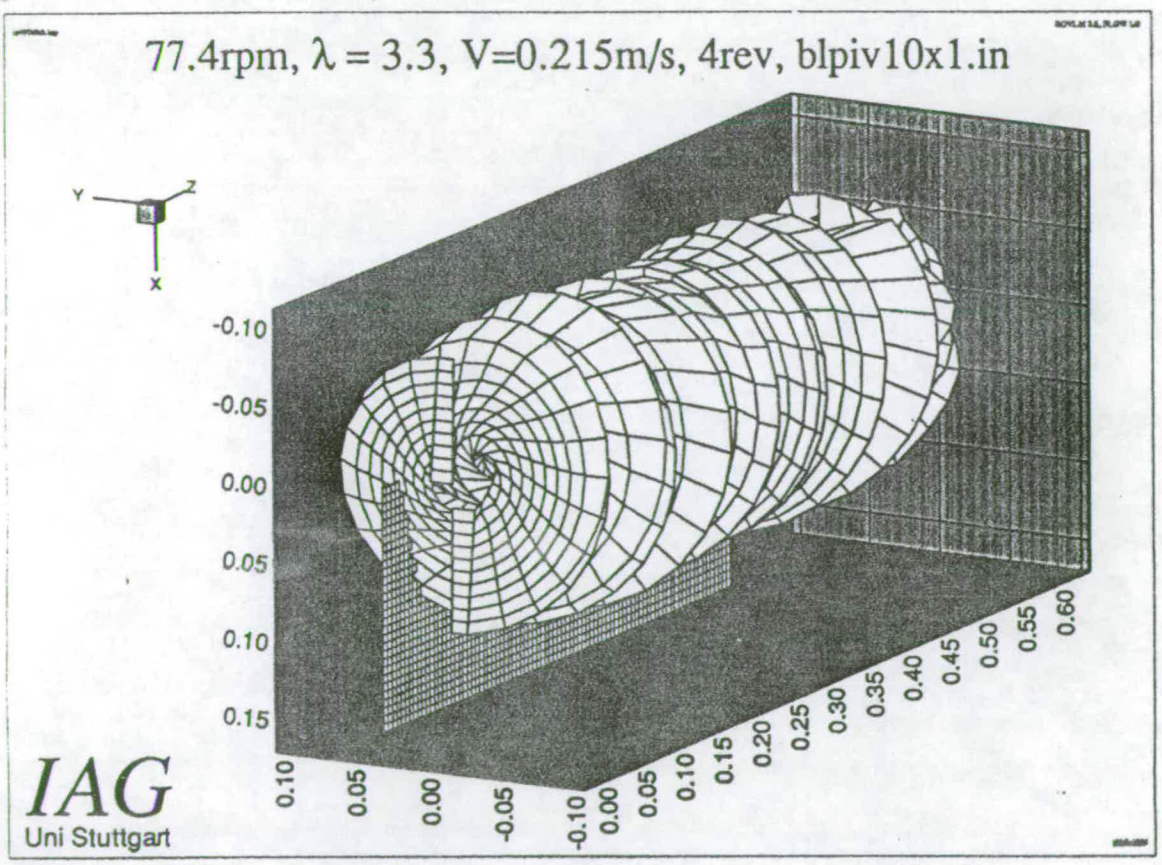


Figure 5.2.1(ii) A typical simulation of the 2-blade PIV experiments by the ROVLM code.

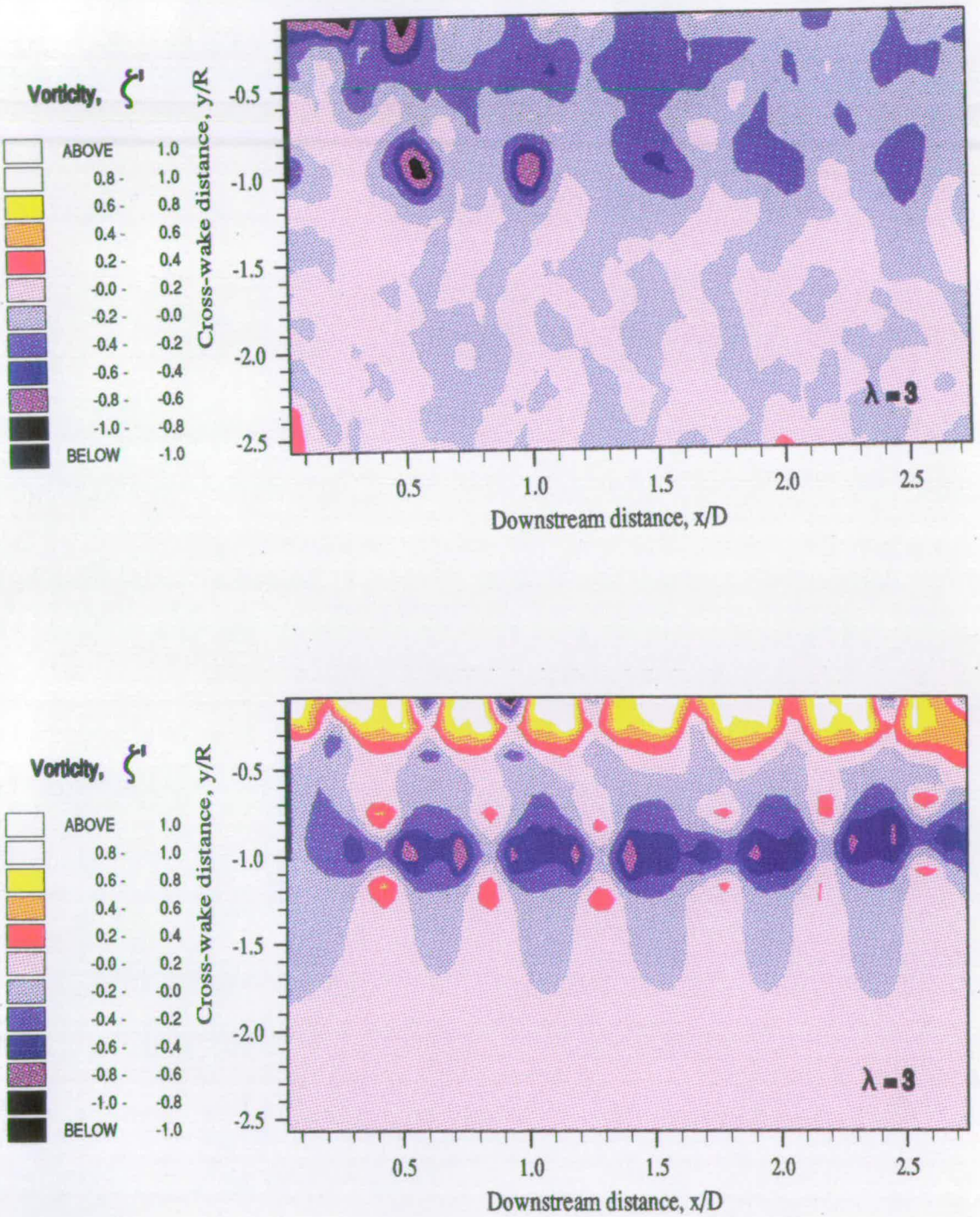


Figure 5.2.2(i) Comparison of PIV vorticity contour plot of the lower wake at $\lambda = 3$ (above) with corresponding ROVLM calculation (below).

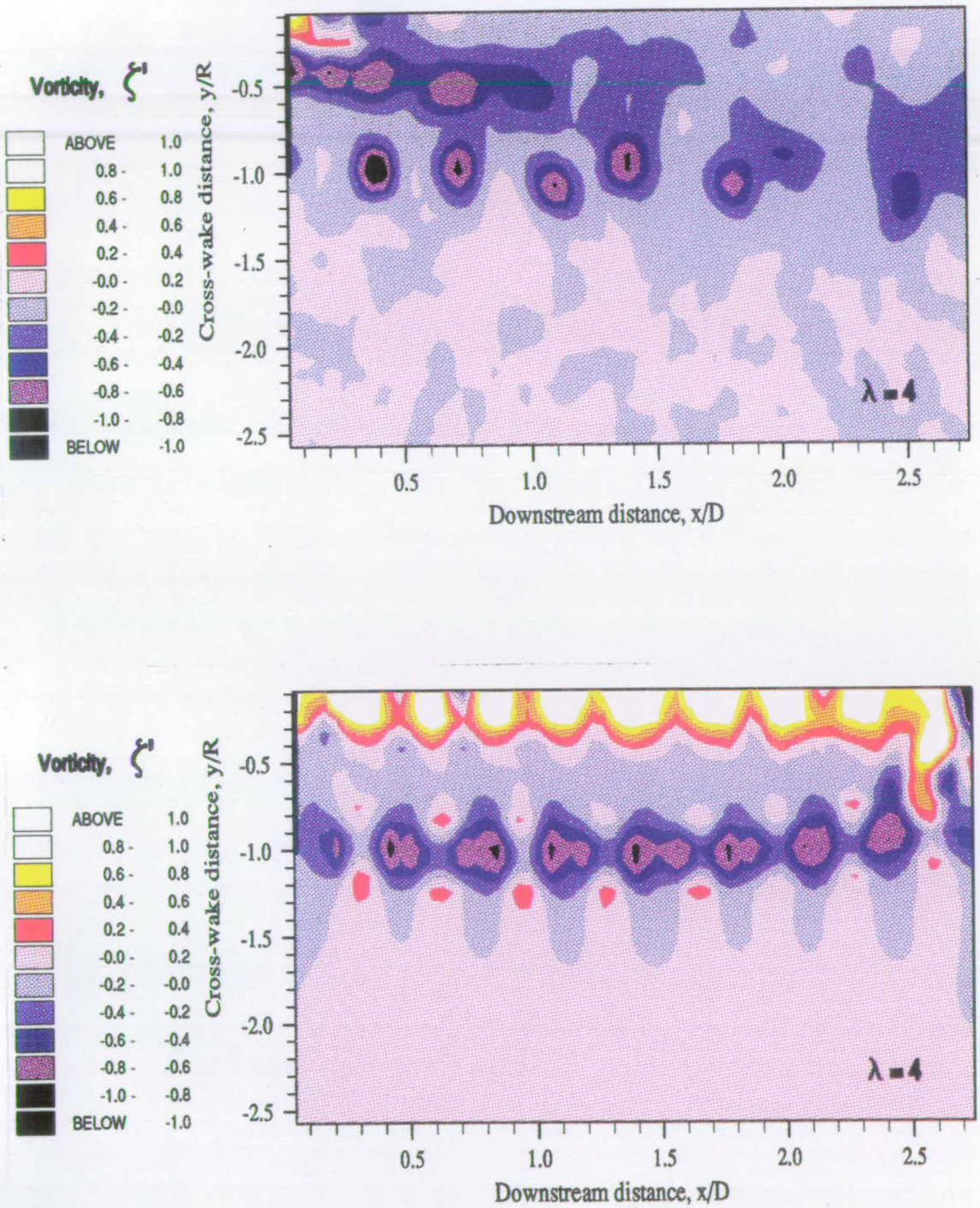


Figure 5.2.2(ii) Comparison of PIV vorticity contour plot of the lower wake at $\lambda = 4$ (above) with corresponding ROVLM calculation (below).

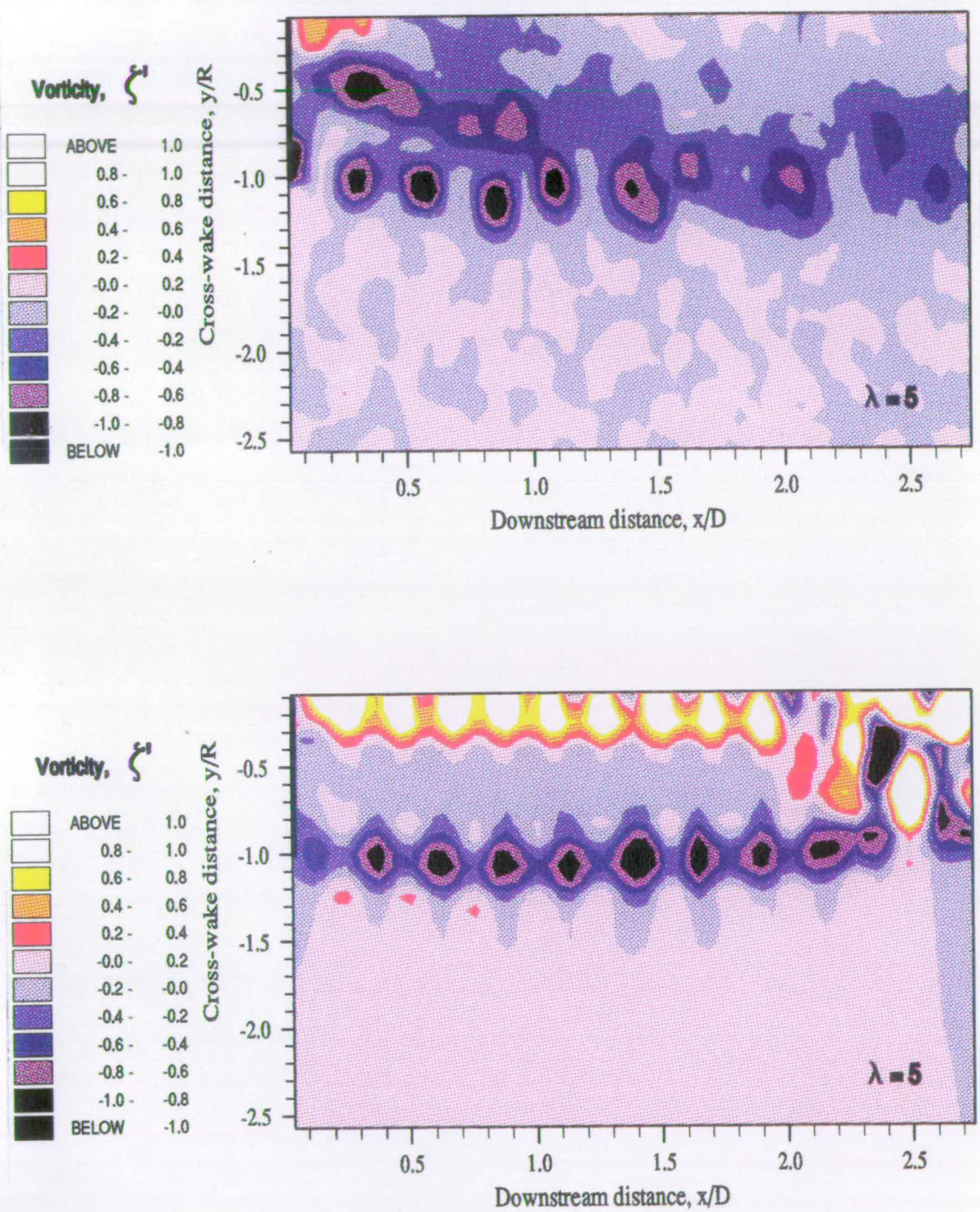


Figure 5.2.2(iii) Comparison of PIV vorticity contour plot of the lower wake at $\lambda = 5$ (above) with corresponding ROVLM calculation (below).

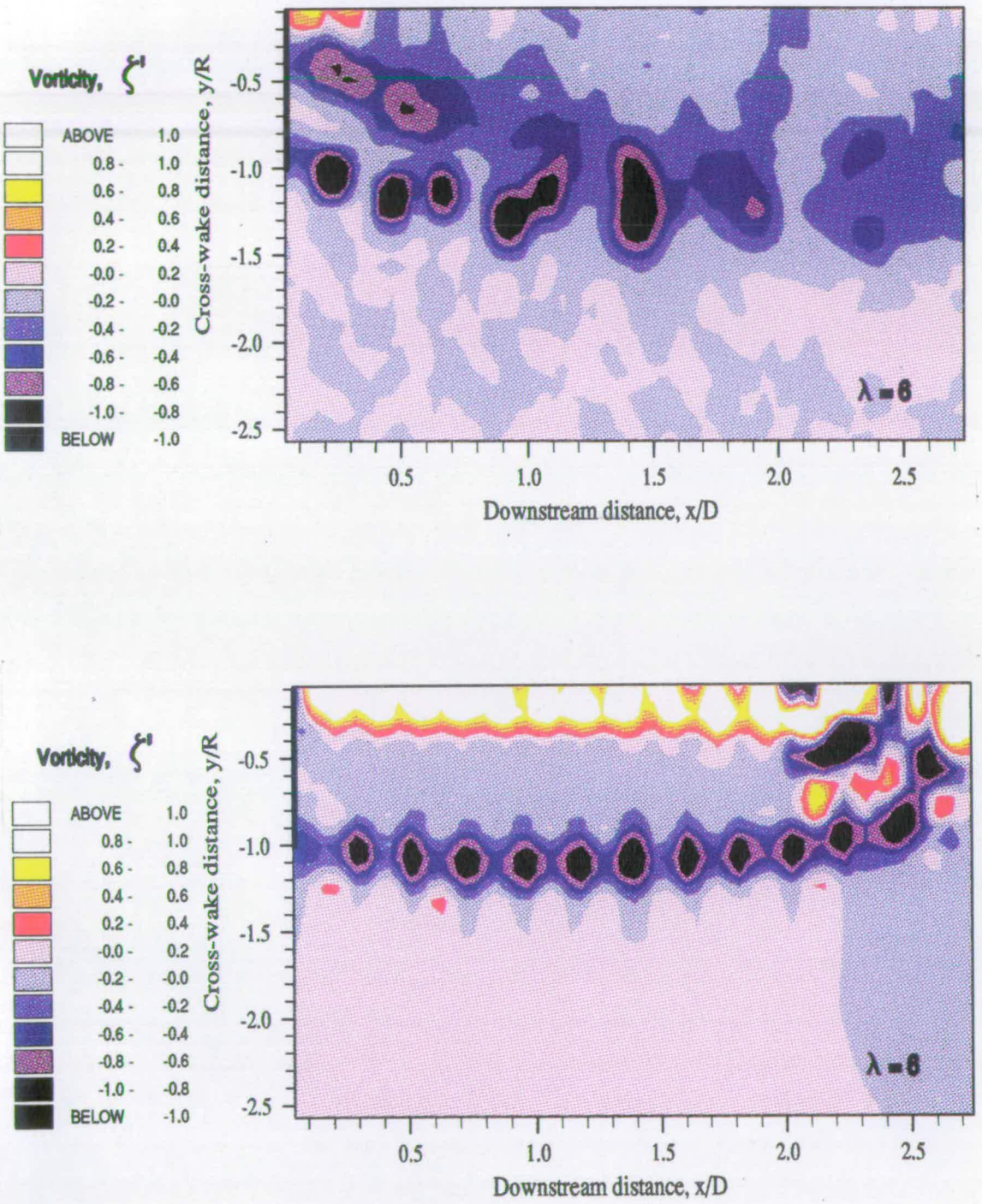


Figure 5.2.2(iv) Comparison of PIV vorticity contour plot of the lower wake at $\lambda = 6$ (above) with corresponding ROVLM calculation (below).

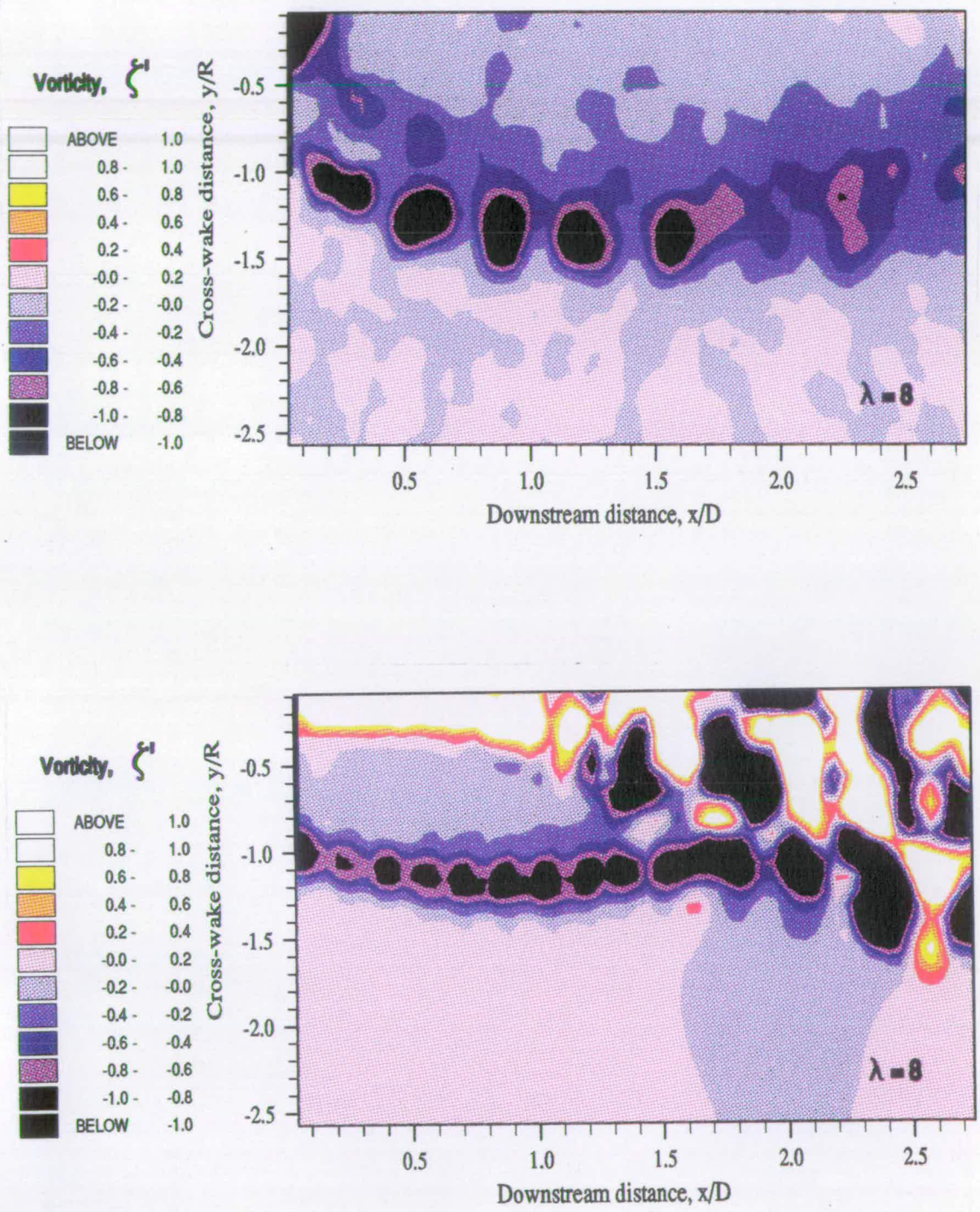


Figure 5.2.2(v) Comparison of PIV vorticity contour plot of the lower wake at $\lambda = 8$ (above) with corresponding ROVLM calculation (below)

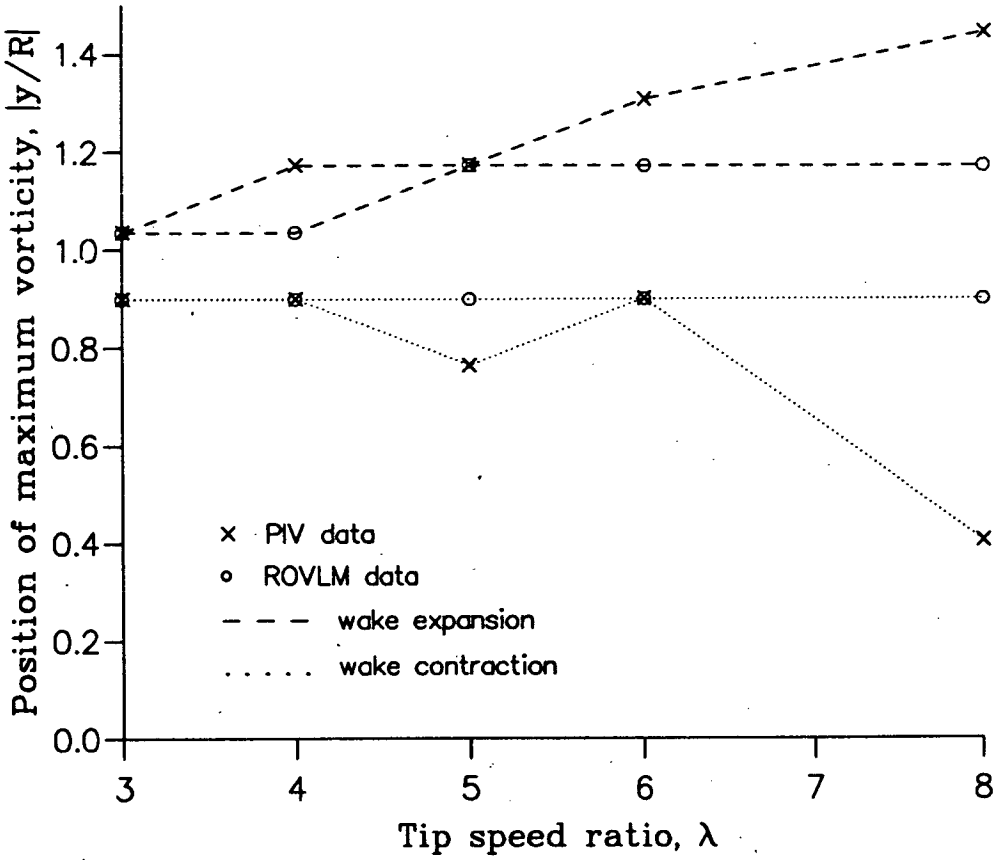


Figure 5.2.2(vi) Comparison of wake width between PIV measurement and ROVLM simulation.

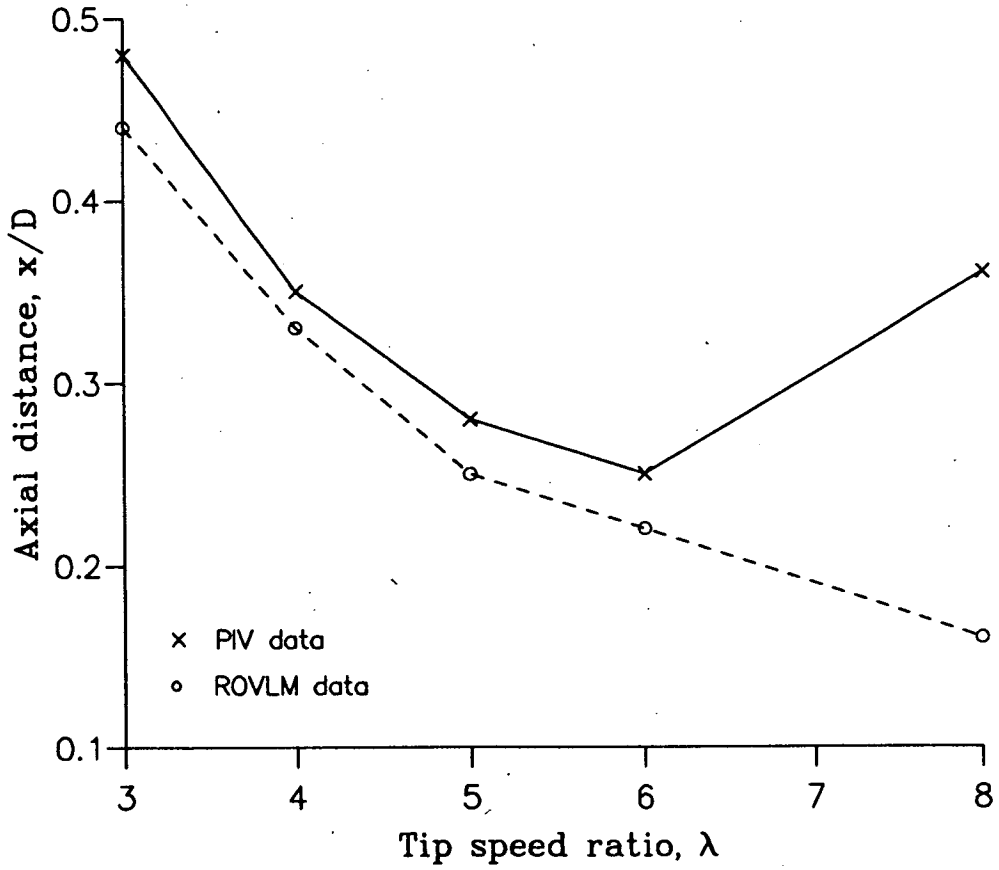


Figure 5.2.2(vii) Comparison of tip vortex spacing between PIV measurement and ROVLM simulation.

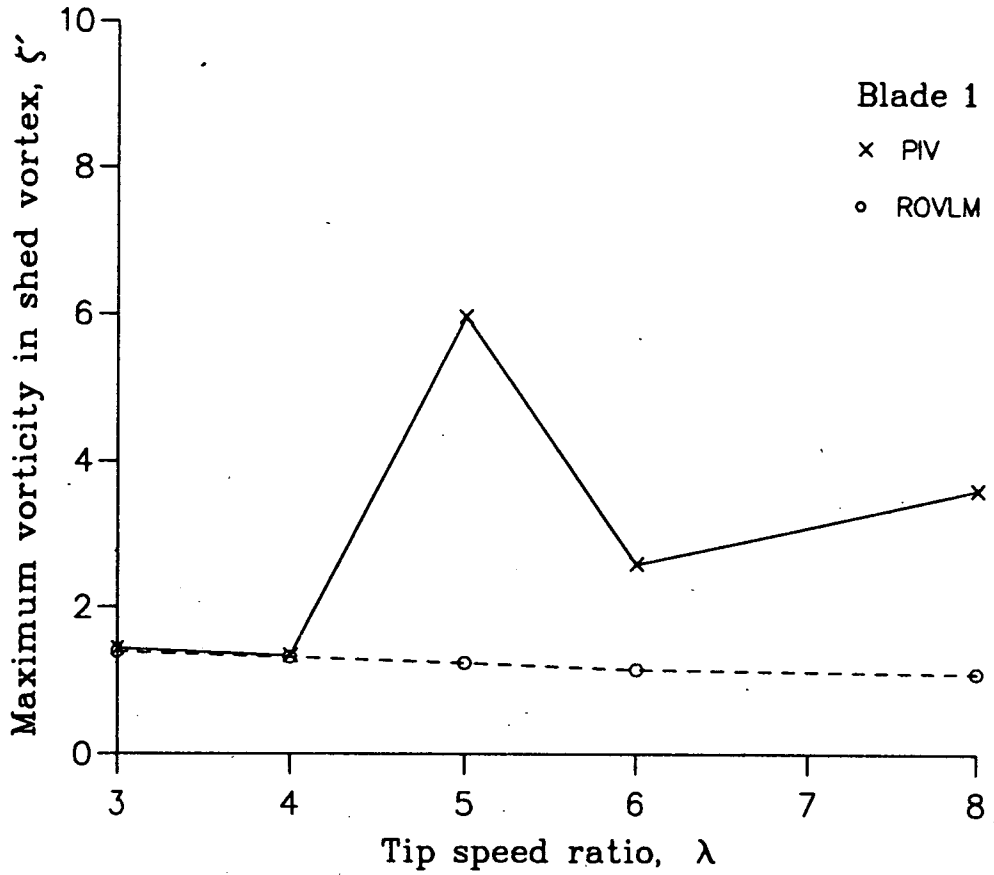


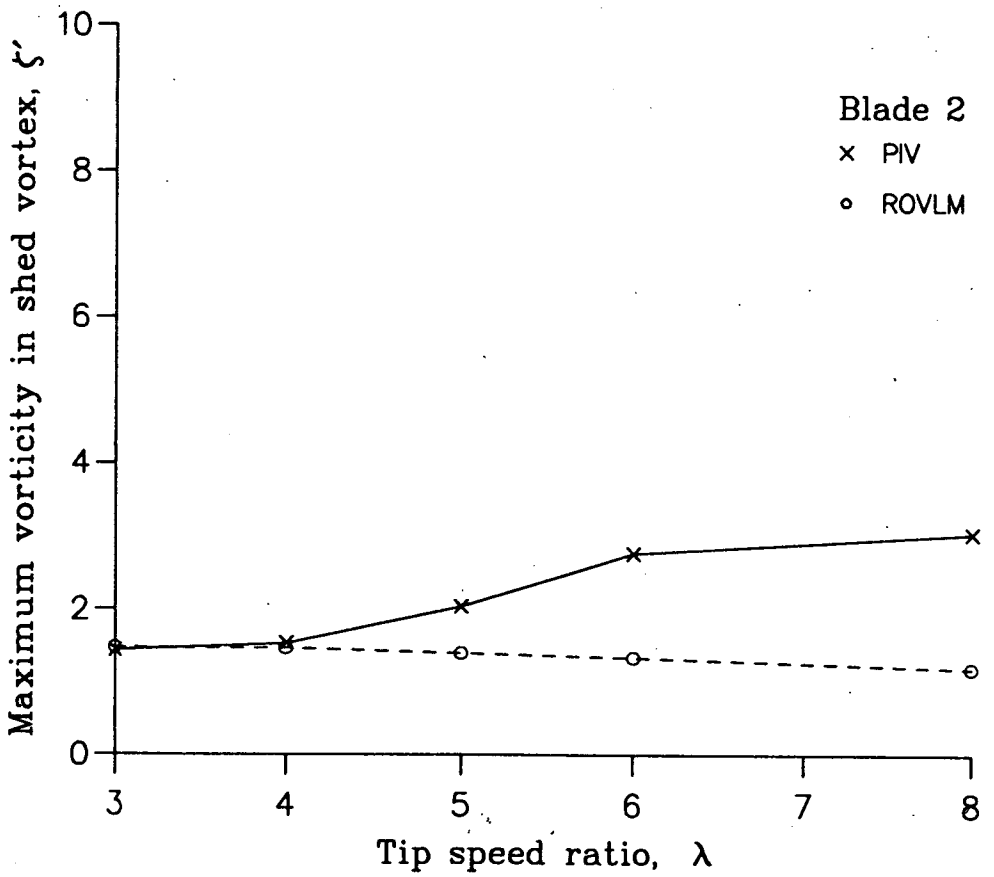


Figure 5.2.2(viii) Comparison of the strength of the vortex most recently shed from blade 1 (above) and from blade 2 (below) in the PIV experiments and ROVLM simulations.

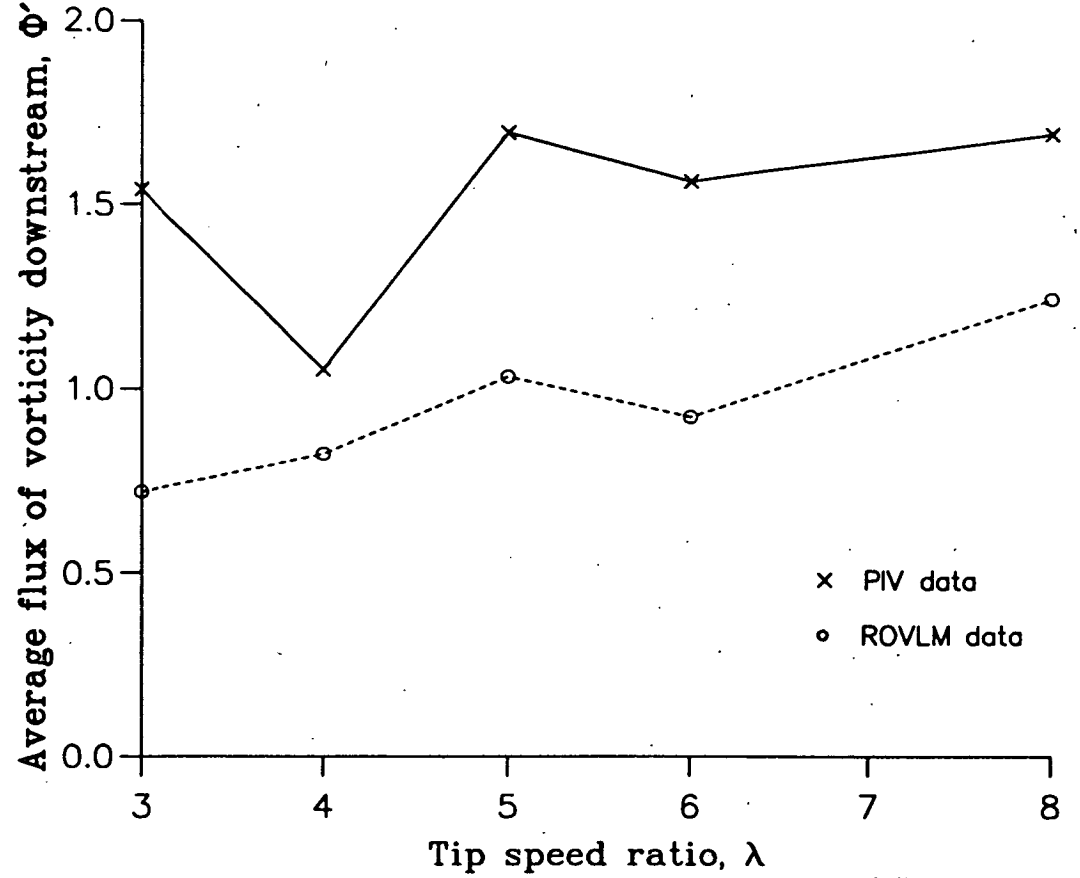


Figure 5.2.2(ix) Comparison of transport of vorticity between PIV measurement and ROVLM simulation.

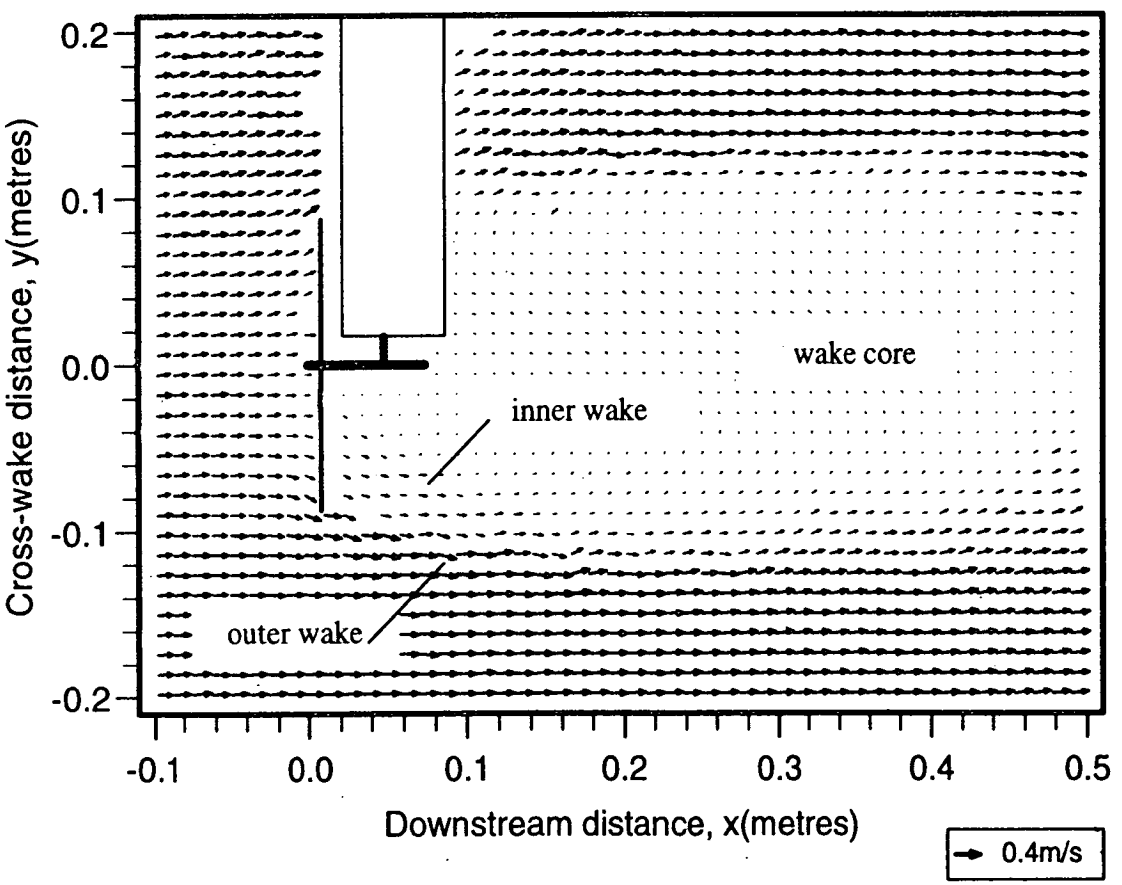


Figure 5.3 PIV velocity vector map of the 2-blade rotor at $\lambda = 8$, illustrating different regions of the wake.

# Chapter 6

## SCALE EFFECT, AND SOURCES OF ERROR

### Overview

In this chapter, an assessment of the PIV experiments is given in order to place the results of the PIV tests in perspective with results from other surveys. In particular, the similarities between the flow at model scale and flow around a full-scale wind turbine are discussed. The concept of scale effect is introduced and differentiated from errors in velocity measurement incurred using the PIV technique. An indication of the likely effects of scale on the wake flow are given, based on the expected changes in blade flow with Reynolds number.

## 6.1 Similarity with Full-scale Flow

The similarities between the flow around the model turbine in the water channel and flow at full-scale are classified in terms of geometric, dynamic and kinematic similarity.

### 6.1.1 Geometric Similarity

#### (a) The model rotor

A high level of geometrical similarity was sought for the 3-blade model replica of the WM19S machine from the Samos Island wind park. Despite the small scale, the model was accurately profiled with twist, chord and thickness distributions based on the manufacturers' original drawings. The total solidity of the rotor, calculated as the ratio of blade area to the swept area, for the 3-blade rotor is 7.8%. Data from a Vestas V20/100 machine was also used in the comparisons with the model replica, as it represented a convenient 3-blade stall-regulated machine. However, its somewhat lower solidity of 5.5% makes the comparison imperfect.

The 2-blade flat-plate blade has a solidity of 9.1%, but was not compared with any full-scale results. One aspect of the 2-blade model was its much higher local solidity at the inboard stations than the 3-blade model. For the inner 20% of the blades, the solidity of the 2-blade model is close to 50% while the 3-blade model has a solidity of around 30%. This may be attributed to the fact that the 2-blade model had no root cut-out.

#### (b) The flume boundaries

The influence of the side walls of the flume on the flow past the rotor is a potential source of error and is therefore investigated. Blockage in the channel results in an increment of speed at the edge of the boundary layer of the walls that is greater than would exist at the same distance from a turbine in the field. The peak effect opposite the model is called *solid* blockage, $\epsilon_{sb}$, and the maintained effect behind it it called *wake* blockage, $\epsilon_{wb}$. A similar procedure to that of wind tunnel blockage corrections can be followed. The method of images is used to simulate the effect of solid boundaries in the flow[79]. For a solid body in a closed rectangular section, the body may be mathematically represented by a source-sink system.

The channel boundaries may be represented by an image system consisting of a doubly-infinite system of source-sink combinations. The images are spaced a channel-height apart vertically and a channel-width apart horizontally.

In order to estimate the blockage for the model turbine, the case of a sphere with the same radius as the rotor (87.5mm) is considered. Assuming the free surface acts as a solid boundary, the body is contained within a test section of $C$= 400mm x 750mm. Assuming irrotational flow, each source doublet simulating a sphere in the image system acts at the body with velocity potential

$$\phi = -\frac{1}{2}Ua^2\frac{\cos\theta}{r^2} \tag{6.1}$$

where $(r, \theta)$ are the polar co-ordinates of the dipoles in the image system. The incremental velocity induced at the sphere is then given by

$$\epsilon_{wb} = \frac{\Delta V}{V_u} = \sum \frac{a^3 \sin\theta}{r^3} \tag{6.2}$$

where $V_u$ is the uncorrected velocity. Noting the fast convergence of the series, due to $\frac{1}{r^3}$ terms, an estimate of $\epsilon_{wb} = 3\%$ is provided by using the nearest neighbours to the body in the image system.

The Thom[95] equation for solid blocking for a 3-dimensional body is

$$\epsilon_{sb} = \frac{Model\ volume}{C^{\frac{3}{2}}} \tag{6.3}$$

In the case of the sphere this gives a value of $\epsilon_{sb} = 1.7\%$. The total blockage $\epsilon_t = \epsilon_{wb} + \epsilon_{sb}$ is then of the order of 5% but the model turbine rotor would be less of an obstruction to the current in the water channel and $\epsilon_t$ would be expected to be smaller. Pope and Harper[79] suggest using

$$\epsilon_t = \frac{1}{4}\frac{Model\ frontal\ area}{Test\ section\ area} \tag{6.4}$$

At high tip speed ratios, the rotor can be replaced by a disc of the same radius. Then the total blockage correction, taking into account the tower shroud, is

$$\epsilon_t = \epsilon_{disc} + \epsilon_{shroud} \tag{6.5}$$

This is calculated to be 2.5%, and can be regarded as negligible.

### 6.1.2 Dynamic Similarity

#### (a) Reynolds number

The condition of dynamic similarity is achieved by reproducing a number of dimensionless quantities that describe the flow. The most important of these, in low-speed experiments where the Mach number is much less than unity, is the Reynolds number (see Section 3.2.1).

At a point on the blade located at 70% span, the blade Reynolds numbers of the full-scale WM19S machine and the 3-blade model replica may be compared. Over the tip speed ratio range $\lambda = 1.6-4.8$, the Reynolds numbers fall in the range

$$\begin{aligned} Re_{machine} &= 2 \times 10^6 - 2.5 \times 10^6 \\ Re_{model} &= 2.6 \times 10^3 - 6 \times 10^3 \end{aligned}$$

Closer agreement in terms of Reynolds number exists between the wind tunnel tests of Green[52] and the 2-blade PIV experiments. At $\lambda = 4$,

$$\begin{aligned} Re_{tunnel} &= 2.2 \times 10^4 \\ Re_{model} &= 8.2 \times 10^3 \end{aligned}$$

#### (b) Scale effect

The departure from complete similarity due to the variation in the non-dimensional coefficients with Reynolds number, is known as scale effect. From above, the Reynolds number of the PIV tests is 3 orders of magnitude less than those typical of full-scale flow. As pointed out by Galbraith *et al.*[41], care must be taken when comparing the performance of a model wind turbine to that of a full-scale machine. The boundary-layer flow over wind turbine blades is heavily dependent on Reynolds number which dictates the phenomena of transition to turbulence, separation and reattachment at the blade.

At the low Reynolds number conditions of the PIV tests, extensive areas of laminar flow may occur at the model. Under these conditions, it would be expected to find laminar separation of the boundary layer occuring close to the leading edge of the blade. This may re-attach as a turbulent boundary layer which moves towards the trailing edge of the blade, as angle of incidence is increased, until the section of blade is stalled. For the typical full-scale machine, no laminar separation occurs before the boundary layer becomes turbulent. Separation of the turbulent boundary layer then takes places at the trailing edge and, as incidence increases, progresses toward the leading edge. The two cases lead to very different behaviour in the lift coefficient characteristics along the blade. Since it is the circulatory lift distribution, trailed behind the rotor, which forms the wake, it can be inferred that the wake geometry will be heavily dependent on Reynolds number.

The changes in blade boundary layer flow with Reynolds number, proposed in the literature[67, 41], may give some indication of the differences in wake structure expected between the model and full-scale flow. A turbulent boundary layer and delayed separation reduces the width of the separated wake. A laminar boundary layer and early separation across the body results in a broader wake[96]. At low Reynolds numbers, the viscous effects are relatively large, causing high drags. These could be significant factors contributing towards the large wake expansion and high velocity deficits found at model scale.

At large values of Reynolds number, $Re$, the boundary layer on a body of length $L$ has a thickness of order $LRe^{-\frac{1}{2}}$[23]. The ratio of the thickness of the boundary layer to the chord length on the model blades is greater than at full-scale by a factor of 30. This may be responsible for thicker helical vortex filaments shed from the trailing edge of the blade. This could explain the thick shear layers in the vorticity contour plots of Chapter 5. The spanwise proportion of the blade experiencing separated flow is increased at low Reynolds number. $(C_L, \alpha)$ curves for a typical airfoil[40] shows that at $Re < 10^5$, stall occurs for angles of attack, $\alpha < 10^o$, whereas at $Re > 10^6$, blades stall at $\alpha \approx 16^o$. This may explain the substantial areas in the wake of the model, close to the blade root, where large velocity gradients exist.

However, it must be pointed out that comparable data from full-scale wind turbines is extremely scarce and little is known about the relationship between Reynolds number and the near wake properties. It is possible that the near wake may be less sensitive than blade flow to blade Reynolds number. Green defines a Reynolds number based on a location in the wake rather than a point on the blade. The inertial force term in this *wake* Reynolds number involves the difference in velocities across the width of the wake. Thus,

$$Re = \frac{2(U_0 - U_c)b}{\nu} \tag{6.6}$$

where $U_c$ is the velocity on the centreline and $b$ is the width of the wake. Comparison of wake Reynolds numbers between the 2-blade PIV results and Green's wind tunnel tests at 2 diameters downstream reveals

$$\begin{aligned} Re_{tunnel} &= 3.2 \times 10^4 \\ Re_{model} &= 3.4 \times 10^4 \end{aligned}$$

The two values compare well. Due to its definition, however, differences in wake Reynolds number are largely determined by the choice of downstream location. It would be unwise to use the numerical value of the wake Reynolds number as the basis for a precise extrapolation to full-scale but it is useful in the broader context as an indication of the relative importance of inertial and viscous forces at a particular location in the wake.

Gould[47] states that the broader aspects of fluid flow patterns usually show much less change than the corresponding lift-coefficients over the same range of Reynolds numbers. Low Reynolds number flow visualization tests are often quite suitable for showing the flow pattern changes associated with changes in lift-coefficients measured at a higher Reynolds number. Analysis of measured wake structures from small scale may therefore yield a fundamental understanding of rotor flows, in the same way that the principles of flight can be understood on the basis of model aircraft experiments.

### (c) Turbulence

Ambient turbulence is highly influential in wake development and may reduce the significance of Reynolds number scale effects. The Reynolds number at which the flow becomes turbulent is dependent on the degree of turbulence in the mainstream. At this critical Re, mixing of the boundary layer on the blade with the faster moving fluid outside the boundary layer results in re-energization of the layer and delays the point of separation. Thus a large disparity in Reynolds number may not be such a severe limitation as it may first appear, if the transition to turbulence in the boundary layer can be provoked by a high level of ambient turbulence. In these experiments, turbulence manipulators were employed to reproduce the turbulent intensities observed upstream of the WM19S machine. Re-adjustment of the manipulators would be required in order to reproduce similar turbulent length scales at the blades.

### (d) Compressibility effects

Density changes in the fluid are strongly affected by the Mach number,

$$M = \frac{V}{c_f} \tag{6.7}$$

where $V$ is the velocity in the fluid and $c_f$ is the speed of sound in the fluid. The Mach number at the tip of a full-scale wind turbine can be written as

$$M_{machine} = \frac{U_0\sqrt{\lambda^2+1}}{c_{air}} \tag{6.8}$$

Problems are encountered when the Mach number is not small enough for the fluid to be treated as incompressible.

Comparing the WM19S turbine, operating in the range $\lambda = 2{-}4.4$, and the 3-blade replica, operating in the range $\lambda = 1.6{-}4.8$ reveals

$$\begin{aligned} M_{machine} &= 0.14 - 0.16 \\ M_{model} &= 3.2 \times 10^{-4} - 8.2 \times 10^{-4} \end{aligned}$$

From tables of pitot-tube measurements[71], it is seen that for $M < 0.2$ compressibility affects the pressure difference across the pitot-tube by less than 1%. Thus it is sufficiently accurate to treat the flow, both at full- and model-scale, as incompressible. Compressibility effects are more significant in high-speed wind-tunnel testing.

### (e) Cavitation

The absolute pressure must nowhere be low enough for the release of dissolved air bubbles from the liquid. This effect is known as cavitation[26]

Considering the flow outside the vortex structure in the wake, Bernoulli's equation gives

$$p_0 + \frac{1}{2}\rho U_0^2 = p + \frac{1}{2}\rho u^2 \tag{6.9}$$

where $p_0$, $U_0$ are conditions far upstream where the flow is unaffected by the presence of the rotor and $p$, $u$ are conditions at a point in the wake. The maximum pressure drop in the wake is then given by

$$\frac{p_0 - p}{\rho} = \frac{1}{2}U_0^2 \tag{6.10}$$

For $U_0 = 0.25$m/s, the expected pressure drop is of the order of 30Pa.

With high rotation rates, cavitation effects are more likely to occur due to low pressures in the centre of the vortices shed from the blade tips. Assuming a tip vortex of strength $\Gamma$ and radius $a$, the local velocity at the vortex is given by

$$u_a = \frac{\Gamma}{2\pi a} \tag{6.11}$$

Since the flow is irrotational outside the vortex, Bernoulli's equation can be applied and the pressure drop at the vortex is

$$\frac{p_0 - p}{\rho} = u_a(U_o + \frac{1}{2}u_a) \tag{6.12}$$

From the PIV vorticity contour plots, upper bounds can be placed on the size and strength of the shed vortices. For $a = 0.02$m and $\Gamma = 0.04 m^2 s^{-1}$, the expected maximum pressure drop is of the order of 120Pa.

The hydrostatic pressure in the wake is calculated from

$$p_{hs} = \rho g h \tag{6.13}$$

where $h$ is the depth below the water surface. When the blade reaches the top of its rotation, $h = 0.3$m and the minimum hydrostatic pressure is estimated as $p_{hs} = 3$kPa. In comparison to the hydrostatic pressure, the pressure drop due to the rotor is negligible. The absolute pressure is given by $p_{abs} = p_{atm} + p_{hs}$ where $p_{atm}$ is 101.3kPa at 15°C. Thus, there is no danger of the absolute pressure falling to that of the vapour pressure of water, $p_{vp} = 1.7$kPa at 15°C, and cavitation can be dismissed as a source of error in these experiments. This was borne out by observation during the experiments.

### 6.1.3 Kinematic Similarity

Kinematic similarity was assured by maintaining the tip-speed ratio, which implies that the ratios of velocities at the full-scale machine were reproduced at the model.

## 6.2 Errors in the PIV Technique

A comprehensive treatment of the errors incurred during both the PIV acquisition and analysis stages has been reported by Gray[48] and covered further by Skyner[88]. Errors can be classified into systematic errors and random errors. These are now discussed.

### 6.2.1 Systematic Errors

#### (a) Seeding particle dynamics

One potential source of error concerns the ability of the seeding to faithfully follow the flow. The densities of the $70\mu m$ diameter pollen particles have proved to be well matched to the density of water. The pollen remained suspended in still water for several hours without any visible signs of drifting or settling. The error in the assumption of neutral buoyancy has been estimated at 0.1% by Skyner. The agreement in densities between pollen and water particles ensures that the pollen seeding would accurately follow the flow under conditions of temporal acceleration of the fluid.

Large spatial velocity gradients in the flow, however, could potentially affect the ability of the pollen to follow the flow. The basic premise of PIV, however, is that the velocities in the flow are constant within an interrogation area on the film (see Section 2.1.2). This rules out the possibility of large velocity gradients across a particle diameter, exerting spin on the pollen particle according to Magnus' law[71]. In addition, Stokes law[23] can be used to find the drag of the fluid on the particle. For these experiments, the slip velocity of the pollen particle (the relative velocity between the fluid and the pollen) was calculated using Stokes law to be $u_s = 1 \times 10^{-3}$m/s. Thus, the conifer pollen can be treated as respondingly accurately to fluid acceleration.

### (b) Positional/displacement errors

Geometric distortions are introduced by deviations of the laser sheet from a uniformly flat sheet. Imperfection of the camera lens will also lead to geometric distortions between the flow and the recorded PIV image. In the set-up for these experiments, these errors are reduced by refractive index changes due to the air/glass/water interface. However, all positional/displacement errors are accounted for by conducting still water tests and subtracting the results from the PIV flow records. The image-shifting system is also calibrated in this way.

### (c) Pulse separation errors

A systematic error is incurred by determining the pulse illumination interval through use of a photo-diode placed in the path of the scanning-beam. Subsequent particle illuminations are at different positions in the measurement zone and hence at different phases of the scan cycle. This error is estimated at 0.0–0.2%.

### (d) Out-of-plane motion

Out-of-plane motion of the flow could, in principle, lead to considerable errors in the measurement of the two in-plane components of velocity. The major out-of-plane motion in the flow is due to wake rotation or swirl. To estimate this swirl velocity, consider the wake forming behind the rotor to be a cylinder of radius $R = 87.5$mm and length $l$ at time $t$. The torque impulse on the rotor, $Qdt$ results in an equal and opposite angular momentum $Id\omega$ in the air flow downstream of the rotor. A value for the maximum torque on the rotor can be obtained from $(C_Q, \lambda)$ curves for a typical airfoil. For the NACA4415 airfoil

$$C_{Qmax} = \frac{Q}{\frac{1}{2}\rho U_0^2 \pi R^3} \approx 0.12 \tag{6.14}$$

Equating this with the torque on the cylinder, results in a value for the angular velocity of the wake of

$$\omega_{max} = 0.12U_0/R = 0.343\text{rad/s} \tag{6.15}$$

The maximum swirl velocity is thus

$$V_{Smax} = \omega R = 0.03\text{m/s} \tag{6.16}$$

This is 12% of the freestream value.

Any out-of plane component of the flow in the laser sheet will introduce errors in the recording of the velocity vectors in the PIV measurements, due to parallax error. This error will be largest at the extremes of the measurement area. Figure 6.2.1 is provided to aid explanation.

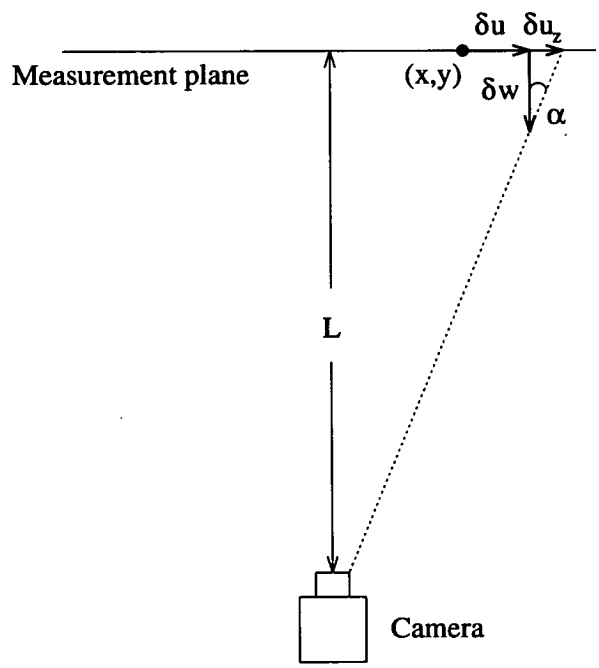


**Figure 6.2.1** Parallax error in PIV recording due to out-of-plane motion in the flow

Assume the camera is positioned a distance $L$ from the laser sheet, and the true axial velocity at a point $x, y$ in the sheet is $\delta u$. The perceived axial velocity, $\delta u_p$ is given by

$$\delta u_p = \delta u + \delta u_z \tag{6.17}$$

where $\delta u_z$ is the error due to the out of plane component. This error can be estimated from geometrical considerations as

$$\delta u_z = \delta w \tan \alpha \tag{6.18}$$

where $\delta w$ is the out-of-plane component of velocity and $\tan \alpha \approx x/L$.

In the PIV experiments, the camera distance was $L \approx 1$m, the distance from the edge of the measurement zone to the centre was $x \approx 0.3$m and from the above calculation the magnitude of the swirl component is $\delta w = 0.03$m/s. The maximum error in velocity measurement is then

$$\epsilon = \frac{\delta u_p - \delta u}{U_0} = 3.6\% \tag{6.19}$$

However, the most important measurements, in the near wake of the rotor, were made in the centre of the image where out-of-plane motion does not affect in-plane measurements to the same extent and the effects of the distortion become negligible.

### (e) Velocity gradient bias

In the PIV anaylsis, there is a systematic error associated with high velocity gradients in the flow. The larger particle image separations in the interrogation zone will have a greater chance of the multiple particle image lying outwith the zone, thus biasing the average displacement measurement towards the lower displacements. Theoretical studies[61] have shown that the systematic bias varies linearly with displacement gradient. An estimate of maximum displacement gradient can be derived from velocity ratios of the 2-blade rotor at high tip speed ratio. From Figure 4.1.2(iv) of Chapter 4, an estimate of the maximum drop in velocity across the rotor is given by $0.75U_0$. Thus the displacement gradients are bounded by

$$\Delta t du/dx = \frac{2.5 \times 10^{-3} \times 0.75 \times 0.25}{0.012} \approx 0.04 \tag{6.20}$$

From comparison with work by Skyner, the systematic error due to velocity bias is 2.5%. However, most of the displacement gradients in the vector maps will be

much less than 0.04 and a figure close to 1% is more accurate as a value for the systematic error.

### 6.2.2 Random Errors

#### (a) Photographic errors

Random errors can be introduced due to practical limitations of the recording medium. However, the TMAX film used in these experiments was of high sensitivity (400 ASA) and high resolution (125 lines/mm at 1:1000 contrast). In addition, constant agitation of the developing tank prevented 'adjacency effects' which may, due to uneven development, influence the shape (and hence position) of the image centres.

Estimating the magnification factor from the negative of the calibration grid, using the darkroom enlarger, introduced errors that were calculated to be less than 1%.

#### (b) Pixelation/discretisation errors

In the PIV analysis, digitising the power spectrum data introduces quanitisation errors. In addition, there are rounding errors in the numerical calculation of the autocorrelation function. These errors depend on the type of CCD camera and image digitiser used in the analysis system. The components of the PIV analysis system at Edinburgh have been chosen to produce an optimal system in terms of reducing errors.

#### (c) Random correlation noise

Detection of the displacement peaks in the autocorrelation plane can lead to errors if there is strong background random correlation. For the PIV analysis system

used in these experiments, this has been investigated by Gray. PIV negatives, of varying degrees of correlation noise, were artificially generated and the result of the study showed that the errors due to random correlation noise could be placed in the range 0.0–0.5%. Calibration of the analysis rig was also achieved by analysing 'mock' negatives of known displacements. Skyner produced calibration values for the relationship between the correlation peak and the image separation to an accuracy of 0.1%.

#### (d) Velocity gradient bias

The motion of the particles in the measurement plane gives rise to a discrete and random representation of a continuous flow field. Particle image pairs representing the same fluid motion will produce slightly different mean displacements due to their different positions within the interrogation area. Thus, random sampling of the particles in the interrogation area introduces an uncertainty in the location of the centre of the correlation peak. This uncertainty increases as the range of particle displacements increases and the correlation peak broadens. Random errors associated with velocity gradients for these experiments are in the range 0.3–0.5%. They are less serious than systematic errors as they manifest themselves clearly when the analysed data is inspected and can be dealt with at the editing stage.

### 6.2.3 Errors in Vorticity Information

The method of calculating vorticity in the PIV post-processing analysis compounds the errors in the raw velocity values. Discretisation of the calculation of vorticity in equation (5.1) reveals that the relative error in vorticity is at least four times the smallest relative error in velocity. Averaging of velocity vector maps, however, diminishes this effect to some extent by reducing the random errors in the PIV technique. In addition, vorticity levels associated with the tip vortex

structure were relatively large in magnitude and, in that case, errors associated with velocity values would not dominate the calculation of vorticity.

For a point in the wake, close to the rotor and in the vicinity of the tip vortex structure, equation (5.1) in discrete form is

$$\zeta = \frac{\Delta u - \Delta v}{2d} \pm \frac{2\varepsilon}{d} \tag{6.21}$$

where $\varepsilon$ is the absolute error in velocity and $d$ is the grid spacing between the four nearest neighbours of the point. Averaging of vector maps reduces the random error in the velocity at the point by a factor of $1/\sqrt{6}$. For the purposes of error analysis, out-of plane motion in the fluid is classified as random. Following the methods of Barlow[21], the combined random and systematic error in velocity gives a value of $\approx 6\%$ for relative errors in vorticity, in the region of the tip vortex structure.

## 6.3 Summary and Discussions

This chapter has assessed the flow around the model rotor in terms of geometric, dynamic and kinematic similarity with full-scale. The 3-blade WM19S model replica was accurately modelled with respect to profile and solidity. One feature of the 2-blade model was its high solidity at inboard stations compared to the 3-blade model. A study of the influence of the walls of the flume on the flow past the model rotor produced an estimate of correction for blockage of 2.5%.

Dynamic similarity is influenced by the Reynolds number which, at model scale, is 3 orders of magnitude lower than that at full-scale. Boundary layer separation, re-attachment and the transition to turbulence are likely to be very different at model scale than on a full-scale blade. Prediction of the differences in blade boundary layer flow as a function of Reynolds number allowed some insight into the effect of scale on the wake structure. A thicker boundary layer on the model blade than at full-scale may be responsible for the thick shear layers evident in the PIV vorticity

contour plots of Chapter 5. In addition, early separation of flow and high drag could explain the large velocity deficits of the PIV results.

However, not enough information has been gained in these experiments to accurately predict the behaviour of the blade boundary layer at model scale. Structure in the near wake, especially regarding the vorticity concentration, may be less sensitive to Reynolds number than blade flow. Since the concentration of vorticity is virtually an unknown quantity in the near wake, tests at low Reynolds number can provide complementary data for full-scale experiments. In the same way that the principles of flight can be understood from model aircraft, the fundamental principles of rotor wakes may be observed from the PIV tests.

An assessment of the pressures and speeds involved in the flow proved that the experiments were not compromised by cavitation or compressibility effects. Kinematic similarity was assured by running the model at tip speed ratios relevant to a full-scale machine.

Errors in the PIV aquisition and analysis technique were classified into systematic and random errors. By careful design and use of high quality components, errors in the PIV technique were minimized. In principle, corrections could be made to data by measuring the systematic errors. However, the estimates above revealed that for the majority of data in the near wake of the rotor, the combined systematic error is less than 3%, and was declared negligible. Random errors in the PIV technique were found to be less than 1% and can often be detected by inspection of the analysed data.

The method of calculating vorticity in the PIV post-processing analysis compounds the errors in the raw velocity values. The combined random and systematic error in velocity gives a value of $\approx 6\%$ for relative errors in vorticity, in the region of the tip vortex structure.

## 6.4 Conclusions

An error analysis of the PIV experiments has been undertaken. The most important findings of this chapter are listed as follows:

1. This chapter contains an account of a number of sources of experimental error from the PIV tests which, when quantified, were shown to be almost negligible. Systematic errors from the PIV technique contributed less than 3% error in velocity measurement and random errors were responsible for about 1% error. Errors in velocity measurement were shown to be compounded during vorticity calculations. Vorticity errors were estimated at around 6% in the region of the wake, close to the tip vortex structure.

2. The most important concern has been identified as that as scale effect; the variation of the non-dimensional parameters of the flow with Reynolds number. Although not enough information has been gained to reveal the behaviour of the boundary layer on the model blades, it is likely that there would be a difference in the phenomena of separation and re-attachment at the blade compared to full-scale, which may be conveyed to the wake structure. The large velocity deficits and thick shear layers of the PIV results are likely to be the effects of scale.

3. Although full-scale wake structures may differ from those observed at model scale, there is a strong possibility that they will share fundamental similarities. Just as the phenomena of circulatory lift and trailing vorticity are found on aircraft at all scales, from balsa-wood models to wide-bodied airliners, so it is with wind turbines. Analysis of measured wake structures from small scale may therefore yield a fundamental understanding of rotor flows, in the same way that the principles of flight can be understood on the basis of model aircraft experiments.

# Chapter 7

SUMMARY AND CONCLUSIONS

### Overview

In this chapter, the main results of the thesis are summarised for the 2-blade and 3-blade model rotors. The flow visualisation and wake analyses of Chapters 4 and 5 are used to examine the relationship between velocities and vorticity in the wake structure. An assessment of the PIV experiments is given, based on the results of Chapter 6. In particular, the extent to which the results may be extrapolated to full-scale is discussed. The principal conclusions of the study are stated and some ideas for further work in this area are presented.

## 7.1 Summary of Main Results

### 7.1.1 Results for 2-blade rotor (frozen wake)

Whole-field velocity maps were obtained for the wake of a 2-blade flat-plate model wind turbine rotor, extending from the rotor plane to approximately 3 diameters downstream, covering the entire near-wake region. The tests were repeated for tip speed ratios of $\lambda = 3, 4, 5, 6$ and 8. Map-averaging techniques were developed to enable a 'frozen' wake analysis, in which the wake structure is captured as an

instantaneous picture, enabling blade tip and root vortices to be studied in fine detail. Vorticity maps were obtained by post-processing the 'frozen' wake data. This was the first time, to the best of the author's knowledge, that a complete instantaneous full-field picture of the wake vorticity behind a wind turbine had been mapped. For the first time, experimental vorticity maps could be compared with theory and the results were compared directly with the output of a free-wake numerical code (ROVLM) developed at the University of Stuttgart. The influence of tip speed ratio on the vortex wake structure was extensively studied, by testing the models over a range of rotor speeds. A number of features emerged which were not accounted for in current theoretical models.

The model exhibited rotor flow states characteristic of a full-scale wind turbine, as defined by Eggleston and Stoddard[38]. At low tip speed ratios the rotor operated in the windmill state where mild wake expansion is observed. This concurs with simple wake theory. At high tip speed ratio, however, the wake was seen initially to expand, but at about 2D downstream to contract. This preceded the breakdown of the structured wake into a highly turbulent state. Blade element-momentum (BEM) theory does not predict this phenomenon. Initial comparisons between the PIV and ROVLM results were favourable in terms of predicting wake contraction at high $\lambda$. This tended to validate both the code, and the small-scale PIV experiments, at least for this case.

The aircraft propeller used in the development of the PIV method attained the vortex ring state at high tip speed ratios. This may be attributed to the twist on the blade. For two blade elements at the same spanwise location on a twisted and an untwisted blade, the effect of the pitch angle is to lower the angle of attack. Given the same angle of incidence for each element, the twisted blade effectively operates at a higher local $\lambda$. Comparison of the flat-plate results with measurements made on Green's modified aircraft propeller[52] supports this argument.

Vertical traverses from the hub upwards in LDA measurements by Green led to the conclusion that the momentum deficit of the flow is predominantly contained in an annulus. Close study of the PIV velocity vector maps in Chapter 4 extended

this description to classify the wake structure according to three distinct regions of flow.

The first region is a *wake core*, containing very small velocities. At very high $\lambda$, the flow immediately behind the rotor is almost stagnant, while further downstream areas of turbulence and recirculating flow establish themselves. The second region is the *outer wake*, comprising the tip vortex structure, while the third region is an *inner wake* with inboard vorticity moving under the influence of rapidly expanding flow. This matched Glauert's description of the wake as a vortex system comprising an intense tip-vortex outer region and a weakly-diffused vortex sheet inner region. Tip vortices were revealed to get out of step with the vortex sheets. This has been confirmed in other tests. Green describes the tip vortices as 'roller bearings', acting between the faster outer flow and the retarded inner wake. Velocity ratios greater than 1.0 at the extremes of the wake profiles supported the idea of the outer wake as a region of accelerated flow.

The inner wake vorticity, emanating from the trailing edge of the blade, corresponds to a shear layer of velocity. The 2-blade PIV vorticity contour plots showed that the shear layer moved under the influence of wake expansion to merge with the tip vortex system. At $\lambda = 8$, the tip vortices were embedded in an area of concentrated vorticity of thickness roughly equal to the rotor radius. The results of Pedersen & Antoniou[77] suggest the area of influence of the tip vortex system is much less at full-scale, where a thinner inner wake region produces a wider velocity profile with a flatter central section. Although the PIV analysis also revealed the presence of 'square' profiles, especially at high $\lambda$, these occured during the transition from a highly structured to a turbulent wake. This transition effectively marked the boundary of the near and intermediate wake and the shape of the profile may indicate that the turbulent mixing process had not yet penetrated the whole of the wake core. In wind tunnel tests, Green also commented upon the observation of 'square' profiles at the boundary of the near wake region.

Contrasting the 2-blade PIV data with wind-tunnel work both by Green at Loughborough and by researchers at the Marchwood Engineering Laboratories produced

some favourable comparisons. Velocity deficits were shown to display closer agreement with downstream distance. Notwithstanding the difference in scale, this may be due to the high solidity at the inboard stations of the flat plate blades. The blades had no cut-out at the root which could be a factor in producing velocity profiles of large deficit immediately behind the rotor. The effects of high blockage of flow at the blade root would recover with downstream distance.

The phase-averaging technique employed in 2-blade PIV experiments was successful in extracting the vortex wake structure shed from the blades, from the superposed turbulence. The 2-blade turbulence results displayed a significant increase in turbulence with $\lambda$. At high $\lambda$, the highest levels of turbulence were witnessed at around 2.5D downstream. This could be due to large areas of recirculating flow, forming downstream of the rotor, as the rotor enters a turbulent wake state.

The wake vorticity analysis of the PIV results revealed behaviour in the wake which influenced the geometry and stability of the vortex system. Areas of recirculation were suggested as the cause of the marked contraction of the wake at around 2 diameters downstream for high tip speed ratios. The areas of recirculation could encourage re-entrainment of the freestream resulting in acceleration of the outer wake. The downstream speed-up of the wake has been suggested by other workers in the field[74]. This is in contradiction to the basic premises of BEM theory, which assumes an asymptotic slow down of the wake. However, interaction of the inner wake vorticity with the tip vortex system was, in some cases, seen to result in an instability of the wake structure brought on by the coalition of adjacent tip vortices. The coalescing of tip vortices may give the impression that the outer wake is accelerating. In either case, the PIV images confirmed that the simple wake expansion model on which BEM theory is based is fundamentally flawed.

The size and strength of the tip vortices shed from the blades were more sensitive to $\lambda$ in the case of the PIV experiments than in the ROVLM simulations. For the PIV results, tip vortices persisted furthest downstream when the rotor was

operating in the mid-$\lambda$ range. This was consistent with results from full-scale[85]. However, it was noted that since different tip speed ratios were achieved in the PIV tests by running the rotor at different speeds, the blade Reynolds number may vary significantly from one test to another. Thus, effectively two variables ($\lambda$ and $Re$) were changed in producing a new value for $\lambda$. Hence, it is difficult to be conclusive about the effect of tip speed ratio alone on the wake vortex structure.

Due to inviscid assumptions, the ROVLM calculations do not incorporate the effects of dissipation or stall near the hub. Thus the root vortices were very strong and persistent. In contrast, the PIV data showed that the root vortices were very quickly dissipated within a blade revolution. This was consistent with full-scale observations[77]. At high $\lambda$, both the PIV and ROVLM results showed breakdown of the vortex structure into large scale turbulence at 2D−3D downstream. The ROVLM simulations did not display evidence of inboard vorticity in the inner wake and breakdown of the vortex system appeared to be due to interaction of the strong root vortices rather than mixing of the freestream or dissipation. Wake breakdown is absent from most rotor codes, of either BEM or vortex-wake type.

### 7.1.2 Results for 3-blade rotor (averaged wake)

A replica of a 3-blade Vestas WM19S machine was used in laboratory simulations of full-scale conditions encountered by the Vestas turbine on Samos Island, Greece in 1991. Whole-field PIV velocity vector maps were captured at an offset distance from the wake centre corresponding to the distance above hub-height of the full-scale anemometer unit. The tests were repeated for tip speed ratios of $\lambda = 1.6, 2.7, 3.2, 4.2$ and 4.8. Averaging of wake images, recorded in different phases, introduced temporal averaging akin to the full-scale experiments. Mean velocity and turbulent velocity profiles were extracted from the 'time averaged' wake data and compared with wake measurements made on the Samos Island machine. Further full-scale comparisons were made with a Vestas V20/100 machine from the Test Station for Windmills at Risø and with the Nibe 'B' turbine. Data chosen for comparison with the full-scale machines came from a select set of

data that was suitable due to similarities in the operating conditions of the model and the full-scale turbine. Vorticity data for the 3-blade model PIV tests were presented in the form of vorticity contour plots.

The shape of the PIV velocity profiles differed in significant respects from comparison with full-scale measurements. In general, the 3-blade PIV data yielded narrow, deep velocity profiles whereas measurements from the field produced wider profiles with homogeneous central portions. In the comparison with the WM19S of Samos Island, the largest discrepancies occurred at high $\lambda$ where the centreline velocity ratios were shown to be more sensitive to $\lambda$ than the corresponding full-scale values. Comparison of velocity profiles with the Vestas V20 machine from the flat terrain of the Risø site proved more favourable.

The small sample size of the PIV data restricted the extent to which conclusions could be drawn from the 3-blade turbulence results. However, the data suggested a trend in the amount of turbulence in the wake with respect to tip speed ratio. High levels of turbulence were observed at low and high $\lambda$. This was attributed to separated flow behind the blades and the breakdown of strong vortex structure, respectively. Turbulence levels in the wake visited a minimum at an intermediate value for the tip speed ratio, around $\lambda = 3$. This matched the trends in turbulence for the 2-blade rotor, although care must be taken in making this comparison due to the different process of data averaging in each case. However, a similar trend was identified for the Samos Island measurements, although the full-scale results revealed higher values of centreline turbulent velocity ratios. It was suggested that the complex terrain of the Samos Island site may impose energetic turbulent motions which affect the wake. Comparison of turbulent velocity with the flat terrain of the Nibe results proved more favourable.

The difference in scale was the most obvious reason for the discrepancies between laboratory and field measurements. The Reynolds number of the PIV tests was lower than full-scale by a factor of 1000. However, it was noted that uncertainties involved in the field measurements could be significant. In the Samos Island experiments, it was difficult to compensate for the effects of the complex terrain.

The complex terrain of the wind farm may produce large scale inhomogeneities, of the order of the size of the wake, which affect the wake properties. Thus large areas of stable recirculating flow, which were witnessed in the laboratory environment, may not be feasible in the field. Cross-wake smoothing and wake meandering were also reasons suggested for the displacement of laboratory and full-scale profiles.

The map averaging technique employed during the PIV recording of the 3-blade rotor resulted in vorticity contour plots which, despite losing all time-dependent vortex structure, yielded steady-state axisymmetric patterns. This was an important development from the PIV study as the plots provide vorticity data which is directly comparable with the assumptions of actuator disk models. In some analyses, the 3-blade vorticity contour plots were transposed onto the centreline under the assumption of an axisymmetric distribution of vorticity in the wake. This resulted in an absence of data from an inner core of the wake of radius 0.42R.

The contour plots contained evidence of strong inboard vorticity which moved downstream under the influence of slight wake expansion. Drawing a parallel with the 2-blade results, this can be attributed to a shear layer of velocity in the inner wake. Evidence of a shear layer between the outer wake and the retarded flow in the wake core, was also reported at full-scale[77]. However, this layer may not be as thick as that found at model scale which could explain why, in general, measurements from the field produced wider profiles than the 3-blade PIV data, often with homogeneous central portions.

## 7.2 Assessment of Results

### 7.2.1 Validity of the Technique

#### (a) Water as a medium for wind turbine experiments

Despite the anomalies due to Reynolds number, conducting the experiments in water has distinct advantages over wind tunnel testing[47]. For the same Reynolds number and a given size of model, the wind speed needs to be 12.6 times that in the water tunnel. High speed testing in wind tunnels may introduce compressibility effects. In addition, high slipstream velocities cause particles separating at the trailing edge of the blades to disperse out of the light sheet. Thus wind tunnel researchers have experienced problems of illuminating the wake structure and their studies have been restricted to flow close to the blade. This limits the potential for wake analysis. The results of this study have shown that water can accomodate a sufficient density of seeding to provide a high level of detail in the wake of the models. Further, tip speeds in the water tunnel were sufficiently low to ensure that there were no problems with either compressibility or cavitation.

#### (b) Averaging procedures

Averaging of the PIV vector maps was used to provide mean and turbulent, freestream and wake flow statistics. One result of this is the production of a steady-state axisymmetric vortex pattern. In particular this provides vorticity data which is directly comparable with the assumptions of actuator disk models. In the 3-blade experiments, PIV photographs were taken at discrete intervals during the blades revolution. This provides some justification in the comparison of the 3-blade measurements with time-dependent values taken by mast anemometers at full-scale. There is more cause for concern over the small sample size involved in the PIV averaging. The sample size was ultimately determined by the

time required for exposing, developing and analysing each film. Recent advances in Digital PIV (see Chapter 2) have rid the PIV technique of this bottleneck in the flow-to-vector-map process. Having a larger sample size would allow much more confidence in drawing conclusions from the turbulence measurements. This is discussed further in Section 7.4.2.

### 7.2.2 Extrapolation to Full-scale

The difference in scale between the model and a full-scale wind turbine is likely to be associated with differences in boundary layer flow over the blades which may influence the wake structure. An accurate knowledge of the blade boundary flow over the model blades was beyond the scope of these experiments. However, in Chapter 6, some thought was given to the expected properties of the boundary layer at model scale, which may give an insight into the effect of scale on the wake geometry. Compared to flow on a full-scale blade, the flow over the blades at model scale may separate earlier, with a greater spanwise proportion of the model blade experiencing separated flow. It is possible that, at model scale, there is a thicker boundary layer on the blades as well as a thicker region of separated flow in the wake. This may explain the deep velocity profiles and and thick shear layers of the PIV results, compared to full-scale.

However, although full-scale wake structures may differ from those observed at model scale, there is a strong possibility that they will share fundamental similarities. In aircraft studies, the phenomena of circulatory lift and trailing vorticity are found at all scales from balsa-wood models to wide-bodied airliners. Analysis of measured wake structures from the small-scale wind turbines may therefore yield a fundamental understanding of rotor flows, in the same way that the principles of flight can be understood on the basis of model aircraft experiments.

The power of the small-scale PIV approach is exemplified in Figure 7.1.1. A vorticity contour plot of a 'frozen' wake behind the 2-blade rotor at $\lambda = 8$ is presented. Overlaid on the contour plot are corresponding wake velocity profiles,

taken from Figure 4.1.2(iii), for downstream stations 1−2.5D. The combination of velocity and vorticity information serves to illustrate the structure of the helical vortex system created by the rotor. In particular, the maximum velocity gradient in each cross-wake profile is clearly seen to occur across the annular tip vortex system in the outer wake.

This study has presented the first complete instantaneous images of the wake behind a wind turbine rotor, at any scale. The images have confirmed that, under certain circumstances, the prediction codes currently used by the wind energy industry are in error. At this stage, any experimental data which allows wake theory to be rigorously tested is welcome, and numerical codes can be adjusted to model low Reynolds number flows more easily than wake vorticity can be mapped on a full-scale wind turbine. Hence, the most sensible way to proceed is to try to model these conditions using an advanced vortex code at low Reynolds number, rather than trying to replicate the experiments at full-scale simply for the convenience of existing numerical models.

## 7.3 Principal Conclusions

The principal conclusions of this thesis are stated below.

1. PIV has been shown to provide detailed full-field data of the near wake of a model wind turbine. An experimental database for wake velocities and structure has been established.

2. The results strongly justified using the PIV technique to study the flow behind a model wind turbine rotor. The amount of high quality detailed data of the entire flow field obtained by the uncomplicated, quick and flexible approach of PIV compared favourably with previous investigations.

3. As far as the author is aware, the experiments were the first in which full-field velocity and vorticity maps have been captured in the wake of a wind turbine at any scale. This made it possible, for the first time, to compare the results of other surveys and numerical predictions of wake structures with detailed experimental data from a complete instantaneous image of the wake behind a rotor.

4. PIV wake velocity profiles were compared with full-scale data and shown to contain greater velocity deficits. The results showed large discrepancies at high $\lambda$. However, the complex terrain of the Samos Island wind park may have affected the wake properties of the WM19S machine and full-scale measurements made in flat terrain appeared more promising in terms of agreement with the PIV results. Overall, comparisons of the PIV profiles with wind tunnel data displayed more agreement than comparisons with full-scale measurements.

5. PIV vorticity contour plots of the model turbine data revealed fundamental properties concerning the near wake structure. In particular, a thick shear layer of velocity was identified in the inner wake. At high $\lambda$, the wake was seen to undergo a contraction at around 2D downstream. In addition, there was interaction between the shear layer and the tip vortices.

6. The PIV images confirmed that the simple wake expansion model on which blade-element/momentum (BEM) theory is based is fundamentally flawed, and for the first time quantitatively illustrated the processes involved in the development of the near wake.

7. The PIV results were compared with results from a free-wake vortex code (ROVLM) from the University of Stuttgart. Both PIV and ROVLM predicted wake contraction and breakdown, wake properties that are absent from BEM theory and most vortex-wake prediction codes. Breakdown of vortex structure in the simulations from the ROVLM code may have been due to interaction of strong root vortices.

8. Scale effect was identified as the most important concern in terms of discrepancies with results from other surveys. The *blade* Reynolds number of the PIV tests was lower than full-scale by a factor of 1000. The difference in scale between the model and a full-scale wind turbine is likely to be associated with differences in boundary layer flow over the blades which may influence the wake structure. The large velocity deficits and thick shear layers of the PIV data may be as a result of early separation and high drag at the model blade combined with a thick boundary layer, compared to full-scale. In addition, a greater spanwise proportion of the blade at model scale may experience separated flow.

9. Analysis of measured wake structures from the small-scale wind turbines may yield a fundamental understanding of rotor flows, in the same way that the principles of flight can be understood on the basis of model aircraft experiments. Although full-scale wake structures may differ from those observed at model scale, there is a strong possibility that they will share fundamental similarities.

10. The comparison with the ROVLM code may be viewed as a first step in developing an advanced rotor performance method that will incorporate the detailed physical processes governing wake behaviour. This may lead to codes that can predict an optimal rotor geometry and more accurately assess the forces on the rotor blades under all conditions. Better design will lead to improved reliability and efficiency of wind turbines.

## 7.4 Further Work

By shedding light on the physical processes governing the development and structure of the wake of a wind turbine, PIV could play an important role in the future of aerodynamic prediction codes for wind turbines. A recommendation for future experiments and analyses, based on the present work, is outlined below.

### 7.4.1 Further Analysis using the Existing PIV Data

The new detailed knowledge of the wake structure revealed by the PIV tests could allow theoretical modellers to assess and develop their numerical codes while comparisons with field measurements would place the PIV results in the context of wake behaviour from full-scale machines.

An extension of the comparative work with Stuttgart could involve incorporating the effects of Reynolds number within the vortex-wake code, ROVLM. An important case is modifying the code to include stalling of the blade.

The CFD codes, PHOENICS and FIDAP, have recently been used in conjuction with wake turbulence models for wind turbines[14]. The k-$\epsilon$ and the Reynolds-Stress turbulence models are capable, at least in principle, of providing detailed information on mean and turbulent flow components in a turbine wake for a wide range of conditions. However, the codes rely on near-wake input data which influences the results considerably. Detailed PIV measurements could be used to provide a better description of the near-wake in order to improve calculated results.

The study has highlighted the need for more wake data in order to compare and assess the PIV results. Measurements taken in flat terrain may be more suitable for comparison with the existing data.

### 7.4.2 New Experiments

#### (a) Variable current facility

In the above experiments, different tip speed ratios were achieved by running the rotor at different speeds. Thus, the blade Reynolds number varied significantly from one test to another. This was a limitation of the tests and makes a strong case for further tests in a tank with variable current velocity. Conducting the tests with a fixed RPM rotor would then give a near-constant Reynolds number. In this way, the effects of tip speed ratio on the vortex structure in the wake could be separated from Reynolds number effects.

#### (b) New rig design

The PIV records of the rotor wakes were affected by the wake from the 'tower' support of the present rig. A new rig design could incorporate a long thin rod or 'sting' which could be used to remove the rig framework from the laser sheet. Thus the wake would not be corrupted by interference from tower shadow. This is desirable for comparison with simulations from vortex codes.

There is also a case for designing a new turbine rig which would allow thrust and torque measurements to be made on the operational model. This is discussed in Section 7.4.3.

#### (c) Digital PIV

Adoption of the recently developed Digital PIV technique would dramatically improve the speed of the PIV acquistion process. In the Digital PIV[105] method, images are captured by the CCD camera and transferred to a PC equipped with a framegrabber board. Software has been developed at Edinburgh University by a small company, Optical Flow Systems, to perform analysis of the images and

produce the velocity vector maps. With the addition of a 400MB hard-disk in order to store the images, over 100 images could be captured overnight. This would lead to assessing turbulence results with more confidence.

### 7.4.3 New Analyses

The measurement of thrust and torque on the model rotor during PIV recording would mean that, for the first time, detailed velocity and vorticity structure in the wake could be correlated with net rotor loads.

In the present study, a preliminary analysis was undertaken concerning the transport of vorticity shed from the rotor. This is a fundamental quantity since the rate that vorticity is shed downstream is related to the rate that vorticity is generated at the blades. A new analysis could be carried out to correlate the vorticity flux to circulation around the blade, and torque on the rotor.

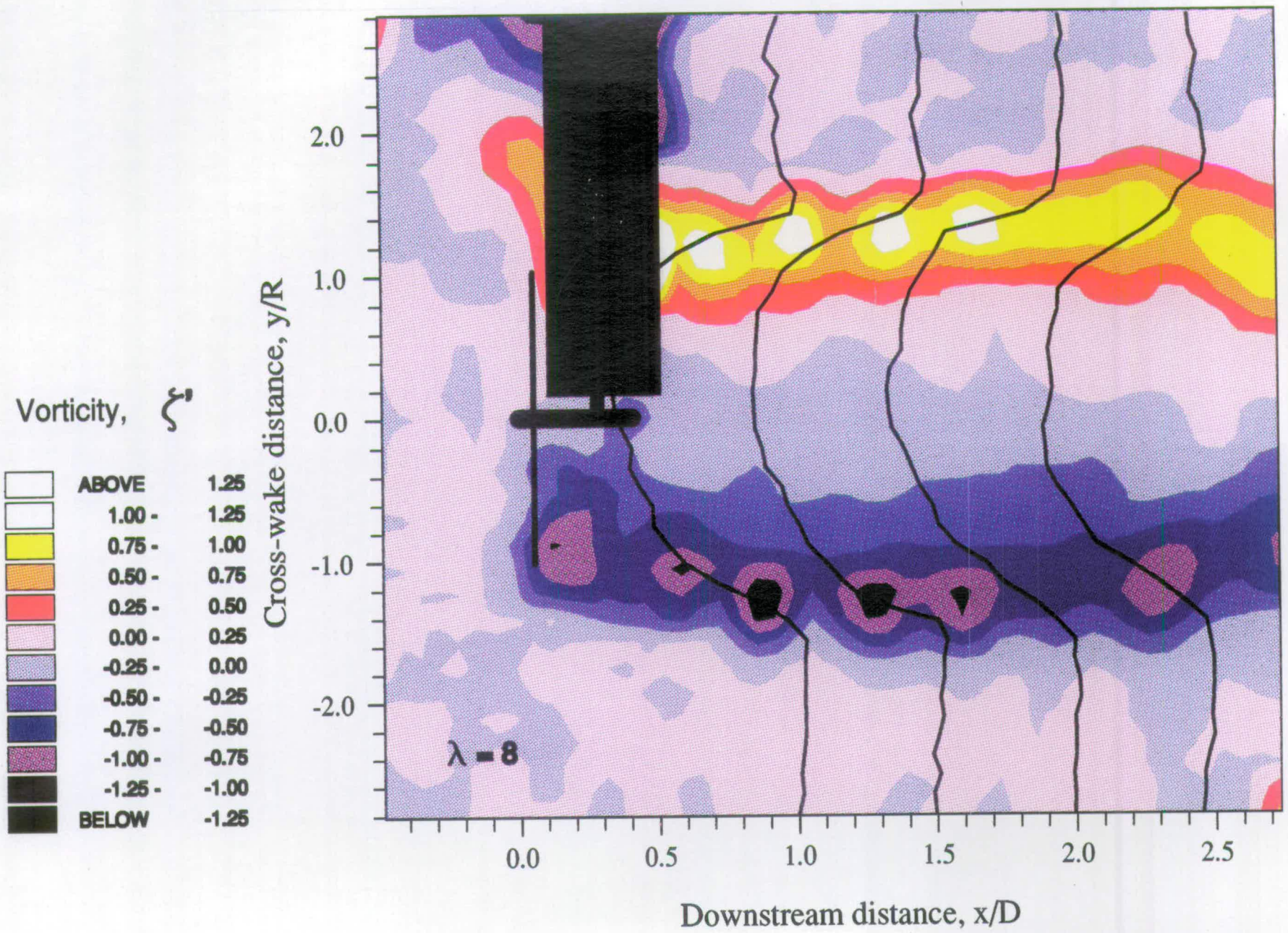


Figure 7.1.1 PIV vorticity contour plot of the 2-blade rotor at $\lambda = 8$ with corresponding wake velocity profiles.

# References


[1] R.J. Adrian. Scattering particle characteristics and their effect on pulsed laser measurement of fluid flow: speckle velocity versus particle image velocimetry. *Applied Optics*, 23(11):1690–1691, 1984.

[2] R.J. Adrian. The role of particle image velocimetry in fluid mechanics. *Proc. IMECHE: Optical methods and data processing in heat and fluid flow, City University, London*, pp 1–6, 1992.

[3] R.J. Adrian and C.S. Yao. Pulsed laser technique application to liquid and gaseous flows and the scattering power of seed material. *Applied Optics*, 24(1):127–145, 1985.

[4] A.A. Afjeh and T.G. Keith. A prescribed wake model for performance prediction of horizontal axis wind turbines. *Proc. EWEA Conf., Rome*, pp 509–512, 1986.

[5] A.A. Afjeh and T.G. Keith. A simplified free wake method for horizontal-axis wind turbine performance prediction. *ASME Trans. J. Fluids Eng.*, 108:400–406, 1986.

[6] A.A. Afjeh and T.G. Keith. A simple computational method for performance prediction of tip-controlled horizontal-axis wind turbines. *J. Wind Eng. and Industrial Aerodynamics*, 32:231–245, 1989.

[7] J.F. Ainslie. Development of an eddy-viscosity model for wind-turbine wakes. *Proc. of 7th BWEA Conference, Oxford*, pp 61–66, 1985.

[8] J.F. Ainslie. Calculating the flowfield in the wake of wind turbines. *J. Wind Eng. and Ind. Aerodynamics*, 27:213–224, 1988.

[9] P.H. Alfredsson and J.A. Dahlberg. A preliminary wind tunnel study of windmill wake dispersion in various flow conditions. *Technical Note FFA UA-1499, Part 7*, 1979.

[10] P.H. Alfredsson, J.A. Dahlberg, and J. F. H. Bark. Some properties of the wake behind horizontal-axis wind turbines. *Proc. 3rd Int. Symposium on Wind Energy Systems, Copenhagen*, 1980.

[11] C.G. Anderson, A.J. Niven, P. Jamieson, R.R. Knight, and D.J. Milborrow. Flow visualisation studies on rotating blades. *Proc. 9th BWEA Conf., Edinburgh*, pp 169–173, 1987.

[12] J.D. Anderson, Jr. *Fundamentals of Aerodynamics.* McGraw-Hill, 1984.

[13] M.B. Anderson, D.J. Milborrow, and J.N. Ross. Performance and wake measurements on a 3m diameter HAWT : comparison of theory, wind tunnel and field test data. *ETSU contract E/5A/CON/ 1090/177/020 Cavendish*, 1982.

[14] T. Ansorge, M. Fallen, P. Ruh, and T. Wolfanger. Numerical simulation of wake-effects in complex terrain and application of a reynolds-stress turbulence model. *Proc. Europ. Wind Energy Conf., Thessaloniki*, pp 448–453, 1994.

[15] M.P. Arroyo and C.A. Greated. Stereoscopic particle image velocimetry. *Meas. Sci. Technol.*, 2:1181–1186, 1991.

[16] R.W. Baker and S.N. Walker. Wake velocity deficit measurements at the Goodnoe Hills MOD-2 site. *Report No. BPA 84-15, DOE/BP/29182-15*, 1985.

[17] R.W. Baker, S.N. Walker, and P.C. Katen. Wake measurements around operating wind turbines. *J. Solar Energy Eng.*, 107:183–185, 1985.

[18] R. Bareiß, G. Guidati, and S. Wagner. An approach towards refined noise prediction of wind turbines. *Proc. Europ. Wind Energy Conference, Thessaloniki*, pp 785–790, 1994.

[19] R. Bareiß and S. Wagner. The free wake/hybrid wake code ROVLM - a tool for aerodynamic analysis of wind turbines. *Proc. E.C. Wind Energy Conference, Lübeck-Travemünde*, pp 424–427, 1993.

[20] D.B. Barker and M.E. Fourney. Measuring fluid velocities with speckle patterns. *Applied Optics*, 1(4):135–137, 1977.

[21] R. Barlow. *Statistics - a guide to the use of statistical methods in the physical sciences*, Chapter 4, pp 48–67. Wiley and Sons, 1989.

[22] M.J. Barnsley and J.F. Wellicome. Wind tunnel investigations of stall aerodynamics for a 1.0m horizontal-axis rotor. *Wind Energy, Technology and Implementation - Proceedings of EWEC, Amsterdam : PART I*, pp 8–12, 1991.

[23] G.K. Batchelor. *An Introduction to Fluid Dynamics*, Chapter 5, pp 331–343. Cambridge University Press, 1967.

[24] R. Behr and S. Wagner. A vortex-lattice method for the calculation of vortex sheet roll-up and wing-vortex interaction. *Finite Approximations in Fluid Mechanics II - Notes on Numerical Fluid Mechanics*, 25:1–14, 1989.

[25] A. Bicciolo, A. Cenedese, and A. Paglialmga. Tracking analysis of multi-exposed photographs. *Proc. ICALEO*, 1988.

[26] G. Birkhoff and E.H. Zarantonello. *Jets, wakes and cavities.* Academic Press Inc., 1957.

[27] P. J. H Builtjes. Wind turbine wake effects. *MT-TNO Report 79-08375*, 1979.

[28] J.M. Burch and J.M.J. Tokarski. Production of multiple beam fringes from photographic scatterers. *Optica Acta*, 15:101–111, 1968.

[29] L. Celaya, J.M. Jonathan, and S. Mallick. Velocity contours by speckle photography. *Opt. Comm.*, 18(4):496–498, 1976.

[30] C.V. Cook. The structure of the rotor blade tip vortex. *AGARD Conf. Proc. CP-111*, pp 3.1–3.14, 1972.

[31] J.M. Coupland and N.A. Halliwell. Particle image velocimetry : rapid transparency analysis using optical correlation. *Applied Optics*, 27:1919–1921, 1988.

[32] J.M. Coupland, C.J.D. Pickering, and N.A. Halliwell. Particle image velocimetry: the ambiguity problem. *Optical Engineering*, 27(3):193–196, 1988.

[33] A. Crespo, L. Chacón, J. Hernández, F. Manuel, and J.C. Grau. UPM-PARK : a parabolic 3D code to model wind farms. *Proc. Europ. Wind Energy Conf., Thessaloniki*, pp 454–459, 1994.

[34] A. Crespo and J. Hernandez. A numerical model of wind turbine wakes and wind farms. *Proc. EWEA Conference, Rome*, 1986.

[35] O. DeVries. On the theory of horizontal-axis wind turbines. *Annual review of Fluid Mechanics*, 15:77–96, 1983.

[36] T.D. Dudderar and P.G. Simpkins. Laser speckle photography in a fluid medium. *Nature*, 270:45–47, 1977.

[37] Durand W.F. (ed.). *Aerodynamic Theory*, Chapter 7, pp 169–360. Springer, 1935.

[38] D.M. Eggleston and F.S. Stoddard. *Wind Turbine Engineering Design*, Chapter 1, pp 30–35. Van Nostrand Reinhold, 1987.

[39] B.C.R. Ewan. Particle velocity distribution measurement by holography. *Applied Optics*, 18(18):3156–3160, 1979.

[40] L.L. Freris. *Wind Energy Conversion Systems*, Chapter 4, pp 67–72. Prentice Hall International, 1990.

[41] R.A.McD. Galbraith, F.N. Coton, E. Saliveros, and G. Kokkodis. Aerofoil scale effects and the relevance to wind turbines. *Proc. 9th BWEA Conf., Edinburgh*, pp 143–153, 1987.

[42] V. Gauthier and M.L. Reithmuller. Application of PIDV to complex flows : measurement of the third component. *Von Karman Institute for Fluid Dynamics, Lecture Series 1988-06*, 1988.

[43] H. Glauert. Airplane propellers. In W.F. Durand, editor, *Aerodynamic Theory.* Springer, 1935.

[44] J.C. Gohard. Free wake analysis of wind turbine aerodynamics. ASRL TR-184-14, Aero. and Struc. Research Lab, Dept. of Aeronautics and Astronautics, MIT, 1978.

[45] S. Goldstein. *Modern Developments in Fluid Dynamics, Volume I.* Dover Publications, 1965.

[46] J. Gould and S.P. Fiddes. Computational methods for the performance prediction of HAWTs. *Wind Energy, Technology and Implementation - Proceedings of EWEC, Amsterdam : PART I*, pp 29–33, 1991.

[47] R.W.F. Gould. Design of a low-speed water channel. *NPL AeroReport*, pp 2–3, 1968.

[48] C. Gray. *The development of particle image velocimetry for water wave studies.* PhD thesis, Edinburgh University, 1989.

[49] C. Gray. The evolution of particle image velocimetry. *Proc. IMECHE: Optical methods and data processing in heat and fluid flow, City University, London*, pp 19–35, 1992.

[50] C. Gray and C.A. Greated. The application of particle image velocimetry to the study of water waves. *Optics and Lasers in Engineering*, 9:265–276, 1988.

[51] C. Gray, C.A. Greated, D.R. McCluskey, and W.J. Easson. An analysis of the scanning beam PIV illumination system. *J.Phys :Measurement Science and Technology*, 2:717–24, 1991.

[52] D.R.R Green. *Modelling large wind turbines and wakes.* PhD thesis, Loughborough University, 1985.

[53] A.C. Hansen and C.P. Butterfield. Aerodynamics of horizontal-axis wind turbines. *Annual review of Fluid Mechanics*, 25:115–149, 1993.

[54] U. Hassan, G.J. Taylor, and A.D. Garrad. The dynamic response of wind turbines operating in a wake flow. *Int. Conf. on Windfarms, Leeuwarden, Holland*, 1987.

[55] E. Hecht. *Optics (second ed.)*, Chapter 11, pp 500–505. Addison-Wesley, 1987.

[56] C.G. Helmis, D.N. Asimakopolous, K.H. Papadopolous, P.G Papageorgas, A.T. Soilemes, and H.D. Kambezidis. An experimental study of wind turbine wakes over complex terrain. *Proc. ISES Solar World Congress*, 8:287–292, 1993.

[57] U. Högström, D. N. Asimakopoulos, H. Kambezidis, C.G. Helmis, and A. Smedman. A field study of the wake behind a 2MW wind turbine. *Atmospheric Environment*, 22(4):803–820, 1980.

[58] J.M. Huntley. An image processing system for the analysis of speckle photographs. *J. Physics E: Scientific Instrum.*, 19:43–49, 1986.

[59] D.G. Infield, I. Grant, G. Smith, and X. Wang. Development of particle image velocimetry for rotor flow measurement. *Proc. 15th BWEA Conf., Stirling*, pp 73–78, 1994.

[60] M.L. Jakobsen, W.J. Hossack, C.A. Greated, and W.J. Easson. PIV analysis using an optical addressed spatial light modulator. *Optics and Lasers in Engineering*, 19:253–260, 1993.

[61] R.D. Keane and R.J. Adrian. Optimization of particle image velocimeters. Part II: multiple-pulsed systems. *Meas. Sci. Technology*, 2:963–974, 1991.

[62] D. Kocurek. Lifting surface performance analysis for horizontal axis wind turbines. *SERI/STR-217-3163*, 1987.

[63] A.J. Landgrebe. An analytical method of predicting rotor wake geometry. *J. American. Helicopter Society*, 14(4), 1969.

[64] A.J. Landgrebe. Analytical and experimental investigation of helicopter rotor and hover performance and wake geometry characteristics. *USAAM-RDL Tech. Report 71-24*, 1971.

[65] A.J. Landgrebe and M.C. Cheney. Rotor wakes - key to rotor performance prediction. *AGARD Conf. Proc. CP-111*, pp 1.1–1.9, 1972.

[66] A. Larsen and P. Velk. Wind turbine wake interference - a validation study. *Proc. Europ. Wind Energy Conf., Glasgow*, pp 482–487, 1989.

[67] P.B.S Lissaman. Energy effectiveness of arbitrary arrays of wind turbines. *J. of Energy*, 3(6):323–328, 1979.

[68] R.I. Loehrke and H.M. Nagib. *Experiments on management of free-stream turbulence*, Chapter 3, pp 11–14. Technical Editing and Reproduction Ltd, 1972.

[69] E. Luken. Literature data-base on wind turbine wakes and wake effects. *MT-TNO Report 86-351 (IEA -9-NL04) Apeldoorn, Holland.*, 1986.

[70] H.A. Madsen and U.S. Paulsen. An integrated rotor and wake model compared with experiment. *Proc. E.C. Wind Energy Conf., Madrid*, pp 269–273, 1990.

[71] B.S. Massey. *Mechanics of Fluids (4th edition)*, Chapter 12, pp 405–407. Van Nostrand Reinhold, 1979.

[72] D.J. Milborrow. The performance of arrays of wind turbines. *J. Ind. Aero.*, 5:403–430, 1980.

[73] R.H. Miller. The aerodynamics and dynamic analysis of horizontal-axis wind turbines. *J. Wind Eng. and Industrial Aerodynamics*, 15:329–340, 1983.

[74] B. Montgomerie. The need for more measurements. *Proc. Int. Energy Agency Aerodymanics Symposium, Rome*, 1990.

[75] P. Musgrove. European News. *Wind Directions*, 14(4):19–21, 1995.

[76] U.S. Paulsen. The impact of the induced velocity in the near flow field of a horizontal axis wind turbine. *RISØ National Laboratory, Report M-2835*, 1989.

[77] T.F. Pedersen and I. Antoniou. Visualisation of flow through a stall-regulated wind turbine rotor. *Proc. European Wind Energy Conference, Glasgow*, pp 83–89, 1989.

[78] C.J.D. Pickering and N.A. Halliwell. Speckle photography in fluid flows: signal recovery with two step processing. *Appl. Optics*, 23(8):1128–29, 1984.

[79] A.Y. Pope and J.J. Harper. *Low-speed wind tunnel testing.* Wiley and Sons, 1966.

[80] M. Raffel and J. Kompenhaus. Theoretical and experimental aspects of image-shifting by means of a rotating mirror system for particle image velocimetry. *Meas. Sci. Technol.*, 6:795–808, 1995.

[81] J.J. Riley, E.W. Geller, M.D. Coon, and J.C. Schedvin. A review of wind turbine wake effects. *Flow Research Company RLO/316080/1*, 1980.

[82] A. Rosen, I. Lavie, and A. Seginer. A general free-wake efficient analysis of horizontal axis wind turbines. *Proc. E.C. Wind Energy Conference, Madrid*, pp 264–268, 1990.

[83] J.N. Ross and J.F. Ainslie. Wake measurements in clusters of wind turbines using laser doppler anemometry. *Proceedings of the 3rd British Wind Energy Conference, Cranfield*, pp 185–194, 1981.

[84] H. Royer. Full 3-d measurements : the holographic approach. *Von Karman Institute for Fluid Dynamics, Lecture Series 1988-06*, 1988.

[85] J.M. Savino and T.W. Nyland. Wind turbine flow visualisation studies. *Proc. U.S. Wind Energy Conference, San Francisco*, pp 559–564, 1985.

[86] A.M. Scott. Wake interaction studies on the HWP-300/22 and WEG MS-1 wind turbine generators on Burgar Hill, Orkney. *James Howden & Co. Ltd*, 1987.

[87] F.J. Simoes and J.M.R. Graham. A free vortex model of the wake of a horizontal axis wind turbine. *Proc. 12th BWEA Wind Energy Conf., Norwich*, pp 161–166, 1990.

[88] D.J. Skyner. *The mechanics of extreme water waves.* PhD thesis, Edinburgh University, 1992.

[89] D. Smith and G.J. Taylor. Further analysis of turbine wake development and interaction data. *Proc. 13th BWEA Conf., Swansea*, pp 325–331, 1991.

[90] G.H. Smith, I. Grant, A. Liu, and D.G. Infield. Diagnostics of wind turbine aerodynamics for particle image velocimetry. *Proc. 12th BWEA Conf., Norwich*, pp 259–264, 1990.

[91] P. Surman. Wind Power makes its mark in Europe. *Physics World*, 8(10):29–32, 1995.

[92] A. M. Talmon. The wake of a horizontal-axis wind turbine model: measurements in uniform approach flow and in a simulated atmospheric boundary layer. *MT-TNO Report 85-010121*, 1985.

[93] G.J. Taylor. Full scale measurements in wind turbine arrays. *Proceedings of the European Community Wind Energy Conference in Madrid, Spain*, pp 154–158, 1990.

[94] G.J. Taylor. Wake measurements on the NIBE wind turbines in Denmark - part II - data collection and analysis. *CEC contract EN3W.0039.UK(H1)*, 1990.

[95] A. Thom. Blockage corrections in a high-speed wind tunnel. *Reports and Memoranda of the Air Research Committee, 2033*, 1943.

[96] D.J. Tritton. *Physical Fluid Dynamics.* Oxford University Press, 1988.

[97] L. van der Snoek. Wake and wind farm modelling. *Proceedings of the European Community Wind Energy Conference in Madrid, Spain*, pp 159–162, 1990.

[98] N-J. Vermeer and G.J.W. van Bussel. Velocity measurements in the near wake of a model rotor and comparison with theoretical results. *Proc. E.C. Wind Energy Conf, Madrid*, pp 218–222, 1990.

[99] P.E.J. Vermeulen. Studies of the wake structure of model wind turbine generators. *TNO Report 79-012904 Apeldoorn, Holland*, 1979.

[100] P.E.J. Vermeulen. An experimental analysis of wind turbine wakes. *Proc. 3rd Int. Symp. Wind-Energy, Copenhagen*, pp 431–450, 1980.

[101] L.A. Viterna and R.D. Corrigan. Fixed pitch rotor performance of large HAWTs. *DOE/NASA Workshop on Large HAWTs, Cleveland, Ohio*, 1981.

[102] A. Vogt, M. Raffel, and J. Kompenhans. Comparison of optical and digital evaluation of photographic PIV recordings. *Proc. 6th Int. Symp. on Appl. of laser techniques to fluid mechanics, Lisbon, Portugal*, 270:45–47, 1977.

[103] S.G. Voutsinas, K.G. Rados, and A. Zervos. On the effect of the rotor geometry on the formation and the development of its wake. *Wind Energy, Technology and Implementation - Proceedings of EWEC, Amsterdam : PART I*, pp 402–406, 1991.

[104] J. Westerweel and F.T.M Niewstadt. Laser speckle photography in a fluid medium. *Nature*, 270:45–47, 1977.

[105] C.E. Willert and M. Gharib. Digital particle image velocimetry. *Expts. in Fluids*, 10, 1991.

[106] R.E. Wilson and S.N. Walker. A fortran program for the determination of performance load and stability derivatives of windmills. Grant G1-41840, Oregon State University, Dept of Mech. Eng., 1974.

[107] C.S. Yao and R.J. Adrian. Orthogonal compression and 1-d analysis technique for measurement of 2-d particle displacements in pulsed laser velocimetry. *Appl. Optics*, 23(11):1687–1689, 1984.

[108] A. Zervos. Near and far wakes - parallel session report. *Wind Energy, Technology and Implementation - Proceedings of EWEC, Amsterdam : PART II*, pp 59–62, 1991.

# Bibliography

Prandtl, L.
*The Essentials of Fluid Dynamics*
Blackie, 1952.

Landau, L.D. and Lifschitz, E.M.
*Fluid Mechanics*
Pergamon Press, 1959.

van Dyke, M.
*An Album of Fluid Motion*
The Parabolic Press, p42, 1982.

## Publications


Whale, J. and Anderson, C.G. (1993)
*An experimental investigation of wind turbine wakes using Particle Image Velocimetry*
Proc. EC Wind Energy Conf. '93, Lübeck-Travemünde, Germany.

Whale, J. and Anderson, C.G. (1993)
*The application of PIV to the study of wind turbine wakes*
Proc. 5th Int. Conf. on Laser Anemometry, Veldhoven, The Netherlands.

Helmis, C.G., Whale, J., Papadopolous, K.H., Anderson, C.G., Asimakopolous, D.N. & Skyner, D.J. (1994)
*A comparative laboratory and full-scale study of the near wake structure of a wind turbine*
Proc. Europ. Wind Energy Conf.'94, Thessaloniki, Greece.

Whale, J., Helmis, C.G., Papadopoulos, K.H., Anderson, C.G.
& Skyner, D.J. (1995)
*A study of the near wake structure of a wind turbine comparing measurements from laboratory and full-scale experiments*
Submitted to ASME J. Solar Energy (accepted February 1996).